

(DRAFT)

Narrow-Beam Low Earth Orbit Communications and Stochastic Geometry: Non-Temporal and Temporal Interference Analysis

Ilari Angervuori

November 3, 2025

A?

Aalto University
School of Electrical
Engineering

One can assimilate a work of art, or, let us say, just a work, to the information we can put on a document, seal in a bottle which we will throw into the middle of the ocean. Will it ever be found? When and by whom and how will it be read, interpreted?

— Iannis Xenakis, *Formalized Music: Thought and Mathematics in Musics*, Pendragon Press, Hillsdale, NY, Pendragon Revised Edition, 1992.

Preface

[Some earlier efforts are] severely limited in usefulness, by lack of generality and physical insight, and a concomitant dependence on local, empirical data, and circumstances.

— David Middleton, [1].

While not downgrading other published stochastic geometry works on satellite networks (I have learned something new from each one that I have come across), inspired by David Middleton and his classics in the seventies, I have had an urge for simple (yet not simplistic) results that come with clear insight into whichever performance metric is of interest. Indeed, in my opinion, the purpose of mathematical analysis is to produce insight. Hence, instead of complex-looking equations, simple expressions are sought in the thesis—even though this would mean a trade-off between realism and accuracy. The crucial system model simplification in the thesis is the narrow-beam assumption for the receivers and the Poisson assumption for the random locations of the transmitters. The narrow-beam assumption enables us to model the Earth as an infinite plane, and that the spatial path losses are equal for all (relevant) transmitters, whereas the Poisson point process is the analytically simplest. However, these simplifications are not restrictive: a wonderful generality regarding the (actual) transmitter locations, fading conditions, orbital characteristics, and individual signal waveforms will be argued, and many results encapsulate a broad range of system settings into a reduced number of parameters. Of course, we can not go and merely trust in beauty and elegance as a measure of truth. In this regard, simulations go hand in hand with the simplified system model and analysis: the (more realistic) simulations verify to what degree, and within what parameter regimes, the analytical insights apply to the desired system model—which they do well under in the explored use cases. Unfortunately, even with the simplifications, we cannot avoid complicated equations: sometimes, the expressions become formidable, and either closed forms or analytical forms are difficult to acquire. However, even in

this case, the analytical results contain insight within the analytical inquiry itself. Such insight and intuition are out of the reach of artificial intelligence (which is, as of today, *computing*), and it has always been my ultimate goal in the years of my doctoral pursuit. I am confident that other stochastic geometry composers more or less agree with me. May the reader (and future) decide if I (we) have succeeded or not.

A considerable part of my explorations is constructed almost ex nihilo without many precursor works on the stochastic geometry analysis of satellite networks (I believe this is a characteristic of the doctoral labor), while also standing on the shoulders of giants and utilizing the tools and results from stochastic geometry analysis in terrestrial networks. As of today, I can refer to myself as a mathematically inclined communication engineer with a unique system-level perspective on wireless networks and a firm understanding of the LEO communication features.

Structure of the work

The thesis surveys recent research on narrow-beam LEO modeling and is structured into four chapters. The chapters are a synopsis and refinement of the most important results in [Publication II-Publication V](#), and also contain additional inquiry. The publication [Publication I](#) deserves to be referenced as a well-recognized pioneering work in stochastic geometry and LEO networks, preluding the other publications and the core subject of the thesis.

Chapter [1](#) is a general overview of the LEO and the stochastic geometry modeling of the LEO as well as terrestrial networks. Some general future challenges regarding the emerging satellite networks are discussed, and the most important stochastic geometry explorations are presented. Special attention is paid to the interference waveform modeling in terrestrial networks to emphasize that the differences in topology contribute to non-Gaussian waveform statistics, which deviate from our results. In this regard, to the best of our knowledge, the thesis covers novel work that addresses such waveform statistics in LEO networks, utilizing stochastic geometry analysis.

Chapter [2](#) introduces the temporal and non-temporal channel model proposed in the thesis, including fading, Doppler shift, and antenna attenuation. Coherence time and its dependence on the carrier frequency are carefully simulated and studied. Furthermore, the simplified planar Earth model, in which the mathematical analysis will be based, is formulated. It is compared to a spherical, more realistic system model. Essentially, the narrow-beam LEO BS assumption, which is an assertion that follows the entire thesis, validates the planar system model.

Chapter [3](#) introduces the non-temporal stochastic geometry analysis. In the first section [3.1](#), a mathematically precise characterization for the stochastic process is given, and in Section [3.2](#), the important properties of

the homogeneous PPP are introduced and studied. The reader familiar with the point process theory might skip these sections. The reader who is not familiar with the properties of the homogeneous PPP, but is not interested in the analytical details, can briefly familiarize themselves with the yellow-colored parts. Sections 3.1 and 3.2 do not contain new analytical results, but introduce partially contemporary analysis on the subjects. Section 3.3 onwards, we introduce and analyze the Gaussian projection process, which centers on the kernel of this thesis. The interference distribution is studied, as well as the signal-to-interference ratio (SIR), signal-to-interference-plus-noise ratio SINR, and throughput distribution. The meta distribution of the SIR is explored, as well as successive interference cancellation. Finally, an optimal satellite constellation density is proposed that maximizes the throughput. All approaches and the derived results in the chapter are novel work of the authors.

Finally, in Chapter 4, the temporal interference waveform is carefully studied through the correlation functions and the power spectral density (PSD). Interference cancellation techniques based on filtering reducible frequencies from the total received signal to improve the SIR are being put forth and analyzed.

Acknowledgments

Since year 2020, working with Dr. Niloofar Okati and Prof. Taneli Riihonen—for whom I am endlessly grateful for including me as an author in the outstandingly popular paper, despite my limited input—I have witnessed the emergence of the rise of stochastic geometry applications on the LEO networks. Initially, despite having no clear understanding of wireless networks, I did the necessary labor in studying the crucial concepts at undergraduate and graduate level courses on communication at Aalto University. The courses on probability theory and random graphs were also helpful.

I am grateful to my advising professor, Prof. Risto Wichman, for smelling this research gap and opportunity and for having the confidence in the freshly graduated mathematician that I was back then when he hired me.

English is not my mother language. Hence, the professional real-human language feedback has been invaluable; I wish to express my gratitude to Aalto University's language center for providing writing tutoring for my articles and this thesis. Furthermore, machine learning (ML) tools, artificial intelligence (AI), or more specifically, language model (LM) tools, namely Gemini®, Grammarly®, and ChatGPT®, have been beneficial in language checking and aid.¹

¹AI has increased my productivity and that of society as a whole. AI (as the broad umbrella term) has revolutionized many areas, such as programming and statistical inference of (noisy) data. AI and LM play an indistinguishable role in future technologies and will develop rapidly; it is worth learning to utilize the surplus value, regardless of the discipline one is practicing. This said, after the initial enthusiasm and overuse of LM tools, I have concluded that LM is not likely

I am infinitely gratified by the half-year research visit to the University of Notre Dame under the supervision of Prof. Martin Haenggi. Without the visit, the thesis would have much less novel contribution and value.

I want to express my gratitude to all my other colleagues with whom I have had eye-opening discussions and received invaluable feedback over the years. Thanks to Dr. Alexis Dowhuszko for the feedback on my first serious journal article as the first author. Worth mentioning is also Peitsa Pesola, with whom we have had long-lasting discussions in the areas of mathematics, delving into metamathematics and philosophy, and who has shared his MATLAB® and programming wisdom with me. Peitsa's motto "mathematica necesse est" is indisputable.

Lastly, I want to thank my family for the necessary support. Further, I thank all my friends for the constructive, sometimes heated, discussions on politics, philosophy, literature, music, poetry, and other ups and downs life has had to offer. Dr. Konsta Kotilainen is worth pointing out, not least because he mentioned me in the thesis as "a truth-seeking person". I may toss the same statement there.

Helsinki, November 3, 2025,

Ilari Angervuori

to replace human thought in the near or medium term. When it comes to the LMs and the language check, they have their weak spots in recognizing context and in approving (or producing) many style-related language usages that are otherwise accepted and standard within the discipline. Furthermore, I am perplexed by the ability of the AI tools to generate nonsense with endless confidence: the inability to admit "Good question, I have no direct answer, but maybe we can work this out together." Consequently, as of today, I try to avoid the direct use of LM in producing language (or any symbolic content) and use it merely as a grammar check and search engines, for which they are excellent if used with a grain of salt.

Abstract

Since 1981, the Nordiska Mobiltelefongruppen (NMT), new generations of cellular network technologies have emerged every tenth year. The 4th generation (LTE, 4G) developed into the 5th generation (5G), which is currently being implemented and actively marketed to customers as a fast mobile phone subscription option in Finland and all around the world. Furthermore, 6th generation (6G) technologies are actively being studied and designed in academia and industry, and, most likely, the development of wireless communication will continue beyond our comprehension horizon.

The 5G and 6G networks require more antennas, higher bandwidth, and a higher density of base stations. Particularly, this is the case with the Internet of Things (IoT). Often, they are composed of multiple tiers consisting of various types of devices; these networks are referred to as heterogeneous networks (HetNets), which can also exhibit scale-free (fractal) behavior. Furthermore, modern technology includes airborne network terminals, known as aerial base stations (ABSs), or non-terrestrial terminals (NTNs), which complement terrestrial networks. The low Earth orbit (LEO) satellites fall into this category. The most internationally recognized LEO system may be Starlink, which already offers terrestrial LEO terminals in the retail market. Another collaboration project is the Infrastructure for Resilience, Interconnectivity, and Security by Satellite (IRIS²), slated for deployment by the European Union (EU) by 2027. The LEO networks enhance capacity and connectivity, but also increase the complexity of the totality; the LEO introduces another tier and spatial dimension to HetNets. This drives the search for alternative comprehensive system-level analysis methods of cellular networks. Here, stochastic geometry analysis offers a viable option, modeling the network transmitters as random point patterns, i.e., point processes (p.p.'s), and exploiting the enormous mathematical toolbox available for the subject. While basic stochastic geometry formalism is well-established, it has only recently been applied to LEO.

We aim for clarity and insight into the results. We ultimately deliver an insightful, tractable, and simple (but not simplistic) framework for the stochastic geometry analysis of LEO networks and satellite base station (LEO BS) performance. The proposed novel stochastic geometry framework, modeling the Earth as a flat infinite plane, establishes access and utilization of the most sophisticated methods and results developed for terrestrial networks over the years. The studied performance metrics include the signal-to-interference ratio (SIR), signal-to-interference-plus-noise ratio (SINR), and Shannon throughput. Furthermore, the meta distribution of the SIR (SIR MD) is explored, which reveals fine-grained information about the reliability of the typical LEO BS. Further, we study the interference distribution. Regarding the design of the design of LEO networks, one of the crucial analytical insights arising in various works, including the

articles included in this thesis, is that for a given altitude of the LEO BSs, there exists an optimal density of the LEO constellation/Earth transmitters that maximizes the (Shannon) capacity of the network: Under the noise-limited channel and the transmitters forming a Poisson point process (PPP), there exist “an optimal average number of Earth transmitters inside a LEO BS – 3 dB footprint” that maximizes the average SINR and throughput. However, this density leads to highly varying instantaneous performance over the LEO BSs, which means that the network user terminals, which we consider as omnidirectional mobile user equipments (UEs), are not treated fairly. To tackle the highly varying performance, we introduce successive signal cancellation (SIC) and ALOHA medium access control (MAC) schemes. Many results are intuitive and insightful. For example, under broad network settings, the interference can be characterized by a gamma distribution, and the SIR follows a Lomax distribution.

In addition to the non-temporal analysis, we conduct a temporal analysis of the interference waveform. We derive closed-form estimations for the autocorrelation functions and the power spectral density (PSD). The analysis justifies that the interference is a stationary Gaussian process for which we propose a novel autocovariance model. While providing a simple (not simplistic) priori model for the LEO channel, the characterizations are utilizable in modern statistical signal processing in LEO networks operating on Gaussian interference models, including those that utilize machine learning (ML) or artificial intelligence (AI).

The results enlighten the system-level characteristics of the network, ultimately allowing for more efficient allocation of simulation resources. The stochastic geometry analysis expands our comprehension and insight into the LEO networks as they become increasingly dense, and as terrestrial networks expand to high frequencies, causing interference in the frequency bands currently operated only by NTNs. The analysis guides us into the intriguing mathematical realms, such as Lévy processes, power laws, and Gaussian processes. The results benefit coding, system-level design of the LEO communication systems in various MAC schemes, and signal processing. As a by-product, even a purely mathematical novel result is presented regarding the generalized hypergeometric function.

Contents

Preface	5
Contents	11
List of Publications	15
Author's contributions	17
Abbreviations	19
Symbols	23
1. Introduction	27
1.1 Suspicions	27
1.1.1 Privacy	28
1.1.2 Environment and space sustainability	28
1.1.3 Health	29
1.2 Motivation of thesis	29
1.2.1 Contributions of the thesis	31
1.3 Random variables, probability and stochastic processes	31
1.3.1 Randomness in communication	34
1.4 Stochastic geometry analysis and wireless networks	36
1.4.1 Stochastic geometry analysis of Terrestrial networks	36
1.4.2 Stochastic geometry analysis of LEO networks	39
2. LEO System Modeling	41
2.1 Antenna beams	42
2.1.1 Earth transmitter antennas	42
2.1.2 Satellite base station antennas	43
2.2 Spherical system model	45
2.3 Planar system model	47
2.3.1 Planar model vs. spherical model	50
2.4 Satellite (LEO BS) locations	52

2.5 User equipment (UE) locations and interference	52
2.5.1 Incarnation of the homogeneous Poisson point process	53
2.6 Monte Carlo simulation of the Poisson point process on the plane and sphere	55
2.7 Doppler shift, antenna attenuation, propagation delay, coherence time, and multipath fading	55
2.7.1 Multipath fading and the non-temporal distributions	59
2.7.2 Temporal fading characteristics	62
2.7.3 Antenna attenuation due to satellite movement	63
2.7.4 Doppler shift due to the satellite movement	64
2.7.5 Fading correlation time	66
2.7.6 Simulated example of a Narrow-beam LEO Rician chan- nel response of a sinusoidal signal	67
3. Non-temporal analysis of the narrow-beam LEO	75
3.1 Mathematical formulation of stochastic processes	75
3.2 Homogeneous Poisson point process	78
3.2.1 Palm calculus	79
3.2.2 Stationarity and ergodicity	82
3.2.3 Campbell's formula and probability generating functional	83
3.3 Gaussian projection process	84
3.4 Total interference and the central limit theorem	93
3.5 Factorial moment measure	104
3.5.1 Order statistics	104
3.6 Signal-to-interference-plus-noise ratio	105
3.6.1 SIR of the nearest transmitter	106
3.6.2 SINR of the nearest transmitter	108
3.6.3 SIR of the strongest transmitter and SIR order statistics	110
3.6.4 Successive interference cancellation	113
3.7 Meta distribution of the SIR	120
3.8 Throughput and optimal constellation density	126
4. Temporal analysis of the narrow-beam LEO	129
4.1 Correlation functions of the total interference	131
4.2 Power spectral density	137
4.3 Interference cancellation: Filtering the reducible fre- quencies	138
4.3.1 Exploiting the multipath fast-fading: Average SIR in the spread spectrum	138
4.3.2 Filtering the spread frequencies	139
4.3.3 Frequency domain interference cancellation of the an- tenna attenuation components	142
References	153

Publications

161

List of Publications

This thesis consists of an overview and of the following publications which are referred to in the text by their Roman numerals.

- I** A. Yastrebova and I. Angervuori and Niloofar Okati and Mikko Vehkaperä and Marko Höyhtyä and Risto Wichman and Taneli Riihonen. Theoretical and Simulation-based Analysis of Terrestrial Interference to LEO Satellite Uplinks. In *IEEE Globecom*, Taipei, Taiwan, 2020, pp. 1-6, doi: 10.1109/GLOBECOM42002.2020.9347980, 2020.
- II** I. Angervuori and R. Wichman. A Closed-Form Approximation of the SIR Distribution in a LEO Uplink Channel. In *IEEE Globecom Workshops (GC Wkshps)*, Rio de Janeiro, Brazil, 2022, pp. 856-861, doi: 10.1109/GCWkshps56602.2022.10008485, 2022.
- III** I. Angervuori, M. Haenggi and R. Wichman. Meta Distribution of the SIR in a Narrow-Beam LEO Uplink. *IEEE Transactions on Communications*, vol. 73, no. 9, pp. 8260-8273, Sept. 2025, doi: 10.1109/T-COMM.2025.354773, 2025.
- IV** I. Angervuori and R. Wichman. Order statistics of the SIR and Interference Cancellation in a Narrow-Beam LEO Uplink. Submitted to *IEEE Letters on communications*, 2025.
- V** I. Angervuori, A. Afridi and R. Wichman. Spatial and Temporal Correlation of the Interference in a Narrow-Beam LEO network with ALOHA Medium Access Control. Submitted to *IEEE Letters on communications*, 2025.

Author's contributions

Publication I: “Theoretical and Simulation-based Analysis of Terrestrial Interference to LEO Satellite Uplinks”

The system model, analysis, part of the introduction section, and numerical results (apart from the STK simulations) are by the author.

Publication II: “A Closed-Form Approximation of the SIR Distribution in a LEO Uplink Channel”

All of the text, analysis, and simulations are by the author, with valuable feedback from other authors.

Publication III: “Meta Distribution of the SIR in a Narrow-Beam LEO Uplink”

All of the text, analysis, and simulations are by the author, with valuable feedback from other authors.

Publication IV: “Order statistics of the SIR and Interference Cancellation in a Narrow-Beam LEO Uplink”

All of the text, analysis, and simulations are by the author, with valuable feedback from other authors.

Author's contributions

**Publication V: “Spatial and Temporal Correlation of the Interference
in a Narrow-Beam LEO network with ALOHA Medium Access Control”**

All of the text and analysis, excluding part of the introduction section, is by the author, with valuable feedback from other authors.

Abbreviations

4G Fourth generation

5G Fifth generation

6G Sixth generation

ABS Aerial base station

AEA Average envelope amplitude

AI Artificial intelligence

AirComp Over-the-air computation

ALOHA ALOHA random access control

ASIR Average-signal-to-average-interference ratio

AWGN Additive white Gaussian noise

AWN Additive white noise

BS Base station

BPSK Binary phase shift keying

CASIR Average-signal-to-average-canceled-interference ratio

CCDF Complementary cumulative distribution function

CDF Cumulative distribution function

CDMA Code division multiple access

CLT Central limit theorem

EU European Union

GHG Greenhouse gas

Abbreviations

GP Gaussian projection process (also, gain process)

HOS Higher-order statistics

ICT Information and communications technology

ITU-R International Telecommunication Union recommendations

LEO Low Earth Orbit

LEO BS Satellite BS

LM Language model

LoS Line-of-sight

LTE Long term evolution

MA Moving average

MAC Medium access control

MANET Mobile ad hoc network

MIMO Multiple-input and multiple-output

NT Nearest transmitter

NLoS Non-line-of-sight

NMT Nordiska Mobiltelefongruppen

NOMA Non-orthogonal multiple access

NTN Non-terrestrial network

NSR Noise-to-signal ratio

PDF Probability distribution function

PGFL Probability generating functional.

PPP Poisson point process

p.p. Point process

QoS Quality of service

r.v. Random variable.

SBS Satellite BS (same as LEO BS)

SIC Successive interference cancellation

SIC-SIR The SIR with successive interference cancellation

SINR Signal-to-interference-plus-noise ratio

SIR Signal-to-interference ratio

SIR MD Meta distribution of the SIR

STIR Signal-to-total-interference ratio

STK Satellite system toolkit

UAV Unmanned aerial vehicle

UE User equipment

UN United Nations

WN White noise

Symbols

\mathbb{R}^d Euclidean d -dimensional space

\mathbb{R}^2 The Euclidean plane

$A \cap B$ Intersection of the set A and B

$A \cup B$ Union of the set A and B

$A, B \subset \mathbb{R}^d$ Sets in \mathbb{R}^d

$|A|$ The Lebesgue measure (area) of A

\mathcal{F} A family

\mathcal{A} An event $\mathcal{A} \in \mathcal{F}$

$\mathbb{P}(\mathcal{A})$ Probability of the event \mathcal{A}

x A point location in \mathbb{R}^d

$\|x\|$ Euclidean norm

Φ Homogeneous Poisson p.p. (PPP) on \mathbb{R}^d

Ψ Homogeneous PPP on the (spherical) Earth surface

$\Phi(A)$ A random counting measure on A

$\Phi(t)$ The homogeneous PPP at time t

$\Phi + x$ The PPP with each point translated by x

$\Phi_x^!(A)$ Palm distribution on A conditioned at x

\mathcal{G} The GP

$\mathcal{G}(t)$ The GP at time t

\mathcal{G}_1 The gain process with deterministic H

Symbols

$\lambda(t)$ Density of a p.p. at $t \in \mathbb{R}^d$

$\Lambda(A)$ Expected number of points in $A \subset \mathbb{R}^d$

κ A parameter that reflects the approximate mean number of UEs inside a LEO BS -3 dB footprint

$\tilde{\kappa}$ The GP parameter; $\kappa / \log(2)$

$\mathfrak{G}_{\mathcal{G}}(f)$ The PGFL of \mathcal{G} at $f(\cdot)$

x, X A point in Φ or \mathcal{G}

$x_{(k)}, X_{(k)}$ An ordered point in Φ or \mathcal{G}

$X_{\{k\}}$ An non-ordered point in \mathcal{G}

B Bandwidth

$[^b_k]$ Unsigned Stirling number of the first kind

$C(\tau)$ Autocorrelation function at the time lag τ

$K(\tau)$ Autocovariance function at the time lag τ

$D(x, \delta)$ A disc of radius δ centered at x

h Altitude of the LEO BSs

ϵ Elevation angle of the LEO BSs

φ_x The angle of the transmitter x in the antenna gain pattern of the LEO BS

φ_{RX} Width of the -3 dB gain

$D_{h,\epsilon}$ A scaling constant of $\|x\|$; $D_{h,\epsilon} = \sin^2(\epsilon)/h$

$D_{h,\epsilon,\varphi_{RX}}$ An expanded scaling constant $(D_{h,\epsilon}/\varphi_{RX})^2$

o The origo (origin) of \mathbb{R}^2 ; the center of the LEO BS footprint, *i.e.*, the antenna boresight location on the Earth surface

o_E The origo (origin) of the spherical Earth surface; the center of the LEO BS footprint, *i.e.*, the antenna boresight location on the Earth surface

$d_{h,\epsilon}$ The distance between the LEO BS and its footprint center (o_E) in the spherical model

ξ The central angle between o_E and the LEO BS in the spherical model

$\hat{d}_{h,\epsilon}$ The distance between the LEO BS and its footprint center (o) in the planar model

f_c Carrier frequency

f_m	Modulation frequency
f_{Dsat}	Doppler shift
$f_{(n)}(x_1, \dots, x_n)$	The PDF of the n th order statistics
$F_X(t)$	The CCDF of X at t
$G(\varphi)$	A Gaussian antenna gain
X	A random variable
\mathbf{X}	A random vector
$\mathbb{E}(X)$	Expectation value of X . Same as: average and mean
$\text{var}(X)$	Variance of X
$\mathcal{L}_X(s)$	Laplace transform of X at $s \in \mathbb{C}$
$I = I(t)$	Total interference at the typical LEO BS at time t
$I_{\text{AEA}}(t)$	Total interference AEA at the typical LEO BS at time t
$I_{\text{AEA-LoS}}(t)$	Total interference AEA LoS component
$I_{\text{AEA-MP}}(t)$	Total interference AEA fading component
$Y_x = Y_x(t), y_x$	A WN signal of the transmitter x
$H_x = H_x(t), g_x, h_x$	An amplitude or power fading gain of the transmitter x
K	The Rician fading parameter
$f(\cdot)$	A function
$\text{Li}_{2-k}(\cdot)$	Polylogarithm
$\text{triang}(\cdot)$	Triangular function
$M^{(n)}$	The n th factorial moment measure
$M_b(\theta)$	b th moment of the SIR meta distribution
$\mu^{(n)}$	The density of the n th moment measure
ν	Complementary atomic measure at zero of the defective exponential r.v.
p	ALOHA parameter
R_\oplus	Radius of the Earth
μ	Mean
σ^2	Variance

Symbols

$\vec{v}_{\text{sat,rel}}$ Relative velocity of the LEO BSs

v_{sat} Orbital speed of the LEO BSs

$\mathbf{1}(\mathcal{A})$ The identity function of the event \mathcal{A}

τ_c Fading coherence time

τ_a Antenna gain coherence time

\mathcal{T} Shannon throughput

θ SIR threshold for a successful transmission

1. Introduction

Stochastic geometry is widely used for the analytical study of the performance of Cellular networks, including terrestrial and non-terrestrial networks (NTNs), as well as mobile ad hoc networks (MANETs). Access controls, such as ALOHA random medium access control (MAC) or code division multiple access (CDMA), are feasible for stochastic geometry study, in uplink and downlink [2]. The stochastic geometry also links to random graphs and percolation theory in the routing protocol models. These routing protocol models are also applicable to inter-satellite communication, as proposed in [3] and [4]. The subject of this thesis is in the interference characterization, more specifically in the low Earth orbit (LEO) uplink (other interpretations are possible), and fundamentally in the resulting statistics of the SIR and the SINR.

The primary topic of the thesis is in mathematically oriented technical analysis and signal processing. However, before we delve into the kernel topics of the thesis, let us take a brief look at the topical social and environmental challenges (and solutions) that the LEO networks, and information and communications technology (ICT) in general, face.

1.1 Suspicions

As of 2025, from a mobile phone end-user perspective, the LTE (or 4G) network performs (almost) as well as 5G in video and audio streams and calls. Practically, this applies to all typical modern use cases—possibly with the exclusion of real-time online gaming. Perhaps this is the reason why some people have taken the suspicion of new cellular network technologies to the level of physical outrage towards the 5G base stations in Great Britain, the Netherlands, Sweden, and even Finland [5]. Apart from being a money-making machine, an idealistic world-bettering pursuit, and at least an exciting engineering challenge, modern ICT systems raise multiple concerns regarding sustainability, health, and privacy.

1.1.1 Privacy

In authoritarian-inclined countries, such as China or Russia, the improved connectivity is engaged in Orwellian-like surveillance, propaganda, and censorship. Neither are the democratic countries protected against information warfare, neither from outside the border nor within. Apart from foreign attempts to influence public discourse, ICT giants, such as Google®, Apple®, and Meta®(formerly Facebook®), have an incentive to gather as much information as possible about their customers. The latter security problems have been recognized by, for example, the European Union (EU), which has implemented numerous restrictions for the companies [6]. There are some options for these services, essentially based on open (or free) source, relying on crowdfunding, such as Signal®, Librem®and Jolla®, of which the latter two has a respectable mission to provide ambiguity and uncompromising security across both the smartphone, tablet, and laptop software *and hardware* [7]. Unfortunately, these products are currently left in the margin, and cannot seriously challenge the status quo of the more commercially driven companies. In fact, arguably, the ICT companies have become more powerful than most national states [8]. Some authors go as far as claiming the new era of techno feudalism [9]. Even though one might argue that attempts are being made to improve security in proprietary platforms, such as WhatsApp®, have been addressed, their use for the most sensitive messaging is not advised [10]. To the best of my knowledge, no convincing reason exists for the use of proprietary software other than its popularity among users. On the contrary, open and free source software should be utilized for transparent privacy and safety, which is very easy to do.

Further, a privacy challenge, which will be increasingly important in the near future, is quantum cryptography. In this regard, quantum technologies, including post-quantum cryptography, are also being widely implemented in the NTNPs [11].

1.1.2 Environment and space sustainability

The 5G systems are power-hungry. The carbon emissions from the ICT industry have been steadily growing and globally contributed 2 percent by year 2012 of the total greenhouse gases (GHG) with a GHG footprint close to 55 GtCO₂e [12] by year 2020. This issue has been well-recognized in the academic literature, and ideally, energy efficiency is taken as a serious performance metric in the design and practical implementation of communication networks. Energy efficiency can be improved by technologies such as multiple-input and multiple-output (MIMO), which enhance the quality of service (QoS) by increasing the number of antennas instead of the transmission power [13]. Furthermore, beamforming, such as reconfigurable

phased array antennas and multibeam architectures, can reduce power consumption in LEO networks [11].

Each collision then creates more fragments, in a runaway cascade that turns low Earth orbit into a hazard zone.

— Margo Anderson, [14].

Space debris, or space-junk, is non-functional man-made objects that orbit the Earth. In the LEO networks, in addition to the aesthetic effect on the night sky (which potentially will be populated by hundreds of flickering light dots, ruining the night sky, and even posing challenges to terrestrial astronomy), the uncontrolled collision of the satellites leads to a whirlwind of dead metal shards and other tumbling debris, which poses a challenge as the constellations scale up in size. While there are guidelines by the United Nations (UN) and European Union (EU), as well as by individual countries, such as Finland, a functional international debris management system is yet to be established [11].

1.1.3 Health

High energy radiation is harmful in excess; however, 5G base stations are not likely to cause health harms as long as the potential risk is taken seriously [15]. The high frequency means that the signals are prone to significant attenuation.

In the mental perspective, platforms, such as TikTok® or X® (formerly Twitter®), have led to fragmentary information delivery driven by black-box algorithms meant by construction to be addictive, causing political polarization and personal problems, such as anxiety and depression [16]. Recently, the media has reported how, at least in the Western world, people are increasingly dependent on their phones. While, say, twenty years ago, people hardly had mobile phones before high school, in this era, the children master sweeping and scrolling before they exit kindergarten [17]. Human kind is still adapting to the new era of chronic mobile phone use, and the effects on the mental faculties are to be taken seriously.

1.2 Motivation of thesis

Satellites could be used as backup connections especially in locations where terrestrial network is not available.

— Marko Höyhtyä et. al., [11].

This is one motivation for the emergence of the LEO networks, which are

being widely implemented, and the trend is unavoidable. The potential of the LEO networks increases the capacity of the network, which is crucial, especially in far-flung areas. Combining such networks with terrestrial networks can facilitate a seamless coverage continuum [18]. Many LEO network projects are already being developed and planned, including Starlink, Kuiper, LeoSat, OneWeb, Telesat, and IRIS². Furthermore, 3GPP aims to adapt existing satellite and terrestrial networks to provide direct connectivity from hand-held equipment to LEO satellites using frequencies assigned to mobile satellite services or those assigned to legacy terrestrial networks. Optimizing the performance of the LEO networks requires a deep understanding of their fundamental nature. Especially in the ever-denser networks, the design requires in-depth simulations. These simulations become quickly cumbersome to implement, and extracting statistically significant insight is laborious in the case of multiple tiers of base stations, users, and other terminals. In this regard, [Stochastic Geometry](#) provides a tool for tractable analysis: For example, megaconstellations can be modeled by random point processes, and the enormous mathematical toolbox of the field can be exploited. This enables more efficient allocation of simulation resources and better design of the LEO networks.

As of today, multiple interesting properties of the LEO networks have emerged from a stochastic geometry analysis perspective, labored by various authors. These properties include the existence of an optimal network density of co-channel Earth transmitters and satellite constellation that maximizes the average network speed, *i.e.*, the average (Shannon) capacity, also called throughput, by which we refer to as the information theoretical maximum rate of data bits per unit time (sometimes further normalized by the channel bandwidth; spectral efficiency) that is possible to be transmitted through the terrestrial-LEO link. A crucial observation is that the dense LEO networks can be modeled as random point patterns, random point fields, or, as we refer to them in this work, point processes [19]. For example, a Walker constellation can be accurately modeled with the Binomial p.p. (BPP) or the Poisson p.p. (PPP), which lies at the core of stochastic geometry theory. Furthermore, if we assume that the constellation density is constant (locally, this holds for a large class of constellations), we can use the homogeneous PPP, which is the simplest and best-known (non-trivial) point process. Moreover, with a narrow-beam LEO BS antenna, we can use a planar Earth model approximation, even more simplifying the analysis. The Earth transmitters can also be modeled as a homogeneous PPP, especially if we assume independent mobility patterns, leading to the independent instantaneous locations characterized by the PPP. These simplifications in the system model yield a tractable and simple, yet useful, insight.

Although not yet utilized as a standard method throughout the industry (which, arguably, is the aspiration rather than merely an academic exercise), we confidently say that the stochastic geometry analysis of the LEO com-

munication networks benefits other system-level and link-level simulation and analysis methods. It conveys insight into increasingly complex communication systems, ultimately enabling better system design and optimal allocation of simulation resources in the forthcoming 5G, 6G, and beyond projects.

1.2.1 Contributions of the thesis

This thesis proposes a novel tractable statistical analytical framework for the stochastic study of the LEO network performance. The results bring insight into the network design, deepening the intuitive understanding of LEO communication. Furthermore, the interference models put forth a priori estimations that are useful in statistical signal processing.

Is the Gaussian prior a reasonable prior interference model or not?

This is one of the questions we give an enlightened answer to: Yes, it is.

The novel contribution of this work is a narrow-beam LEO uplink with Poisson distributed Earth transmitters. The narrow-beam (which is realistic, considering the actual LEO networks) assumption simplifies the system model and enables analytically tractable stochastic geometry analysis. While some of the expressions are complicated, we produce strikingly insightful and intuitive results; for example, the SIR has a characterization as the Lomax distribution, leading us into the realm of heavy-tailed distributions and even power laws. Furthermore, the non-Gaussian statistics are common in the earlier stochastic geometry studies on the *terrestrial* networks. However, due to differing topology, this does not apply to the LEO networks (as far as it goes in the proposed stochastic geometry model). These findings are not just mathematical artifacts. The statistical properties have practical implications, for example, on the likelihood function in Bayesian inference, which plays a crucial role in modern ML and AI-aided signal processing. The stochastic geometry analysis of the LEO networks reveals how the quantitative and qualitative statistical characteristics arise from the properties (topology, density, fading, *etc.*). This thesis provides a novel framework for the design of future dense LEO networks, and provides a temporal and non-temporal inquiry of the interference and various performance metrics.

1.3 Random variables, probability and stochastic processes

While it is debated if reality is deterministic or not, there is consensus that worldly phenomena are causal. In the following, we ponder the motivation for the random modeling of natural and man-made phenomena.

For it is impossible for anything to come into being without cause.

— Plato, *Timaeus*.

However, the cause does not have to be a deterministic object occupying a definite location in the spatial domain and time but can exhibit uncertainty, which we call randomness. To be more precise, randomness is commonly interpreted as a practical characterization of a, *in principle*, deterministic system when we have limited knowledge about its spatial and/or temporal states and/or which exhibit chaotic behavior, *i.e.*, arbitrary small changes in the initial state cause large dispersion in the outcomes. For example, for a flipper, the outcome, also called a *random event* or *realization*, of the coin flip is the cause of all her actions. Unless the flipper is a talented cheater (or *Laplace's demon*), the face upon which the coin will land is unpredictable, *i.e.*, random, or one could say, *pseudorandom* (because it is ultimately a deterministic, Newtonian system). Namely, in addition to the energy of the airborne coin spanned by a million muscle tensions, every little breeze of wind or roughness in the landing site, *etc.*, contributes to the realization of the coin toss; hence, its prediction is practically impossible. Alternatively, one can prevent cheating altogether by, instead of using a coin, by using pure randomness, *e.g.*, a quantum flipper. Namely, there are physical examples where the system randomness seems as inherent and as inseparable fundamental property as the causality: quantum mechanics.¹

The terms *random* and *stochastic* are often used interchangeably; however, we can understand the former to describe the nature of the phenomena, and the latter refers to the statistical modeling approach of it. The word “stochastic” stems from the Creek *stochos*, meaning a kind of target, goal, or aiming at a mark: a stable state, described by statistics, towards which the system asymptotically develops under the law of large numbers—after sufficiently many (infinitely many) flips of a fair coin, *almost surely* 50% of the flips land to heads, and 50% land to tails. This is the statistical description, or the *probability distribution*, of the r.v. and the *stochastic process* representing a coin flip. Interpretation of the probability has nothing to do with the mathematical formulation of its distribution: Whether a r.v. is purely random or merely pseudorandom is irrelevant.

Often, deterministic and stochastic approaches are to varying extents intertwined. Weather forecasting is an excellent example of this: the chosen initial conditions uniquely determine the outcome of the (deterministic) Navier-Stokes equations that are solved numerically. However, in practice, we can not avoid the uncertainty in the initial conditions (because of the

¹A reductionist reducing the coin flip to quantum mechanics could point out here that also the coin flip (and everything, in that manner) is fundamentally purely random and indeterministic. However, there is an antithesis to this: despite challenging drawbacks of the *hidden variables* theories, as of today, many have argued that quantum randomness is also only a manifestation of our limited knowledge of the underlying, deeper, deterministic reality.

limited accuracy of the measurement devices and their limited allocation resolution). Hence, it is often said that something like “it is raining next Tuesday with the probability p ”, which is based on the observation that the fraction p of the initial conditions led to rain on Tuesday in the simulations. Vaguely speaking, this is a Bayesian, subjective interpretation of the probability: the probability describes the uncertainty in our knowledge. On the contrary, a frequentist assigns a probability only to repeatable events: for example, the coin toss (one can hardly call the weather *next Tuesday* a repeatable event—however, the weather *each year on the first Tuesday of May* is such). Unfortunately, the chaotic nature of the equations and the actual weather system they describe will make the different solutions *blow up* all over after a finite time: because of the butterfly effect, the deterministic approach, with the unavoidable uncertainty to the initial conditions (however, how small), the equation do not, in practice, provide any meaningful information about the weather, say, after a year. To make predictions of the weather after one year, we can abandon the mechanistic Navier-Stokes equations (even though mechanistic climate models *can be* helpful here) and study the historical distribution of rainy days at a given location over a given season.

Let us get back to the weather example, and set X = “the daily total rainfall in the typical city in Finland in November”. But sometimes, there is no direct access to the desired X . Maybe we only indirectly observe; “the average monthly rainfall is 60 mm in *the typical* city of Finland in November”.² Alternatively, we could observe; “the average monthly November rainfall in the Finnish cities is 60 mm; furthermore, 90% of the days contribute to half of the total rainfall.”³ Unfortunately, neither example delivers exhaustive information on X . The former provides only information about the *average* rain, synonymous with the *mean* and *expected value*, or the first moment $\mathbb{E}(X)$. On the contrary, fortunately, the latter includes additional information, on which we can rely for educated estimates of the rainfall statistics. Namely, the sporadic nature of the heavy rains indicates that the rain is *not* uniform over the days: should the three days of the month contribute to 30 mm of rain out of 60 mm, either some days are dry or the rain is moderate. We can infer that the variance is likely to be large. This may also suggest a high skewness, even high kurtosis (determined by the first four moments $\mathbb{E}(X)$, $\mathbb{E}(X^2)$, $\mathbb{E}(X^3)$ and $\mathbb{E}(X^4)$), *i.e.*, a kind of heavy-tailed behavior. The heavy-tailed rain distribution can be the case if the area is prone to storms that cause sporadic but outstandingly heavy rainfall. *Order statistics*, which are also under study in this thesis, would

²The term “the typical city” tacitly refers to a (here, unrealistic) assumption that the rain r.v.’s are identical and independently distributed (i.i.d.) in each city. We will return to this concept later in the context of stationary p.p. in the form of *the typical point*.

³The rainfall statistics serve as an example and are not intended to be precise.

describe the distribution of the heaviest daily rainfall, the second heaviest, *etc.*

In other words, by educated statistical inference, we can make refined predictions of the distribution of X even though X is not fully characterized by the observational data, which describes only $\mathbb{E}(X)$ plus some information about the higher moments, as in the Finnish weather example. From the moments, we can predict properties such as “the average number of days that one needs a raincoat in November in Finland”, which event can be formulated simply as “the probability that there is rain during a day in a Finnish city in November”. On the contrary, more fine-grained statistics, such as “the probability that it is raining in the morning, conditioned that it will rain during the day” can not be inferred from the information at hand.

1.3.1 Randomness in communication

The weather analogy goes along with the wireless networks: we can solve the Maxwell equations (in a time-stationary case, the simpler Helmholtz equation might suffice) for each electromagnetic wave carrying the signal of the base stations in predetermined locations, and determine the signal propagation properties in a given environment at a receiver at a given location. In the lack of full information, we can also utilize stochastic Maxwell equations that impose randomness into the scope of the model. Even though the Maxwell equations are *linear*, *i.e.*, we might be able to avoid the chaotic behavior (unless we take the properties of the conducting materials involved seriously), solving such models is time-consuming and lacks general insight. Hence, possibly based on models involving partial differential equations or empirical measurements, we may use simpler statistical models. For example, one might observe that “the base station (BS) locations follow the Poisson point process (PPP) and their signal powers follow an exponential distribution after the random propagation.” The mentioned random fluctuation of the signal powers caused by the random propagation is often referred to as the fading. As with the weather example, the statistics can depend on the spatial and temporal resolution: for example, the locations of two distinct transmitters become indistinguishable from the perspective of a radio wave receiver within the scales of the *coherence length*, which is proportional to the second exponent of the wavelength, reflecting the distance within which the fading of the two signals are strongly correlated.

It is crucial to recognize the limitations and choose the appropriate model and meaningful performance metrics. For example, the distribution of the instantaneous received signal waveform is not the same as the distribution of the average signal over a time window, or a use period. This distinction becomes clear if the instantaneous power of additive Gaussian white noise (AWGN) is contrasted to its average power over a time window, which

is a constant. Both metrics are relevant, depending on the application. The exponential fading model corresponds to the Rayleigh fading model, which is typical of, say, cellular urban networks, lacking any line-of-sight (LoS) connection between the BSs and their served transmitters, and all components of a signal arrive at the receiver through multipaths in random phases. In such an urban scenario, the PPP locations of the BSs have been shown empirically to be feasible in large cities, *e.g.*, in Sydney [20].

Through the point processes, we are drawn into the realm of stochastic geometry. Stochastic geometry studies random geometrical structures, which exhibit stochastic behavior. At the heart of stochastic geometry are, indeed, the p.p.'s, which generate random spatial patterns, including random tessellations or graphs representing cells and connectivity in communication networks—such as spatial phenomena like the random structure of human tissue or, for example, a rock. In one dimension, the spatial notion is often replaced by time, such as in queuing theory models. The p.p.'s can also be spatio-temporal, occupying space and time. The PPP represents “complete spatial randomness”, which can be made mathematically precise by *Palm conditioning*, but has the clear intuition that the points are independently located: one cannot draw any additional information about the position of a point from knowledge of the position of another point, or several points. The concept boils down to the *exponentially distributed* distance between each pair of the nearest points, which have the key property of being *memoryless*. These kinds of phenomena exist all over the world, not restricted to “natural” processes. These include radioactive decay, grocery store queues, the locations of the water drops in a paddle, and, indeed, the locations of the base stations or mobile phone users in a cellular network. However, as with almost every random phenomena modeled by the PPP, it is merely an approximation that hold up to certain scale: the people are more likely to choose a queue with less people in it, two water drops merges into one another if sufficiently close, and the mobile phone devices or base stations are not arbitrarily close to each other in the real-world (sensical) scenarios. As such an approximation, the PPP is analytically most tractable and well-studied. (The statistical independence, in fact, simplifies the analysis in many cases, not only in the case of stochastic processes, but generally in probability theory.) Unless we have an explicit description of the underlying laws that make a p.p. non-Poisson, introducing a *correlation* structure in the point process can be inappropriate, and the PPP is the best initial guess (in my opinion). Furthermore, in the context of wireless networks, random attenuation of signals and independent mobility patterns can cause a point process to exhibit Poisson statistics, even though the initial process is not PPP (see Section 2.5.1).

1.4 Stochastic geometry analysis and wireless networks

In this section, an overview of stochastic geometry in the modeling of communication networks is provided. We present a historical overview of the stochastic geometry works on interference characterization, SINR, and throughput in terrestrial wireless systems. The terrestrial networks are included for comparison and as a necessary basis for the stochastic geometry study of the LEO networks. Let us present some of the most relevant stochastic geometry works in terrestrial networks, as well as comprehensive sources for the analysis in LEO networks.

1.4.1 Stochastic geometry analysis of Terrestrial networks

The modeling of the interference and analytical study of the interference using the PPP dates at least back to the seventies and David Middleton's seminal work on the subject [1]. He derives distributions for the envelope of electromagnetic interference in three different scenarios that are characterized by the impulsiveness of the interference. These distributions are referred to as Middleton class A, B, and C distributions. The class A distribution represents interference that occurs if the interference source is narrow-band w.r.t. the receiver and there are "gaps in time" in the envelope (after the receiver's ARI filter stages), class B represents the interference of a broadband case, and class C is a combination of the classes A and B. In both classes, the interference is characterized by its "impulsivity", Gaussian waveform statistics and Rayleigh distributed envelope being at the lower end regarding the impulsivity. An essential analytical and empirical observation is that, indeed, the interference does not always have Gaussian form—even in the case of an infinite number of interference sources, when one could first expect that the conditions (sufficiently, the Lindeberg's condition [21]) for the central limit theorem would hold.

One of the more recent studies where the PPP is used to model the locations of interferers to characterize the interference waveform is [22]. Assuming signals with finite expected amplitude and singular path loss, the in-phase and quadrature components of the interference waveform are i.i.d. and follow the α -stable distribution [23] with the parameter $0 < \alpha \leq 2$, depending on the path loss exponent. While $\alpha = 2$ corresponds to the Gaussian distribution, for $\alpha < 2$, the interference waveform is "heavy-tailed", having infinite variance. Furthermore, the mean of the α -stable distribution is infinite for $\alpha < 1$, corresponding to severely impulsive interference. Similarly, in [24], Gaussian, Middleton class A, and α -stable distributions are compared in approximating the interference in cellular networks with various topologies, the interferers located either on the entire plane \mathbb{R}^2 , inside a finite-area annular region or outside a finite annular region (*i.e.*, there is an exclusion zone around the receiving transmitter). The α -stable

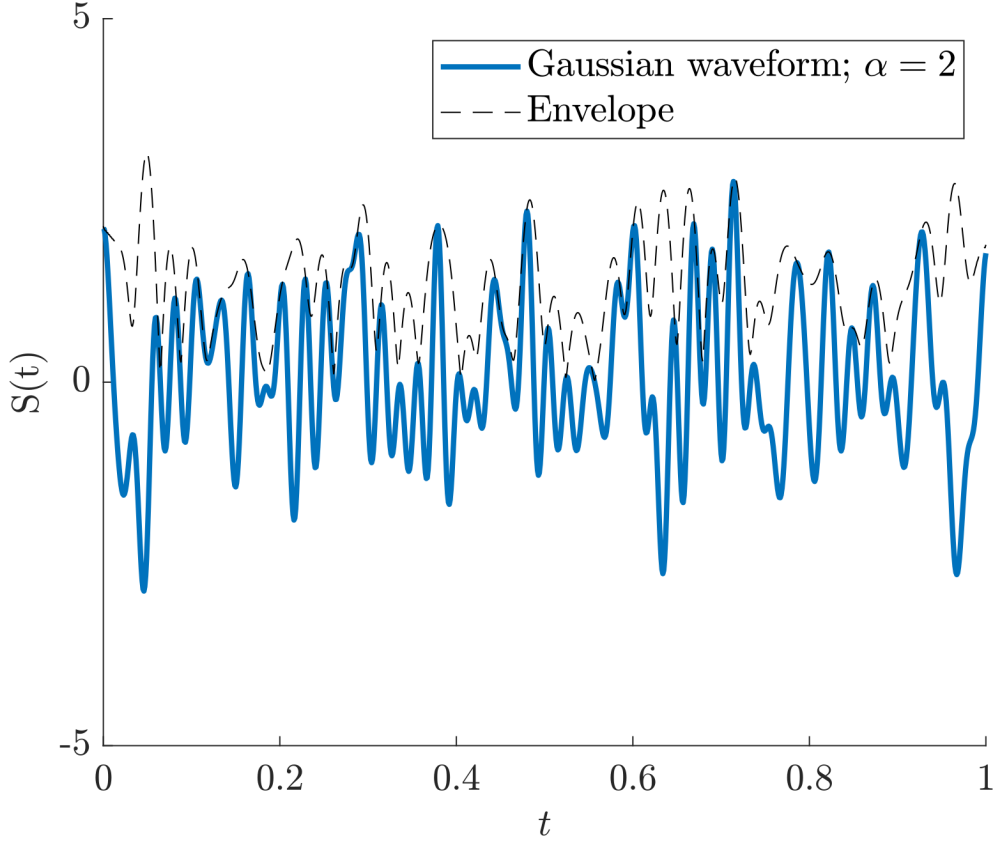


Figure 1.1. Gaussian analog baseband waveform.

distribution formulation is exact in the first case, whereas, in the latter two, the Middleton A model approximates well (at least) the tail distribution—this draws a picture of impulsive interference waveform characteristics even with the exclusion zone around the receiver, as the tail decay rate of the Middleton class A distribution is between the Gaussian and α -stable distributions. In the terrestrial networks, the α -stable waveform is due to a singular path loss with no exclusion zone between the interferers and the receiver. The interference in an infinite planar model was proposed in the entire plane, in a disc, and in an annular area outside a disc, as presented in [25], [24], and [26]. [24] showed that the interference waveform can exhibit impulsiveness even if we assume a minimum distance between the receiver and the interferers.

A gamma distribution approximation for the interference power was used in [26] using an exclusion zone. In [27], it was observed that the gamma distribution and inverse Gaussian distributions are a good fit in modeling the interference power in the case of non-singular path loss under Rayleigh fading. With singular path loss, the interference power distribution has a heavy tail for the power path loss exponent strictly larger than 2.

As noted, the interference does not generally follow Gaussian statistics: the interference distribution's tail decays significantly slower than what

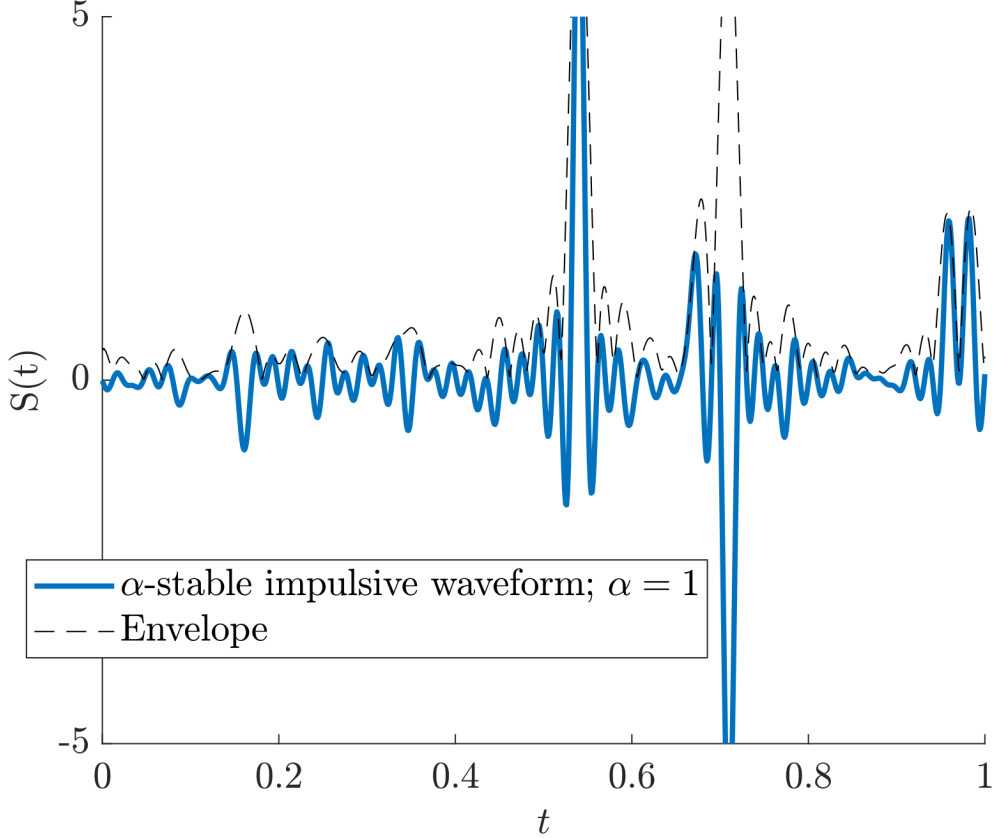


Figure 1.2. Impulsive analog baseband waveform.

corresponds to a Gaussian waveform (or to the two-dimensional Gaussian distributed complex baseband signal representing the in-phase and quadrature components of the signal modulation, for example, in ASK, PSK, QAM, FSK, APSK, or BPSK). The topology of the domain of interferers and the receiver's response function affects the interference quality. In particular, if the interferers can be arbitrarily near the receiver with a singular path loss function, the interference waveform, envelope, and (average) power distributions exhibit heavy tails for the power path loss exponent $\gamma > 2$. Furthermore, the fading and shadowing contributes to the interference characterization.

Gaussian and impulsive α -stable baseband waveforms $S(t)$ with similar signal powers $\int_0^1 |S(t)|^2 dt$ are plotted in Figures 1.1 and 1.2, respectively. The signal envelopes derived using the Hilbert transform $S(\cdot) \mapsto H(S)(\cdot)$ [28] are depicted in the figures representing the absolute value of the analytic signal $S(t) + iH(S)(t) \in \mathbb{C}$. In 1.1, the *waveform* $S(t)$ is Gaussian distributed, the *envelope* $|S(t) + iH(S)(t)|$ is Rayleigh distributed, and the instantaneous *signal power* $|S(t) + iH(S)(t)|^2$ is exponentially distributed.

1.4.2 Stochastic geometry analysis of LEO networks

In recent years, the number of works on the stochastic geometry analysis of the LEO networks has been published at an increasing pace. The reader can find an extensive literature review on the most relevant papers in the publications attached to the end of this thesis. A comprehensive literature review addressing other LEO scenarios can be found in [29]. Furthermore, the book [30] has been published on the subject.

The process of the main lobe gains of the UEs at the typical narrow-beam LEO BS, *i.e.*, the gain process (GP), first proposed in [Publication III](#) and extensively studied in Section 3.3, as an analytically tractable framework for acquiring insights on the waveform of the interference in the LEO networks.

2. LEO System Modeling

Two distinct spatial models are considered for the mathematical analysis and the Monte Carlo simulations, respectively:

- planar system model,
- spherical system model.

In the planar system model, the Earth is modeled as an infinite and flat plane \mathbb{R}^2 . In the spherical system model, the Earth is modeled as a sphere of radius $R_{\oplus} = 6378$ km.

As the link-level model, we consider narrow-band transmission during a short period of use consisting of single or multiple coherence time blocks, during which multiple symbols are transmitted, and random fading attenuates the signal between encoded blocks. We usually consider high-frequency transmissions, and the coherence time is relatively short, and the LEO BS and the UEs are considered spatially stationary during a single period of use.

The system model is from the perspective of *the typical* LEO BS at the elevation angle ϵ . This typical LEO BS represents all LEO BSs in a uniform constellation: the approach is justified by the stationarity of the PPP of the UEs. The Poisson layout follows from the independent mobility patterns (see Section 2.5.1). The satellite's antenna is steered toward a location on the Earth surface, considered the nearest focus point of the elliptical footprint (more precisely, a footprint contour, *e.g.*, the -3 dB footprint). The requirements for the constellation in which the typical LEO BS belongs are that the constellation consists of at least hundreds of satellites and that it is homogeneous (or uniform)—at least in a local sense (physically, hardly any constellations are strictly uniform—especially the constellations consisting of polar orbits). Numerous large LEO constellations have been studied within stochastic geometry, including the well-recognized Walker-Delta and Iridium (see the literature review in Publication III) constellations. However, in this thesis, I skip further study since the proposed analysis is independent of such orbital details of the constellations.

Both the planar and the spherical system model frameworks are interpreted under the conditions

1. the UEs have omnidirectional antennas,
2. the LEO BSs have narrow Gaussian antennas,
3. the UEs have independent locations and mobility patterns,
4. the LEO BSs form a (at least locally) uniform large constellation, and
5. transmissions are non-correlated and narrow-band.

As indicated in [31], multiple implementation schemes are possible for the LEO; the LEO BS footprint is large and hence can include multiple UEs; at least intercell interference is likely to be present. Interference-mitigation techniques are, to a varying extent, a trade-off between the achievable data rate and system complexity. Exhaustive standardized schemes for interference mitigation are yet to emerge. Furthermore, because effective beamforming for mobile phones does not yet exist, the proposed system model abstraction of independently located UEs with non-directional UE antennas is justified. In the discipline of stochastic geometry modeling of the NTN, as of today, it is arguably the natural system model when considering the hand-held UE-LEO BS terminal communication in the NTN. The proposed system model yields straightforward analysis and meaningful insights regarding the narrow-beam LEO performance metrics.

2.1 Antenna beams

2.1.1 Earth transmitter antennas

The Earth transmitter terminals, UEs, are cellular phones, also referred to as mobile phones or smartphones. Such UE-LEO BS NTN systems are under active development. For example, 3GPP aims to adapt existing satellite and terrestrial networks to provide direct connectivity from hand-held equipment to LEO satellites using frequencies assigned to mobile satellite services or those assigned to legacy terrestrial networks [31]. In such mobile phone user terminals, beamforming signal processing faces multiple practical and theoretical challenges: it is computationally complex and power-hungry, and also requires sophisticated hardware. While at least rough beamforming towards the desired satellite can well be feasible, as of today, it remains unclear to what extent we can mitigate interference leakage towards undesired directions and with what effort such technology will reach hand-held mobile devices. Hence, it is sensible to assume that the UEs radiate in all directions in the sky. In this regard, although not

entirely physically realistic, the constant antenna gain model is a widely used approximation of omnidirectional antennas.

The UEs transmit omnidirectionally with equal signal powers and cause an additive response (undesired signals are interference) at the typical LEO BS. In the case of interfering UEs, they operate in the same frequency band using non-orthogonal polarization modes and signal modulation, nor are any similar interference mitigation methods implemented (prior to the processing of the aggregate signal).

2.1.2 Satellite base station antennas

The LEO BS antenna is modeled with a Gaussian beam: this represents the main lobe of general antenna gain patterns. In simulations, the value $\varphi_{\text{RX}} = 1.6^\circ$ is used, corresponding to the LEO antenna pattern proposed in the International Telecommunication Union Recommendations (ITU-R) [32, ITU-R LEO reference radiation patterns]. The analysis is not restrictive for the antenna beam width as long as the beam is sufficiently narrow. Despite being an idealized antenna pattern, the Gaussian response accurately models the main lobe (-10 dB lobe) of many antenna patterns, particularly the ITU-R pattern, cf. Figure 2.1 (we omit the explicit definition of the gain here): this works as long as the UE density is high enough and the served UE is likely to be in the main lobe. A plot demonstration comparing a realistic LEO BS ITU-R antenna beam and the Gaussian beam is given in Figure 2.1.

The antenna gain $G[\cdot] : [0, \infty) \rightarrow (0, 1]$ is assumed to be Gaussian, i.e.,

$$G[\varphi] = 2^{-\varphi^2/\varphi_{\text{RX}}^2} = e^{-\log(2)\varphi^2/\varphi_{\text{RX}}^2}, \quad (2.1)$$

where φ_{RX} is the halfwidth of the -3 dB antenna gain.

Sidelobe modeling

Unless otherwise stated, the thesis assumes a Gaussian antenna pattern model for the LEO BS. However, analogously to the semi-analytical simulation methods [33], the possible aggregate signal component from the sidelobes can be modeled as additive white Gaussian noise (AWGN) with constant power (a validation for the Gaussian waveform statistics can be deduced from the forthcoming Theorem 3.4.4). The variance in the power (the “power” understood as the variance of the waveform during a use period) of this term is negligible compared to that of the total received power received from the main lobe (-10 dB). Hence, this sidelobe power can be modeled as a constant by averaging over the use periods (to be precise, over the realizations of the PPP). The sidelobe average power can be derived theoretically or simulated, although we do not explicitly present it here. The constant sidelobe total received power modeling has benefits in simplifying the analysis while achieving good realism. Furthermore, many results in the thesis involving noise are generalized, which can now be interpreted to include the sidelobes or a combination of noise and sidelobes.

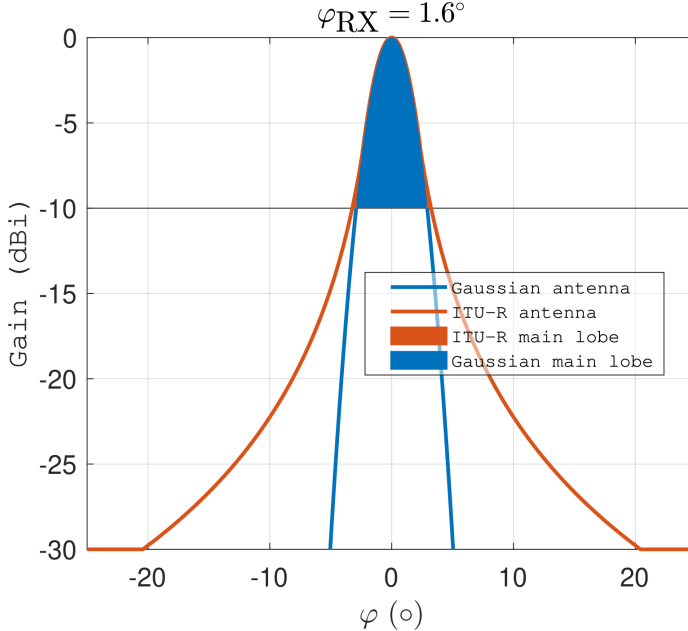


Figure 2.1. Comparison between the Gaussian and ITU-R LEO reference radiation pattern. The gain of the Gaussian antenna in the main lobe (-10 dB lobe) is almost identical to the ITU-R main lobe. However, there is a slight difference towards the edges of the main lobe. The fast-decaying Gaussian beam essentially corresponds to the main lobe component.

Please find Figure 2.2 for a comparison of the complementary cumulative distribution (CCDF) derived from the theory and Monte Carlo simulation of the ITU-R antenna incorporating the sidelobes. The elevation angle of the satellite and altitude are $\epsilon = 90^\circ$ and $h = 1200$, respectively. The average number of transmitters inside the -3 dB footprint is $\kappa = \log(2)$. Rayleigh fading is assumed for convenience, and the non-shifted theoretical distribution is the exponential distribution, as will be later observed in Corollary 3.3.4.

Alternative interpretations

There are at least the following two possible interpretations for the model.

- The LEO BSs have omnidirectional antennas, and the UEs have directional narrow Gaussian antennas.
- The UEs can have efficiently directional antenna beams (such as disc antenna terminals), and the “omnidirectional” antenna patterns represent constant side lobes of the interfering UEs, each steered at their serving LEO BSs. In this scenario, the interference originates from these sidelobes.

However, in this work, the simulations are performed by modeling the scenario as described in the section.

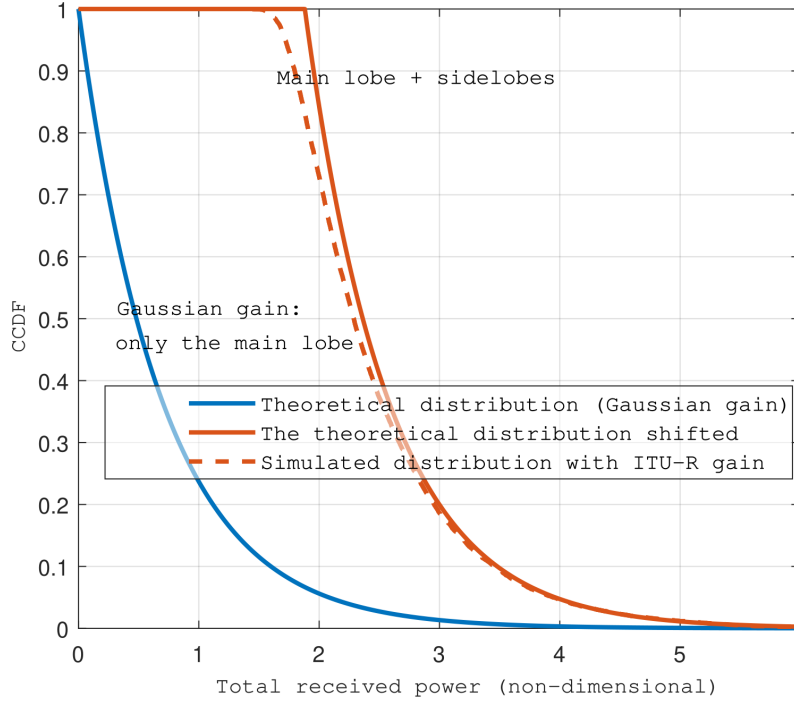


Figure 2.2. The CCDF of the theoretical total received power (by convention, usually referred to as the *total interference* power in the thesis) from a transmitter located according to the PPP. The plot depicts the theoretical (planar model) versus simulated (spherical model) distributions. The simulation uses the ITU-R antenna with realistic sidelobes. The sidelobes are modeled as constant noise, additive to the total received power of the main lobe component, shifting the theoretical power distribution to the right.

2.2 Spherical system model

The Monte Carlo simulations in [Publication III](#)-[Publication IV](#) are based on the model of this section (apart from an ITU-R antenna is modeled in [Publication IV](#) instead of the Gaussian antenna). The analysis utilizes the planar model introduced in Section 2.3 and approximates the spherical model presented in this section. [Publication I](#) utilizes the MATLAB®satellite toolbox for the simulations, but we omit its implementation details.

A short period of use (such as a symbol block) over a single or multiple fading and/or shadowing coherence times in a narrow-band and narrow-beam terrestrial-satellite link in a single-tier network is considered. The link quality from the perspective of a LEO BS is investigated. For the Monte Carlo simulated metrics, we assume that UEs with omnidirectional antennas, such as mobile phones, are randomly located on the Earth surface according to the PPP. The simulations utilize a spherical Earth model of a radius of $R_{\oplus} = 6378$ km. The serving satellite is at the altitude h and elevation angle ϵ w.r.t. the Earth transmitters. The studied performance metrics, such as

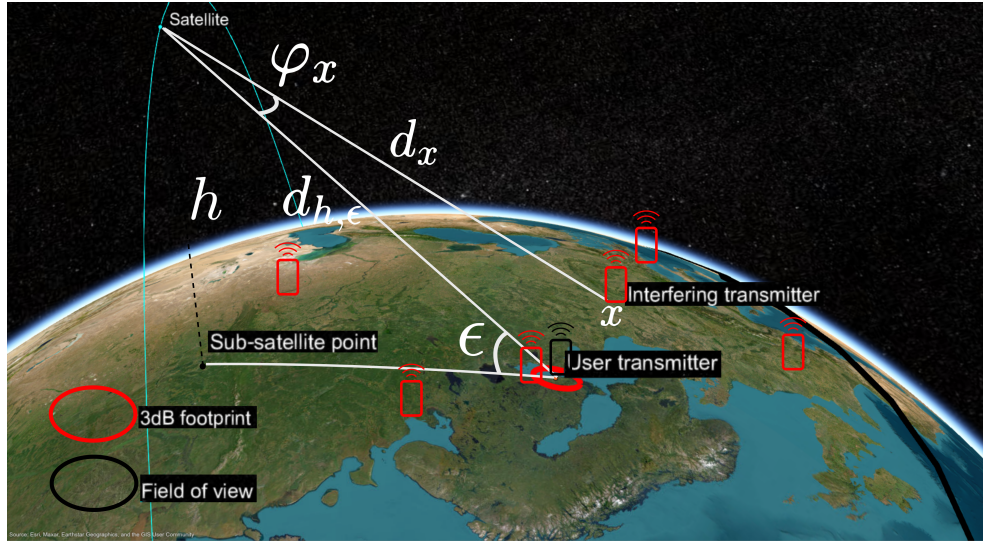


Figure 2.3. A sketch of the spherical narrow-beam LEO uplink model is illustrated in the MATLAB®satellite toolbox. Please note the small relative scale of the -3 dB footprint: In the figure, the distances to the interfering transmitters are exaggerated for clarity; however, in practice, $d_{h,\epsilon} \approx d_x$ for all relevant transmitters.

the SIR and SINR, are mediated by additive noise and interference from the UEs that are not being served by the LEO BS. The interference is essentially treated as additive noise. The LEO BS can work as an independent network or complement a terrestrial network, and the interfering transmitters can be considered to be within the same cell, adjacent cells, overlapping cells, or part of a terrestrial network served by a terrestrial BS. The SBSs form a homogeneous point pattern (deterministic or random), allowing the ergodic interpretation of performance metrics over the SBSs. The LEO BS antennas are narrow-beam Gaussian beams considered to serve a local homogeneous environment, such as a rural or urban area. Consequently, the scattering and attenuation caused by the weather conditions and Doppler shifts are the same for all relevant UEs, thus not affecting their relative signal strengths at the LEO BS. (However, such models can be incorporated in the analysis through an additional random attenuation variable.) Linear additivity of the average signal powers during the use period is considered, requiring that the separate signals are not mutually correlated, *i.e.*, the cross-correlation is close to zero. Some of the crucial spatial metrics of the spherical model and the related geometrical relations are presented in Figure 2.4 and equations (2.2)-(2.3), respectively. The results are traditional geometry and are well-established in the literature.

See Figure 2.4. Directly from the law of cosines,

$$d_{h,\epsilon}(\xi) = \sqrt{R_\oplus^2 + (R_\oplus + h)^2 - 2R_\oplus(R_\oplus + h)\cos(\xi)}. \quad (2.2)$$

Furthermore, one may derive the relation between ϵ and ξ : The law of

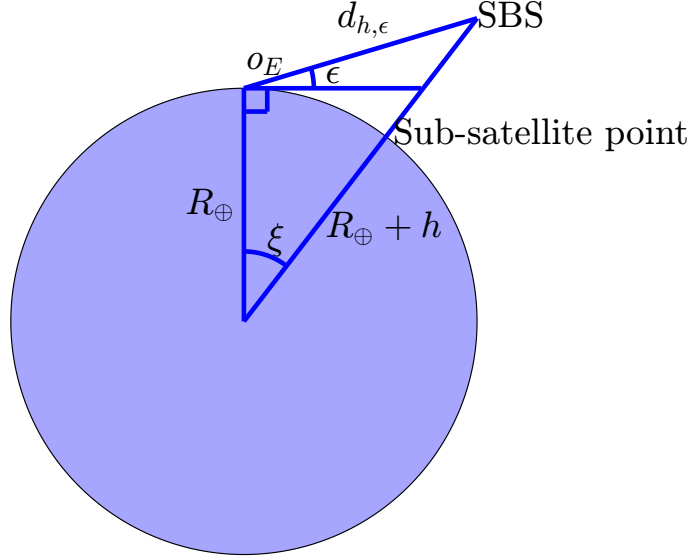


Figure 2.4. Sketch of the geometry of the spherical model. **N.b.** the terminology: the SBS is the LEO BS.

cosines states that

$$(R_\oplus + h)^2 = d_{h,\epsilon}(\xi)^2 + R_\oplus^2 - 2d_{h,\epsilon}(\xi)R_\oplus \cos(\pi/2 + \epsilon), \quad (2.3)$$

which is analytically solvable for ξ .

2.3 Planar system model

Definition 2.3.1 (Plane). The word “planar” refers to the entire two-dimensional Euclidean space \mathbb{R}^2 or to a two-dimensional subset of it. In the context of [Publication III](#) and [Publication IV](#), as well as the analysis of the thesis, including this section, the concept refers to \mathbb{R}^2 .

The planar model essentially consists of the Earth modeled as an infinite plane, a narrow Gaussian antenna beam, and spatial path loss approximated as equal for all transmitters (*c.f.*, Figure 2.3). A rigorous derivation of the model is presented in [Publication III](#). The UEs form a homogeneous PPP $\Phi \subset \mathbb{R}^2$ of density λ . A demonstrative plot of an uplink interpretation, with the served UE as the nearest transmitter, and crucial geometric calculation of the spatial distances and antenna gains of the UEs and the typical LEO BS, is as follows. The calculations refer to Figures 2.5a-2.5b.

The values of h and ϵ determine the distance to the satellite, given by the geometric relation

$$\hat{d}_{h,\epsilon} \triangleq h / \sin(\epsilon). \quad (2.4)$$

In this work, we focus on LEO altitudes of $h \in [200, 2000]$ km. We will consider that $\epsilon \geq 35^\circ$, which is the minimum elevation angle proposed in [34].

The approximate spatial path loss in the planar model is

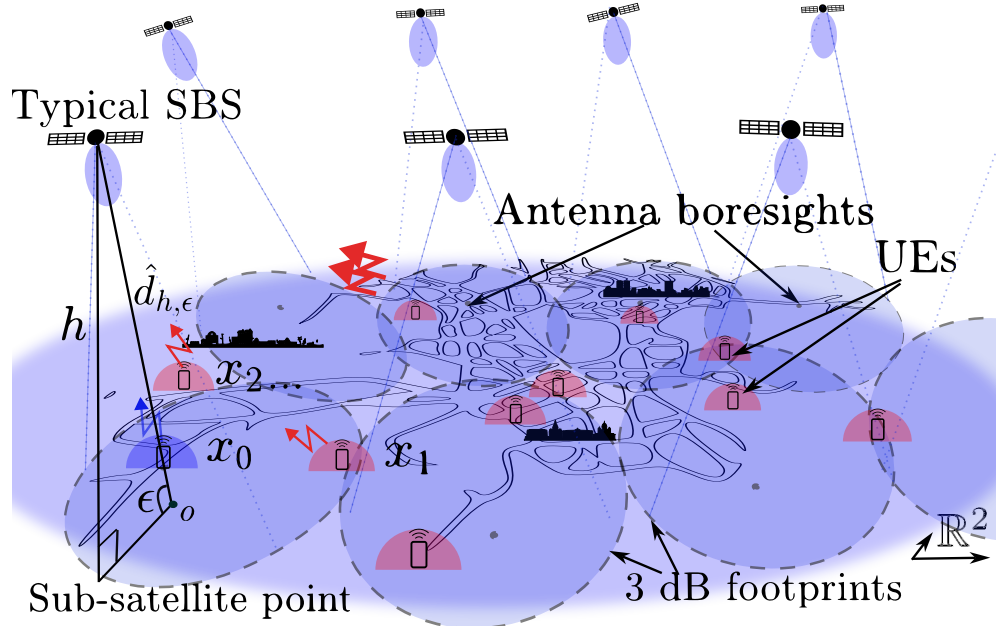
$$\ell(\hat{d}_{h,\epsilon}) \triangleq (\hat{d}_{h,\epsilon}/d_0)^{-\gamma}, \quad (2.5)$$

where d_0 is a normalizing distance addressing the dimension of $\hat{d}_{h,\epsilon}$.

For each angle φ_x between the transmitter $x \in \Phi$ and the typical SBS antenna boresight,

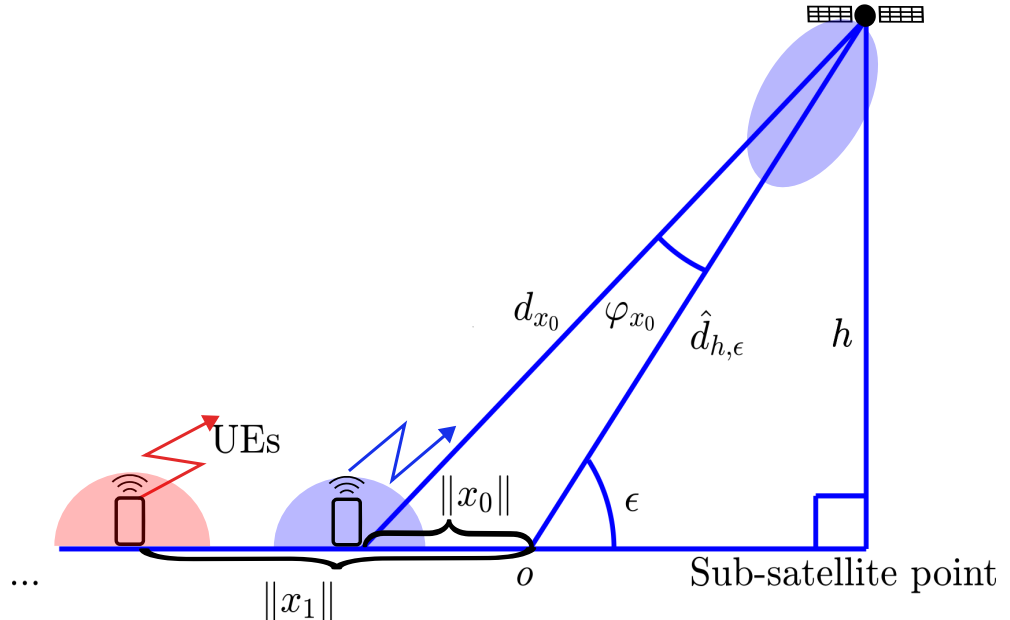
$$\varphi_x \approx D_{h,\epsilon} \|x\|, \quad (2.6)$$

where $D_{h,\epsilon} \triangleq \sin^2(\epsilon)/h$ is the derivative of the function $\|x\| \mapsto \varphi_x$ at $\|x\| = 0$. (2.6) is the first-order Taylor expansion of φ_x at $\|x\| = 0$; the approximation is sufficient if the antenna pattern decays fast for large φ_x . Since $\{x\}$ lies on the plane, the analysis essentially reduces to planar stochastic geometry inquiry, which is a well-established area widely studied in the literature. Hence, many mathematical results are enabled for use.



(a) Interpretation of the *planar* system model with the SBSs in adjacent orbits serving an urban area and a realization of the UEs. The altitudes are not to scale (the scale is illustrated in Figure 2.3). **N.b.** the terminology: the SBS is the LEO BS.

Typical SBS



(b) The typical SBS as seen from the side. The transmitters are projected into line $(0, \infty)$ according to their norm.

Figure 2.5. The simplified narrow-beam LEO uplink system model. The SBS antenna boresight is oriented towards o , the focus point of the elliptical footprint. The omnidirectionally transmitting UEs $\{x_i\}$ are located according to the HPPP on the plane. Here, the nearest transmitter, x_1 , is the served UE. **N.b.** the terminology: the SBS is the LEO BS.

2.3.1 Planar model vs. spherical model

The planar stochastic geometry models of wireless networks are well-established and studied in terrestrial models in hundreds or thousands of papers. Furthermore, multiple works on planar stochastic geometry modeling involving unmanned aerial vehicles (UAV) have been proposed in the literature. This section focuses on the LEO networks, particularly on the narrow-beam LEO, which is the main focus of the thesis.

A planar model was successfully used in [Publication I](#) (although this was a pure accident, as the author forgot to incorporate the appropriate scaling factor that would have mapped the integral onto the sphere), and the interference modeling corresponds well to the Satellite ToolBox simulations in MATLAB®. In [Publication I-Publication IV](#), the planar models were (intentionally) used to simplify the analysis. An extensive literature review can be found in [35]; the paper also presents a rigorous study on planar versus spherical models, and proposes that the planar LEO model is feasible with antennas narrower than 7.5° ; this is well wider than $\varphi_{RX} = 1.6^\circ$, which is a standard in the thesis (and proposed by the ITU-R). Comparison and validation of the planar model for narrow beams are also presented in [Publication III](#) with demonstrative plots. To the best of our knowledge, the work in this thesis is the first to combine the planar model with the narrow-beam Gaussian antenna pattern (representing the main lobe). This provides a lubricative mathematical analysis and insightful results while maintaining realism. In the orthodox LEO modeling approaches, simple results may be possible with a boxcar-type antenna pattern; however, with a realistic antenna pattern, the analysis facilitates, to the best of my knowledge, complex representations of the performance metrics that are laborious to evaluate and, in our opinion, contain little insight. The thesis aims for clarity in the derived expressions: The Gaussian antenna pattern and infinite planar model aim to resolve the complexity issue in the analysis of the stochastic geometry LEO models.

Let us make a back-of-the-envelope calculation for illustration. See Figure [2.6](#) (note that the distances or the angles are not in scale. We consider that the LEO BS is at the zenith, *i.e.*, its antenna lobe is steered directly toward the Earth's center. We study the curvature within the main lobe by considering the differences between $d_1 + d_2$ and d_2 , which represent distances to the LEO BS from the edge of the -10 dB footprint in the spherical and planar models, respectively. It is straightforward to see that the -10 dB angle is given by $\varphi_{ml} = \varphi_{RX} \sqrt{\log_2(10)}$, where φ_{RX} is the width of the -3 dB lobe (recall the definition of the Gaussian antenna in (5)). We can use the law of cosines to derive

$$d_1 + d_2 = (h + R_\oplus) \cos(\varphi_{ml}) - \sqrt{(h + R_\oplus)^2 \cos^2(\varphi_{ml}) - h(h + 2R_\oplus)}, \quad (2.7)$$

where $R_\oplus = 6378$ km is the mean radius of the Earth, *i.e.*, the radius of the

Earth in the spherical model.

On the other hand, by basic trigonometry,

$$d_1 = h / \cos(\varphi_{\text{ml}}). \quad (2.8)$$

Let $\varphi_{\text{RX}} = 1.6^\circ$. The largest curvature is for the largest altitude; hence, we consider $h = 2000 \text{ km}$. We have $d_1 + d_2 = 2003.4 \text{ km}$, $d_1 = 0.81 \text{ km}$, and $d_2 = 2002.6 \text{ km}$. The distance d_2 from the plane representing the planar model of the Earth is $d_2 / (d_1 + d_2) \cdot 100\% = 99.96\%$ of the distance $d_1 + d_2$ to the sphere. In this regard, we may argue that the curvature within the main lobe footprint is negligible. Having $d_1 + d_2 \approx d_2 \approx h$ also clarifies why we can approximate the spatial path losses to be equal for all transmitters with the narrow beam.

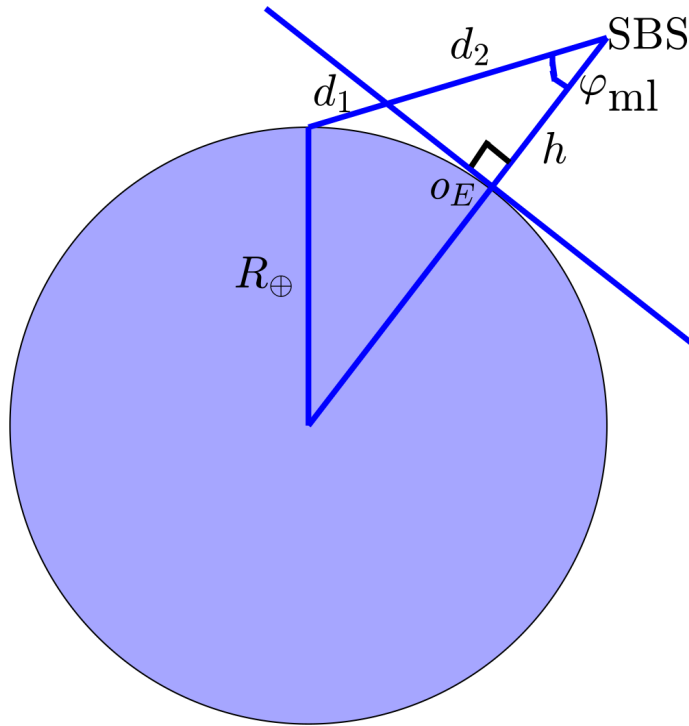


Figure 2.6. The distances $d_1 + d_2$ and d_2 to the edges of the footprints (determined by the angle φ_{ml} , i.e., the -10 dB angle, w.r.t. the boresight) in the spherical and planar system models, respectively. **N.b.** the terminology: the SBS is the LEO BS.

2.4 Satellite (LEO BS) locations

Throughout this section, we consider the planar system model unless otherwise stated.

When we refer to the “satellite constellation,” it means uniformly located points on the plane (planar model) or on the sphere (spherical model) (“uniformity” is a vague concept on the plane; hence, to be more precise, we can assume that the constellation is a PPP in the planar model). The constellation can be a regular point pattern or, for example, a homogeneous PPP, as long as the “density” of the points remains spatially invariant and there is no clustering. The (infinite) uniform constellation represents, in a local sense, the spherical constellation orbiting the Earth. As of today, many p.p. models for the LEO constellations have been proposed in recent years, and the binomial p.p. and the homogeneous PPP have shown through Monte Carlo simulations that both satisfactorily represent the statistics of a deterministic constellation as the satellites move w.r.t. the Earth transmitters (see, *e.g.*, [36], [37], [38] and [Publication I](#)). Particularly, with multiple layers of constellations, the regularity of the relative satellite positions can lead to spatially independent-like behavior.

The uniformity is the only requirement for the constellation in the interpretation of the stochastic geometry NTN model of this thesis. Other than that, the constellation characteristics are irrelevant to this work. In the practice of the analysis, the typical LEO BS is considered to be located at a definite point on the plane (or more precisely, its sub-satellite point is located in the plane representing the Earth surface). We will unravel the uniformity requirement in the following section.

2.5 User equipment (UE) locations and interference

The Earth transmitters, or user equipments (UEs), are located on the Earth surface and have no interaction with each other, *i.e.*, they are independently spatially distributed. Further, their density remains constant. Hence, the UEs follow the homogeneous Poisson point process (PPP). The UE layout under the typical LEO BS is a random point realization of the PPP. Further, the PPP is ergodic on the plane and approximately ergodic on the sphere (see Section 3.2.2 for the exact definition); *i.e.*, the spatial average—or the average over the LEO BSs in the uniform constellation—equals the ensemble average at the typical LEO BS. The statistics of the typical LEO BS have the interpretations as

- the statistics during a single use period—during which the LEO BSs are practically non-mobile—over all LEO BSs in the constellation serving a deterministic layout of UEs,

- the statistics over multiple use periods at the typical LEO BS as the LEO BS move over a deterministic layout of UEs (performing handovers on the served UEs),
- the statistics over multiple use periods at the typical LEO BS—during which the LEO BS is practically non-mobile—and UEs independently sequentially either transmit or are quiet (*e.g.*, ALOHA), and
- any combination of these.

Figures 2.7 and 2.8 depict two statistical interpretations of the system model, as proposed in [31]. In Figure 2.7, the typical satellite is moving over a deterministic Poisson realization of transmitters. In Figure 2.8, the co-channel UEs are considered to form the PPP. We will categorize the interference into *intracell plus intercell* and *intercell* interference (only intercell co-channel interference is present in the figure).

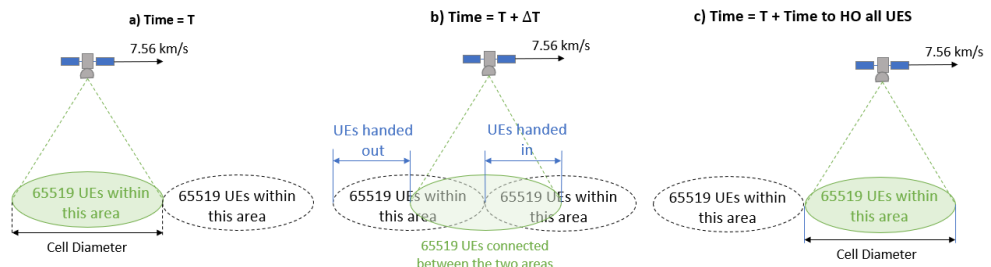


Figure 2.7. The model interpretation as the satellite moves over a deterministic layout of UEs [31, Figure 7.3.2.1.6-1].

2.5.1 Incarnation of the homogeneous Poisson point process

It is not self-evident why we use the homogeneous PPP in the system model, and not something else. One of the most important reasons is that it is analytically highly tractable. Second, the PPP is a natural point process that arises in various contexts, such as independently located hand-held UEs with independent mobility patterns, as will be argued in this section.¹ (In a bounded domain, the binomial process might not be a bad choice either, although it postulates the exact total number of transmitters.) The PPP can be defined in Euclidean space of arbitrary dimension or on a manifold, for example, on the surface of a sphere. Randomizing the density is the Cox process, which is a close relative of the PPP. However, in this work, we concentrate on the homogeneous PPP.

Regarding the Earth transmitters, the Poisson assumption can be justified by the independent mobility patterns of UEs. Furthermore, the multipath

¹I would go so far as to claim that, should there be no prior information, other than the density of the transmitter locations, which might be moving or not (density as the average number of transmitters per unit area), the PPP is *the best guess* for the (non-temporal) location characteristics.

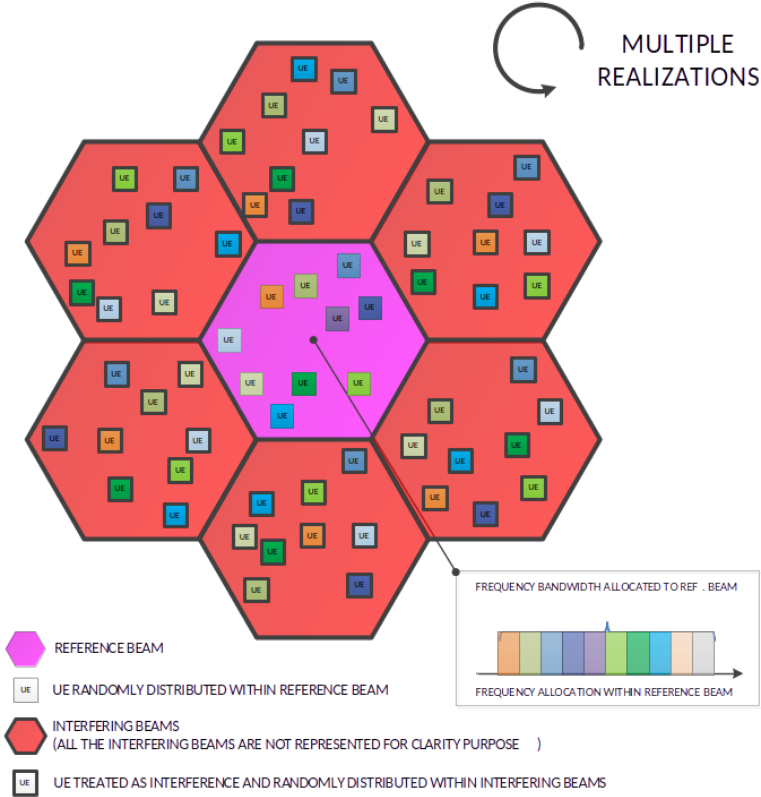


Figure 2.8. The model interpretation when the UEs are randomly appearing inside the intracell (reference beam) and the interfering cells (interfering beams) [31, Figure 6.1.3.2-2].

fading of the signals can make an arbitrary network seem Poisson at the receiver [18, Sec. 4.3]. The PPP is analytically most tractable and has been used in related papers. Furthermore, it has been established that the process after randomly displacing all points (the displacement can, for example, be incorporated to represent the impact of fading or mobility) in a non-Poisson process approaches Poisson after many displacements, [39][R-4, Chapter 11, Section 4: Convergence Concepts and Limit Theorems, Random Translations], or even for a single displacement [18, Chapter 4, Section 3: Networks Appear Poisson Due to Random Propagation Effects]; in this sense, the PPP is a universal point process. It has a special role in the structural theory of point processes: Like the normal distribution in the theory of probability distributions, the PPP is an attractor in the point process theory. As such, it is the maximal entropy point process, towards which systems develop.

Please see Figure 2.9 for a demonstration: A generation of a two-dimensional Poisson realization is demonstrated in Figs 2.9a-2.9d. Starting from the regular layout, each point is randomly moved a fixed distance in a uniformly distributed direction. While remnants of the initial spatial correlation appear in Figure 2.9c (the points are still somewhat mutually repulsive), Figure

2.9d already exhibits complete spatial randomness, which is a characteristic feature of the PPP.

As already noted, regarding satellite constellations, it has been repeatedly shown in the literature that the PPP and binomial p.p. model adequately determine dense LEO constellations. As of today, the trade-off between simple analysis and realism has been widely in favor of choosing analytically tractable p.p. in the stochastic geometry models of LEO networks. This is the case even if all satellites part of a deterministic uniform cancellation are serving transmitters for which the satellite is in the zenith. In this regard, randomly steered antenna beams increase the randomness of the footprint locations on the Earth: Even though the constellation would be regular, the footprint locations are not if they are steered to random directions at random elevation angles.

2.6 Monte Carlo simulation of the Poisson point process on the plane and sphere

The PPP can be produced from the regular point pattern by randomly displacing the points. However, this is not practical. A point realization is simulated in a rectangle $A = (-\pi, \pi) \times (-1, 1)$ as follows.

1. Pick a Poisson variable N of a given density λ .
2. Produce N uniformly distributed points in A .

Furthermore, the points can be mapped into spherical coordinates by the area-preserving mapping $A \ni (x, y) \mapsto (1, x, \sin^{-1}(y))$.

2.7 Doppler shift, antenna attenuation, propagation delay, coherence time, and multipath fading

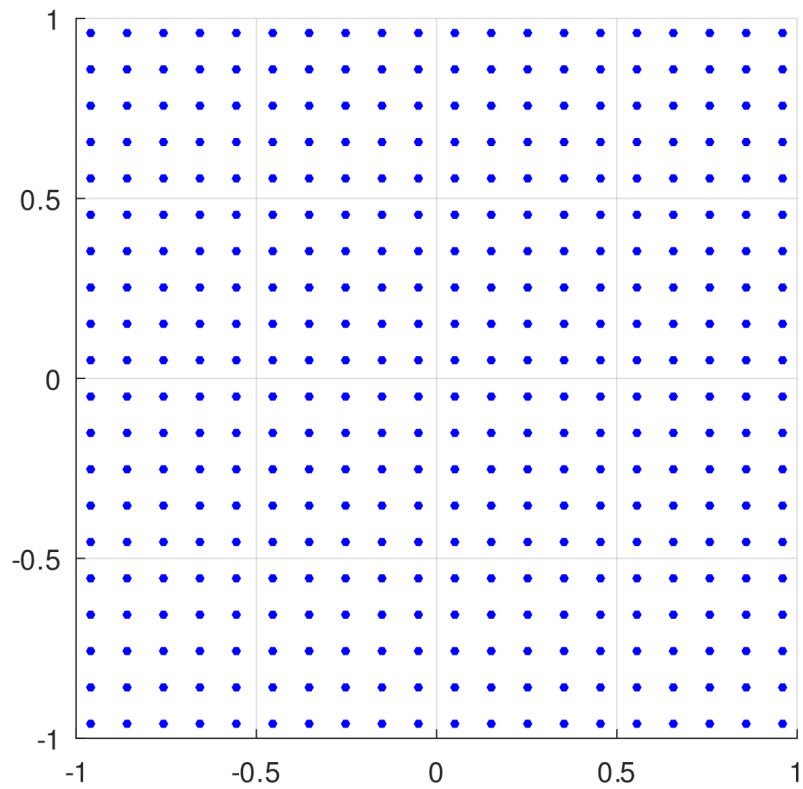
In the LEO systems, one challenge is the high velocity of the satellites that causes significant Doppler shifts affecting the frequencies and the phases of the signals (however, the differences in the Doppler shifts of the relevant main beam signals are small with narrow LEO BS antenna beams). While there are stochastic geometry studies on the distribution of the Doppler shift in LEO systems [[40], [41]]—to the best of our knowledge—the analytical interference amplitude waveform characterization using stochastic geometry has yet to be explored for LEO.

Since atmospheric, transmitter, and base station mobility, topological phenomena such as Doppler shift, propagation delay, delay spread, dispersion, as well as weather phenomena, *etc.*, attenuate the signal at the receiver. Furthermore, in narrow antenna LEO communications, the narrow beam suppresses signal strength temporally rapidly. In this section, we briefly

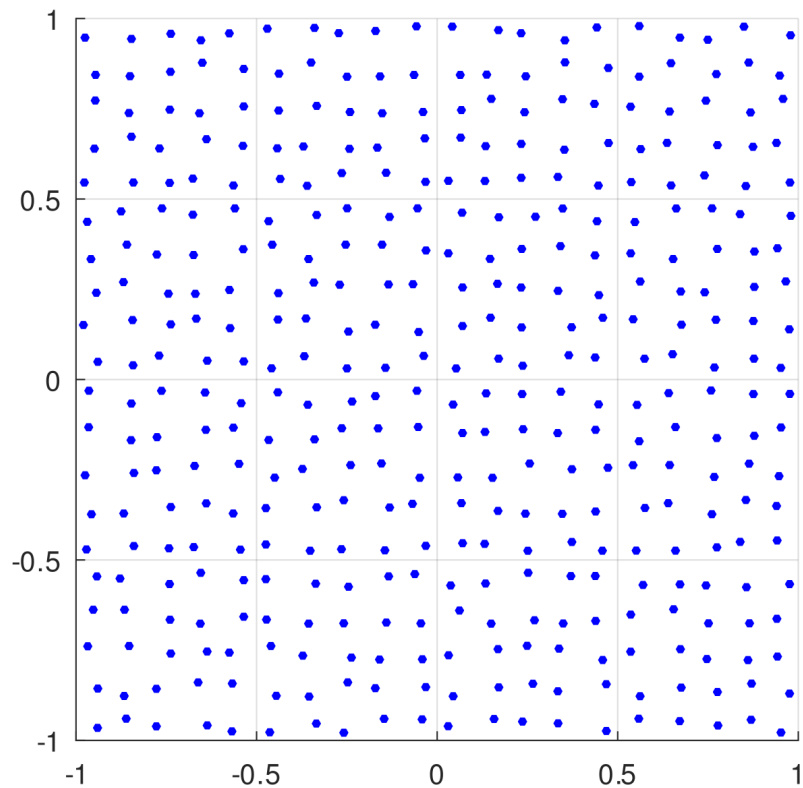
discuss the subjects, with some simple back-of-the-envelope calculations. Empirical and theoretical research within LEO communications has been extensive for well over twenty years, and the empirical propagation studies of other satellite systems date back to the 1950s when the USSR launched Sputnik. The theoretical models date even further. Instead of introducing novel multipath fading and Doppler shift models, the main focus of the work is the stochastic geometry modeling of the LEO communications. An in-depth literature review of the propagation impairments in the signal response in the LEO channel would deserve extensive work of its own. More thorough satellite channel model references will be referred to in this section.

The thesis explores the LEO channel attenuation phenomena numerically and analytically through stochastic geometry analysis and Monte Carlo simulations. We restrict the channel model to the following factors.

- Doppler shift,
- multipath fading,
- attenuation due to the narrow receiver antenna beam.

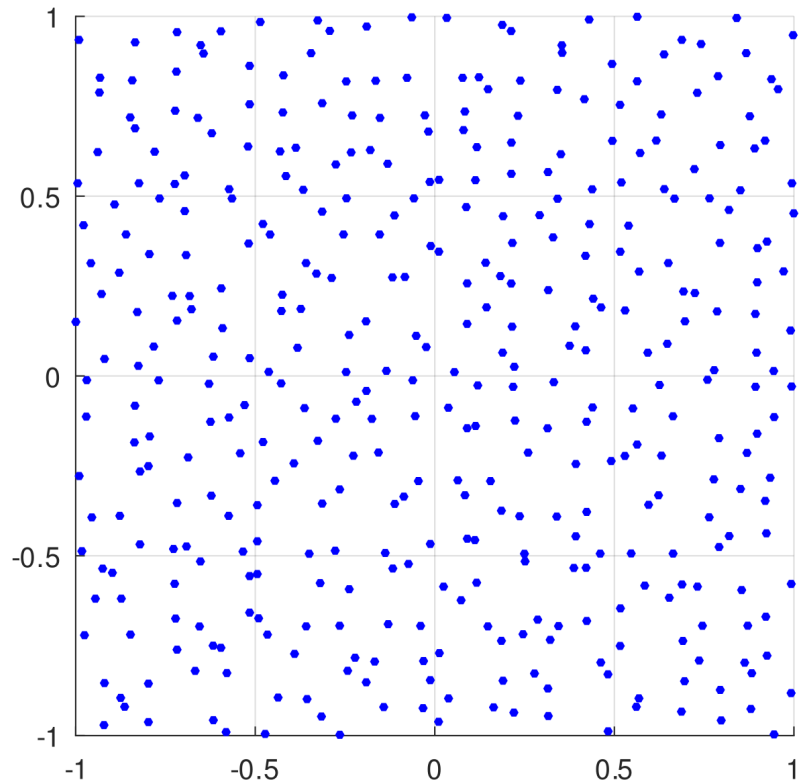
Regular layout of points in $[-1, 1] \times [-1, 1]$ 

(a) A regular grid of points.

Perturbed points in $[-1, 1] \times [-1, 1]$ 

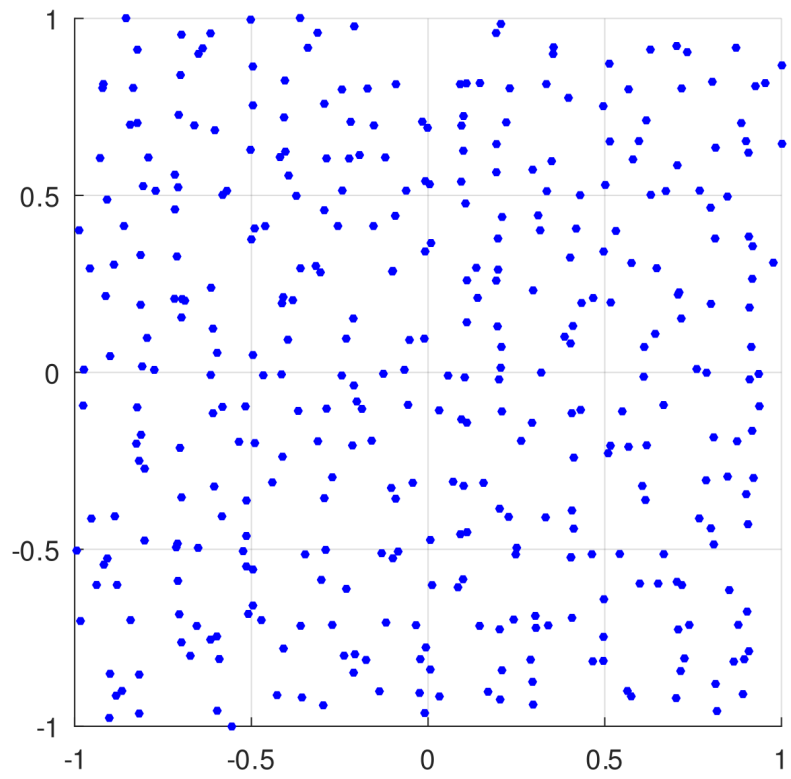
(b) Randomly move each point to uniformly distributed directions.

Perturbed points in $[-1, 1] \times [-1, 1]$



(c) Randomly move each point to uniformly distributed directions.

Perturbed, Poisson points in $[-1, 1] \times [-1, 1]$



(d) The resulting layout approaches Poisson.

Figure 2.9. Emergence of a homogeneous PPP from a regular .

2.7.1 Multipath fading and the non-temporal distributions

We concentrate on multipath propagation caused by obstacles, such as buildings. Such multipath fading occurs especially in urban/suburban environments, but also in natural environments. Propagation through multiple paths causes the signal to arrive at the receiver in different phases; hence, the signal interferes with itself and its magnitude fluctuates (in a random way). Fast fading refers to small-scale signal attenuation that, according to a definition used in this thesis, occurs within a timescale during which all transmitters can be considered non-mobile, whereas shadowing is a temporally longer-lasting phenomenon. Fast fading is a rapid change in the signal strength (which is related to a change in its phase) that can fluctuate during a short *use period* (but fluctuation can not be more rapid than the transmission time of the smallest quanta of data: in digital communication, called bits or symbols). In this context, *Deep fades* are occurrences when the fading remarkably deteriorates the signal-to-noise ratio, making communication practically impossible. On the other hand, fast fading signal attenuation can also improve the data rate by amplifying the signal. In LEO communications, the multipath fast fading attenuation is worth paying serious attention to, especially at high carrier frequencies that are larger than, say, 100 kHz.

Shadowing refers to a large (vis-à-vis the wavelength) object blocking one's direct visibility, *i.e.*, the LoS path, to the desired receiver. On the other hand, as with the fast fading, the "shadowed" signal can be amplified by a spatially and temporally firm object (such as a mountain), which reflects the signal in a favorable direction and works as a *waveguide*. This amplification can be remarkable. For example, the log-normal shadowing models have remarkably *fat tails* causing extreme power gain events to be an intrinsic factor in the network performance.

Three important statistical fading models are as follows. The fadings are referred to in terms of the distribution of the instantaneous envelope amplitude.

1. Rayleigh fading (exponentially faded power),
2. Rician fading (noncentral chi-squared faded power),
3. Nakagami fading (gamma faded power),
4. Log-normal shadowing fading (log-normally faded power).

Let v^2 denote the power from the direct path and $2\sigma^2$ the power from the (scattered) multipaths, respectively. Further, denote by $\Omega = v^2 + 2\sigma^2$ the total power from both paths. The amplitude fast fading gain is modeled as a random variable (r.v.) $h \in (0, \infty)$ (also denoted with g, H , etc.) that follow the complementary cumulative distribution function (CCDF) for $y > 0$

1.

$$\mathbb{P}(h > y) = e^{-y^2/(2\sigma^2)}, \quad (2.9)$$

2.

$$\mathbb{P}(h > y) = Q_1(v/\sigma, y/\sigma), \quad (2.10)$$

where $Q_1(v/\sigma, \cdot)$ is the Marqum Q-function. The related Rician parameter is defined by $K \triangleq v/(2\sigma^2)$ or

3.

$$\mathbb{P}(h > y) = \Gamma(m, y^2 m / \Omega) / \Gamma(m), \quad (2.11)$$

where $m > 1/2$ is the fading parameter, and $\Gamma(m, \cdot)$ and $\Gamma(m)$ denote the gamma function and upper incomplete gamma function, respectively.

Let $\mu_{\text{LoS}}, \mu_{\text{NLoS}}$ denote the mean power, measured in dB, of the direct, LoS and the non-line-of-sight (NLoS) paths, respectively. Further, let $\sigma_{\text{LoS}}^2, \sigma_{\text{NLoS}}^2$ denote the respective variances. Conditioning on either path, $i \in \{\text{LoS}, \text{NLoS}\}$, the attenuation of the power measured in decibels follows the distribution $10 \log_{10}(h) \sim \mu_i + \sigma_i^2 N(0, 1)$, where $N(0, 1)$ is the normal distribution. Let $\rho = \log(10)/10$ be a scaling parameter. The shadowed power has a log-normal distribution with the distribution function

4.

$$\mathbb{P}(h > y) = \frac{1}{2} \left[1 + \operatorname{erf} \left(\frac{\rho \mu_i - \log(y)}{(\rho \sigma_i)^2 \sqrt{2}} \right) \right], \quad (2.12)$$

where $\operatorname{erf}(\cdot)$ is the error function.

The combined distribution of the LoS and NLoS components involves the LoS probability p_{LoS} and is defined as a mixture Gaussian distribution (see [Publication IV](#)). Note that $\log(\cdot)$ denotes the natural logarithm (as always).

Sometimes it is merely a matter of tractability, which fading model is the most useful. In stochastic geometry models, the Rayleigh fading is usually the simplest (also compared to the LoS channel) because the exponential distribution function conveniently transforms the problems to the Laplace domain. Furthermore, especially in broad system-level stochastic geometry models (that describe averages over a sufficiently large statistical ensemble), Rayleigh fading can be as feasible as Rician fading, particularly in SIR and SINR modeling in a simple coverage region for SIR and SINR values greater than 0 dB (see Sections [3.6.1](#) and [3.6.2](#)). Should we require more generality and accuracy (*e.g.*, regarding the average SIR and SINR values in the region $(-\infty, 0)$ dB), the Nakagami fading is closely related to the Rician distribution, while retaining analytical tractability due to the gamma distribution belonging to the exponential distribution family. The Nakagami fading can also be used to model shadowing through approximating the shadowed Rician distribution [42]. Surprisingly enough, the Rayleigh fading

can also be used as an approximation of log-normal shadowing with a minor modification; namely, for an even simpler shadowing model than the Nakagami, a feasible compromise between tractability and realism is the *defective exponential power fading distribution*

$$\mathbb{P}(h > y) = \nu e^{-yc}, \nu \in (0, 1], c > 0, \quad (2.13)$$

which can be used to model the log-normal mixture shadowing through matching the first two moments of the fading distributions: This shadowing distribution will be used in the interference cancellation in Section 3.6.4 (Publication IV includes more details and a comparison to Monte Carlo simulated actual log-normal shadowing).

Multiple refined models exist. Fading models exist that include the Doppler effects (see, *e.g.*, [43]), which can be utilized in the stochastic geometry analysis presented in the work. However, we leave them without further attention, since the scope of the thesis is in system-level stochastic geometry characterization of LEO communications rather than punctual link-level signal modeling and processing. While, of course, realism is of value, the ultimate aim is clarity and insight.

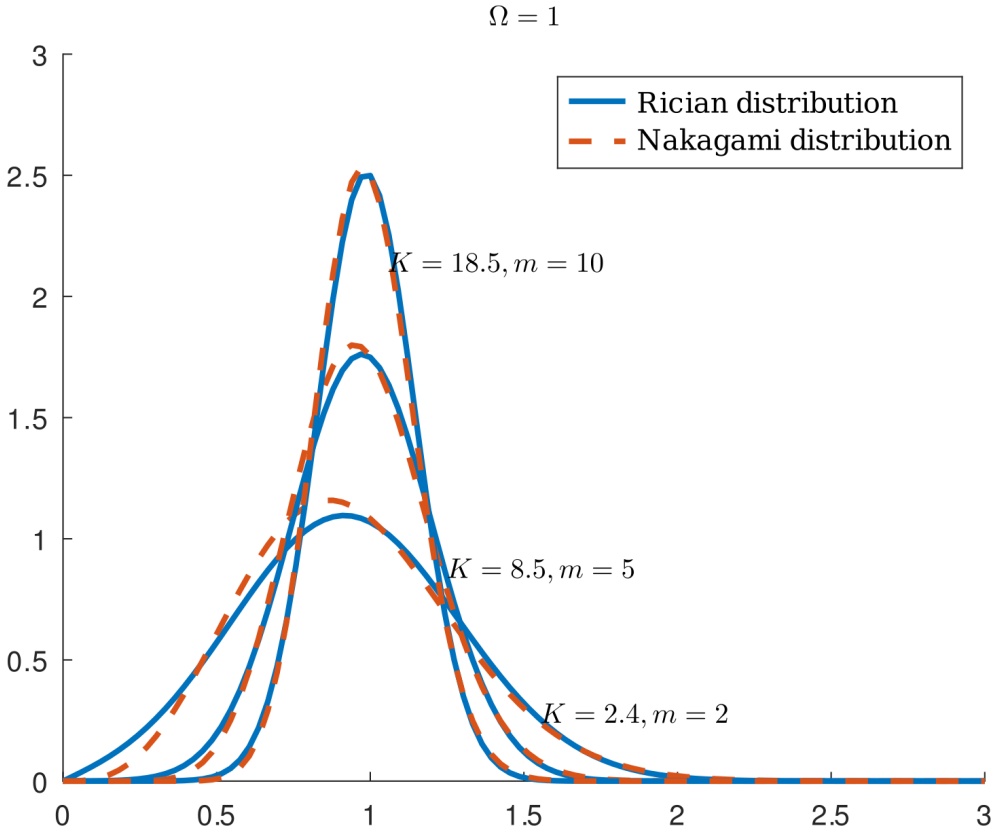


Figure 2.10. Comparison between the PDFs of the Rice- K and Nakagami- m distributions with equal mean and variance of the distributions of the squared r.v.'s, corresponding to matched first two moments of the power fading.

2.7.2 Temporal fading characteristics

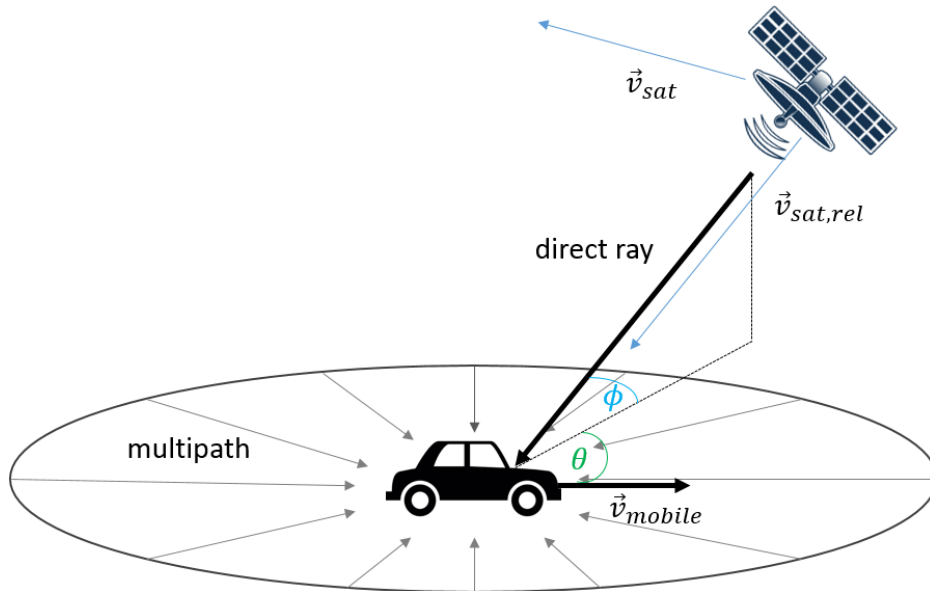


Figure 2.11. Geometry for Doppler effects in the satellite. (The figure is from a Wikipedia article.)

Doppler shift at the LEO BS is caused by the movement of the Earth transmitter, the movement of the satellite, and the movement of the Earth. Accordingly, the crucial properties are the orbital velocity of the satellite and its relative velocity w.r.t. the Earth transmitter: \vec{v}_{sat} and $\vec{v}_{sat, rel}$, respectively. The Doppler shifts will not cause such distortion to the signals (through dispersion and group delay effects) that would fall into the wide-band category, *i.e.*, we persist with the narrow-band assumption throughout the thesis. The Doppler shift is directly linked to the temporal structure of fast fading.

As depicted in Figure 2.11, one of the simplest models for a fading and Doppler LEO channel is that the multi-path components arrive at the receiver from uniformly distributed directions. This may be the most plausible scenario in a downlink transmission from the satellite to Earth; see Figure 2.11. However, a similar model applies to the uplink. The maximum Doppler shift is determined by the absolute value of the velocity vector of the Earth transmitter, *i.e.*, the speed, $f_{Dmax} = |\vec{v}_{mobile}| / \lambda_c$, where λ_c is the wavelength of the transmission carrier and the Doppler shift due to $\vec{v}_{sat, rel}$. For the direct path, the Doppler shift caused by the Earth transmitter movement is $f_{Ddir} = |\vec{v}_{mobile}| / \lambda_c \cos(\phi) \cos(\theta)$.

In the thesis, we omit the movement of the terrestrial transmitters and the movement of the Earth. In the model, the farther multipath scatterers are uniformly distributed around the transmitter, and the Doppler spectrum is

symmetric to the carrier frequency. The theoretical PSD of a pure sinusoid response in the Doppler channel is described with a first-order Butterworth-like Jake's power spectrum [44]:

$$S_{\text{Doppler}}(f) = \begin{cases} \frac{B}{\sqrt{1-(f/f_{\text{Dsat}})^2}} & \text{for } |f| \leq f_{\text{Dsat}}, \\ 0, & \text{otherwise,} \end{cases} \quad (2.14)$$

where B is a normalization constant so that the filter energy is equal to one, and f_{Dsat} is the Doppler shift, which will be characterized in this section. The variation characteristics of a signal responding to the Doppler-shifted channel are driven by the Doppler spectrum (2.14) and its counterpart autocovariance function

$$K_{yy} \triangleq \mathbb{E}(y(t)y(t - \tau)), \quad (2.15)$$

which describes the correlation of the signal y with itself in lagged time τ . The autocovariance function of a Rayleigh faded sinusoid $y(\cdot)$ involves the zeroth-order Bessel function of the first kind $K_y(\tau) = J_0(2\pi\tau f_{\text{Dsat}})$. Consequently, the fading envelope amplitude correlation time, or coherence time, of the multipath component of the fading gain (denoted here by $H(t)$) has an approximate autocovariance $K_H(\tau) = J_0(2\pi\tau f_{\text{Dsat}})^2$. However, this is an unnecessarily complex model, particularly considering its Fourier transform, *i.e.*, the PSD, which has no closed-form nor analytical representation. Hence, adequate for the accuracy scope of this work, in the temporal analysis, we use the triangular autocovariance function

$$K_H(\tau) = \text{triang}(\tau f_{\text{Dsat}}), \quad (2.16)$$

which governs the correlation of the multipath component of the fast fading gain of a continuous signal in a *block fading* channel. The PSD describes the spread of frequencies due to multipath scattering in the frequency power domain $f \in \mathbb{R}$, and it is given as the Fourier transform of (2.16):

$$C_H(f) = \frac{1}{f_{\text{Dsat}}} \text{sinc}^2 \left(\frac{f}{f_{\text{Dsat}}} \right). \quad (2.17)$$

2.7.3 Antenna attenuation due to satellite movement

Since we concentrate on narrow beams, the signal gain of a terrestrial transmitter at the LEO BS is suppressed relatively quickly. The satellite moves at its orbital speed, and the signal of a non-mobile terrestrial transmitter will attenuate as the satellite moves over the transmitter. For the -3 dB halfwidth $\varphi_{\text{RX}} = 1.6^\circ$, the attenuation time varies from 6 seconds to 60 seconds for the altitudes $h \in \{200, 2000\}$ km, respectively. For signal processing, it is crucial to recognize whether the antenna attenuation time dominates the fading coherence time or vice versa. To address this, we

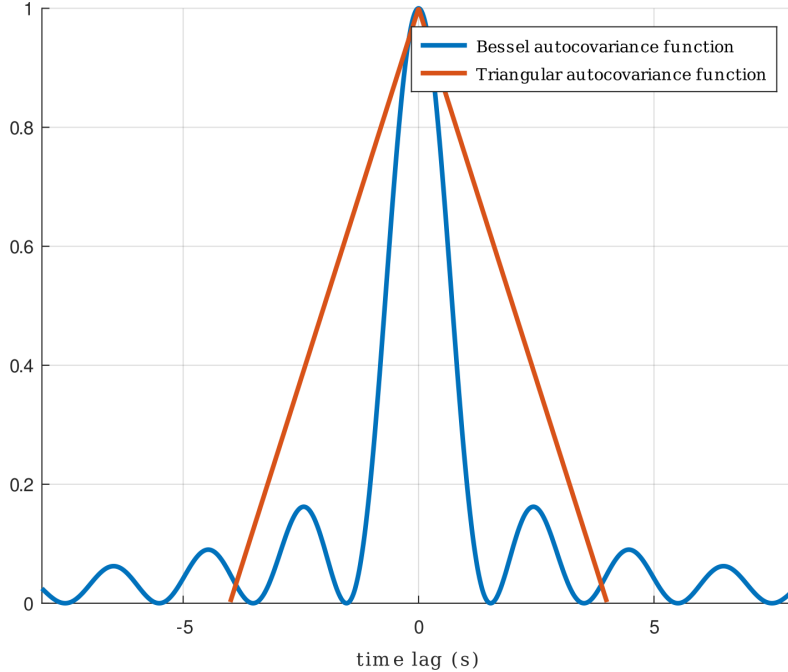


Figure 2.12. The Bessel model and the corresponding block fading triangular autocovariance model. The coherence time is $1/f_{\text{Dsat}} \approx 4$ s.

define the antenna gain envelope amplitude correlation time for a Gaussian antenna attenuation as a fraction $1/5$ of the attenuation time of the -3 dB lobe:

$$\tau_a \triangleq \frac{\varphi_{\text{RX}} h}{5 \sin^2(\epsilon) v_{\text{sat}}}, \quad (2.18)$$

where h , ϵ , φ_{RX} (rad), and v_{sat} are the altitude, elevation angle, -3 dB antenna gain halfwidth, and the orbital speed of the satellite, respectively.

Example 2.7.1. For $\epsilon = \pi/2$, and $\varphi_{\text{RX}} = 1.6^\circ = 0.0279$. The amplitude correlation times for the altitudes $h \in \{200, 1000, 2000\}$ km are

$$\tau_a \in \{0.2, 0.8, 1.6\} s, \quad (2.19)$$

respectively. See Figure 2.13 for a demonstration.

2.7.4 Doppler shift due to the satellite movement

We can consider the Doppler shift to be equal for all transmitters within the narrow beam. The Doppler shift depends on the relative speed w.r.t. to the Earth transmitters. The relative speed is zero at the zenith and increases steeply for smaller elevation angles. A rough upper-bound approximation of a LEO satellite relative speed is the approximate orbital speed

$$|\vec{v}_{\text{sat, rel}}| \approx 7.4 \text{ km/s}. \quad (2.20)$$

The direction of $\vec{v}_{\text{sat, rel}}$ is towards the transmitters; hence, the Doppler shift is always positive. Based in these notions and experimental data (see Figs

[2.14a-2.14b](#)), the Doppler shift (also of the baseband signal) due to the satellite movement is

$$f_{\text{Dsat}} \triangleq |\vec{v}_{\text{sat, rel}}| / \lambda_c = |\vec{v}_{\text{sat, rel}}| f_c / c \approx 5/2 \times 10^{-5} f_c, \quad (2.21)$$

where λ_c [m] is the carrier wavelength and f_c [Hz] is the carrier frequency, and $c \approx 299,792$ km/s is the speed of light. [\[45\]](#) provides a more thoughtful study of the LEO Doppler shifts.

Antenna attenuation at the LEO BS Gaussian antenna

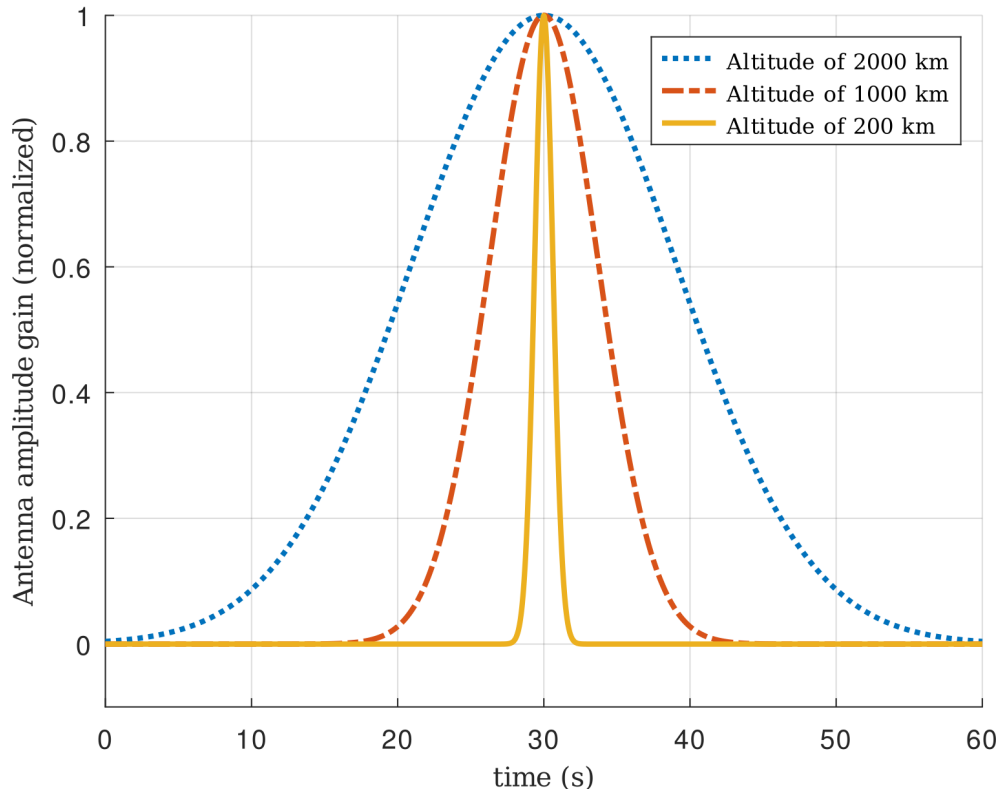


Figure 2.13. Antenna attenuation gain of a transmitted signal as the LEO BS satellite moves over the terrestrial transmitter. The satellite orbit altitudes $h \in \{200, 1000, 2000\}$ km are simulated in the spherical model. The -3 dB halfwidth $\varphi_{\text{RX}} \approx 1.6^\circ$.

Figures 2.14a-2.14b show the simulated Doppler shift and its theoretical counterpart in the baseband equivalent LEO ($h = 200$ km) channel with a carrier frequency $f_c = 100$ kHz, corresponding to a Doppler shift $f_{\text{Dsat}} = 2.5$ Hz. In Figure 2.14a, the shift becomes visible after the LEO BS has progressed an adequate distance from the zenith. The simulated Doppler shift is close to the approximation of the Doppler shift 2.14b when the LEO BS is at a sufficient distance from the zenith.

2.7.5 Fading correlation time

The envelope amplitude correlation time (coherence time) of the faded signal depends on the carrier frequency, altitude, and the spread of the scatterers. A correlation distance of tens of meters is proposed for the LEO link (*n.b.:* not time) in [45]. The amplitude correlation time is not the direct scope of this thesis. However, based on the simulation (the code at the end of the section), an estimate for the amplitude correlation time, as the satellite moves at its orbital speed and the transmitter is non-mobile, is

$$\tau_c \triangleq 1/f_{\text{Dsat}} \approx \frac{4\pi \times 10^5}{5f_c}, \quad (2.22)$$

which gives a *rough* temporal scale of the fading coherence assuming that the scatterers are spread in a -3 dB footprint-sized area.

Example 2.7.2. For $f_c = 1$ GHz, $\tau_c \approx 0.04$ s. Hence, the fading amplitude correlation time is clearly shorter than the antenna envelope attenuation correlation time, $\tau_a = 0.2$ s, in the L, S, C, X, Ku, K, Ka bands and beyond, for the narrow-beam LEO BSs at altitudes $h \in [200, 2000]$ km.

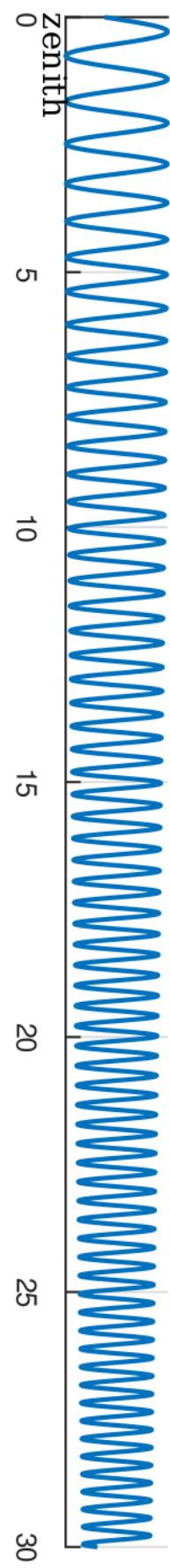
In Chapter 3, we are for the most part interested in the average signal power over a coherent or non-coherent use period in a *non-temporal* sense. Whether we consider the Earth transmitters to be moving or not, the direct characterization of the Doppler shifts—and the Doppler spread—is abstracted in the random propagation model. The movement of the satellite shifts the signals in the frequency spectrum by the magnitude (2.21). However, for narrow-band and narrow-beam LEO BS settings, it is reasonable to assume that dispersion due to the delay spread is negligible, and we can consider that the Doppler shifts do not alter for the transmitters in a small footprint of a narrow antenna beam. Hence, the relative signal powers in the frequency band during the use period are invariant. The multipath fading effects, which are related to the Doppler shift in the temporal sense, a large variety of statistical models are feasible for the analysis, including many statistical propagation models of the received signal envelope or power magnitude with the Doppler effect incorporated. The simplest model is the Rayleigh model for the multipath propagation component, which, in the temporal sense, connects to the Doppler shift through Jake's model and the corresponding PSD and the autocorrelation function.

The temporal channel responses are studied in Chapter 4. Novel autocorrelation and PSD models are proposed specifically for narrow-band and narrow-beam LEO systems. Temporal stochastic geometry modeling and analysis of LEO communications based on stochastic geometry will be proposed. The models are a balance between tractability, insight, and realism.

2.7.6 Simulated example of a Narrow-beam LEO Rician channel response of a sinusoidal signal

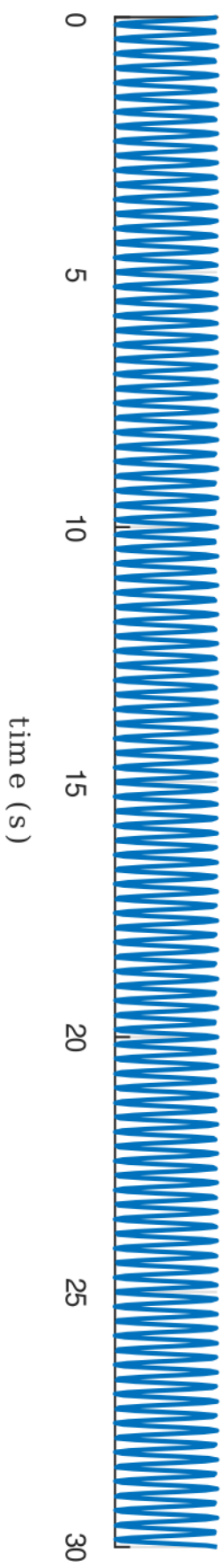
See Figure 2.15 for a simulation of the channel response of a signal at the narrow beam LEO BS receiver at the altitude $h = 200$ km and elevation angle $\epsilon = 90$ deg w.r.t. the sub-satellite point (the antenna is constantly directed towards the Earth center), as the satellite moves over the transmitter. The Rician multipath channel is modeled with Poisson locations of scatterers on the (spherical) Earth surface. The Earth rotation is not modeled, and the satellite is in a non-inclined orbit. A signal of a single tone $S_b(t) = A \exp\{-2\pi f_m t i\}$, where $A > 0$, $f_m = 10$ Hz and $i^2 = -1$, is quadrature amplitude modulated (QAM) onto a carrier wave of frequency $f_c \in \{1\text{ kHz}, 1\text{ GHz}\}$, probed through the channel, then downconverted back to the baseband equivalent complex signal and further its real part using ideal filtering at the LEO BS (see [28][Sec. 2.2.2 Baseband Equivalent Model] for further details). The signal is affected by the fading, Doppler shift, and phase shift, of which the latter is not of direct interest but can be calculated easily from the delay by using (2.2) or (2.4). The Octave code for the simulation is given at the end of the section.

LoS channel and omnidirectional LEO BS antenna, $f_m = 1 \text{ Hz}$, $f_c = 100 \text{ kHz}$



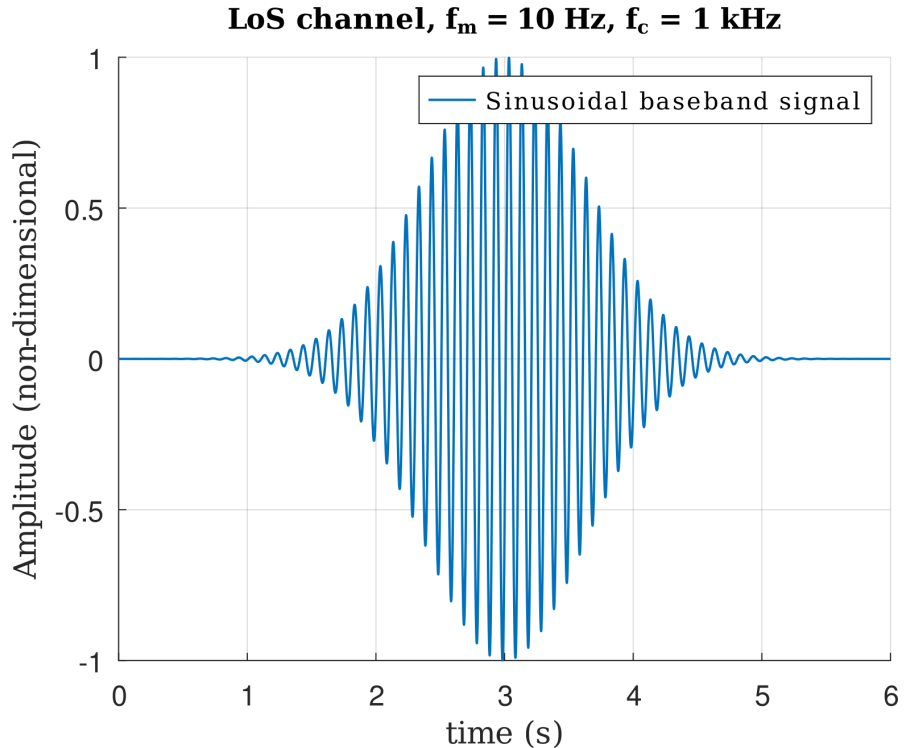
(a) Simulation.

The theoretical Doppler shifted signal



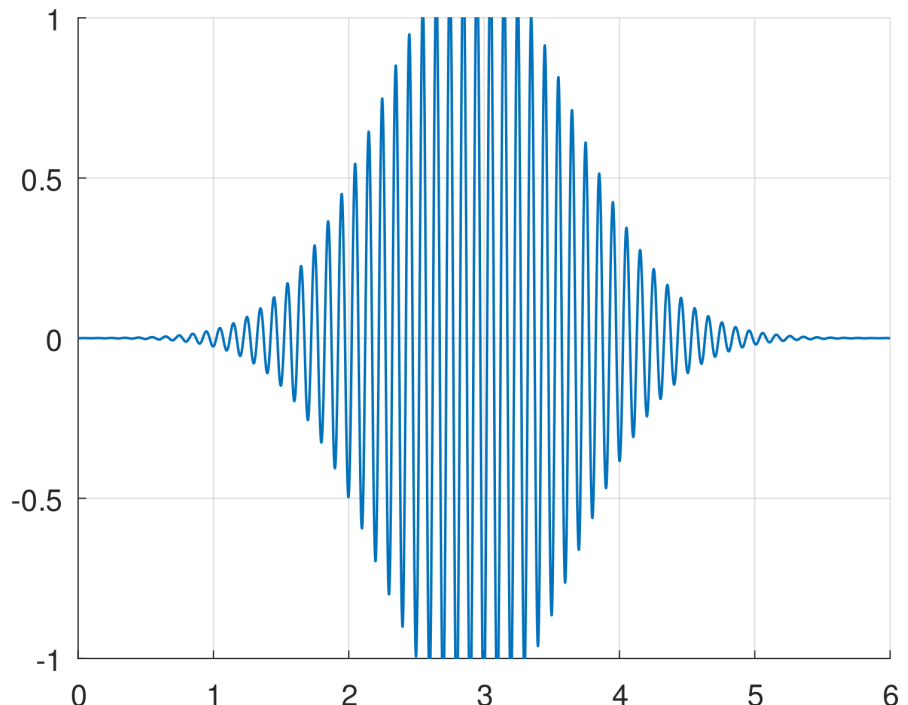
(b) Theory.

Figure 2.14. Simulated and the Doppler shift model used in the theory.

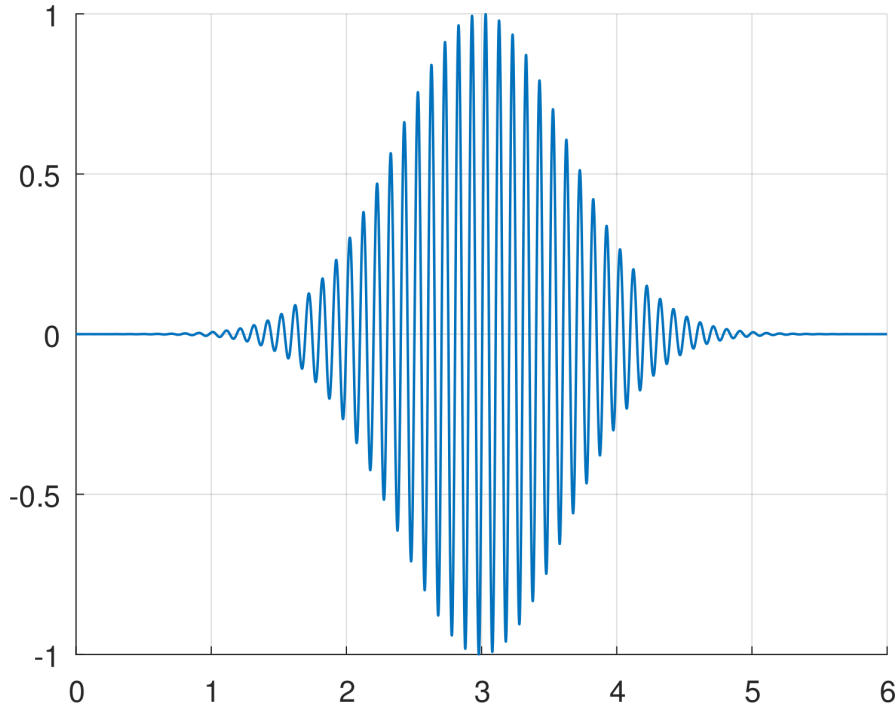


(a) The channel response is with a small carrier frequency in a pure LoS channel. Only antenna attenuation and Doppler shift (which is not visually apparent) are present.

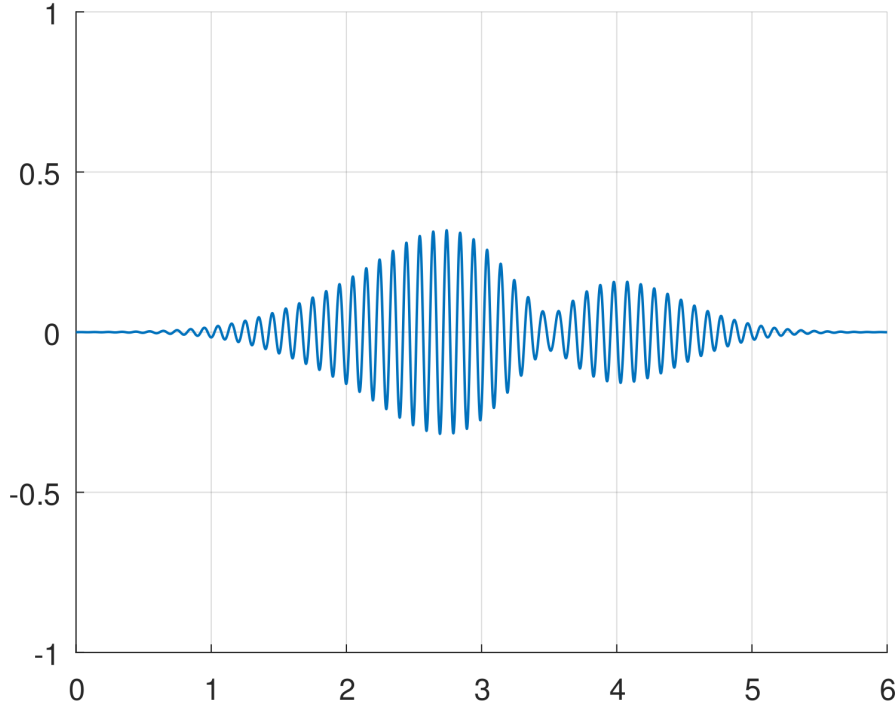
Rician channel $K = 1$, $f_m = 10$ Hz, $f_c = 1$ kHz



(b) The channel response is with a small carrier frequency in a Rician fading channel. The fading coherence time is longer than the antenna attenuation envelope amplitude correlation time; $\tau_c > \tau_a$. In the example, the signal is amplified due to fading.

LoS channel, $f_m = 10$ Hz, $f_c = 0.1$ GHz

(c) The channel response is with a high carrier frequency in a LoS channel. Only antenna attenuation and Doppler shift are present: In the LoS channel, for the high carrier frequency, the response is almost identical to Figure 2.15a.

Rician channel $K = 1$, $f_m = 10$ Hz, $f_c = 0.1$ GHz

(d) The channel response is with a high carrier frequency in a Rician fading channel. The fading coherence time is a similar time-scale to the antenna attenuation correlation time; $\tau_c \approx \tau_a$. In the example, the response has a deep fade at $t \approx 3.5$ s.

Figure 2.15. The channel response of a tone affected by Doppler shift, multipath scattering, and narrow-beam antenna attenuation.

```

function [Gss taus LoSloc, signals] = satellite_baseband_simulation()
    ## The algorithm simulates the baseband equivalent signal in the LEO
    ## channel when the satellite passes over a transmitter. The LEO BS is
    ## at zenith w.r.t. its sub-satellite point. The multipath propagation is
    ## modeled with Poisson distributed scatterers around the transmitter.
    ## At each scatterer, the signal is reflected at a random phase towards
    ## the satellite, and the propagation delay is calculated according to
    ## the scatterer location. (The propagation between the transmitter
    ## and each scatterer is not modeled.)
    ##
    ## Outputs a plot of the signal and the following observables:
    ## Gss: the maximal gain of the propagated signal components at each simu-
    ## lated time instance given in Gs(1, :), the minimum gains in Gs(2, :)
    ## taus: the maximal propagation delays at each simulated time instance
    ## in tau(1, :), and the minimum delays in tau(2, :)
    ## LoSloc: the location of the Earth transmitter (LoS ray) at each
    ## simulated time instance in polar coordinates
    ## signals: a vector of the received faded signal in discrete times

R = 6378 * 1000; # Radius of Earth in m
h = 200 * 1000; # Altitude of the satellite
K = 1; # Rician parameter

scatterers = 1000; # Number of scatterer-obstacles
refs = refpoints(scatterers); # Initialize scatterer locations into 'refs'
A = h; # Amplitude of the transmitted signal
fm = 10; # Modulation frequency
fc = 1 * 10 ^ 5; # Carrier frequency

## bbsignals(.) is utilized by the nested function RXbaseband(.)
bbsignals = @(t) [A * sqrt(K / (K + 1)) .* exp(-i * 2 * pi .* fm * t)];
## Random phases for initial baseband transmissions
randphases=rand(1, length(refs(1, :)) - 1);
## Combine the LoS and scattered components
bbsignals = @(t) [bbsignals(t(1)) A / (sqrt(scatterers).*sqrt(1 + K))...
    .* exp(-i * 2 * pi .* t(2: length(t))...
    .* fm + randphases .* 2 * pi * i)];
## Distance to the satellites in m, utilized in RXbaseband(.)
d = @(gamma) sqrt((cos(gamma) .* (R + h) - R) .^ 2 + ...
    (sin(gamma) .* (R + h)) .^ 2);
## The angle in the antenna pattern, utilized in RXbaseband(.)
varphi = @(gamma) acos((d(gamma) .^ 2 + (R + h) .^ 2 - R ^ 2)...
    ./ (2 .* d(gamma) .* (R + h)));

```

```

## Gaussian antenna gain, utilized in RXbaseband(.)  

G = @(gamma) 2 .^ (-varphi(gamma) .^ 2 / deg2rad(1.6) .^ 2);  
  

N = 6000; # Number of time samples  

t = 0; # Initial time  

refs = rotateearth(-3, refs); # Initialize the Earth position  

[signal Gs] = RXbaseband(t); # Initialize the first baseband signals  

thop = 1 / 1000; # The time hop per each rotation  
  

taus = zeros(2, N); # Reserve the memory for the output vectors  

Gss = zeros(2, N);  

LoSloc = zeros(2, N);  
  

for iii = 1 : N  

    ## Observe the progress  

    if(mod(iii, 25000) == 0)  

        iii  

    end  

    Gss(1, iii) = max(Gs); # Save the maximal gain  

    Gss(2, iii) = min(Gs); # Save the minimum gain  

    taus(1, iii) = max(tau); # Save the maximal propagation delay  

    ## taus(2, iii) = min(tau); # Save the minimum propagation delay  

    taus(2, iii) = tau(1); # Save the propagation delay of the LoS ray  

    LoSloc(:, iii) = refs(:, 1); # Save the transmitter location  
  

    refs = rotateearth(thop, refs); # Rotate Earth.  

    [signal Gs] = RXbaseband(t); # New received baseband signal  

    signals(iii) = signal;  

    t = t + thop; # Next time instance  

end  
  

## Plot the resulting signal  

figure;  

hold on;  

plot(linspace(0, t, N), real(signals), 'linewidth', 1);  

axis([[0, t], [-1, 1]]);  

xlabel('time_(s)', 'fontname', 'DejaVu_Serif', 'fontsize', 12);  

legend('Sinusoidal_baseband_signal', 'fontname', 'DejaVu_Serif',...  

    'interpreter', 'tex', 'fontsize', 12);  

grid on;  

ylabel('Amplitude_(non-dimensional)', 'fontname',...  

    'DejaVu_Serif', 'interpreter', 'tex', 'fontsize', 12);  

set(gca,'fontsize',12);  

title('LoS_channel,_f_m=_10_Hz,_f_c=_0.1_GHz',...

```

```

'fontname', 'DejaVu_Serif', 'interpreter', 'tex', 'fontsize', 12);
hold off;

## In the following, define two nested functions for the derivation of the
## baseband signal at each time instance, and other for the Earth rotation

## The received baseband signal at time t
function [signal Gs] = RXbaseband(t)
c = 299792458; # Speed of light
if(!isempty(refs))
    a = 1 ./ d(refs(1, :)); # Spatial amplitude path losses
    Gs= G(refs(1, :)); # Gaussian antenna pattern
    ## Gs=ones(1, length(refs(1, :))); # Omnidirectional antenna pattern
    tau = d(refs(1, :)) / c; # Propagation delays
else
    a = [0];
    tau = [0];
end
## Received individual signals
ab = Gs .* a .* exp(-i * 2 * pi .* tau .* fc);
signal = sum(ab .* bbsignals(t - tau)); #Aggregate received signal
endfunction

## Rotates the Earth (moves the satellite) and the scatterer locations in
## 'refs' over the period thop, which can be negative

function newrefs = rotateearth(thop, refs)
GM = 3.986 * 10 ^ 14; # Gravitational constant
orbitalspeed = sqrt(GM / (h + R)); # Satellite speed in m/s
angularspeed = orbitalspeed / (h + R); # Angular speed of the satellite
rotation = angularspeed * thop; # Rotation of Earth
## Transform the polar coordinates to euclidean coordinates
eucpos = pol2euc(refs);
## Rotation about x-axis
newpos = [[1 0 0]; [0 cos(rotation) -sin(rotation)];...
           [0 sin(rotation) cos(rotation)]] * eucpos;
newrefs = euc2pol(newpos); # Back to the polarcoordinates
endfunction

endfunction

## Returns a table of numbPoints Poisson points around the north pole
function refs = refpoints(numbPoints)

```

```

refs = [0; 0]; # LOS component location.
## Generate the Poisson distributed random obstacle locations
## Change yMin to control the area width of the scatterers
## yMin = 1 - 0.00035; yMax = 1; # -3 dB footprint for h = 2000 km
yMin = 1 - 0.0000035; yMax = 1; # -3 dB footprint for h = 200 km
xMin = -pi; xMax = pi;
xDelta = xMax - xMin; yDelta = yMax - yMin; # Rectangle dimensions
## Pick points from uniform distribution
x = xDelta * (rand(numbPoints, 1)) + xMin;
y = yDelta * (rand(numbPoints, 1)) + yMin;
## Map the reference points to spherical coordinates
refs = [refs pi / 2 - asin(y)'; x'];
end

function p = euc2pol(e) # Euclidean 3D coordinates to polar
R = 6378 * 1000; # Radius of Earth
p = [acos(e(3, :) ./ R); (e(2, :) >= 0) .* atan2(e(2, :), e(1, :)) ...
      + (e(2, :) < 0) .* (atan2(e(2, :), e(1, :)) ...
      + 2 * pi)];
end

function e = pol2euc(p) # Polar coordinates to 3D Euclidean
R= 6378 * 1000; # Radius of Earth.
e = [R * cos(p(2, :)) .* sin(p(1, :));...
      R * sin(p(2, :)) .* sin(p(1, :));...
      R * cos(p(1, :))];
end

```

3. Non-temporal analysis of the narrow-beam LEO

3.1 Mathematical formulation of stochastic processes

We can study the statistical properties of a sampled data $X = \{x_1, x_2, \dots, x_N\} \in \mathbb{R}^n$ consisting of real numbers:

1. average; $\mathbb{E}(X) = \sum_{i=1}^N x_i/N$,
2. variance; $\text{var}(X) = \mathbb{E}(X^2) - \mathbb{E}(X)^2 = \sum_{i=1}^N x_i^2/N - \mathbb{E}(X)^2$,
3. skewness,
4. kurtosis (heavy-tailedness),
5. etc.

Each property is determined by the order $n \in \{1, 2, 3, 4, \dots\}$ moments $\mathbb{E}(X^n)$, respectively. Generally, the $\mathbb{E}(X^n)$, $n > 2$, is called the higher-order statistics (HOS). Under the law of large numbers, as the sample size grows arbitrarily large, $N \rightarrow \infty$, the sample HOSs are equal to the HOSs of the underlying r.v.¹ The average value and HOS are a sufficient characterization of a r.v. on a bounded domain. However, in the following, we will formulate the measure-theoretic definition of the r.v.

Slightly abusing the notation, we proceed with the definition of a r.v. X having the outcomes in \mathbb{R} by equating it with an indefinitely large sample data

$$X = \lim_{N \rightarrow \infty} \{x_1, x_2, \dots, x_N\}.$$

Let us assume that the limiting properties of the data assign a *probability* $0 < \mathbb{P}(A_i) \leq 1$ to interval (t_1, t_2) as the fraction of sample appearances within the interval *vis-à-vis* the total number of samples. Furthermore, the applies for a chosen family of open or closed sets $\{A_i\}_{i \in \mathcal{J}} \subset 2^{\mathbb{R}}$ (the index set

¹Taking here a more or less frequentist stance that such an r.v. with objective stochastic properties exists.

\mathcal{I} can be countable or not). For the sake of the mathematical description, we insist that all such sets under the interest belong to a family $\mathcal{F} \subset 2^{\mathbb{R}}$, which must include, at minimum, the set \mathbb{R} and the empty set \emptyset , plus the countable unions, countable intersections, and mutual complementations of all its members. The *sample space* \mathbb{R} has the probability $\mathbb{P}(\mathbb{R}) = 1$ (by definition, any sample is certainly in \mathbb{R}) and the probability that nothing happens $\mathbb{P}(\emptyset) = 0$. The sum of the probability measures of the disjoint subsets is countably additive, adding at most to 1 and summing precisely to 1 if they cover all \mathbb{R} . By this definition, the family \mathcal{F} forms a σ -algebra, corresponding to the *event space* that, combined with the probability measure $\mathbb{P}(\cdot) : \mathcal{F} \rightarrow (0, 1)$, constitutes the *probability space*,

$$\mathcal{P} = (\mathbb{R}, \mathcal{F}, \mathbb{P}(\cdot)). \quad (3.1)$$

An event $A \in \mathcal{F}$ with probability $\mathbb{P}(A) > 0$ and the events without a zero-probability neighborhood, *i.e.*, $\mathbb{P}\{S \cap A\} > 0$, for all open $\mathcal{F} \ni S \supseteq A$, is called an observable event or observable realization—or only an *event* or *realization*. We will use the notations $\mathbb{P}\{X > x\} = \mathbb{P}\{(x, \infty)\}$ and $\mathbb{P}\{X = x\} = \mathbb{P}\{\{x\}\}$, *etc.*, interchangeably.

Definition 3.1.1. The *probability distribution* is a function representing the probability measure $\mathbb{P}(\cdot)$. For a one-dimensional r.v. X ,

$$F(t) = \mathbb{P}\{X > t\} = \mathbb{E}\{\mathbf{1}(X > t)\}. \quad (3.2)$$

The distribution function reflects the probability of an event that the r.v. exceeds $t \in (-\infty, \infty)$. The latter, useful, equivalence includes the indicator function $\mathbf{1}(\cdot)$ of a given event, mapping X into a biased coin toss for a given t . Having the pointwise probabilities well-defined, (3.2) can be identified with the probability distribution, admitting a representation by a *right-continuous* complementary cumulative distribution function (CCDF); $F(\cdot)$. The possible discontinuities in the CCDF correspond to *atomic* probability measures of singleton sets at the jump locations: The distribution function can describe the statistics of discrete, continuous, or mixed r.v.'s.

Remark. If the CCDF is strictly decreasing and continuous at some t , arbitrary small neighborhoods $(t - \varepsilon, t + \varepsilon), \varepsilon > 0$ have a non-zero probability: $\mathbb{P}\{(t - \varepsilon, t + \varepsilon)\} = F(t - \varepsilon) - F(t + \varepsilon) > 0$. Considering the limit $\varepsilon \rightarrow 0$, one can consider $X = t$ a possible event and an observable realization, even though $\mathbb{P}\{X = t\} = 0$. This is a mathematical artifact stemming from the measure-theoretic formulation of probability theory. However, there can be null events so remote from the domain of non-zero measure that, with all the best stretching of the imagination, can not be considered “observables”. (Consider, for example, a CCDF of a coin flip and the null sets it induces—the CCDF defined on \mathbb{R} as a two-step function). This is exactly the reason we describe the realizations to exclude the measure-zero events that are sufficiently “far”, *i.e.*, which have measure-zero events in

their neighborhood, from non-zero events. The term “almost never”, or its complement, “almost surely” (*a.s.*), is commonly used and refers to such possible zero-probability events. Alternatively, we could redefine the sample and event space and minimize the irrelevant null events, but this is not always feasible. While the mathematical analysis is practical by considering the continuum for the sample space, in reality, sample spaces are finite at the core. For example, when implementing a stochastic process on a digital computer, all observable events have a positive probability because of the limited resolution and memory space.

In the *Monte Carlo simulations* technique, the probability distribution of a random variable is determined by the average $\mathbb{E}(\mathbf{1}(X > t)) = \mathbb{P}(X > t)$ from a large set of observation data simulated by a computer; this also entails the study of moments $\mathbb{E}(X^n)$, *etc.* The indicator function $\mathbf{1}(\cdot)$ denotes that a given event is observed.

A set of one-dimensional r.v.’s combined is a multidimensional r.v., or random vector, $\mathbf{X}_s = (X_1, \dots, X_m)$, $m \in \mathbb{N}$. Further, a set of sets (a family) of r.v.’s $\Xi = \{\mathbf{X}_s\}_{s \in \mathcal{I}}$ is a generic random process. If each \mathbf{X}_s is associated with a probability space determined from the probability spaces of X_i , then the probability space $\mathcal{P}_\Xi = \mathcal{P}(\Omega_\Xi, \mathcal{F}_\Xi, \mathbb{P}_\Xi(\cdot))$ of Ξ is a combination. Determining this probability space does not have a general, straightforward single-hand methodology. Let us verbalize our working definition of a stochastic process:

The *stochastic process* encompasses the observable events of a random phenomenon, each event associated with a *probability measure* represented by one or multiple *probability distribution* functions.

We consider the stochastic process as the mathematical description of a random process with a well-defined statistical structure (probability space); however, this philosophical distinction between “random” and “stochastic” is not definite and is used interchangeably in this work.

Example 3.1.1 (Binomial point process.). The stochastic process of a single uniformly distributed point in a finite box $(0, L) \times (0, L) \subset \mathbb{R}^2$ is easy to construct as a combination of two uniformly distributed one-dimensional r.v.’s. Consider $\mathbf{X} = (X, Y)$, where X and Y are independent uniform r.v.’s on $(0, L)$. From the independence, \mathbf{X} admits the joint distribution function $F(x, y) = F_X(x)F_Y(y)$, where

$$F_X(x) = \mathbb{P}\{X > x\} = \begin{cases} \mathbf{1}(x \leq 0) & x \leq 0 \text{ or } L \leq x, \\ 1 - t/L & 0 < t < L. \end{cases} \quad (3.3)$$

and equivalent for Y . Furthermore, the process of N such independent points is called the binomial p.p. $\{\mathbf{X}_i\}_{i \in [N]}$. Its distribution is $\prod_{i \in [N]} F(x_i, y_i)$ for all $(x_i, y_i) \in (0, L) \times (0, L)$. Following the definition, for each subset $A \subset \mathbb{R}^2$, the number of points within the subset follows the binomial distribution

depending on the size of the set A , L , and N . Hence, the binomial process can be interpreted as a *random counting measure* on the subsets of $(0, L) \times (0, L) \subset \mathbb{R}^2$ (straightforwardly generalizing to \mathbb{R}^n).

3.2 Homogeneous Poisson point process

We are finally ready to formalize the Poisson point process (PPP). The homogeneous Poisson point process (PPP) can be seen, in a sense, as a limit of the binomial process as $L \rightarrow \infty$, $N \rightarrow \infty$. However, because defining the distribution of a “uniform” r.v. on the entire \mathbb{R} is troublesome, constructing the PPP is not this straightforward merely by combining random points as in Example 3.1.1. We will characterize the Poisson point process (PPP) on the plane directly as a combination of *random measures* on the subsets of \mathbb{R}^2 .

Consider a Poisson r.v. $X = \Phi(A)$, representing the number of points on a set $A \subset \mathbb{R}^2$ of the area, *i.e.*, *Lebesgue measure*, $|A|$, with the CCDF

$$\mathbb{P}\{\Phi(A) > t\} = 1 - e^{-\lambda|A|} \sum_{j=\lceil t \rceil}^{\infty} \frac{(\lambda|A|)^j}{j!}, \quad (3.4)$$

where $\lceil t \rceil$ is the ceiling function, *i.e.*, the smallest integer greater than or equal to t . The λ is called *the density parameter*. The value $\lambda|A|$ is called the intensity measure. We have the following alternative representation of the probability measure as the probability mass distribution function:

$$\mathbb{P}\{\Phi(A) = k\} = \frac{(\lambda|A|)^k e^{-\lambda|A|}}{k!}, \quad (3.5)$$

for $k \in \mathbb{N}$ and 0 otherwise.

Next, we formulate the homogeneous PPP on any space \mathcal{S} (say, the plane or the surface of a sphere), or more precisely, on its *measurable* subsets that form a σ -algebra that contains the compact sets of \mathcal{S} (smallest such being the Borel algebra).

Let $\Phi_s = (\Phi(A_{s_1}), \dots, \Phi(A_{s_m}))$ be a random vector of the Poisson distributed r.v.’s on disjoint compact measurable (Borel) sets A_{s_i} . The homogeneous PPP is the stochastic process $\{\Phi_s\}_{s \in \mathcal{J}}$, with the index set \mathcal{J} indexing a family of compact sets. And indeed, such a p.p. can be defined: the sum of Poisson distributed independent r.v.’s $\sum_{i=1}^m \Phi(A_{s_i})$ follows a Poisson distribution with the intensity measure $\sum_{i=1}^m \lambda|A_{s_i}|$. Conversely, if the sum of independent r.v.’s is Poisson distributed, then are the r.v.’s [46].

Since $\Phi(A) \in \mathbb{N}$, Φ is a Poisson counting measure. From now on, we denote by Φ the homogeneous PPP regardless of whether we refer to it as the measure on the σ -algebra or any other formal definition. In practice, $\mathcal{S} = \mathbb{R}^2$ is sufficient for the analysis of the work, which we will continue asserting. Let us further clarify the notations regarding the PPP and the events in the following.

Definition 3.2.1 (Event). By $\Phi(A)$, we refer to the random counting measure (of the points) on A . By Φ , we refer to random point realizations, which are families of point sets. On the other hand, with a slight abuse of the notation, but without ambiguity, we may emphasize the space of the point process point realizations by denoting $\Phi \subset \mathbb{R}^2$. The individual random points in the p.p. are denoted as $x \in \Phi$. We denote $\mathbb{P}\{\Phi \in \mathcal{A}\}$ as the probability of an abstract event \mathcal{A} in the Borel algebra \mathcal{F}_Φ ; for example, $\mathcal{A} = \{\text{"There exists an unit circle containing 4 points."}\} \in \mathcal{F}_\Phi$. Another example of notation usage is

$$\begin{aligned} & \mathbb{P}\{\Phi(A \cap B) > t\} \\ & \equiv \mathbb{P}\{\Phi \in \{\text{"more than } t \text{ points in the intersection of } A \text{ and } B"\}\}. \end{aligned}$$

If the events $\mathcal{A}_1 = \mathcal{A}_2$ in distribution, we mean $\mathbb{P}(\mathcal{A}_1 > t) = \mathbb{P}(\mathcal{A}_2 > t)$ for all $t \in \mathbb{R}$. A conditioned PPP Φ on the event \mathcal{A} is denoted as $(\Phi|\Phi \in \mathcal{A})$, and in the single point case, $\Phi_x \equiv (\Phi|x \in \Phi) \equiv (\Phi|\{\Phi(\{x\}) = 1\})$, etc. The probability as a function of the event space can also be denoted as $\mathbb{P}\{\Phi \in \cdot\}$ (c.f., the standard function notation $f(\cdot)$). Among the mathematical jargon and multiple notations, we use the most convenient depending on the scope.

By definition, all events are superpositioned by the counting measures on the compact sets on \mathbb{R}^2 .

We observe important properties.

Theorem 3.2.1 (Crucial properties of the homogeneous PPP).

The homogeneous PPP has the following properties.

- (I) Simple; all points are distinct,
- (II) The points are spatially completely independent,
- (III) Translation invariant, stationary and ergodic,
- (IV) Conditionally a binomial p.p.

Proof. The results are well-known, and we will briefly go through them in this section (also seeking a somewhat contemporary approach). \square

3.2.1 Palm calculus

Intuitively, a p.p. is a random set of points, each exhibiting more or less dependence on the other point locations. The PPP has no dependence between the points: Φ exhibits *complete spatial randomness*. Namely, conditioning on any point does not alter the statistics of the PPP: This is *Slivnyak's Theorem*. In this section, we formalize this important property for

the homogeneous PPP. First, we define the single-point event as a countably infinite intersection of compact discs.

Definition 3.2.2 (Point-event). Let $D(x, \varepsilon), \varepsilon > 0$, be a compact disc of radius ε . We can formulate the singleton or point event, *i.e.*, the random measure $\Phi(\cdot)$ on a point set, as a countable intersection of discs:

$$\Phi\left(\lim_{\delta \rightarrow 0} D(x, \delta)\right) \triangleq \Phi\left(\bigcap_{n=1}^{\infty} D(x, \varepsilon/n)\right) = \Phi(\{x\}). \quad (3.6)$$

Because the homogeneous PPP is absolutely continuous w.r.t. the Lebesgue measure (all probabilities $\mathbb{P}\{\Phi(D(x, \varepsilon)) = k\}$ are (well-)defined by $\lambda \times |(D(x, \varepsilon)|$). Inductively, a point set realizations ϕ of Φ follows by combining point-events of Φ , and has the corresponding probability structure defined by the limiting process.

Although observable, the probability of the single-point event $\Phi(\{x\}) > 0$ occurring is zero; however, it is reasonable to assume that some such events must always occur. Further, recall property (I): if there is a point at $\{x\}$, there are no other points at an equivalent location. That is, the homogeneous PPP is simple, which we formally prove in the following. The logical conclusion is, concisely put, if $\{x\}$ has some points of a realization of Φ , there is *only* one point at $\{x\}$.

Corollary 3.2.2 (The homogeneous PPP is simple). *If $\Phi(\{x\}) > 0$ then $\Phi(\{x\}) = 1$.*

Proof. By (3.4), the void probability,

$$\mathbb{P}\{\Phi(D(x, \delta)) = 0\} = e^{-\lambda\pi\delta^2}. \quad (3.7)$$

By conditional probability, we have for $k \in \mathbb{N}_+$

$$\begin{aligned} & \mathbb{P}\{\Phi(\{x\}) = k | \Phi \in \{\text{"}\{x\}\text{ is non-empty"\}}\} \\ &= \lim_{\delta \rightarrow 0} \mathbb{P}\{\Phi(D(x, \delta)) = k | \Phi(D(x, \delta)) > 0\} = \lim_{\delta \rightarrow 0} \frac{\mathbb{P}\{\Phi(D(x, \delta)) = k\}}{\mathbb{P}\{\Phi(D(x, \delta)) > 0\}} \\ &= \lim_{\delta \rightarrow 0} \frac{(\lambda\pi\delta^2)^k e^{-\lambda\pi\delta^2}}{k!(1 - e^{-\lambda\pi\delta^2})} \stackrel{(a)}{\underline{=}} \lim_{\delta \rightarrow 0} \frac{\delta^{2k}}{(1 - e^{-\lambda\pi\delta^2})} \stackrel{(b)}{\underline{=}} \lim_{\delta \rightarrow 0} \frac{2k\delta^{2k-1}}{2\delta e^{-\lambda\pi\delta^2}} = 1, \end{aligned} \quad (3.8)$$

only if $k = 1$ and 0 for $k > 1$. In (a), the product rule of the limit is used, and (b) uses the product rule and L'Hôpital's rule. \square

Define the conditioned and conditioned, then reduced, PPP as $\Phi_x \equiv \Phi \in \{\Phi(\{x\}) = 1\}$ and $\Phi_x^! \equiv \Phi \in \{\{\Phi(\{x\}) = 1\} \setminus \{x\}\}$, respectively. To clarify the latter, in $\Phi_x^!$, we condition $x \in \Phi$ and then reduce it from the p.p.

Lemma 3.2.3 (Palm distribution on compact sets). *The counting measure distribution $\Phi(\cdot)$ holds for all $A \subset \mathbb{R}^2$, $k \in \mathbb{N}$;*

$$\mathbb{P}\{\Phi_x(A \setminus \{x\}) = k\} = \mathbb{P}\{\Phi(A) = k\}. \quad (3.9)$$

Furthermore, for all compact $A \subset \mathbb{R}^2$, we have

$$\mathbb{P}\{\Phi_x^!(A) = k\} = \mathbb{P}\{\Phi(A) = k\}. \quad (3.10)$$

Proof. Proof of (3.9): By the conditional probability of independent events,

$$\begin{aligned} & \lim_{\delta \rightarrow 0} \mathbb{P}\{(\Phi(A \setminus D(x, \delta)) = k) | (\Phi(D(x, \delta)) = 1)\} \\ &= \lim_{\delta \rightarrow 0} \frac{\mathbb{P}\{\Phi(A \setminus D(x, \delta)) = k\} \mathbb{P}\{\Phi(D(x, \delta)) = 1\}}{\mathbb{P}\{\Phi(D(x, \delta)) = 1\}} = \mathbb{P}\{\Phi_x(A \setminus \{x\}) = k\} \\ &= \mathbb{P}\{\Phi(A) = k\}, \end{aligned}$$

because $\mathbb{P}\{\Phi(\{x\}) = 1\} = 0$.

Proof of (3.10): By the conditional probability of independent events,

$$\begin{aligned} & \lim_{\delta \rightarrow 0} \frac{\mathbb{P}\{\Phi(A \setminus D(x, \delta) = k) \mathbb{P}\{\Phi(D(x, \delta)) = 1\}}}{\mathbb{P}\{\Phi(D(x, \delta)) = 1\}} \\ &= \lim_{\delta \rightarrow 0} \mathbb{P}\{\Phi_x(A \setminus D(x, \delta)) = k\} = \mathbb{P}\{\Phi_x(A \setminus \{x\}) = k\} \\ &= \mathbb{P}\{\Phi_x^!(A \cup \{x\}) = k\} = \mathbb{P}\{\Phi(A \cup \{x\}) = k\} \stackrel{(a)}{=} \mathbb{P}\{\Phi(A) = k\}; \quad (3.11) \end{aligned}$$

(a) follows because $\Phi(\{x\}) = 0$ almost surely. \square

Property (II):

Theorem 3.2.4 (Slivnyak's Theorem). *The original PPP distribution is equal to the reduced Palms distribution:*

$$\mathbb{P}\{\Phi \in \cdot\} = \mathbb{P}\{\Phi_x^! \in \cdot\}. \quad (3.12)$$

Proof. Consider the family of Poisson random vectors of counting measures $\{(\Phi(A_1), \dots, \Phi(A_n))\}$ on disjoint compact sets $\{A_i\}$, each variable depending on $\lambda|A_i|$. For all such sets, Theorem 3.2.3 holds. The result follows for general events $\mathcal{A} \in \mathcal{F}_\Phi$, considering the definition of an event 3.2.1. \square

An important insight from Slivnyak's theorem is that, for example, we can condition the studied typical transmitter at an arbitrary location (usually at the origin), and the statistics of the other transmitters in the PPP remain invariant. Furthermore, it makes no difference whether we consider the typical transmitter to the PPP or not for the metrics that consider only the other transmitters, such as the interference at the typical transmitter. In the described sense, the typical point (transmitter) of the PPP is equivalent to the typical (any) location for the homogeneous PPP.

3.2.2 Stationarity and ergodicity

Property (III):

Corollary 3.2.5 (Stationarity). *The homogeneous PPP is stationary, also called translation invariant.*

$$\mathbb{P}\{\Phi \in \cdot\} = \mathbb{P}\{\Phi + x \in \cdot\} \text{ for all } x \in \mathbb{R}^2, \quad (3.13)$$

where $\Phi + x$ is a translation of all point in Φ .

Proof. For homogeneous PPP for any $A \subset \mathbb{R}^2$. $\Phi(A) = \Phi(A + x)$, where $A + x$ is the set translated by the vector $x \in \mathbb{R}^2$. This is a direct consequence of the definition that the distribution of $\Phi(A)$ depends only on the size $|A|$. The result generalizes to the event $\mathcal{A} \in \mathcal{F}_\Phi$ by Definition 3.2.1. \square

Because of translation invariance and Slivnyak's theorem 3.2.4, we can observe the point process from the typical location, for example, the origo $o \triangleq (0, 0)$, without loss of generality. According to Slivnyak's theorem, the typical location is also the typical point of the PPP.

Definition 3.2.3 (Mixing). According to the stationary and independence of the counting measures on distinct sets, the homogeneous PPP is a mixing.

$$\mathbb{P}\{(\Phi + x \in \mathcal{A}) \cap (\Phi \in \mathcal{B})\} = \mathbb{P}\{\Phi \in \mathcal{A}\}\mathbb{P}\{\Phi \in \mathcal{B}\}, \|x\| \rightarrow \infty$$

for all events $\mathcal{A}, \mathcal{B} \in \mathcal{F}_\Phi$, as defined in Definition 3.2.1, that are defined on a bounded set.

The Mixing condition implies ergodicity.

Corollary 3.2.6 (Ergodicity). *The homogeneous PPP is ergodic.*

$$\lim_{t \rightarrow \infty} \frac{1}{(2t)^2} \int_{[-t,t]^2} \mathbb{P}\{(\Phi + x \in \mathcal{A}) \cap (\Phi \in \mathcal{B})\} dx = \mathbb{P}\{\Phi \in \mathcal{A}\}\mathbb{P}\{\Phi \in \mathcal{B}\}.$$

for such events $\mathcal{A}, \mathcal{B} \in \mathcal{F}_\Phi$.

In words, ergodicity means that the spatial average equals the ensemble average.

Example 3.2.1. Consider $\mathcal{B} = \phi$ is a point set realization of Φ restricted to the bounded set $[-t, t]^2$ for each t , and assume the event $\Phi \in \{\phi\}$. Using conditional probability and by ergodicity,

$$\lim_{t \rightarrow \infty} \frac{1}{(2t)^2} \int_{[-t,t]^2} \mathbf{1}\{(\phi + x) \in \mathcal{A}\} dx = \mathbb{P}\{\Phi \in \mathcal{A}\}. \quad (3.14)$$

Ergodicity is a crucial concept regarding the simulation and interpretation of the analysis of the homogeneous PPP: The ensemble average of the typical point equals the average over all points in a given point realization, a.s.

3.2.3 Campbell's formula and probability generating functional

Corollary 3.2.7 (Intensity measure). *The expected number of points, also called the intensity measure of A , is given for the homogeneous PPP by*

$$\mathbb{E}\{\Phi(A)\} = \sum_{k=0}^{\infty} k \mathbb{P}\{\Phi(A) = k\} = e^{-\lambda|A|} \sum_{k=0}^{\infty} k \frac{(\lambda|A|)^k}{k!} = \lambda|A|. \quad (3.15)$$

Note that $\mathbb{E}\{\Phi(A)\} = \lambda \int_A dx$, where λ is called the *intensity parameter*. This representation outlines the following theorem.

Theorem 3.2.8 (Campbell's formula). *For a real-valued measurable $f(\cdot)$,*

$$\mathbb{E}\left(\sum_{x \in \Phi \cap A} f(x)\right) = \lambda \int_A f(x) dx \quad (3.16)$$

Proof. Because

$$\mathbb{E}\{c_i \Phi(A_i)\} = \mathbb{E}\left(\sum_{x \in \Phi} c_i \mathbf{1}(x \in A_i)\right) = \lambda \int_{\mathbb{R}^2} c_i \mathbf{1}(x \in A_i) dx,$$

the result holds for the simple function $f_m(x) = \sum_{i=1}^m c_i \mathbf{1}(x \in A_i)$ on the support $A = \cup_{i=1}^m A_i$. The final result follows as a monotone approximation $f_m(\cdot) \xrightarrow{m \rightarrow \infty} f(\cdot)$ by dividing A into ever narrower segments. \square

Property (IV): Let us observe the PPP ($\Phi | (\Phi(A) = N)$) in the window $A = \cup_{i=1}^m A_i$ the sets $\{A_i\}_{i=1}^m$ of equal sizes. In the homogeneous PPP, each of the N points $\{x_i\}_{i=1}^N$ are independently distributed in A and are at equal probabilities in a set A_i ; $p = \mathbb{P}(x_n \in A_i) = |A_i| / |A|$. The probability that $0 \leq n \leq N$ points are in A_i is a Bernoulli trial of n successes with the success probability of p . Hence, the conditioned, $\Phi(A) = N$, homogeneous PPP in a bounded window A is a Binomial process. Each point is independently uniformly distributed in A .

We can use this fact in the derivation of the probability generating functional.

Theorem 3.2.9 (Probability generating functional of the homogeneous PPP). *Let $f(\cdot) : \mathbb{R}^2 \rightarrow [0, 1]$ s.t. $f(x) \rightarrow 1$ as $\|x\| \rightarrow \infty$. The probability generating functional (PGFL) of the homogeneous PPP is given by*

$$\mathfrak{G}(f) = \mathbb{E}\left(\prod_{x \in \Phi} f(x)\right) = \exp\left\{-\lambda \int_{\mathbb{R}^2} (1 - f(x)) dx\right\}, \quad (3.17)$$

$$\exp\left\{-2\pi\lambda \int_0^\infty r (1 - f(r)) dr\right\} \quad (3.18)$$

whenever exists.

Proof.

$$\begin{aligned}
\mathbb{E} \left(\prod_{x \in \Phi \cap A} g(x) \right) &= \sum_{k=0}^{\infty} \mathbb{P}(\Phi(A) = k) \left(\int_A g(x) dx / |A| \right)^k \\
&= e^{-\lambda|A|} \sum_{k=0}^{\infty} \frac{(\lambda|A|)^k}{k!} \left(\int_A g(x) dx / |A| \right)^k \\
&= \exp \left\{ -\lambda \left(\int_A (1 - g(x)) dx \right) \right\}.
\end{aligned}$$

The result follows by the substitution $g(x) = \mathbf{1}(x \in A)f(x)$, and by letting $A \rightarrow \mathbb{R}^2$. \square

3.3 Gaussian projection process

A *projection process* projects the homogeneous PPP from the plane into the real line as a function of the norms. An exponential function, or a *stretched exponential function*, $r \mapsto \exp\{-ar^b\}$, can be used as the projection mapping. Such processes have been studied before in the literature modeling the spatial path loss in terrestrial networks [47]. Maybe not so surprisingly, the Gaussian mapping, *i.e.*, the exponent $b = 2$, yields a significantly simpler analysis than the other exponents.

We present an extensive study and characterization of such a *Gaussian projection process* (GP). We may also use the term “gain process” because of its interpretation as the random process of gains (further, the SNRs with constant noise powers) of the transmitters in a narrow-beam LEO setting. The GP also describes the SIR values of the transmitters and can be dexterously used to characterize the SIR and SINRs. Of course, the properties (I)-(IV) can apply in the underlying, projected, homogeneous PPP (*e.g.*, of terrestrial NTN terminals).

Remark (Connection to the Gaussian processes). Although the abbreviation “GP” is also used in the context of *Gaussian processes*, the Gaussian *projection process*, *i.e.*, also the GP is not to be, at least directly, considered as a Gaussian process. However, I decided to use the terminology since the p.p. under study directly links to the Gaussian function in the definition. Namely, the standard immediate connotations of the term “Gaussian projection process” and its abbreviation “the GP”, even if strictly speaking incorrect, acknowledge the Gaussian nature and the consequent tractable, lubricant analytical framework and inquiry of the GP (referring from now on to the Gaussian projection process). Furthermore, the GP produces a Gaussian process in many natural settings, as will be explored in Chapter 4.

Definition 3.3.1 (Gaussian projection process (GP)). Given the Gaussian mapping $G(r) = e^{-ar^2}$ and a homogeneous PPP Φ on \mathbb{R}^2 , we can assert $r = \|x\|$, $x \in \Phi$ as the argument for $G(\cdot)$. Let $\{h_x\}_{x \in \Phi}$ be i.i.d. r.v's. The Gaussian projection process is defined as

$$\mathcal{G} \triangleq \{h_x G(\|x\|) : x \in \Phi\}. \quad (3.19)$$

If we consider that $h_x \equiv 1$, or being i.i.d. r.v's, we can refer to the typical $h = 1$, and denote

$$\mathcal{G}_1 \triangleq (\mathcal{G}|h = 1). \quad (3.20)$$

We start by analyzing \mathcal{G}_1 . Note that the GP is not homogeneous: for each point, $x \in \mathcal{G}_1 \cap (t_1, t_2)$, the corresponding point in Φ is distributed inside the preimage-torus $D(o, G^{-1}(t_1)) \setminus D(o, G^{-1}(t_2)) \subset \mathbb{R}^2$, with $G^{-1}(\cdot)$ as the inverse function of $G(\cdot)$ with the support on $(0, 1)$; $G^{-1}(t)|_{t \in (0, 1)}$. The intensity measure is

$$\mathbb{E}[\mathcal{G}_1(t, 1)] \triangleq \Lambda_{\mathcal{G}_1}((t, 1)) = \mathbb{E}_{\Phi}[\Phi(D(o, G^{-1}(t)))] = \pi \lambda(G^{-1}(t)^2). \quad (3.21)$$

The derivative

$$\lambda_{\mathcal{G}_1}(t) \triangleq -\frac{\Lambda_{\mathcal{G}_1}((t, 1))}{dt} \stackrel{(a)}{=} -\frac{d\pi \lambda(G^{-1}(t)^2)}{dt} = -2\pi \lambda \left(G^{-1}(t) \frac{dG^{-1}(t)}{dt} \right), \quad (3.22)$$

is called the density parameter of \mathcal{G}_1 . By marking $G^{-1}(t)dG^{-1}(t) = rdr$, we have,

$$-\lambda_{\mathcal{G}_1}(t)dt = 2\pi \lambda rdr. \quad (3.23)$$

$-\lambda_{\mathcal{G}_1}(\cdot)$ is the *Radon-Nikodym derivative* of the measure

$$\Lambda_{\mathcal{G}_1}((t_1, t_2)) = 2\pi \lambda \int_{G^{-1}(t_2)}^{G^{-1}(t_1)} rdr = 2\pi \lambda |D(o, G^{-1}(t_1)) \setminus D(o, G^{-1}(t_2))|$$

w.r.t. the Lebesgue measure on $(0, 1)$. Using this fact and Theorem 3.2.9, we have the PGFL of \mathcal{G}_1 and have a complete characterization of the projection process with deterministic $h = 1$ as an inhomogeneous PPP.

Yet, we have not used the Gaussian assumption. However, it comes into use in the following corollary.

Corollary 3.3.1 (Density of the GP). *The density of \mathcal{G}_1 is*

$$\lambda_{\mathcal{G}_1}(t) = \tilde{\kappa}/t|_{t \in (0, 1)}, \quad \tilde{\kappa} \triangleq \pi \lambda/a. \quad (3.24)$$

Furthermore, with general h , the GP is an inhomogeneous PPP of the density

$$\lambda_{\mathcal{G}}(t) = \frac{\tilde{\kappa} F_h(t)}{t} \Big|_{t \in \mathbb{R}_+} - \frac{\tilde{\kappa}(1 - F_h(t))}{t} \Big|_{t \in \mathbb{R}_-}, \quad (3.25)$$

where $F_h(t)$ is the (possibly degenerate) CCDF of the r.v. h .

Proof. Having $G^{-1}(t) = \sqrt{-\log(t)/a}$, one can derive from (3.22) (a) the density of \mathcal{G}_1 . The latter result is proved in Corollary 3.3.3. \square

Corollary 3.3.2 (A natural interpretation of the GP). *For $a = \log(2)D_{h,\epsilon}^2/\varphi_{\text{RX}}^2 = \log(2)(\sin^2(\epsilon)/(h\varphi_{\text{RX}}))^2$, the parameter $\kappa \triangleq \log(2)\tilde{\kappa}$ has an intuitive interpretation as the average number of UEs inside a LEO BS -3 dB footprint for general altitudes and elevation angles in case of the narrow-beam LEO (see Publication III).*

Example 3.3.1 (Intercell interference). Set

$$F_H(x) = \begin{cases} 1, & \text{if } x < 1/2 \\ 0 & \text{if } x \geq 1/2 \end{cases}. \quad (3.26)$$

Then,

$$\lambda_{\mathcal{G}}(t) = \tilde{\kappa}/t|_{t \in (0,1/2)}. \quad (3.27)$$

Should we consider the served cell (intracell) as the -3 dB footprint, the resulting density has an interpretation as the density of the p.p outside the intracell: This will be a strikingly straightforward way to characterize intercell interference.

Corollary 3.3.3 (PGFL of the GP). *Let $f(\cdot) : \mathbb{R} \rightarrow [0, 1]$, necessarily, s.t. $f(x) \rightarrow 1$ as $x \rightarrow \infty$. The PGFL of \mathcal{G} is*

$$\mathfrak{G}_{\mathcal{G}}(f) = \mathbb{E} \left(\prod_{x \in \mathcal{G}} f(x) \right) = \exp \left\{ - \int_{-\infty}^{\infty} (1 - f(t)) \lambda_{\mathcal{G}}(t) dt \right\}, \quad (3.28)$$

where $\lambda_{\mathcal{G}}(t)$ is given in (3.25).

Proof. The Markov kernel of the \mathcal{G}_1 with each point multiplied by the i.i.d. h is $p(x, y) = f_h(y/x)/x$, where $f_h(\cdot)$ is the PDF of h . We have

$$\begin{aligned} \mathbb{E} \left(\prod_{y \in \mathcal{G}} g(y) \right) &= \mathbb{E}_{\mathcal{G}_1} \left(\int_{-\infty}^{\infty} g(y) \prod_{x \in \mathcal{G}_1} p(x, y) dy \right) \\ &= \mathbb{E} \prod_{x \in \mathcal{G}_1} \left(\int_{-\infty}^{\infty} g(y) p(x, y) dy \right) \\ &\stackrel{(a)}{=} \exp \left\{ -\tilde{\kappa} \int_0^1 \left(1 - \int_{-\infty}^{\infty} g(y) p(t, y) dy \right) / t dt \right\} \\ &= \exp \left\{ -\tilde{\kappa} \int_{-\infty}^{\infty} (1 - g(y)) \int_0^1 p(t, y) / t dt dy \right\} \\ &= \exp \left\{ -\tilde{\kappa} \int_{-\infty}^{\infty} (1 - g(y)) \int_0^1 f_h(y/t) / t^2 dt dy \right\} \end{aligned}$$

$$= \exp \left\{ - \int_{-\infty}^{\infty} (1 - g(y)) \lambda_{\mathcal{G}}(y) dy \right\}.$$

In (a), we used the PGFL of \mathcal{G}_1 , which can be derived from Theorem 3.2.9 (this is only the well-known form of the PGFL of the PPP). The proof is concluded. \square

We present some important results regarding the GP (many are well-known and apply to general PPPs).

Corollary 3.3.4. *The Laplace transform $\mathcal{L}_J(s) \triangleq \mathbb{E}(\exp\{-sJ\})$ of the sum $J = \sum_{x \in \mathcal{G}} g_x f(x)$, where $\{g_x\}_{x \in \Phi}$ are i.i.d. positive r.v's is given by*

$$\mathcal{L}_J(s) = \exp \left\{ - \int_{-\infty}^{\infty} (1 - \mathcal{L}_g(sf(x))) \lambda_{\mathcal{G}}(x) dx \right\}, \quad (3.29)$$

where $\mathcal{L}_g(s)$ is the Laplace transform of the typical g_x , and the density $\lambda_{\mathcal{G}}(x)$ is (3.25).

Proof.

$$\begin{aligned} \mathbb{E} \left(e^{-s \sum_{x \in \mathcal{G}} h_x f(x)} \right) &= \mathbb{E}_{\mathcal{G}, h} \left(\prod_{x \in \mathcal{G}} e^{-s h_x f(x)} \right) \stackrel{(a)}{=} \mathbb{E}_{\mathcal{G}} \left(\prod_{x \in \mathcal{G}} \mathbb{E}_{h_x} \left(e^{-s h_x f(x)} \right) \right) \\ &\stackrel{(b)}{=} \mathbb{E} \left(\prod_{x \in \Phi} \mathcal{L}_h(sf(x)) \right) = \mathfrak{G}(\mathcal{L}_h(sf(\cdot))) = \mathfrak{G}(\mathcal{L}_h \circ sf). \end{aligned}$$

(a) follows because all $\{g_x\}$ are i.i.d.—Furthermore, in (b), we can denote the typical g_x by g , and product elements are, by definition, the Laplace transform of g . \square

Note that we can incorporate two different r.v's into the underlying homogeneous PPP, first into the density parameter of the projection process density parameter (3.25) and secondly, into the multiplication of each term in the sum I , and we have a tractable characterization of I as the Laplace transform (3.29). For example, the r.v's h and g can represent shadowing and fast fading, respectively.

Theorem 3.3.5 (Campbell's formula). *If exists for function $f(\cdot)$, we have the following two representations for the expected sum*

$$\mathbb{E} \left(\sum_{x \in \mathcal{G}} f(x) \right) = \int_{-\infty}^{\infty} f(x) \lambda_{\mathcal{G}}(x) dx = \int_0^1 \mathbb{E}_h(f(xh)) \lambda_{\mathcal{G}_1}(x) dx. \quad (3.30)$$

Proof. The result can be proved by monotonic convergence arguments similarly to the proof in 3.2.9. \square

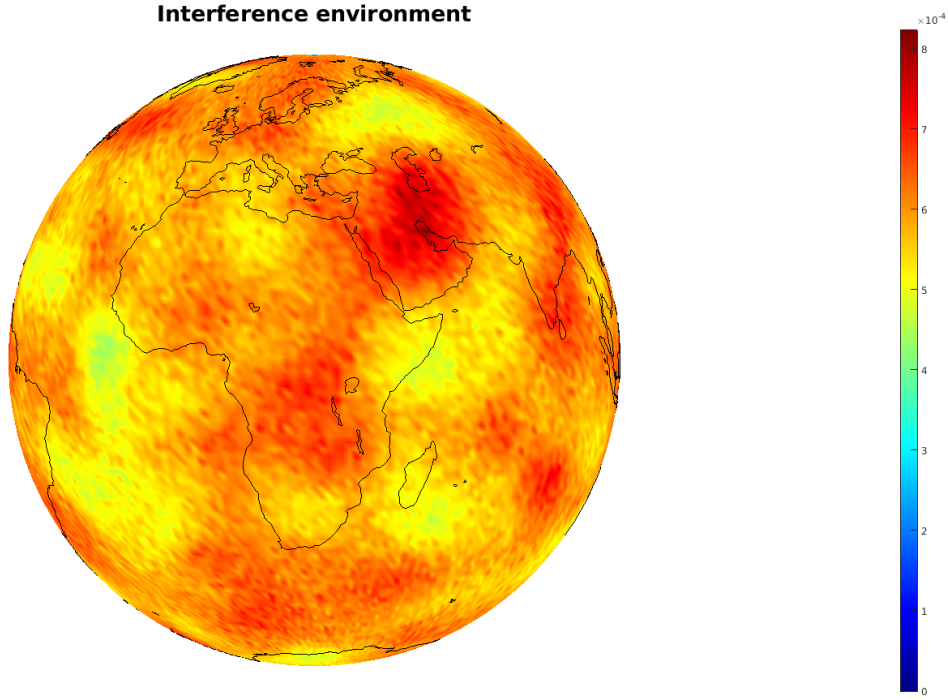


Figure 3.1. A location-wise realization of the total interference at the LEO BS in the spherical model (however, an omnidirectional LEO BS antenna).

The total interference is the sum of the GP. We call it “total” because none of the signals are canceled (for example, the served transmitter signal). For the rest of the thesis, I refers to the following.

Definition 3.3.2 (Total interference).

$$I = \sum_{x \in \mathcal{G}} H_x x = \sum_{x \in \mathcal{G}_1} H_x G_x x, \quad (3.31)$$

where H and G can be fading or shadowing variables, signals with a mean 0 (the latter is also denoted as Y or Z to distinguish it from the fading gain), or a combination of all. Note that we can also incorporate GH in the density of \mathcal{G} , set either one or both to $G, H \equiv 1$, or use some of the combinations—whichever is most convenient for the analysis. The GP point x can represent power gain or amplitude gain as long as appropriate scaling is considered for $\tilde{\kappa}$: If $\kappa = \log(2)\tilde{\kappa}$ represents the average number of terminals in a -3 dB power footprint area (as it is in the thesis), $\tilde{\kappa}$ can be scaled by two for correct amplitude modeling. We will introduce temporal structure to the total interference $I = I(t)$ in Section 4.

The following theorem is an absolute bedrock of this thesis. It characterizes the mean and variance of the total interference in a strikingly straightforward and general manner.

Theorem 3.3.6 (Mean and the variance of the total interference). *Assume that $|\mathbb{E}(H)| < \infty$ and $\mathbb{E}(H^2) < \infty$. The average total interference is*

$$\mathbb{E}(I) = \mathbb{E} \left(\sum_{x \in \mathcal{G}_1} H_x x \right) \stackrel{(a)}{=} \tilde{\kappa} \mathbb{E}(H) \int_0^1 dx = \tilde{\kappa} \mathbb{E}(H). \quad (3.32)$$

The variance is

$$\begin{aligned} \text{var}(I) &= \text{var} \left(\sum_{x \in \mathcal{G}_1} H_x x \right) \stackrel{(b)}{=} \int_{-\infty}^{\infty} x^2 \lambda_{\mathcal{G}}(x) dx \\ &= \tilde{\kappa} \left(\int_0^{\infty} x F_H(x) dx - \int_{-\infty}^0 x (1 - F_H(x)) dx \right) = \tilde{\kappa} \mathbb{E}(H^2)/2. \end{aligned} \quad (3.33)$$

Proof. (a) follows directly from Campbell's formula with $f(x) = x$ and the density of $\lambda_{\mathcal{G}_1}$ given in (3.24). The variance representation (b) can be derived by taking the second derivative of (3.29) and taking the limit $s \rightarrow 0$. \square

Remark (Amplitude gain versus power gain and the GP). When modeling the amplitude, a straightforward method is to scale the formulas (3.32) and (3.33) by a factor of two: This retains the interpretation of $\tilde{\kappa} \log(2)$ as the average number of transmitters within the -3 dB power footprint of the LEO BSs.

There are at least two important applications regarding (3.33) and (3.32). The first corresponds to signal power modeling and matching different distributions by the first two moments, and the second refers to interference waveform amplitude modeling and estimating correlation functions.

1. For a non-negative fading r.v. h ; $\mathbb{E}[H] > 0, \mathbb{E}(H^2) < \infty$, a second-moment approximation between two different fading r.v.'s while preserving the mean and variance of the total interference can be performed using the identities. For example, the forthcoming Theorem 3.3.7 can be applied to general fading by moment matching.
2. For a *white noise*-type (WN) signal, H ; $\mathbb{E}(H) = 0, \mathbb{E}(H^2) < \infty$, the variance equals the average signal power, which we refer to as the total interference power (averaged over a short time period). Without loss of generality, we usually set $\mathbb{E}[H^2] = 1$. Due to its distinct role, we will refer to this kind of typical signal as the WN signal and the sum of such signals at the Gaussian antenna gain as *AWN total interference*, which refers to additive white noise (AWN), and "total" in that none of the signals are canceled. In Section 4, Theorem 3.3.6 plays a crucial role in the interference autocorrelation inference.

Example 3.3.2. (3.33) identifies the total interference power of the AWN total interference with the total power over the bandwidth $(-\tilde{\kappa}/2, \tilde{\kappa}/2)$ of a

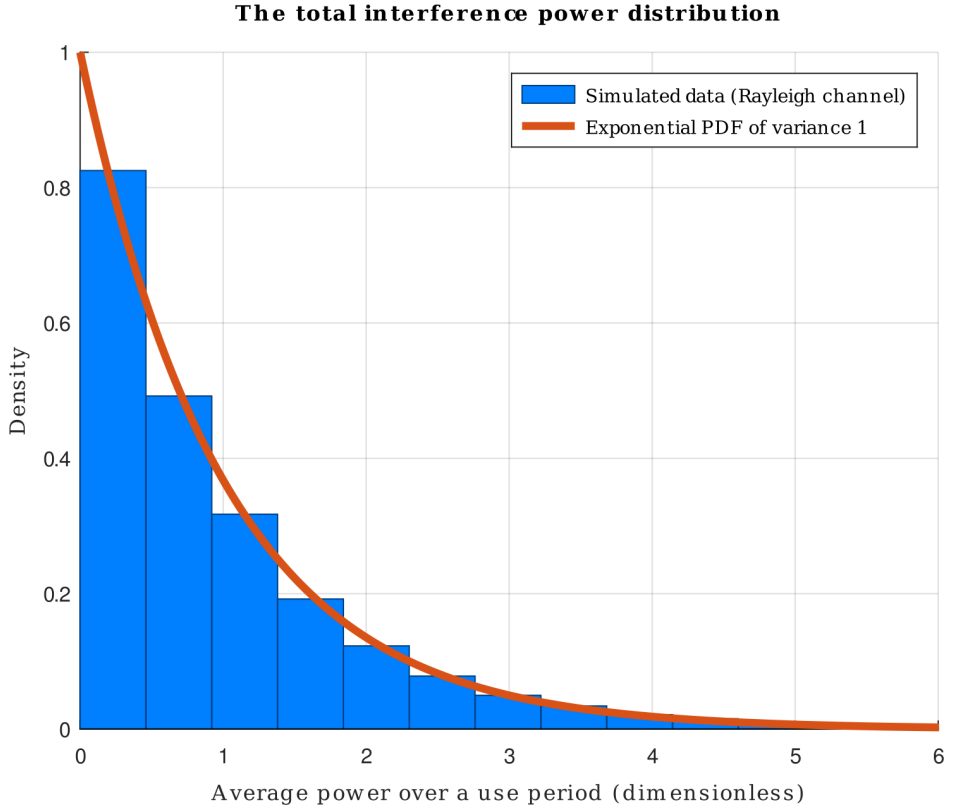
two-sided (indeed two-sided; see the remark in Theorem 3.3.6) WN signal with per-frequency normalized PSD. Even though it would be tempting to associate the total interference waveform with such a signal, the “bandwidth” has no meaning in this context: the aggregate signal—each separate signal filtered through the Gaussian antenna gains—is just a WN signal with amplified or suppressed power compared to the typical signal H . The resulting actual total interference PSD is discussed in Chapter 4.

Theorem 3.3.7 (Total interference power distribution is gamma). *Let G be a normalized exponential r.v. (Rayleigh power fading) and $H \equiv 1$ in (3.31). The Laplace transform of the total interference is*

$$\mathcal{L}_I(s) = (1 + s)^{-\tilde{\kappa}}, \quad (3.34)$$

*which is the Laplace transform of the **gamma distribution** of the shape parameter $\tilde{\kappa}$. Furthermore, the gamma distribution is a good approximation for general fading.*

Proof. Substituting the exponential fading variable in (3.3.4) yields the result. Furthermore, by matching the second moment, the gamma distribution closely approximates the power distribution for general fast-fading, as demonstrated in Figures 3.2 and 3.3 for the Rayleigh channel and the LoS channel. \square



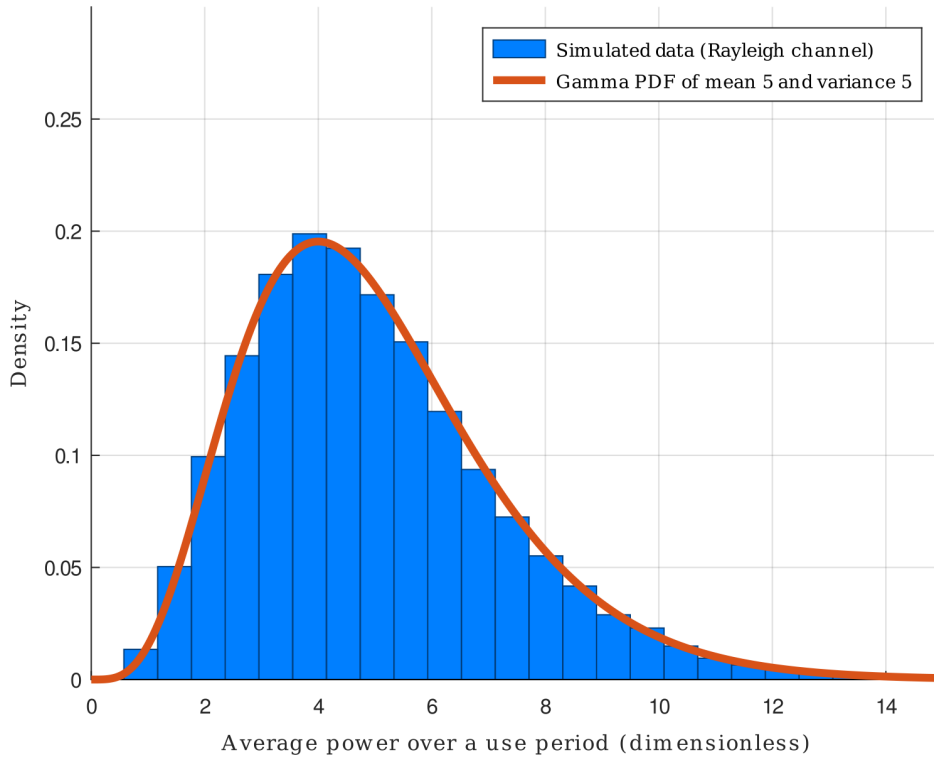
(a) The interference signals are affected by Rayleigh fading.



(b) The interference signals are affected by no fading.

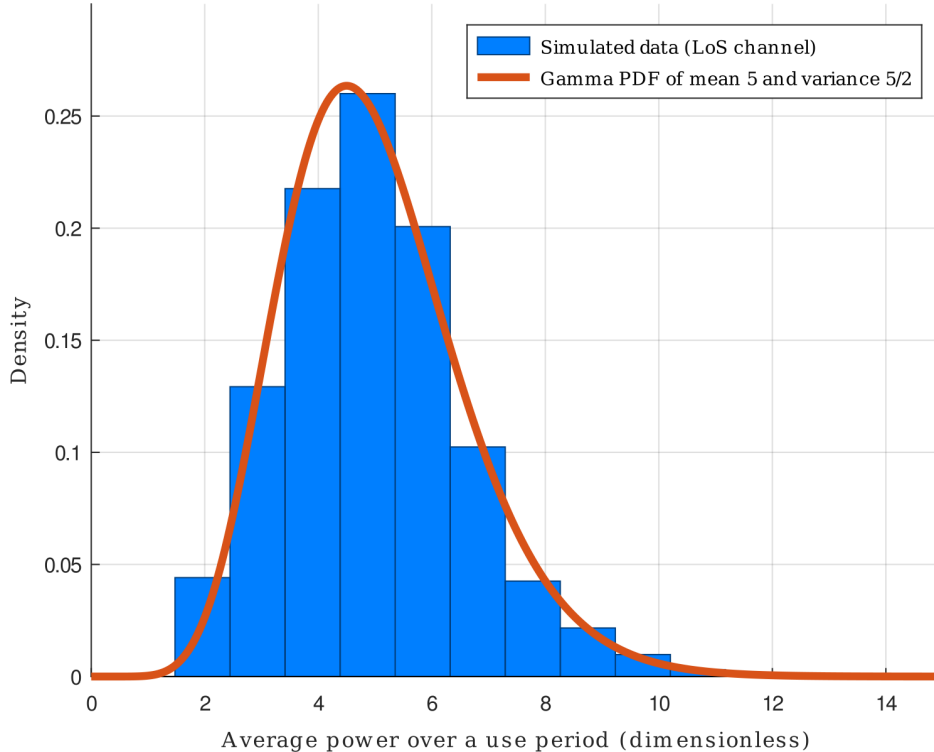
Figure 3.2. The total interference power distribution over each terrestrial terminal realization and power fading, with the transmission responses affected by the Rayleigh fading and the LoS channel. The GP density parameter $\tilde{\kappa} = 1$.

The total interference power distribution



(a) The interference signals are affected by Rayleigh fading.

The total interference power distribution



(b) The interference signals are affected by no fading.

Figure 3.3. The total interference power distribution over each terrestrial terminal realization and power fading, with the transmission responses affected by Rayleigh fading and the LoS channel. The GP density parameter $\tilde{\kappa} = 5$.

3.4 Total interference and the central limit theorem

Define the *AWN total interference* as the total interference (3.31) with $G \equiv 1$, and $H = Y$ is a WN signal (*i.e.*, $\mathbb{E}(Y) = 0$ and $\mathbb{E}(Y^2) < \infty$).

Because of the planar modeling, the GP encompasses, in principle, an infinite number of interfering transmissions, and conditions for the central limit theorem (CLT) are potentially satisfied for the total interference. Indeed, it turns out that the CLT applies if the transmitted signals are WN signals. In this case, the received aggregate interference waveform has a Gaussian distribution over the *entire* statistical ensemble. For some readers, the result might not seem surprising; however, it is not trivial. If one is interested in the framework of Gaussian and non-Gaussian interference modeling in wireless networks and stochastic geometry, please refer to the literature review in Section 1.4.1, which addresses a handful of nominal studies on terrestrial networks. Namely, multiple papers indicate that Gaussian models are inadequate due to the rapidly decaying tail distributions, and even the average interference signal waveform or power is generally ill-defined within the topology of terrestrial networks. Hence, more slowly decaying non-Gaussian statistical models are proposed. On the contrary, we will demonstrate in the following sections that the AWN total interference is a Gaussian process in the case of the narrow-beam LEO BSs. The white noise signal waveform of each transmission is a sufficient condition for the CLT. Further, we will continue with a counter-example of Rayleigh faded power averaged over a use period (*note*; not the instantaneous signal waveform power), which exhibits near-Gaussian behavior only when the spatial density of the signal terminals is significantly large.

In practice, we will show that the **Lindeberg's condition** is satisfied for the AWN total interference.² The argument gets finalized in Theorem 3.4.4, whose proof encompasses Lemmas 3.4.1 and 3.4.3.

Lemma 3.4.1 (Marginal distributions of the order statistics). *Let $X_{k+1} \in \mathcal{G}_1 \subset (0, 1)$ be the $(k + 1)$ th largest point, $k \geq 0$. The marginal (*i.e.*, no reference to other points) distribution function of X_{k+1} is*

$$f_{X_{k+1}}(x) = \frac{d}{dx} \mathbb{P}(X_{k+1} < x) = \frac{\tilde{\kappa} x^{\tilde{\kappa}-1} (-\log(x^{\tilde{\kappa}}))^k}{k!}. \quad (3.35)$$

Proof. Analogous to the definition of the homogeneous PPP (3.5) but using the density of the GP in (a),

$$\begin{aligned} \mathbb{P}(X_{k+1} < x) &= \mathbb{P}\{\mathcal{G}_1 \in \{(k + 1)\text{th largest point in } (0, x)\}\} \\ &= \sum_{i=0}^k \mathbb{P}\{\mathcal{G}_1 \in \{i \text{ points in } (x, 1)\}\} \stackrel{(a)}{=} \sum_{i=0}^k \frac{(-\log(x^{\tilde{\kappa}}))^i x^{\tilde{\kappa}}}{i!}. \end{aligned}$$

²Jarl Waldemar Lindeberg was a Finnish mathematician known for work on the central limit theorem (CLT).

The result can be calculated, *e.g.*, with symbolical aids first evaluating the sum and then derivating. \square

Remark (Largest points and nearest neighbors). For the distances, the PPPs Φ and \mathcal{G}_1 are equivalent by definition. Hence, although conceptually referring to the former and latter p.p.'s, respectively, the terms *nearest neighbor* (or *nearest point*) and *largest point* are used interchangeably in the context of \mathcal{G}_1 . Namely, the n th largest point corresponds to the n th nearest neighbor of the typical point $\mathbf{o} \in \Phi_o$ (Properties (I)-(III), Thm. 3.2.1), which can also be comprehended to refer to the neighbor of the supremum of $(0, 1) \supset \mathcal{G}_1$, *i.e.*, the point $1 \in (0, 1]$ (the boresight of the typical LEO BS). By the mapping \mathcal{G}_1 , we identify the limit points $\{1, 0\} \subset \mathbb{R}$ with the respective $\{\mathbf{o}, \infty\} \subset \mathbb{R}^2$.

Furthermore, the terms *strongest transmitter*, *largest gain*, *etc.*, can be used in the context because of the interpretation of the GP as the p.p. of the antenna gains of the spatially randomly located signal sources at the typical LEO BS. However, these usually refer to the general \mathcal{G} (the fading variable incorporated in the density), not necessarily to \mathcal{G}_1 , in which case these concepts do not contain direct information about the spatial distances in Φ .

The following corollary is a direct and simple implication of Lemma 3.4.1 but deserves a separate mention.

Corollary 3.4.2 (Void probability). *The CCDF of the (1st) nearest neighbor evaluated at x is the void probability of $(x, 1)$. By substituting $k = 0$ into (3.35) and integrating, the void probability has the CDF*

$$\mathbb{P}\{\mathcal{G}_1((x, 1)) = 0\} = \mathbb{P}\{\mathcal{G}_1 \in \{\text{All gains smaller than } x\}\} = x^{\tilde{\kappa}}. \quad (3.36)$$

Note that in the following, the conceptualized point set consisting of the n largest points does not have an *ordering*. However, complementing the marginal order statistics (3.35), we will explore joint order statistics later in Section 3.5.1.

Lemma 3.4.3 (Statistics of mutually non-ordered nearest points). *Let*

$$\mathbf{X}_{\{n\}} \in \{\mathbf{X}_i\}_{i=1}^n \subset \mathcal{G}_1 \subset (0, 1), \quad \mathbf{X}_{(n+1)} < \mathbf{X}_{\{n\}},$$

be the typical point in a non-ordered set of $n \geq 1$ i.i.d. points nearer (w.r.t. the boresight $1 \in (0, 1]$) than the $(n + 1)$ th point. The following identities hold for its distribution.

$$n\mathbb{E}(\mathbf{X}_{\{n\}}) = \tilde{\kappa} \left(1 - \left(\frac{\tilde{\kappa}}{1 + \tilde{\kappa}} \right)^n \right), \quad (3.37)$$

$$n\mathbb{E}(\mathbf{X}_{\{n\}}^2) = \frac{\tilde{\kappa}}{2} \left(1 - \left(\frac{\tilde{\kappa}}{2 + \tilde{\kappa}} \right)^n \right), \quad (3.38)$$

$$n\mathbb{P}(\mathbf{X}_{\{n\}} > x) \sim \Lambda_{\mathcal{G}_1}((x, 1)) = -\tilde{\kappa} \log(x), \quad \text{for } x \in (0, 1], \text{ as } n \rightarrow \infty. \quad (3.39)$$

Proof. Referring to Lemma 3.4.1, denote the $(n+1)$ th largest point with $X_{n+1} \in \mathcal{G}_1$. Picking an arbitrary point from the set of n largest points implies by the standard properties of the PPP (Properties (I)-(IV), Thm. 3.2.1) that all n points are i.i.d.; hence, $X_{\{n\}} \in \mathcal{G}_1 \cap (X_{(n+1)}, 1)$ represents each such point as the typical point.

Recall that, by Campbell's formula,

$$\sum_{x \in \mathcal{G}_1} \mathbf{1}(x) = \int_0^1 \lambda_{\mathcal{G}_1}(t) dt = \int_0^1 \tilde{\kappa}/tdtw = \infty.$$

Hence, the total set of points in a realization of \mathcal{G}_1 has, *a.s.*, countable infinite cardinality: there is no “the smallest point of \mathcal{G}_1 ” (as much as there is a “the most distant point from the origo” in the homogeneous PPP $\Phi \subset \mathbb{R}^2$). Hence, n can be made arbitrarily large.

By the conditional independence of the location of X we can deduce the CCDF with the conditioned $X_{n+1} = x_{\min} \in (0, 1)$ by

$$\mathbb{P}(X_{\{n\}} > x | X_{n+1} = x_{\min}) = \frac{\int_x^1 \lambda(t) dt}{\int_{x_{\min}}^1 \lambda(t) dt} = \frac{\int_x^1 1/tdt}{\int_{x_{\min}}^1 1/tdt} = \frac{\log(x)}{\log(x_{\min})}$$

for $x \in (x_{\min}, 1)$, $\mathbb{P}(X > x | X_{n+1} = x_{\min}) = 1$ for $x \leq x_{\min}$, and
 $\mathbb{P}(X > x | X_{n+1} = x_{\min}) = 0$ for $x \geq 1$.

By the *tower rule* and the expectation value integral identity for the CCDF, the mean is

$$\begin{aligned} \mathbb{E}(X_{\{n\}}) &= \mathbb{E}_{X_{n+1}} \left(\mathbb{E}_{X_{\{n\}}} (X_{\{n\}} | X_{n+1}) \right) \\ &= \mathbb{E}_{X_{n+1}} \left(\int_{X_{n+1}}^1 \mathbb{P}(X_{\{n\}} > x | X_{n+1}) dx + X_{n+1} \right). \end{aligned}$$

Further, after evaluating the integral, utilize the PDF of X_{n+1} from (3.35):

$$\mathbb{E}(X) = \mathbb{E}_{X_{n+1}} \left(\frac{Y_{(n)} - 1}{\log(Y_{(n)})} \right) = \int_0^1 \frac{y - 1}{\log(y)} f_{X_{n+1}}(y) dy,$$

which can be evaluated with the help of symbolic software tools.

The second moment is obtained similarly by acquiring the second conditional moment, $\mathbb{E}_{X_{\{n\}}} (X_{\{n\}}^2 | X_{n+1})$, from the well-known integral identity $\mathbb{E}_{X_{\{n\}}} (X_{\{n\}}^2 | X_{n+1}) = 2 \int_0^1 x \mathbb{P}(X_{\{n\}} > x | X_{n+1}) dx$ and ultimately taking the expectation over X_{n+1} . □

Remark (Homogeneous PPP as a limiting process of a BPP). Although well-defined, the distribution function (3.39) of $X_{\{n\}} \in \mathcal{G}_1$ is degenerate in the limit $n \rightarrow \infty$. Intuitively, this is due to the unboundedly large area of spatial spread with the uniform spatial appearance probability (Properties (IV), Thm. 3.2.1) of the corresponding, projected, planar point $Y_{\{n\}} \in \Phi$, which

has an increasingly high probability of being far away from o as n increases and points unboundedly far appear in the set of n nearest points.³ However, even though the probability that an individual point falls near o (or at any region) gets arbitrarily small for an arbitrarily large n , distributing $n < \infty$ points—through the appropriate logarithmic mapping $(0, 1) \rightarrow \mathbb{R}^2$ of the n -point realization of the GP produced by the law (3.39) combined with uniformly distributed directions—will, of course, lead to a point realization around the origo, which looks typical to the planar homogeneous PPP (in a bounded window).

Note that, as it should, (3.37) and (3.38) approach the expected value of the AWN total interference; (3.32) and (3.33), respectively, as $n \rightarrow \infty$. Furthermore, one can confirm that $(1 + \Lambda_{\mathcal{G}_1}((x, 1))/n)^n$ equals the void probability (3.36) as $n \rightarrow \infty$.

Finally, we are ready for the result to prove that the CLT applies to the AWN total interference.

Theorem 3.4.4 (AWN total interference is Gaussian). *Assuming WN signals for the signal sources (NTN terminals), i.e., if the typical h is a non-degenerate r.v. of mean 0 and PSD $\mathbb{E}(Y^2) < \infty$, the AWN total interference $I = \sum_{x \in \mathcal{G}_1} Y_x x$ satisfies Lindeberg's condition, implying that the CLT holds. Hence, the AWN total interference has a Gaussian distribution with a mean $\mu = \mathbb{E}(I) = \tilde{\kappa} \mathbb{E}(Y) = 0$ and a variance $\sigma^2 = \text{var}(I) = \mathbb{E}(I^2) = \tilde{\kappa} \mathbb{E}(Y^2)/2$.*

*Equivalently, the variance is $\sigma^2 = \tilde{\kappa} \mathbb{E}(Y^2)$ with the interpretation of $\tilde{\kappa}$ reflecting the average number of transmitters inside the -3 dB **power** footprint; see the remark of Theorem 3.3.6.*

Proof. Without loss of generality, let us assume $\mathbb{E}(Y^2) = 1$. While referring to Lemma 3.4.3 and the identities (3.37) and (3.38), $X_{\{n\}} \in \mathcal{G}_1 \subset (0, 1)$ is the typical point in the non-ordered set of i.i.d. points nearer than the $(n+1)$ th nearest neighbor to the boresight $1 \in (0, 1]$. The Lindeberg condition is satisfied if

$$\begin{aligned} & \lim_{n \rightarrow \infty} \frac{1}{\sum_{k=1}^n \mathbb{E}(Y^2 X_{\{n\}}^2)} \sum_{k=1}^n \mathbb{E} \left(Y^2 X_{\{n\}}^2 \mathbf{1} \left(|Y X_{\{n\}}| > \epsilon \sqrt{\sum_{k=1}^n \mathbb{E}(Y^2 X_{\{n\}}^2)} \right) \right) \\ &= \lim_{n \rightarrow \infty} \frac{1}{n \mathbb{E}(X_{\{n\}}^2)} n \mathbb{E} \left(X_{\{n\}}^2 \mathbf{1} \left(|Y X_{\{n\}}| > \epsilon \sqrt{n \mathbb{E}(X_{\{n\}}^2)} \right) \right) \\ &= 2/\tilde{\kappa} \lim_{n \rightarrow \infty} n \mathbb{E} \left(X_{\{n\}}^2 \mathbf{1} \left(X_{\{n\}} > \epsilon \sqrt{\tilde{\kappa}/2} / |Y| \right) \right) = 0 \text{ for all } \epsilon > 0. \end{aligned} \quad (3.40)$$

Re-denote $\epsilon_1 \triangleq \epsilon \sqrt{\tilde{\kappa}/2}$. Conditioning Y by the tower rule, (3.40) is satisfied if

$$\mathbb{E}_Y \left[\lim_{n \rightarrow \infty} n \mathbb{E} \left(X_{\{n\}}^2 \mathbf{1} \left(X_{\{n\}} > \epsilon_1 / |Y| \right) | Y \right) \right] = 0 \text{ for all } \epsilon_1 > 0.$$

³“Appear” means here the farthest n th point observed in some of the numerous point realizations within reasonable computation time in a real-world Monte Carlo simulation of the PPP.

But for any conditioned $\epsilon_1/|Y| \triangleq \epsilon_1/t > 0$. By conditional probability, and by (3.37) and (3.38),

$$\begin{aligned} \lim_{n \rightarrow \infty} n\mathbb{E}\left(X_{\{n\}}^2 \mathbf{1}(X_{\{n\}} > \epsilon_1/t)\right) &= \lim_{n \rightarrow \infty} n\mathbb{E}(X_{\{n\}}^2 | X_{\{n\}} > \epsilon_1/t)\mathbb{P}(X_{\{n\}} > \epsilon_1/t) \\ &\leq \lim_{n \rightarrow \infty} \mathbb{E}(X_{\{n\}}^2)n\mathbb{P}(X_{\{n\}} > \epsilon_1/t) = -\lim_{n \rightarrow \infty} \tilde{\kappa}/(2n)\tilde{\kappa} \log(\epsilon_1/t) = 0, \end{aligned}$$

which concludes the proof. \square

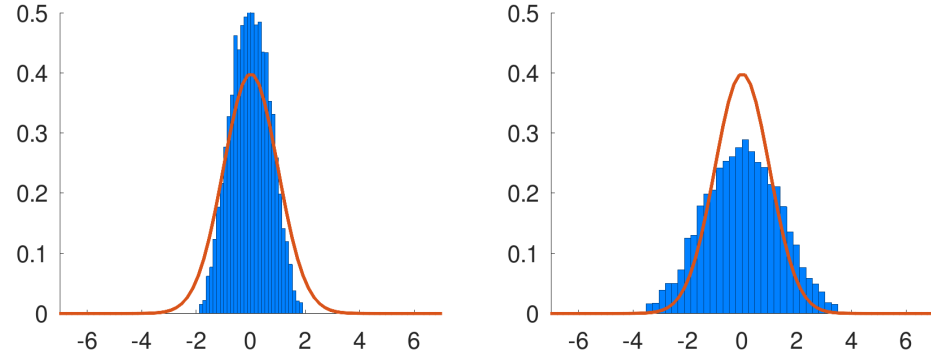
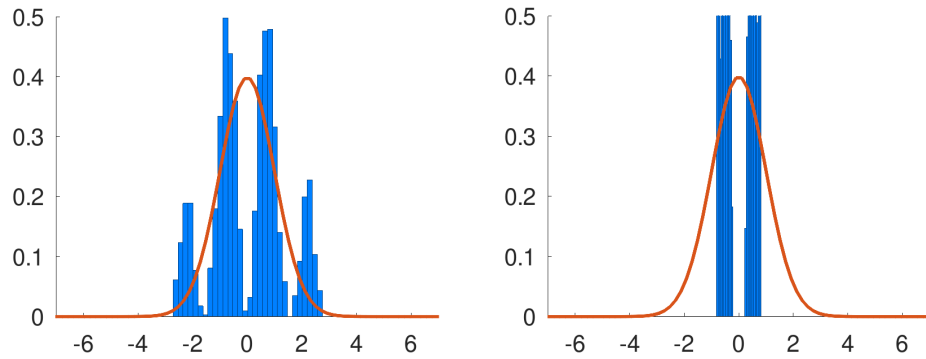
Remark (Interpretation of the Gaussian statistics). Let us carefully discuss the interpretation of the Gaussian signal statistics. Theorem 3.4.4 applies only in the sense of an ensemble average of Φ . On the contrary, should we consider the “temporal” signal statistics stemming from a deterministic non-changing realization of signal source terminals, the CLT does not generally apply: the Gaussian model for the AWN total interference should be applied with caution with an understanding of the underlying signaling assertions and the—usually cross-related—spatial and temporal phenomena, such as bandwidth, frequency band, fading, Doppler effects, mobility of the transmitters (NTNs), signal correlation characteristics, signal response at the receiver, *etc.* An ensemble-average-model-without-a-temporal-structure interpretation may be reasonable under a wide-band-type assumption, in which the aggregate signal stems from short-living signals and the transmitters appear and go silent sequentially multiple times over a period during which the satellites can be considered practically non-mobile during the use period (*vis-à-vis* the mobility of the Earth terminals is even more negligible), or with a medium access control such as ALOHA that shuffles densely located transmitters rapidly. However, under the narrow-band assumption without ALOHA, when the transmitters do not appear and go silent that frequently, the interference waveform distribution is not necessarily Gaussian at each spatial location (*c.f.*, Figures 3.4-3.8). In both cases, the Gaussian waveform (ensemble) statistics can be interpreted in the ergodic sense as a temporal average over a deterministic realization of the NTN terminal locations while the LEO BSs are mobile. In the latter case, the limited orbital speed causes temporal signal correlation because of the definite signal terminal locations. Hence, in the narrow-band communications, a temporal correlation structure is inherent and a crucial part of the AWN total interference—with an exception in the case of extremely slow (regarding the applications, maybe unreasonably slow) signal sampling frequency, which is at least the time interval it takes for the typical LEO BS to move to an non-overlapping served footprint. In this regard, due to the ergodicity of the homogeneous PPP, the AWN total interference statistics equal the ensemble average after a sufficiently long time of movement. A combination of both the ensemble- and ergodic-sense interpretations is also possible. By Theorem 3.4.4, the signal with the described temporal structure is a stationary Gaussian process.

As already discussed, Theorem 3.4.4 entails that the interference waveform is a Gaussian process if the statistics include a sufficiently encompassing spatial and/or temporal observation period during which the LEO BSs (and possibly the Earth NTN terminals) move and/or as distinct terminals subsequently appear and transmit, and go quiet. Figures 3.4e, 3.5e, 3.6e, and 3.7e demonstrate how the ensemble averages differ from the average over a single realization of the Earth terminals for different WN signals: for binary phase-shift keying (BPSK), *i.e.*, the typical transmission $g \in \{-1, 1\}$ with even probabilities in each sample, and for normalized AWGN interferer waveforms. Despite being non-exact given a *deterministic* NTN terminal realization, a Gaussian waveform model for the AWN total interference can be generally reasonable for sufficiently large densities (although the variance fluctuates); *c.f.*, Figures 3.5a-3.5d and 3.7a-3.7d. For small densities, the signal distribution varies remarkably; however, in the case of AWGN signals, the total interference has, empirically, Gaussian statistics when conditioned on a deterministic transmitter realization; *c.f.*, Figures 3.6a-3.6d. On the other hand, for BPSK, the variation in interference distribution shape is prominent over spatial realizations and does not generally exhibit (at least non-mixture) Gaussian behavior; see Figures 3.4a-3.4d. However, in the presence of multipath fading gain, the interference waveform distributions can be near-Gaussian statistics for small densities; *c.f.*, Figures 3.8a-3.8d. Furthermore, phase shifts (which are not modeled in the figures but are realistically present) in the received BPSK signals introduce additional randomness, and the use period waveforms will resemble a Gaussian distribution more.

With knowledge of the fluctuation statistics of the power distribution over the NTN terminal realizations (as studied in Figures 3.2-3.3), mixture or compounded Gaussian distributions can be reasonable for modeling the aggregate random interference signal waveform within a use period over the layouts of interfering NTN terminal locations. The gamma distribution model with mean and variance $\tilde{\kappa}, \tilde{\kappa}/2$, respectively, is a feasible approximation in general fading environments for the power (averaged over a use period) distribution of the AWN total interference.

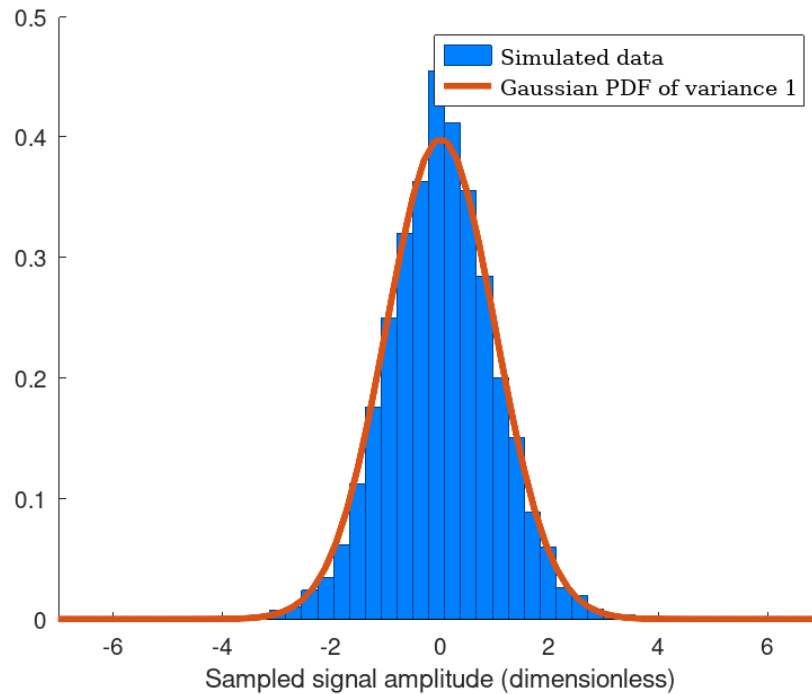
In Figures 3.4 – 3.7, the parameter values $\tilde{\kappa} \in \{1, 5\}$, which determine the density of the interferers, correspond to $\{1, 5\} \times \log(2)$ uplink NTN terminals on average in the -3 dB footprints of the LEO BSs, respectively.

The CLT does not generally apply to the distribution if the WN assumption is not made. A counterexample is the gamma power distribution for Rayleigh fading (3.59), which follows the Gaussian distribution only asymptotically as the density of the transmitters goes to infinity (sufficiently, $\tilde{\kappa} \rightarrow \infty$).

The AWN-total-interference distribution over a single realization of NTN terminals(a) A \mathcal{G}_1 ($\tilde{\kappa} = 1$) realization and BPSK signals. (b) Another spatial NTN terminal realization.

(c) Third realization.

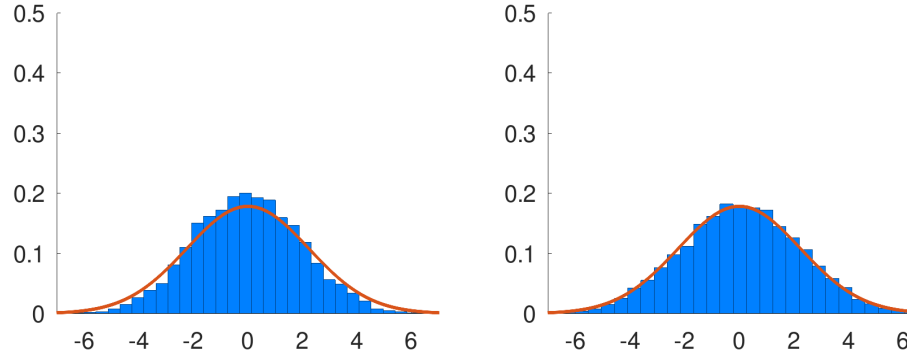
(d) Fourth realization.



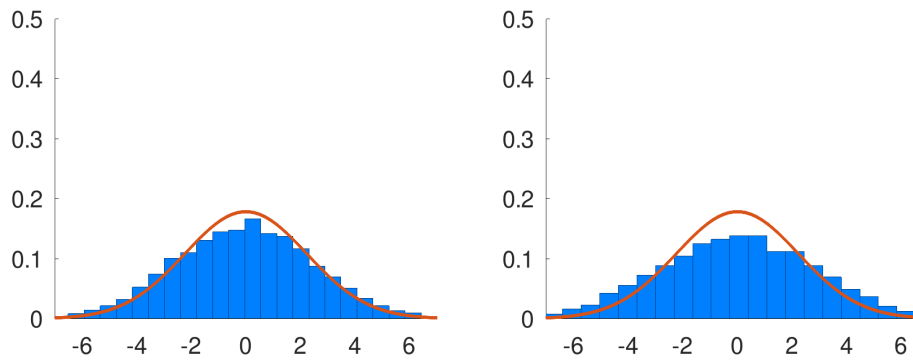
(e) The compound distribution over the realizations is Gaussian of variance 1.

Figure 3.4. The AWN total interference statistics over single versus over the entire ensemble of small-density NTN terminal p.p. with the GP parameter $\tilde{\kappa} = 1$. The individual transmission responses are i.i.d. BPSK symbols.

The AWN-total-interference distribution over a single realization of NTN terminals

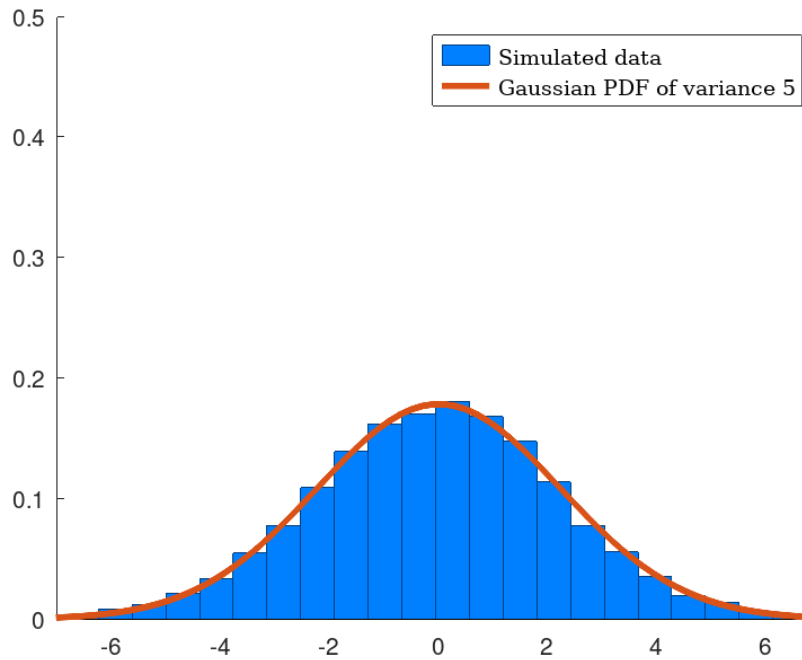


(a) A \mathcal{G}_1 ($\tilde{\kappa} = 5$) realization and BPSK signals. (b) Another spatial NTN terminal realization.



(c) Third realization.

(d) Fourth realization.



(e) The compound distribution over the realizations is Gaussian of variance 5.

Figure 3.5. The AWN total interference statistics over single versus over the entire ensemble of high-density NTN terminal p.p. with the GP parameter $\tilde{\kappa} = 5$. The individual transmission responses are i.i.d. BPSK symbols.

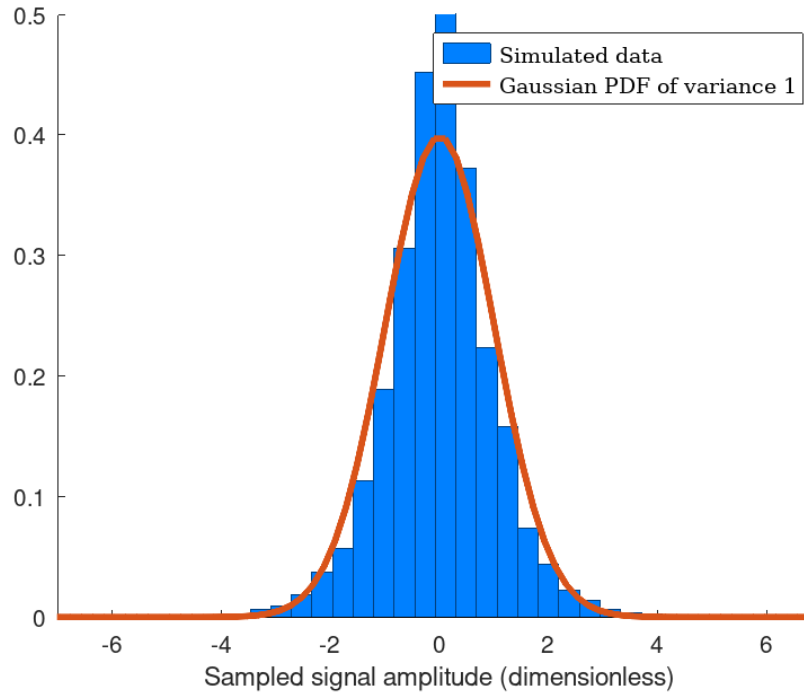
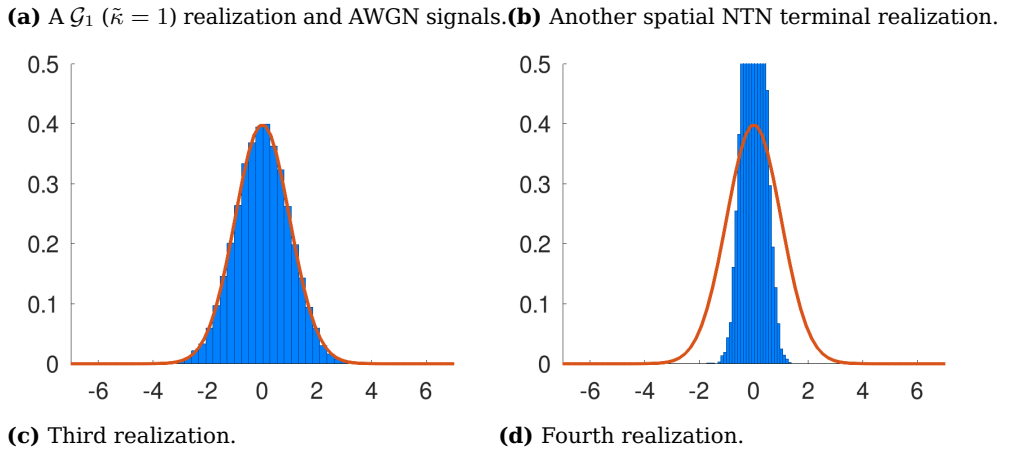
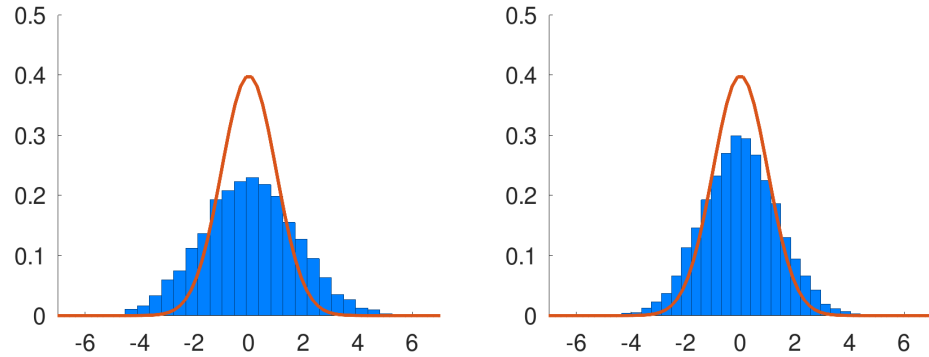
The AWN-total-interference distribution over a single realization of NTN terminals

Figure 3.6. The AWN total interference statistics over single versus over the entire ensemble of small-density NTN terminal p.p. with the GP parameter $\tilde{\kappa} = 1$. The individual transmission responses are i.i.d. AWGN.

The AWN-total-interference distribution over a single realization of NTN terminals

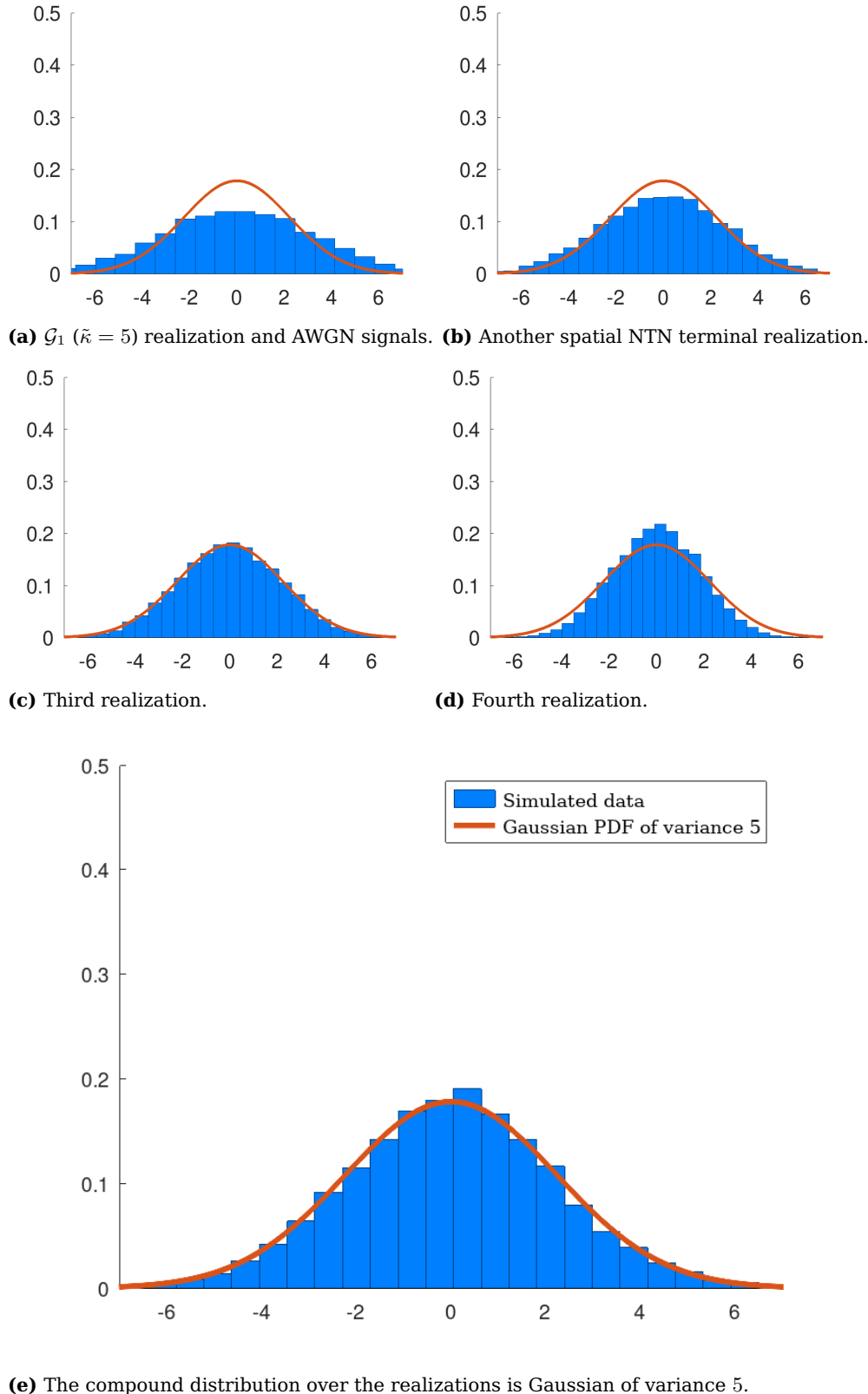


Figure 3.7. The AWN total interference statistics over single versus over the entire ensemble of high-density NTN terminal p.p. with the GP parameter $\tilde{\kappa} = 5$. The individual transmission responses are i.i.d. AWGN.

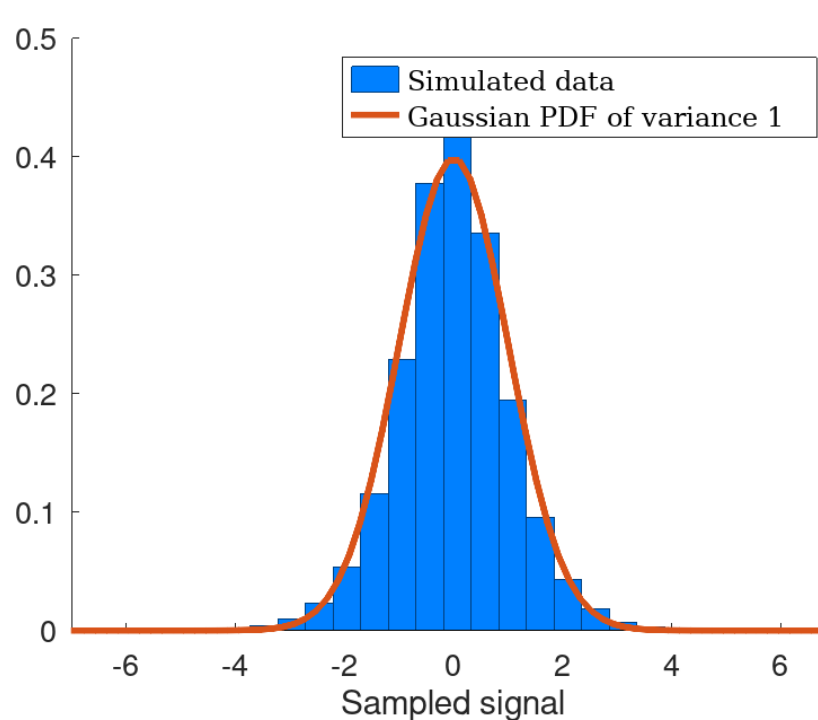
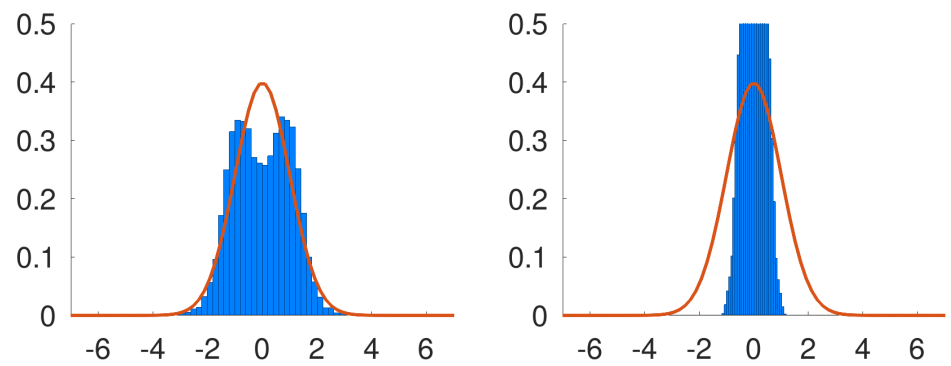
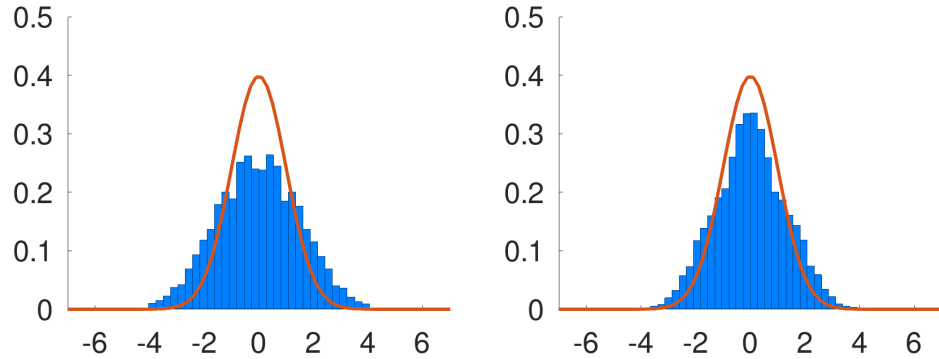
The AWN-total-interference distribution over a single realization of NTN terminals(e) The compound distribution over the realizations is Gaussian of variance $\tilde{\kappa} = 1$.

Figure 3.8. The AWN total interference statistics over single versus over the ensemble of low-density NTN terminal p.p. realizations (use periods) with the GP parameter $\tilde{\kappa} = 1$. Each transmission response is i.i.d. Rayleigh faded BPSK.

3.5 Factorial moment measure

Let $\Psi \subset \mathbb{R}$ be a p.p. (not necessarily Poisson). The n th factorial moment measure is defined as

$$\begin{aligned} M^{(n)}(t_1, \dots, t_n) &\triangleq M^{(n)}((t_1, \infty), \dots, (t_n, \infty)) \\ &\triangleq \mathbb{E} \left(\sum_{(x_1 \neq \dots, \neq x_n) \in (\Psi)^{\times n}} \prod_{j=1}^n \mathbf{1}(x_j > t_j) \right). \end{aligned} \quad (3.41)$$

The density of the n th factorial moment measure is given as the derivative

$$\mu^{(n)}(t_1, \dots, t_n) \triangleq (-1)^n \frac{\partial^n M^{(n)}(t_1, \dots, t_n)}{\partial t_1 \dots \partial t_n}. \quad (3.42)$$

Example 3.5.1 (Density of the factorial moment measure of the GP). Since the point in the PPP has no interaction, the density of the n th factorial moment measure of the GP is given by the multiplication

$$\mu_{\mathcal{G}}^{(n)}(t_1, \dots, t_n) = (-1)^n \lambda_{\mathcal{G}}(t_1) \times \dots \times \lambda_{\mathcal{G}}(t_n), \quad (3.43)$$

and the moment measures are given correspondingly with the n -dimensional integral

$$M^{(n)}(t_1, \dots, t_n) = (-1)^n \int_{t_1}^{\infty} \lambda_{\mathcal{G}}(x_1) dx_1 \times \dots \times \int_{t_n}^{\infty} \lambda_{\mathcal{G}}(x_n) dx_n. \quad (3.44)$$

3.5.1 Order statistics

Let $x_{(i)} \in \Psi \subset \mathbb{R}$ denote the i th largest point in a p.p. Ψ . The order statistics of are denoted as

$$x_{(1)} > x_{(2)} > x_{(3)} > \dots \quad (3.45)$$

The following Lemma is useful [48, Lemma 5.3].

Lemma 3.5.1 (Joint probability distribution function of the order statistics). *Let $\Psi \subset \mathbb{R}$ be a simple p.p. Should the following expression exist in the support of Ψ , the joint PDF of the n th order statistics is*

$$\begin{aligned} f_{(n)}(x_1, \dots, x_n) &= \\ &\sum_{k=0}^{\infty} \frac{(-1)^k}{k!} \int_{x_n}^{\infty} \dots \int_{x_n}^{\infty} \mu^{(n+k)}(x_1, \dots, x_n, \xi_1, \dots, \xi_k) d\xi_1 \dots d\xi_k \end{aligned} \quad (3.46)$$

whenever $x_1 > x_2 > \dots > x_n$ in the support of Ψ and 0 otherwise.

Corollary 3.5.2 (Order statistics of the GP). *Let us assume $\int_x^{\infty} \lambda_{\mathcal{G}}(t) dt < \infty$ for all x (within the support of $\lambda_{\mathcal{G}}(\cdot)$). The order statistics of the n largest*

points in \mathcal{G} are characterized by the PDF

$$\begin{aligned} f_{(n)}(x_1, \dots, x_n) &= \left(\sum_{k=0}^{\infty} \frac{(-1)^k}{k!} \left(- \int_{x_n}^{\infty} \lambda_{\mathcal{G}}(t) dt \right)^k \right) \prod_{i=1}^n \lambda_{\mathcal{G}}(x_i) \\ &= e^{- \int_{x_n}^{\infty} \lambda_{\mathcal{G}}(t) dt} \prod_{i=1}^n \lambda_{\mathcal{G}}(x_i), \end{aligned} \quad (3.47)$$

in the region $x_1 > x_2 > \dots > x_n$, each x_i within the support of $\lambda_{\mathcal{G}}(\cdot)$, and $f_{(n)}(x_1, \dots, x_n) = 0$ otherwise.

Example 3.5.2 (Order statistics of the GP with deterministic h). Let us assume the GP with deterministic $h = 1$ ($F_h(\cdot)$ is a step function). The order statistics of the n largest points in \mathcal{G}_1 , recalling that $\lambda_{\mathcal{G}_1}(x) = \tilde{\kappa}/x|_{x \in (0,1)}$, are characterized by the PDF

$$f_{(n)}(x_1, \dots, x_n) = x_n^{\tilde{\kappa}} \prod_{i=1}^n \frac{\tilde{\kappa}}{x_i}, \quad (3.48)$$

with the support $1 > x_1 > x_2 > \dots > x_n > 0$.

Example 3.5.3 (Order statistics of the SNR of the two strongest transmitters in a LEO downlink). The probability that the largest two point values (or two strongest scaled SNRs) $x_{(1)}, x_{(2)} \in \mathcal{G}_1$ reach the thresholds $1 > \tau_1 \geq \tau_2 > 0$ is equivalent to the probability of the event $\mathcal{A} = \{\{x_{(1)} > \tau_1\} \cap \{x_{(2)} > \tau_2\}\}$:

$$\mathbb{P}(\mathcal{A}) = \int_{\tau_1}^1 \int_{\tau_2}^x f_{(2)}(x, y) dy dx = \int_{\tau_1}^1 \int_{\tau_2}^x y^{\tilde{\kappa}} \frac{\tilde{\kappa}^2}{xy} dy dx = 1 - \tau_1^{\tilde{\kappa}} + \tau_2^{\tilde{\kappa}} \tilde{\kappa} \log(\tau_1). \quad (3.49)$$

Note that the random h is not incorporated here (such as fading or shadowing); hence, the *spatially* nearest transmitter to the origo in the homogeneous PPP $\Phi \subset \mathbb{R}^2$, sufficiently and necessarily, “has the strongest SNR” $x_{(1)} \in \mathcal{G}_1$.

3.6 Signal-to-interference-plus-noise ratio

In this and the following sections, we study the SIR and SINR distributions in a narrow-beamed LEO BS network. In line with [Publication I-Publication IV](#), we may refer to an uplink transmission with the omnidirectional Earth transmitters. However, the system model is also applicable to downlink, considering that the LEO BS footprints are located on the Earth surface according to the homogeneous PPP. Furthermore, because the scenarios are symmetric in the planar system model, the Earth transmitters can be considered to have a narrow beam, and the LEO BSs an omnidirectional (or perfectly aligned) antenna pattern in the uplink and downlink scenarios.

Recall the total interference I ,

$$I \triangleq \sum_{x \in \mathcal{G}} g_x x = \sum_{x \in \mathcal{G}_1} g_x h_x x, \quad (3.50)$$

where $\{h_x\}$ and $\{g_x\}$ are i.i.d. r.v.'s. One natural interpretation is that the typical h (which can be incorporated in the density of \mathcal{G} ; see (3.25)) represents shadowing (slow-fading), and that g represents fast fading. Another meaningful adaptation of h (or g) is the non-temporal waveform statistics modeling of a white noise signal with $\mathbb{E}(h) = 0$ and finite power $\text{var}(h) = \mathbb{E}(h^2) < \infty$, which can be multiplied by the random fading gain. The Laplace transform of I is (3.29) for $f(x) = x$.

The signal to signal-to-interference-plus-noise ratio of the n th strongest transmitter is

$$\text{SINR}^{(n)} \triangleq \frac{g_{x_{(n)}} x_{(n)}}{I - g_{x_{(n)}} x_{(n)} + \text{NSR}_o} = \frac{g_{x_{(n)}} x_{(n)}}{\sum_{x \in \mathcal{G} \setminus \{x_{(n)}\}} g_x x + \text{NSR}_o}, \quad x_{(n)} \in \mathcal{G}, \quad (3.51)$$

where g is an i.i.d. random fading variable, and the noise is represented by the expected noise-to-signal ratio (NSR) of a transmitter at o ; $\text{NSR}_o \triangleq W / (\hat{d}_{h,\epsilon}/d_0)^{-\gamma}$, where $W > 0$ is the noise, and $(\hat{d}_{h,\epsilon}/d_0)^{-\gamma}$ denotes the spatial path loss with the path loss exponent γ and normalizing distance d_0 .

The signal-to-interference-ratio is defined as

$$\text{SIR}^{(n)} \triangleq (\text{SINR}^{(n)} | \text{NSR}_o = 0) = \frac{g_{x_{(n)}} x_{(n)}}{\sum_{x \in \mathcal{G} \setminus \{x_{(n)}\}} g_x x}, \quad x_{(n)} \in \mathcal{G}. \quad (3.52)$$

3.6.1 SIR of the nearest transmitter

Corollary 3.6.1. *The SIR r.v. $\text{SIR}_{(1)}^{\text{NT}}$, which is defined as the SIR of the Nearest Transmitter (equivalently, the transmitter with the strongest signal power averaged over both fading variables) $x_{(1)} \in \mathcal{G}$, has the distribution function*

$$\mathbb{P}(\text{SIR}_{(1)}^{\text{NT}} > t) = \mathbb{P}(H_{x_{(1)}}/I > t), \quad (3.53)$$

where H_{x_1} is a general fading r.v. of the nearest transmitter (possibly different from the interferers). With an exponential $H_{x_1} \sim \exp(1)$,⁴

$$\mathbb{P}(\text{SIR}_{(1)}^{\text{NT}} > t) = \mathcal{L}_I(t), \quad (3.54)$$

where $\mathcal{L}_I(t)$ is given in (3.29) by the substitution $f(x) = x$.

Furthermore, (3.53) implies that the distribution of the SIR of the nearest transmitter does not depend on the conditional distribution of the location of the nearest transmitter. The property entails that the served UE can belong to the same PPP as the interferers or not, yet the statistics of the SIR are equivalent. This is a unique property of the GP.

⁴The result is related to the relation between the interference-to-(average)-signal ratio (ISR) and the Laplace transform of the interference in the terrestrial networks [49][Laplace transform of the coverage probability].

Proof. Let us mark the h and g separately for the interferers, but we denote the fading of the nearest transmitter only by $H_{x(1)}$, although it can represent any r.v. including the composition of shadowing and fast fading.

$$\begin{aligned} 1/\text{SIR}_{(1)}^{\text{NT}} &= \frac{\sum_{x \in \mathcal{G}_1 \setminus \{x(1)\}} g_x h_{xx}}{H_{x(1)} x_1} = \sum_{x \in \Phi \setminus \{x_1\}} g_x h_x e^{a(\|x\|^2 - \|x(1)\|^2)} / H_{x(1)} \\ &\stackrel{(a)}{=} \sum_{x \in \Phi \setminus \{x\}} g_x h_x e^{a(\|x\|^2 - \|o\|^2)} / H_{x(1)} \stackrel{(b)}{=} \sum_{x \in \Phi} g_x h_x e^{a\|x\|^2} / H_{x(1)} = \sum_{x \in \mathcal{G}_1} g_x h_x x / H_{x(1)} \\ &= \sum_{x \in \mathcal{G}} g_x x / H_{x(1)} = I / H_{x(1)}, \end{aligned}$$

where (a) follows from the basic property of the homogeneous PPP $\{\|x(i)\|^2 - \|x(1)\|^2\}_{i \in \{2, \dots, \infty\}}, x(i) \in \mathbb{R}^2$, (indeed homogeneous; see [50, Example 2.9]) on the reals that $\|x(n)\|^2 - \|x(1)\|^2$ is distributed according to the Erlang distribution regardless of $x(1)$. (b) is Slivnyak's theorem.

(3.54) is the standard result; the expectation of the CCDF of an exponential $H_{x(1)}: \mathbb{P}(H_{x(1)} > tI) = \mathbb{E}_I(e^{-tI}) = \mathcal{L}_I(t)$. \square

As stated, quaint to the GP, (3.53) contains the insight that the SIR is independent of the nearest transmitter $x(1) \in \mathcal{G}_1$: we can condition its position in $\mathcal{G}_1 \subset (0, 1)$ (or equivalently in $\Phi \subset \mathbb{R}^2$) to have an arbitrary distribution, including deterministic, and the distribution is equivalent to the SIR with the nearest transmitter being part of the same PPP as the interferers: The distribution of the $\text{SIR}_{(1)}^{\text{NT}}$ is entirely characterized by $H_{x(1)}/I$.

The exponential $H_{(1)}$ is analytically most tractable in the SIR analysis, as demonstrated in (3.54): then the SIR of the nearest transmitter is directly characterized by the Laplace transform of I . For more general fading, we can, *e.g.*, develop g with exponential terms, as done in [Publication III](#) for a gamma r.v., representing the power fading, *i.e.*, Nakagami amplitude fading. Alternatively, one can seek to obtain the distribution function of $I/H_{x(1)}$ (or $H_{x(1)}/I$) by using whatever methods are available for the solution, *e.g.*, through characterizing the Laplace transforms of I and $H_{x(1)}$. For example, the PDF of the I can be acquired by the Plancherel-Parseval Theorem [51][Thm. C3.3, p. 157], and the distribution function of the SIR follows from (3.53);

$$\begin{aligned} \mathbb{P}(\text{SIR}_{(1)}^{\text{NT}} > \theta) &= \mathbb{P}(H_{x(1)} > \theta I) \\ &= \int_{-\infty}^{\infty} \mathcal{L}_I(2i\pi\theta s) \frac{\mathcal{L}_{H_{x(1)}}(-2i\pi s) - 1}{2i\pi s} ds, \quad i^2 = -1. \end{aligned} \quad (3.55)$$

We introduced the symbol θ , by which we usually refer to the threshold for a successful transmission: the CCDF evaluated at θ is the transmission success probability.

Although precise analysis is feasible as described, for computational efficiency and better insight, the following simple expression might satisfactorily approximate the SIR distribution under general fading settings. Let us consider exponential fast fading and no shadowing; $\mathcal{G} = \mathcal{G}_1$ and $g \sim \exp(1)$ in (3.61), i.e., we assume Rayleigh fading. From then on, for simplicity, we denote $x_{(1)} = x_1$.

Proposition 3.6.2 (Fairly general approximation of the SIR distribution in the narrow-beam LEO). *For Rayleigh fading, the SIR of the nearest transmitter $x_1 \in \mathcal{G}_1$ has the distribution function*

$$\mathbb{P}(\text{SIR}_1^{\text{NT}} > t) = (1 + t)^{-\tilde{\kappa}}, \quad (3.56)$$

which is a heavy-tailed **Lomax distribution**. Furthermore, for general Rician and Nakagami fast fading channels, the Lomax distribution approximation of the SIR is tight in the simple coverage region, i.e., for $t \geq 1$.

Proof. For the exponential power fading, i.e., the Rayleigh fading, $H_{x_1} = g \sim \exp(1)$, using (3.54) yields $\mathbb{P}(\text{SIR}_1^{\text{NT}} > t) = \mathcal{L}_I(t) = (1 + t)^{-\tilde{\kappa}}$. Furthermore, the approximation applies to Nakagami- m fading, where $m \geq 1$ is the Nakagami fading parameter, as shown in [Publication III](#) (see Figure 6). As the Nakagami fading is close to Rice fading by matching the first two moments of the power fading distribution (see Figure 2.10), Rice fast fading is also feasible. \square

3.6.2 SINR of the nearest transmitter

We generalize Proposition 3.6.2 to encompass the noise (or side lobes).

Proposition 3.6.3 (Fairly general approximation of the SINR distribution in the narrow-beam LEO). *Under Rayleigh fading, the SINR of the nearest transmitter $x_1 \in \mathcal{G}_1$ has the distribution function*

$$\mathbb{P}(\text{SINR}_1^{\text{NT}} > t) = (1 + t)^{-\tilde{\kappa}} E_{\tilde{\kappa}+1}(\text{NSR}_o t) \tilde{\kappa}. \quad (3.57)$$

Furthermore, for general Rician and Nakagami fast fading channels, this tightly approximates the SINR distribution of $\text{SINR}_1^{\text{NT}}$ in the simple coverage region.

Proof. Let $H_{x_1} = g \sim \exp(1)$.

$$\begin{aligned} \mathbb{P}(\text{SINR}_1^{\text{NT}} > t) &= \mathbb{P}\left(g_{x_1} > \frac{\sum_{x \in \mathcal{G}_1 \setminus \{x_1\}} g_x x}{x_1} + \frac{\text{NSR}_o}{x_1}\right) \\ &\stackrel{(a)}{=} \mathbb{P}\left(g_{x_1} > \sum_{x \in \mathcal{G}_1} g_x x t + \frac{\text{NSR}_o}{x_1} t\right) \stackrel{(b)}{=} \mathbb{E}\left(e^{-\sum_{x \in \mathcal{G}_1} g_x x t - \frac{\text{NSR}_o}{x_1} t}\right) \\ &\stackrel{(c)}{=} \mathbb{E}\left(\mathbb{E}_g\left(e^{-t \sum_{x \in \mathcal{G}_1} x}\right) \mathbb{E}\left(e^{-\text{NSR}_o / x_1 t}\right)\right) \stackrel{(d)}{=} \mathbb{E}\prod_{x \in \mathcal{G}} \frac{1}{1 + tx} E_{\tilde{\kappa}+1}(\text{NSR}_o t) \tilde{\kappa}, \end{aligned}$$

and the result follows. In (a), please refer to the proof of the Corollary 3.6.1 that we can re-denote $\sum_{x \in \mathcal{G}_1 \setminus \{x_1\}} / x_1 = \sum_{x \in \mathcal{G}_1} x$. (b) is the CCDF of the exponential distribution. In (c), please refer to the proof of Corollary 3.6.1 to consider the sum independent of x_1 . In (d), we use the PGFL of I with the exponential power fading and the Laplace transform of $1/x_1$. \square

Figure 3.12 shows the SIR and the SINR Lomax distribution approximations (3.56) and (3.57) (exact for Rayleigh fading) for various noise values and the GP parameter $\tilde{\kappa} = 1$.

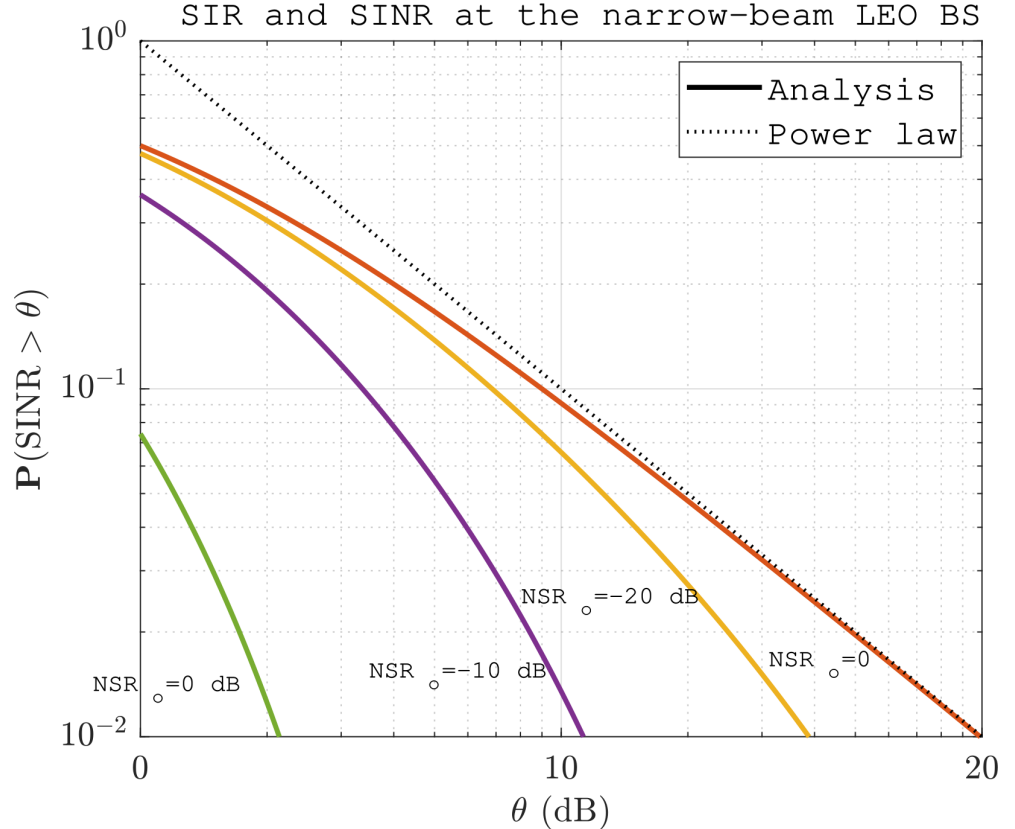


Figure 3.9. The SINR distribution at the LEO BS with various noise magnitudes $NSR_o \in \{1, 1/10, 1/100, 0\} = \{0, -10, -20, -\infty\}$ dB and $\tilde{\kappa} = 1$. The axes scales are logarithmic (log-log plot), revealing the asymptotic power law behavior as $NSR_o \rightarrow 0$.

3.6.3 SIR of the strongest transmitter and SIR order statistics

In this section, we study the SIR statistics associated with the strongest transmitter rather than the spatially nearest transmitter. Under shadowing, the strongest-signal association is sensible because the LEO BSs directly observe the signal strengths rather than the spatial locations of the transmitters. Note that the nearest transmitter is necessarily the strongest signal only in the event when SIR equals or exceeds unity at the LEO BS. Such a coverage threshold region is called the simple coverage region, where the term "simple" embodies that the strongest-signal SIR analysis gets significantly more complex when evaluating link performance metrics for SIR thresholds below 1. The distinction between the simple coverage region and analytically complex region has already been observed with some approximate simple distributions, which are tight in the simple coverage region but less accurate outside the region, as is the case with the Lomax and suppressed Lomax distribution approximations of the SIR and SINR for general fading in (3.56) and (3.57), respectively. The order statistics of the strongest transmitters discussed in this section will further confirm this complexity separation, possibly even in a more concrete sense.

For the section, we consider only shadowing; $g = 1$ in (3.61)—the “only shadowing” referring to the assumption that no fast fading fluctuation is considered during the use period over which the typical LEO BS is connected to the strongest shadowed signal (although there is no mathematical reason why this “shadowing” could not be seen as fast fading).

For analytical tractability and insightful results, while still maintaining appropriate accuracy, we propose a defective exponential fading model, $h \sim \exp_{\nu}(1)$, for modeling Gaussian mixture shadowing. The (normalized) defective exponential r.v. is defined by the CCDF

$$F(t) = \nu e^{-t}, \quad 0 < \nu \leq 1. \quad (3.58)$$

Note the atomic probability measure at zero; ν : its complement corresponds to a case where the signal is entirely attenuated. Recall, 1: by moment matching, the defective exponential fading can be used to approximate a general shadowing distribution, say, the Mixture Gaussian shadowing. ν is proportional to the LoS probability; however, it is not necessarily equal (see [Publication IV](#)).

The defective exponential satisfactorily models the SIR statistics in log-normal shadowing by matching the mean and the variance of I ; see (3.32) and (3.33). Through the approximation, we can identify the random process of the total interference with the **gamma process**, and further, the SIRs with the **Poisson-Dirichlet process**. These insights enable us to exploit the results of these well-studied processes.

The total interference follows the gamma distribution under the defective exponential fading. Namely, similarly to (3.34): the Laplace transform of I

with the defective exponential fading is

$$\mathcal{L}_I(s) = (1 + s)^{-\tilde{\kappa}\nu}, \quad (3.59)$$

which is the gamma distribution with the shape parameter $\tilde{\kappa}\nu$.

The signal-to-total-interference (STIR) process is useful in the study of order statistics. For each $n \in \{1, \dots, \infty\}$,

$$\text{STIR}_n \triangleq \frac{x_n}{I} = \frac{x_n}{\sum_{x \in \mathcal{G}} x}, \quad x_n \in \mathcal{G}. \quad (3.60)$$

Note that $\text{STIR}_n \in (0, 1)$. The SIR process can be recovered from the SIR process as

$$\text{SIR}_n = \frac{\text{STIR}_n}{1 - \text{STIR}_n}. \quad (3.61)$$

Next, we derive the factorial moment measure of the STIR process.

Theorem 3.6.4. *Using the defective exponential shadowing, the density of the n th factorial moment measure of the STIR process is*

$$\mu'^{(n)}(z'_1, \dots, z'_n) = (\tilde{\kappa}\nu)^n \prod_{j=1}^n z_j'^{-1} \left(1 - \sum_{j=1}^n z_j' \right)^{\tilde{\kappa}\nu-1}, \quad (3.62)$$

whenever $z'_1 > \dots > z'_n$ and $\sum_{i=1}^n z'_i \leq 1$, and 0 otherwise.

Proof. We directly refer to [52, Eq. 8]: As the total interference follows the gamma distribution (3.59), I can be interpreted as a gamma process at time $\tilde{\kappa}\nu$. The *normalized increments* $\{\text{STIR}_n : x_n \in \mathcal{G}\} = \{x_n/I : x_n \in \mathcal{G}\}$ follow the Poisson-Dirichlet distribution $\text{PD}(0, \tilde{\kappa}\nu)$, which has the given density. \square

The density of the n th moment measure of the SIR can be derived as [49][Corollary 6.1.3]

$$\mu^{(n)}(z_1, \dots, z_n) = \prod_{j=1}^n \frac{1}{(1 + z_j)^2} \mu'^{(n)}\left(\frac{z_1}{1 + z_1}, \dots, \frac{z_n}{1 + z_n}\right), \quad (3.63)$$

where $\mu'^{(n)}(z'_1, \dots, z'_n)$ is the density of STIR_n . In the following, we derive $\mu'^{(n)}(\cdot)$.

Definition 3.6.1 (n -probability). Let $f'(\cdot)$ denote the joint PDF of the STIR process. Let $\theta' = 1/(1 + \theta)$. Define the n -probability as the probability that the first n strongest transmitters reach the SIR threshold θ :

$$\begin{aligned} \mathcal{P}^n(\theta) &\triangleq \int_{\theta'}^1 \dots \int_{\theta'}^1 f'(z'_1, \dots, z'_n) dz'_1 \dots dz'_n \\ &= \int_{\theta'}^1 \dots \int_{\theta'}^1 \sum_{i=0}^{i_{\max}} \frac{(-1)^i}{i!} \times \\ &\quad \int_{z'_n}^1 \dots \int_{z'_n}^1 \mu'^{(n+i)}(z'_1, \dots, z'_n, \xi_1, \dots, \xi_i) d\xi_1 \dots d\xi_i dz'_1 \dots dz'_n, \end{aligned} \quad (3.64)$$

where $i_{\max} < 1/\theta' - n$ is a restriction to non-zero terms (that potentially can be relaxed), which follows from the directly from the conditioning of $\mu'^{(k)}(\cdot)$.

The evaluation of (3.64) is not generally trivial due to the complicated integral of non-static dimensional $\mu'^{(n+i)}(\cdot)$. Please find an Octave code utilizing Monte Carlo integration at the end of this section.

Example 3.6.1. Combining (3.46), (3.63), and (3.62), we can derive the PDF of the SIR of the *strongest transmitter* (*c.f.*, the *nearest transmitter* in Corollary 3.6.1) in the simple coverage region $z \geq 1$:

$$\begin{aligned} -\frac{d}{dz}\mathbb{P}(\text{SIR}_1 > z) = f(z) &= \mu^{(1)}(z) = \frac{1}{(1+z)^2}\mu'^{(1)}\left(\frac{z}{1+z}\right) \\ &= \frac{\tilde{\kappa}\nu}{(1+z)^2}\frac{1+z}{z}\left(1-\frac{z}{1+z}\right) = \frac{\tilde{\kappa}\nu}{(1+z)^{-\tilde{\kappa}\nu}z}. \end{aligned} \quad (3.65)$$

In terms of the hypergeometric function ${}_2F_1(\cdot)$, in the simple coverage region the CCDF can be derived through integrating $f(z)$:

$$\mathbb{P}(\text{SIR}_1 > z) = z^{-\tilde{\kappa}\nu} {}_2F_1(\tilde{\kappa}\nu; \tilde{\kappa}\nu; \tilde{\kappa}\nu + 1; -1/z). \quad (3.66)$$

Notably, this is close to the Lomax distribution in the tail distribution (*c.f.*, (3.56)) and approaches it tangentially. Formally, $\mathbb{P}(\text{SIR}_1 > z) \sim (1+z)^{-\tilde{\kappa}\nu}$ as $z \rightarrow \infty$. For $z = 1$; $\mathbb{P}(\text{SIR}_1 > z) > (1+z)^{-\tilde{\kappa}\nu}$ —this reflects the property that, instead of averaging over the fading of the nearest transmitter when the deep fades can cause significant drops in the SIR, SIR_1 describes the SIR continuously associated with the strongest signal, thus improving the average SIR performance at the LEO BSs (but not necessarily from the perspective of each user).

In light of the model, comparing (3.66) to the Nakagami fast fading channel in (3.56), shadowing can be detrimental or beneficial compared to the non-shadowed case, depending on the shadowing parameter ν .

Variance of the SIR and the Quality of Service

Let us dedicate a section to the study of the variance of the SIR of the strongest transmitter at the typical LEO BS. The question is interesting: fluctuations in the SIR affect the stability of the QoS as seen by users. For high variance, the variation in the QoS, or user experience, across the network is high and vice versa (as always, recalling the ergodic interpretation of the typical point in the homogeneous PPP). While the SIR in the standard terrestrial network stochastic geometry models is not dependent on the network density (although high density means high interference, the strongest transmitter is more likely to be near its serving BS and the density cancels out), in the LEO networks, especially with narrow-beam LEO BSs, the density of the (co-channel) terminals in the network has a profound effect in the statistics of the SIR.

Recall 3.65, and derive a lower bound for the first moment as

$$\mathbb{E}(\text{SIR}_{1,[1]}^1) \geq \int_1^\infty f(z)z dz = \int_1^\infty \frac{\tilde{\kappa}\nu}{(1+z)^{\tilde{\kappa}\nu}} dz = \frac{2^{1-\tilde{\kappa}\nu}\tilde{\kappa}\nu}{\tilde{\kappa}\nu-1}, \tilde{\kappa}\nu > 1. \quad (3.67)$$

For $\tilde{\kappa}\nu \leq 1$, the mean diverges.

Similarly, the second moment is lower-bounded by

$$\mathbb{E}(\text{SIR}_{1,[1]}^2) \geq \int_1^\infty f(z)z^2 dz = \int_1^\infty \frac{\tilde{\kappa}\nu z}{(1+z)^{\tilde{\kappa}\nu}} dz = \frac{2^{1-\tilde{\kappa}\nu}(\tilde{\kappa}\nu)^2}{(\tilde{\kappa}\nu-1)(\tilde{\kappa}\nu-2)}, \tilde{\kappa}\nu > 2, \quad (3.68)$$

which is divergent for $\tilde{\kappa}\nu \leq 2$.

Combining (3.67) and (3.68), we can derive the variance by the traditional identity $\text{var}(\text{SIR}_{1,[1]}) = \mathbb{E}(\text{SIR}_{1,[1]}^2) - \mathbb{E}(\text{SIR}_{1,[1]}^1)^2$. An immediate observation is that the variance is undefined for $\tilde{\kappa}\nu \leq 1$ and infinite for $\tilde{\kappa}\nu \leq 2$. On the other hand, the high expected SIR in region $\tilde{\kappa}\nu \leq 2$ might be desirable: this is a trade-off between the QoS stability and average performance. In the ergodic interpretation, this is a trade-off between stability and the average QoS over the LEO BSs, *i.e.*, a highly varying user experience across the network in each use period. The variation in the QoS can be reduced by interference cancellation.

3.6.4 Successive interference cancellation

Successive interference cancellation (SIC) is used in non-orthogonal multiple access (NOMA) methods. Furthermore, signal combination-type techniques are used in the emerging over-the-air computation (AirComp). In this section, and in [Publication IV](#), we explore the effect of the SIC on the LEO BS performance. Similar methods can be straightforwardly extended for the signal combination (see [49][Section 6.1.3]).

By exploiting the order statistics of the STIR process, we develop a stochastic geometry model of SIC in the LEO networks of narrow-beam LEO BSs. In SIC—as referred to in this work—is when the strongest transmitter is decoded first if it exceeded a minimum SIR threshold, then the signal is canceled from the interference. After this, the second strongest transmitter is decoded and canceled, *etc.* (The link-level implementation details of the decoding and interference cancellation schemes are not discussed.) We will show that the SIC profoundly reduces the variance of the SIR, while maintaining robust performance. In other words, QoS can be made stable by the SIC, and the tedious trade-off between user experience consistency and performance, discussed in Section 3.6.3, can be avoided.

Let $(x_1 \dots x_n)$, $x_n \in \mathcal{G}$, represent an ordered set of points in the GP, where x_1 denotes the strongest signal at the typical LEO BS. The signals with indices in the set $[k] \triangleq (1, \dots, k)$, $k \geq n$, are cancelled from the total interference I . Denote the SIR of the n th strongest transmitter with interference

cancellation by

$$\text{SIR}_{n,[k]} \triangleq \frac{x_n}{I - \sum_{j \in [k]} x_j}. \quad (3.69)$$

Definition 3.6.2 (SIC-SIR). The SIR with successive interference cancellation (SIC-SIR) is formally defined as follows. Let $\theta > 0$ be the desired SIR for a successful transmission after the interference cancellation, and $\tau \leq \theta$ be the threshold of signal detection.

A necessary condition for the transmission to be considered successful is

$$\text{SIR}_{n,[k]} > \theta, \quad k \geq n. \quad (3.70)$$

This condition is not sufficient. The SIC-SIR consists of canceling signals up to the index $i \in [K]$, $K > 0$, until (3.70) is met or the maximum number of interference cancellation steps $i = K$ is reached. Each step entails the superposition of the conditions

$$\{\text{SIR}_{n,[k]} > \tau\} \text{ for all } k \in \{1, \dots, n+i-1\}. \quad (3.71)$$

Remark. Although practical decoding schemes hardly approach complete certainty in any non-trivial (temporally finite signals under noise) theoretical settings, even under the most idealistic assumptions, we implicitly model exact decoding of the transmitted, intended signals—only given that the adequate SIR threshold τ is exceeded at the receiver end. (For the SIR values $\tau < \theta$, the inferred interfering signal can not be anything but a highly erroneous estimation—unless there is peculiar prior information about all signals other than that of the served transmitter x_n , or the coding or modulation schemes differ.) Imperfect interference cancellation can be modeled as a simple constant error term $\mathcal{E} \in (0, 1)$ with $I - \mathcal{E} \sum_{j \neq n} x_j$, while retaining intrinsically identical analysis, and no generality is lost in this sense.

We already studied $\mathbb{P}(\text{SIR}_{1,[1]} > (\cdot))$ in Section 3.6.3. Before the characterization of the distribution of the SIC-SIR, we formalize a general expression for the distribution function of $\text{SIR}_{n,[k]}$.

Proposition 3.6.5 (CCDF of the n th SIR with interference cancellation). *Recall the STIR defined in (3.60), and define $\theta' \triangleq \theta/(\theta + 1)$. Given the threshold $\theta > 0$ of a successful transmission, the probability of coverage with interference cancellation is*

$$\mathbb{P}(\text{SIR}_{n,[k]} > \theta) = \mathbb{P}\left(\text{STIR}_n + \theta' \sum_{j \in [k] \setminus \{n\}} \text{STIR}_j > \theta'\right). \quad (3.72)$$

Proof. The proof borrows [53][Eq. 69].

Recall the equivalence (3.61) of the SIR and STIR. We have

$$\begin{aligned}\mathbb{P}(\text{SIR}_{n,[k]} > \theta) &= \mathbb{P}\left(\frac{x_n}{I - \sum_{j \in [k]} x_j} > \theta\right) = \mathbb{P}\left(x_n > \theta I - \theta \sum_{j \in [k]} x_j\right) \\ &= \mathbb{P}\left(\frac{x_n}{I} > \theta - \theta \frac{\sum_{j \in [k]} x_j}{I}\right) = \mathbb{P}\left((1 + \theta)\text{STIR}_n + \theta \sum_{j \in [k] \setminus \{n\}} \text{STIR}_n > \theta\right),\end{aligned}$$

which proves the result. \square

Corollary 3.6.6. Consider the SIC-SIR with at most $K \geq n$ interference cancellation stages. Define $\tau' \triangleq \tau/(1 + \tau)$. The coverage probability of the UE with n th strongest signal is given by

$$\mathcal{P}_{\text{SIC}}^{(n,K)}(\theta, \tau) \triangleq \sum_{k=n}^K \Delta_{\text{SIC}}^{(n,k)}(\theta, \tau), \quad (3.73)$$

where

$$\begin{aligned}\Delta_{\text{SIC}}^{(n,k)}(\theta, \tau) &\triangleq \\ &\times \int_0^1 \cdots \int_0^1 f_{(k)}(z'_1, \dots, z'_k) \prod_{m=1}^k \mathbf{1} \left(z'_m + \tau' \sum_{j=1}^{m-1} z'_j > \tau' \right) \\ &\times \left(\mathbf{1}(k > n) \mathbf{1} \left(z'_n + \theta' \sum_{j \in [k-1] \setminus \{n\}} z'_j < \theta' \right) + \mathbf{1}(k = n) \right) \\ &\times \mathbf{1} \left(z'_n + \theta' \sum_{j \in [k] \setminus \{n\}} z'_j > \theta' \right) dz'_1 \dots dz'_k \quad (3.74)\end{aligned}$$

with the upper summation limit bounded by $i_{\max} < 1/\tau' - 1 = 1/\tau$.

Proof. The expression follows applying the joint PDF of the order statistics (3.46) to Definition 3.6.2. Furthermore, the upper l.h.s. conditioning allows the relaxation of i_{\max} . Namely, a necessary condition is $z'_k + \tau' \sum_{j=1}^{k-1} z'_j > \tau'$. By simple algebra, $\sum_{j=1}^{k-1} z_j > 1 - z_k/\tau'$. Recall the condition on the non-zero terms of $\mu'^{(k+i)}$: $\sum_{j=1}^k z'_j + iz'_k = \sum_{j=1}^{k-1} z'_j + z'_k + iz'_k \leq 1$. The condition certainly does *not* hold if $1 - z_k/\tau' + z'_k + iz'_k > 1$. We arrive at the inequality $z'_k (-1/\tau' + 1 + i) > 0$. Divide both sides by $z'_k > 0$, and the general upper bound of i follows. \square

The numerical evaluation of (3.73) is not trivial due to the complicated integral of non-static dimensional $\mu'^{(n+i)}(\cdot)$. Please find an Octave code utilizing Monte Carlo integration at the end of this section.

Numerical results

The theoretical SIR distribution with successive interference cancellation is plotted in 3.10 for the first two transmitters. Further, the n -probabilities (3.64) are plotted. At most $K = 2$ signals were canceled with a signal detection threshold $\tau = -3$ dB. The average number of effective transmitters inside the -3 dB footprint $\tilde{\kappa}\rho = 2$, which, *e.g.*, describes the Earth transmitter density $\lambda = 0.83 \times 10^{-4} / \text{km}^2$, the LEO BSs in the altitude $h = 1000$ km at elevation angle $\epsilon = 70$, with modeling a two-tier Gaussian mixture shadowing having a LoS probability $p_{\text{LoS}} = 0.9$ in an urban environment with the means and variances $\mu_{\text{LoS}} = 0$, $\mu_{\text{NLoS}} = -26$ dB $\sigma_{\text{LoS}}^2 = 4^2$, $\sigma_{\text{NLoS}}^2 = 6^2$, respectively (by moment matching using Theorem 3.3.6). Please refer to Publication IV for further details and results, with a comparison to simulations of the spherical model and accurate log-normal shadowing.

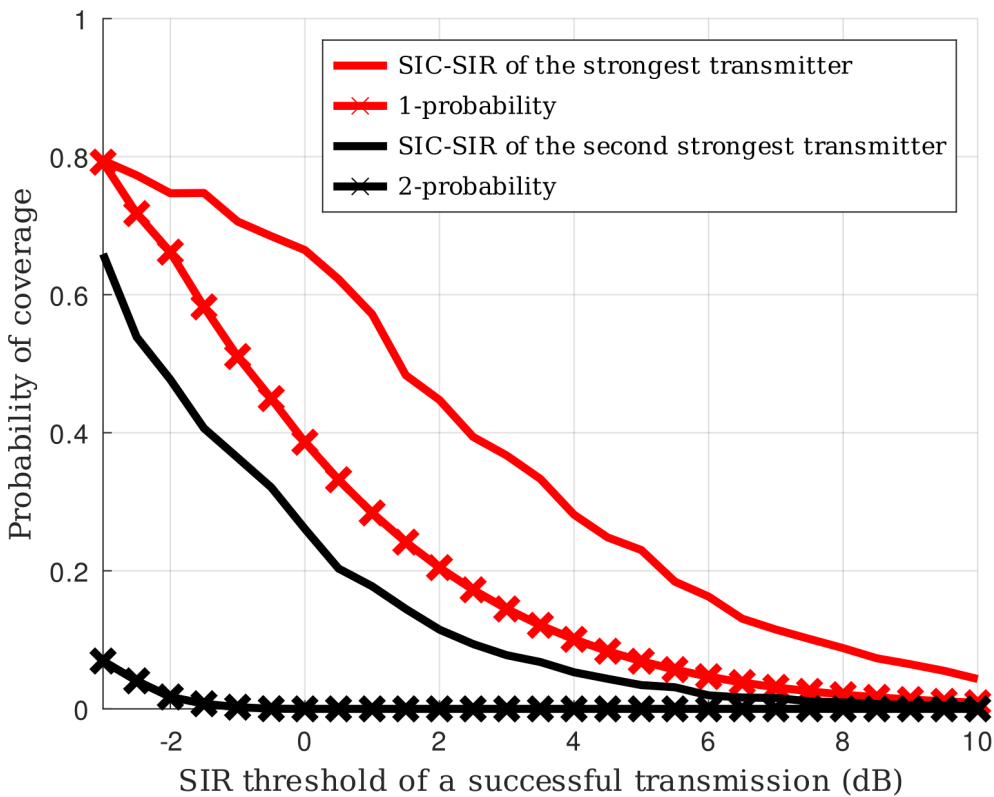


Figure 3.10. The theoretical n -probabilities and SIR-SIC for the first two strongest transmitters. $\log(2)\tilde{\kappa}\rho = 2 \log(2)$ shadowed effective transmitters inside the -3 dB footprint on average in an urban environment. The plot indicates a clear improvement in the transmission success probability after the successive interference cancellation, especially for the second strongest transmitters. The numerical integration method is a probabilistic Monte Carlo method; therefore, the plots exhibit slight fluctuations.

```

function Pn_theta = n_coverage_probability_monte_carlo_SIC(theta, n, SIC)
  ## Pn_theta: Joint pdf of the SIR and successive interference cancellation
  ## Input:
  ## theta: SIR threshold of a successful transmission
  ## n: transmitter's index
  ## SIC: set '0' to evaluate the n-probability, otherwise evaluate SIC-SIR

  K = max(n, 2); # Interference cancellation stages (K >= n)
  M = 5e03; # M: number of Monte Carlo samples
  tic # Measure and print the evaluation time
  nukappa = 2; # "Tildekappa x nu" -parameter
  tau = min(theta, 0.5); # Signal detection threshold (tau <= theta)
  tau_prime = tau / (1 + tau);

  ## Integration lower bound
  theta_prime = theta / (1 + theta);

  ## Upper bound for the series expansion of the joint PDF
  imax = max(0,ceil(1 / theta_prime - n - 1));

  ## If n==1 and SIC == 0 evaluate the built-in numerical integration,
  ## which is much more efficient compared to the Monte Carlo method
  ## in the simple coverage region theta >=1
  if n == 1 && theta >= 1 && SIC == 0 && true
    mu_prime = @t(nukappa ./ t .* (1-t) .^ (nukappa - 1));
    Pn_theta = integral(mu_prime, theta_prime, 1);

    ## Else perform Monte Carlo integration over z'
  else
    Pn_theta = 0;
    if SIC == 0;
      Pn_theta = deltasic(n);
    else
      for k = n : K
        Pn_theta = Pn_theta + deltasic(k);
      endfor
    endif
  endif
  toc

function res = deltasic(k)
  ## Initialize an array to store the calculated function values
  deltasic_k_values = zeros(1, M);

```

```

for iii = 1 : M
  if mod(iii, 250) == 0
    iii
  end

## The conditioning and the integration region are defined separately
## without and with SIC
if SIC == 0
  ## Generate n random samples for z' from the uniform distribution on
  ## (theta_prime, 1) and define the integration domain
  z_prime_samples = theta_prime + (1 - theta_prime) * rand(1, k);
  volume_of_domain = (1 - theta_prime) ^ k; #Integration domain volume
  is_sorted = all(diff(z_prime_samples) < 0); # Sorting condition
  cond = is_sorted;
else

  ## Generate n random samples for z' from the uniform distribution
  z_prime_samples = rand(1, k);
  volume_of_domain = 1; #Integration domain volume
  is_sorted = all(diff(z_prime_samples) < 0); # Sorting condition
  ## Condition 1
  cumulative_sum = cumsum(z_prime_samples);
  shifted_cumulative_sum = [0, cumulative_sum(1:end-1)];
  condition_vector = z_prime_samples...
    + tau_prime .* shifted_cumulative_sum ...
    > tau_prime;
  cond1 = all(condition_vector);
  ## Condition 2
  sum_part = sum(z_prime_samples(1:k-1)) - z_prime_samples(n);
  cond2 = (k>n) * (z_prime_samples(n)... 
    + theta_prime * sum_part < theta_prime) + (k==n);
  ## Condition 3
  sum_part = sum(z_prime_samples(1:k)) - z_prime_samples(n);
  cond3 = z_prime_samples(n) + theta_prime * sum_part > theta_prime;
  cond = is_sorted * cond1 * cond2 * cond3;
endif

## Calculate the joint PDF f'_-(n) for the current sample
## as the series expansion of the joint PDF
deltasic_value = 0;
for j = 0 : imax
  if sum(z_prime_samples) + j * z_prime_samples(end) < 1 && cond
    mu_prime_val = calculate_mu_prime(z_prime_samples, j);
  else

```

```

    mu_prime_val = 0;
endif
term = ((-1) ^ j / factorial(j)) * mu_prime_val;
deltasic_value = deltasic_value + term;
end
deltasic_k_values(iii) = deltasic_value;
end

## Apply the Monte Carlo integration formula
average_deltasic_k = mean(deltasic_k_values);
res = volume_of_domain * average_deltasic_k;

endfunction
## A nested function for the mu_prime
function mu_prime_val = calculate_mu_prime(z_prime_vector, j)
z_prime_dim=length(z_prime_vector);
## z_prime_dim: The dimension of the z' vector provided.
## i: The number of variables (zeta) to integrate over.
## nukappa: The parameter of the gamma process.
## z_prime_vector: The vector of n z' variables (z'_1, ..., z'_n).
## M: The number of Monte Carlo samples.

## The integration domain for each zeta_j is [z'_n, 1].
z_prime_n = z_prime_vector(end);

## Calculate the volume of the integration domain
volume = (1 - z_prime_n) ^ j;
## Initialize a vector to store the values of the integrand
integrand_values = zeros(1, M);

## Perform M Monte Carlo samples
for index = 1 : M

## Generate ordered uniform r.v.'s in rectangle
zeta_samples = z_prime_n + (1 - z_prime_n) * rand(1, j);
zeta_samples=sort(zeta_samples,'descend');
full_t_vector = [z_prime_vector, zeta_samples];

## Check if within the simplex.
sum_is_le_1 = sum(full_t_vector) <= 1;

if sum_is_le_1
## If conditions are met, calculate the value of the density

```

```

product_term = prod(full_t_vector .^ (-1));
sum_term = sum(full_t_vector);
density_val = (nukappa) ^ (z_prime_dim + j) * product_term ...
             * (1 - sum_term) ^ (nukappa - 1);
integrand_values(index) = density_val;
else
    ## If conditions are not met, the density is 0
    integrand_values(index) = 0;
end
end

## Calculate the final integral value using the Monte Carlo formula
average_integrand = mean(integrand_values);
mu_prime_val = average_integrand * volume;
endfunction
endfunction

```

3.7 Meta distribution of the SIR

So far, we have considered the SIR distribution averaged over the fading of the typical receiver. The meta distribution of the SIR (SIR MD)—first introduced by Martin Haenggi for terrestrial networks in 2016 [54]—offers a fine-grained analysis of the SIR distribution, providing information about the fraction of time the SIR exceeds a given SIR during the (short) use period at the receivers. Publication III analyses the meta distribution of the SIR in a narrow beam LEO uplink with the Gaussian antenna pattern, providing strikingly simple analytical, including closed-form, descriptions of the SIR MD (as well as for the SIR and SINR distributions as already discussed in Section 3.6.1 and 3.6.2; see Proposition 3.6.2).

In this section, we analyze the SIR MD in a Rayleigh fading setting, which is the analytically most tractable case, but also reflect—at least in a qualitative sense—the behavior of the SIR MD in a general fading setting in terms of variation in the QoS (also called; user experience) over the transmitters for different densities (sufficiently, different $\tilde{\kappa}$). We derive the SIR MD moments and a beta distribution approximation using moment matching. As a side product, a purely mathematical result regarding the hypergeometric function is proposed. For more detailed and numerical results, including comparison to the accurate spherical model in a Nakagami- m fading setting, please refer to Publication III.

Let us define the conditional SIR distribution by

$$\mathcal{P}(\theta) \triangleq \mathbb{P}(\text{SIR} > \theta | \mathcal{G}_1) = \mathbb{P}(\text{SIR} > \theta | \Phi). \quad (3.75)$$

The SIR MD at the typical receiver is defined for $0 \leq y \leq 1$ as

$$\mathbb{E}_\Phi \mathbf{1}(\mathcal{P}(\theta) > y) = \mathbb{E}_\Phi \mathbf{1}(\mathbb{P}(\text{SIR} > \theta|\Phi) > y) = \mathbb{P}(\mathbb{P}(\text{SIR} > \theta|\Phi) > y). \quad (3.76)$$

Recall the ergodicity of Φ , which allows a meaningful interpretation of the SIR MD: The ensemble average equals the spatial average; hence, the SIR MD describes the fraction of transmitters that reach the SIR threshold θ fraction y of time at their serving LEO BSs in a uniform constellation, when the fading varies during a short use period during which the terminals are considered practically non-mobile.

Note that, should there be no fading, the SIR MD reduces to a single-step function whose value on $(0, 1)$ depends on the SIR threshold θ of a successful transmission: either the connection at a receiver is permanent, or it is permanently down during the modeled use period. The traditional SIR distribution is formally an expectation taken over the GP and the fading; $\mathbb{P}(\text{SIR} > \theta) = \mathbb{E}_{\mathcal{G}_1, h}(\mathbb{P}(\text{SIR} > \theta|\mathcal{G}_1)) = \mathbb{E}_{\mathcal{G}}(\mathbb{P}(\text{SIR} > \theta|\mathcal{G}))$ (recall that, as defined in (3.19), the density of \mathcal{G} encompasses the fading).

Define the moment $b \in \mathbb{C}$ of the SIR MD by

$$M_b(\theta) \triangleq \mathbb{E}(\mathcal{P}(\theta)^b). \quad (3.77)$$

Theorem 3.7.1 (Moments of the SIR MD). *The first two moments, $b \in \{1, 2\}$, in the narrow-beamed LEO BS network at the typical receiver, when all transmissions are experiencing Rayleigh fading, are given by*

$$M_1(\theta) = (1 + \theta)^{-\tilde{\kappa}} \quad (3.78)$$

$$M_2(\theta) = e^{-\tilde{\kappa}\theta/(1+\theta)}(1 + \theta)^{-\tilde{\kappa}}. \quad (3.79)$$

For the general complex moments, $b \in \mathbb{C}$,

$$M_b(\theta) = \exp \left\{ -\tilde{\kappa} \int_0^1 \left(1 - \frac{1}{(1 + \theta r)^b} \right) / r dr \right\} \quad (3.80)$$

$$= \exp \{ -\theta \tilde{\kappa} b {}_3F_1(1, 1, 1 + b; 2, 2; -\theta) \}, \quad (3.81)$$

where ${}_3F_1(1, 1, 1 + b; 2, 2; (\cdot))$ is the generalized hypergeometric function.

Furthermore, for $b \in \mathbb{N}$, the hypergeometric function in the exponent of (3.81) can be expressed as

$$\log M_b(\theta) = - {}_3F_1(1, 1, 1 + b; 2, 2; -\theta) = \frac{\tilde{\kappa}}{(b-1)!} \sum_{k=0}^b \begin{bmatrix} b \\ k \end{bmatrix} \text{Li}_{2-k}(-\theta), \quad (3.82)$$

where $\begin{bmatrix} b \\ k \end{bmatrix}$ is the unsigned Stirling number of the first kind, and $\text{Li}_{2-k}(\cdot)$ is the polylogarithm. The representation is valid for $\theta \in \mathbb{C} \setminus \{-1\}$.

Proof. We prove (3.78)-(3.80). Although the first two moments, $b \in \{1, 2\}$, also follow directly from (3.81) (a black-box representation of (3.80) provided by *Mathematica®*), they can be derived from (3.80) using elementary algebra and integration methods, which we will demonstrate.

We first derive (3.80). For the Rayleigh faded h with normalized power, we have for a conditioned \mathcal{G}_1

$$\begin{aligned}\mathcal{P}(\theta) &= \mathbb{P}(\text{SIR} > \theta | \mathcal{G}_1) \stackrel{(a)}{=} \mathbb{E}_h \left(\mathbb{P} \left(h_1 > \theta \sum_{x \in \mathcal{G}_1} h_{x,x} \middle| \mathcal{G}_1 \right) \right) \\ &\stackrel{(b)}{=} \mathbb{E}_h \left(e^{-\theta \sum_{x \in \mathcal{G}_1} h_{x,x}} \middle| \mathcal{G}_1 \right) \stackrel{(c)}{=} \prod_{x \in \mathcal{G}_1} \left(\frac{1}{1 + \theta x} \right).\end{aligned}\quad (3.83)$$

In (a), we utilize the equation (3.53). In (b) and (c), we use the standard CCDF and Laplace transform of the exponential r.v. h , respectively.

By taking the expectation over \mathcal{G}_1 , using the PGFL of the GP, we have, by (3.28), the following expression

$$\mathbb{E}(\mathcal{P}(\theta)^b) = \mathbb{E} \left(\prod_{x \in \mathcal{G}_1} \frac{1}{(1 + \theta x)^b} \right) = \mathfrak{G}_{\mathcal{G}_1}(f)$$

with $f(t) = (1 + \theta t)^{-b}$. This proves the result.

Next, we prove (3.78) and (3.79). For $b = 1$, the integral in (3.80) is given by

$$\begin{aligned}&= \int_0^1 \left(1 - \frac{1}{1 + \theta r} \right) / r dr \\ &= \int_0^1 \frac{\theta}{1 + \theta r} dr = \int_1^{1+\theta} \frac{1}{u} du = \log(1 + \theta).\end{aligned}$$

For $b = 2$,

$$\begin{aligned}&\int_0^1 \left(1 - \frac{1}{(1 + \theta r)^2} \right) / r dr \\ &= \int_0^1 \left(\frac{2\theta}{(1 + \theta r)^2} + \frac{\theta^2 r}{(1 + \theta r)^2} \right) dr \\ &\stackrel{(a)}{=} \int_0^1 \left(\frac{2\theta}{(1 + \theta r)^2} - \frac{\theta}{(1 + \theta r)^2} + \frac{\theta^2}{\theta + \theta^2 r} \right) dr \\ &= \int_1^{1+\theta} \frac{1}{u^2} du + v \int_\theta^{\theta+1} \frac{1}{v} dv = \frac{\theta}{1 + \theta} + \log(1 + \theta).\end{aligned}$$

In (a), we used the partial fraction expansion for the latter term in the integrand.

Finally, we provide a proof for (3.82). Using the definition of the hypergeometric series, for $|\theta| < 1$ and $b \in \mathbb{N}$,

$$\begin{aligned}_3F_2(1, 1, 1+b; 2, 2; -\theta) &= \sum_{n=0}^{\infty} \frac{(1)_n (1)_n (1+b)_n}{(2)_n (2)_n} \frac{(-\theta)^n}{n!} \\ &= \sum_{n=0}^{\infty} \frac{(1+b)_n}{(n+1)^2 n!} (-\theta)^n = \frac{1}{b!} \sum_{n=0}^{\infty} \frac{(n+1)_b}{(n+1)^2} (-\theta)^n\end{aligned}$$

$$\begin{aligned}
&\stackrel{(a)}{=} \frac{1}{b!} \sum_{n=0}^{\infty} \frac{\sum_{k=0}^b \binom{b}{k} (n+1)^k}{(n+1)^2} (-\theta)^n \\
&= \frac{1}{b!} \sum_{k=0}^b \binom{b}{k} \sum_{n=0}^{\infty} \frac{(-\theta)^n}{(n+1)^{2-k}} \stackrel{(b)}{=} -\frac{1}{b!} \sum_{k=0}^b \binom{b}{k} \frac{\text{Li}_{2-k}(-\theta)}{\theta}.
\end{aligned} \tag{3.84}$$

In (a), we used the expansion of the rising Pochhammer factorial; in (b), we used the definition of the polylogarithm. The expression generalizes onto the region $\mathbb{C} \setminus \{-1\} \ni \theta$ through the *analytic continuation* of the polylogarithm.

□

Remark. To the best of our knowledge, the interesting representation of the generalized hypergeometric function (3.84) in terms of the polylogarithm has not yet been introduced in the literature other than in the special case $b = 0$ in the draft [55]—for which the steps in (3.84) provide an alternative proof. Furthermore, as a mathematical curiosity, the polylogarithm has closed-form representations also for $k \geq 3$ (see [56, Eq. (6.3)]), allowing a closed-form expression for the generalized hypergeometric function ${}_3F_2(1, 1, 1+b; 2, 2; (\cdot))$ for $b \in \mathbb{N}$ (although impractically complicated in the scope of this thesis).

The following second-order moment approximation is sufficient in the Rayleigh fading model.

Proposition 3.7.2 (Approximation of the SIR MD with the beta distribution). *The parameters α and β for the beta distribution are given by the method of moments as*

$$\begin{aligned}
\alpha &= \left(\frac{M_1(\theta)(1-M_1(\theta))}{M_2(\theta)-M_1(\theta)^2} - 1 \right) M_1(\theta) \\
\beta &= \left(\frac{M_1(\theta)(1-M_1(\theta))}{M_2(\theta)-M_1(\theta)^2} - 1 \right) (1-M_1(\theta)),
\end{aligned} \tag{3.85}$$

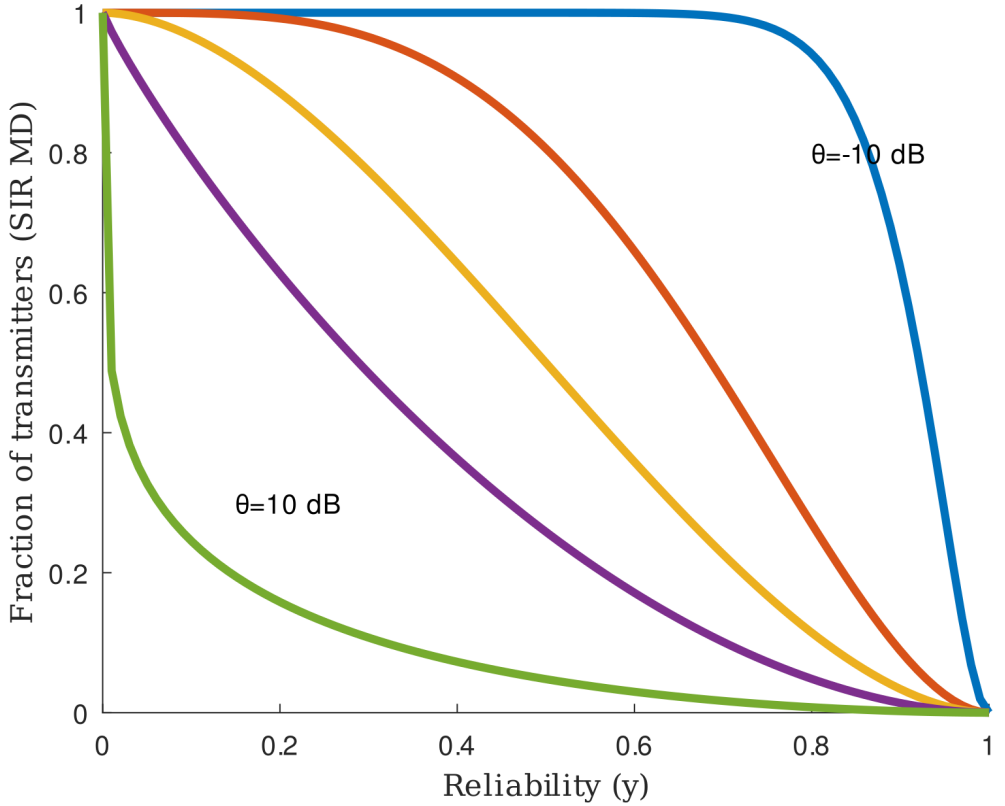
where $M_1(\theta)$ and $M_2(\theta)$ are given in (3.78) and (3.79), respectively. The SIR MD can be approximated by the beta distribution

$$\mathbb{P}(\mathcal{P}(\theta) > y) \approx \begin{cases} 1 - I_y(\alpha, \beta), & y \in [0, 1], \\ 1, & y < 0, \\ 0, & y > 1, \end{cases} \tag{3.86}$$

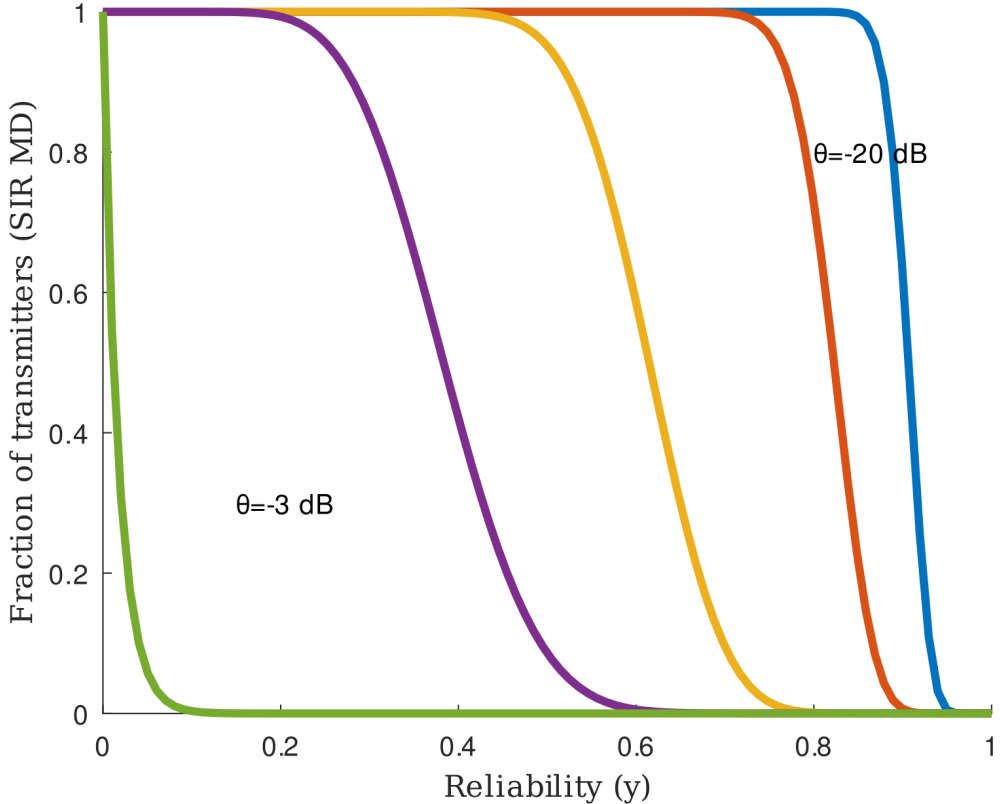
where $I_{(\cdot)}(\alpha, \beta)$ is the regularized incomplete beta function.

Figures 3.11a-3.11b show the beta distribution approximation of the SIR MD for various θ and $\tilde{\kappa}$. The plots reveal that the experience of the link quality is strongly dependent on the average number of transmitters inside the -3 dB footprint. On the other hand, the link quality degrades for high

densities, implying a significant trade-off between the user fairness and the average performance. For denser networks, interference mitigation should be implemented to achieve the same rates as in less dense networks: This can, for example, entail successive interference cancellation. For more results, such as the SIR MD in general Nakagami fading, and comparison to simulations of the spherical model, please refer to [Publication III](#).



(a) $\kappa = \tilde{\kappa} \log(2) = \log(2)$ transmitters inside the -3 dB footprint on average.



(b) $\kappa = 10 \log(2)$. The variation in the link reliability is visibly smaller than in Figure 3.11a.

Figure 3.11. Figs 3.11a and 3.11b show the SIR MD beta distribution approximations for the SIR thresholds (from top to bottom) $\theta \in \{-10, -3, 0, 3, 10\}$ dB and $\theta \in \{-20, -17, -13, -10, -3\}$ dB, respectively.

3.8 Throughput and optimal constellation density

We can use Shannon's formula to characterize the expected *channel capacity*, instantaneous *bandwidth-normalized throughput*, or the *spectral efficiency*, defined by the formula $\mathcal{T} \triangleq \log(1 + \text{SINR})$ [49, Eq. (7.19)]. While a decoder designed for AWGN can be used in a receiver, incorporating additional knowledge of the interference waveform statistics can improve the encoding and decoding, leading to enhanced performance. By using the Lomax distribution for the SIR distribution, one can evaluate the average throughput in the interference-limited channel by

$$\mathcal{T} = \frac{1}{\log(2)} \int_0^\infty \mathbb{P}(\text{SIR}^{\text{NT}} > e^t - 1) dt = \int_0^\infty \frac{(1+v)^{-\tilde{\kappa}-1}}{\log(2)} dv = 1/\kappa, \quad (3.87)$$

where, recall, $\kappa = \log(2)\tilde{\kappa}$ is the average number of transmitters inside the -3 dB footprints.

With noise, similar to (3.87), the average throughput is given by

$$\mathcal{T} = \frac{1}{\log(2)} \int_0^\infty (1+v)^{-\tilde{\kappa}-1} E_{\tilde{\kappa}+1}(\text{NSR}_0 v) \tilde{\kappa} dv. \quad (3.88)$$

Furthermore, (3.87) and (3.88) closely approximate the throughput for general Nakagami fading (and we put forward that this is the case under fairly general conditions in an even larger category of fading distributions).

A widely recognized property of the LEO networks in their stochastic geometry study is that there is an optimal density of transmitters (and satellite constellation) that maximizes the performance (see, *e.g.*, [38] and [42]). This property is reflected in Figure 3.12. In the narrow-beam LEO, the optimal density corresponds to $\log(2)\sqrt{\text{NSR}_0}$ transmitters on average in the -3 dB footprints, where NSR_0 is the noise-to-signal ratio of a transmitter at the typical LEO BS boresight. If each transmitter is associated with one LEO BS, this determines the optimal constellation density directly.

Remark. If we consider that only one Earth transmitter, let us refer to it as user equipment (UE), is located within its serving LEO BS Voronoi cell, the average number of UEs inside the -3 dB footprints $\kappa = \log(2)$ (independently of the elevation angle and altitude) provides the optimal density of co-channel UEs that maximizes the average throughput and directly determines the optimal satellite constellation density within this scenario. For example, with the normalized noise $W = (\hat{d}_{\epsilon,h}/d_0)^{-\gamma}$ (recall that $\hat{d}_{h,\epsilon} = h/\sin(\epsilon)$ is the distance between $o \triangleq (0,0) \in \mathbb{R}^2$ and the LEO BS, d_0 is a normalizing distance, and γ is the path loss exponent—thus the noise w.r.t. to the average signal strength of a UE at o is 0 dB) and given ϵ , the optimal $\kappa = \log(2)$ determines the optimal λ and, further, the optimal density for the satellite constellation, depending on the altitude of the orbits. For

example, for $\epsilon = 90^\circ$, $h = 200$ km and $\varphi_{\text{RX}} = 1.6^\circ = 0.0279$ rad, the optimal λ is given by $\lambda = \log(2)/(\pi h^2 \varphi_{\text{RX}}^2) \approx 7 \cdot 10^{-3}/\text{km}^2$ —this corresponds to $7 \cdot 10^{-3} \cdot 4\pi R_\oplus^2 \approx 3.6 \times 10^6$ UEs on the Earth surface and a similar number of satellites in the constellation—which is literally a mega constellation. However, because the UEs are not likely to be homogeneously distributed on the Earth, the system model presented should not be interpreted globally, but rather to give a local optimal density of the co-channel transmitters and satellites.

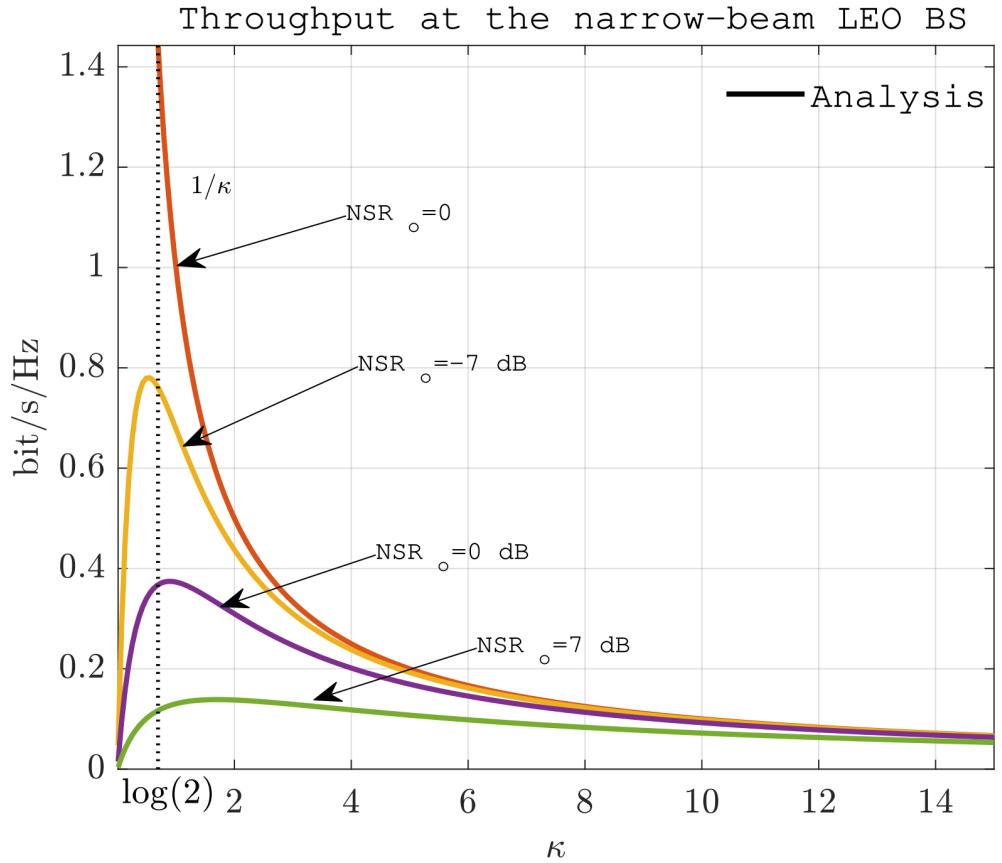


Figure 3.12. The bandwidth-normalized throughput at the LEO BS with various noise magnitudes $\text{NSR}_o \in \{5, 1, 1/5, 0\} = \{7, 0, -7, -\infty\}$ dB and $\kappa \in (0, 15)$. In the presence of noise, $\kappa \approx \log(2)$ maximizes the throughput.

4. Temporal analysis of the narrow-beam LEO

A spatio-temporal analysis of the interference and SIR with an ALOHA MAC can be found in [Publication V](#). In the following, we develop the temporal interference analysis further in a Rician block fading channel.

Recall Section 2.7, where fading and antenna attenuation temporal characteristics were formulated and simulated in a spherical model. In this section, we give a mathematical characterization of these qualities and quantities based on the planar model. It turns out that the autocorrelation of the pure LoS channel has a simple Gaussian and exponential form for the total interference from the entire ensemble of the interferers and for the interference outside the -3 dB footprint, respectively. We refer to these as *intercell plus intracell total interference* and *intercell total interference*, respectively. Furthermore, we include the block fading multipath effect as a triangular AEA autocorrelation and hence a PSD of the form $\text{sinc}(\cdot)^2$. In this section, we characterize a general channel model for the intracell plus intercell and intracell total interferences. A channel model for the nearest signal is also proposed in this section. Since the satellites have definite orbital speeds, the channel properties exhaustively depend on the altitude and the carrier frequency. In this sense, the temporal interference model and nearest transmitter channel responses are well-defined.

The total interference exhibits considerable power variation as the satellite advances and the interferers move inside the footprint. This attenuation component is noncorrelated to the fading spread component, and thus, at least theoretically, separable in the frequency spectrum to improve the SIR. Especially for high carrier frequencies, by merely observing the frequency-spectrum plot, we can perform an interference cancellation by suppressing the slow attenuation frequency components from the total interference, while preserving the shape of the spectrum of the nearest transmitter, *i.e.*, the desired signal (or multiple signals as would be the case if there are handovers).

The studied signal is a baseband signal ideally downconverted from the carrier. The theoretical model relies heavily on Theorem 3.3.6. Furthermore, Theorem 3.4.4 guarantees that the interference waveform is a stationary

Gaussian process. The temporal properties of this Gaussian process, which is stationary by definition, are determined by the autocorrelation functions proposed in this section.¹

The simulation codes based on the planar model are at the end of the section. The planar model is highly accurate for narrow-beamed LEO BS, such as $\varphi_{\text{RX}} = 1.6^\circ$ (see [Publication III](#)).

The spread of frequencies in the channel depends on the bandwidth and can be divided into three qualitative categories of signal attenuation, depending on the carrier frequency.

1. High carrier frequency: The multipath fading amplitude correlation time is shorter *vis-à-vis* the antenna attenuation time: $\tau_c < \tau_a$.
2. Mediocre carrier frequency. The multipath fading amplitude correlation time is similar *vis-à-vis* the antenna attenuation time: $\tau_c \approx \tau_a$.
3. Small carrier frequency. The multipath fading amplitude correlation time is longer *vis-à-vis* the antenna attenuation time: $\tau_c > \tau_a$.

The scenarios (1) and (3) are presented in Figures [4.3b](#) and [4.3a](#), respectively. Recall the definition of the AWN total interference ([3.31](#))

$$I = I(t) = \sum_{x \in \mathcal{G}_1(t)} y_x(t) h_x(t) x, \quad (4.1)$$

where, for this section, $y = y(t)$ is the typical i.i.d. ergodic WN signal, $g = g(t)$ is the typical i.i.d. fast fading variable, and $\{x\}_{x \in \mathcal{G}}$ are *amplitude* gains.

Definition 4.0.1 (Average envelope amplitude (AEA)). We will refer to the average envelope amplitude (AEA), which reflects the moving average (MA) over a use-period epoch of the received interference waveform envelope, defined by

$$I_{\text{AEA}}(t) \triangleq \frac{1}{\sqrt{1 + 4\tilde{\kappa}\mathbb{E}(h)^2}} \sum_{x \in \mathcal{G}_1(t)} h_x(t) x, \quad (4.2)$$

where $1/\sqrt{1 + 4\tilde{\kappa}\mathbb{E}(h)^2}$ is a scaling constant, which derives from Theorem [3.3.6](#), conditioning that the aggregate power $\sum(h_x x)^2 = \tilde{\kappa}$ equals the AEA power $\mathbb{E}(I_{\text{AEA}}^2) = \text{var}(I_{\text{AEA}}) + \mathbb{E}(I_{\text{AEA}})^2 = \tilde{\kappa}$, as it should be. Furthermore, we denote by

$$I_{\text{AEA}_1} \text{ and } I_{\text{AEA}_2}$$

the total interference from the entire ensemble of transmitters (essentially, the main lobe footprint) and the total interference outside the -3

¹As throughout the thesis, the total interference can stem from any signals, not just network terminals. For example, the interference may be from natural sources (for which the Poisson location modeling is highly feasible, since the natural phenomena are often mutually non-correlated). Furthermore, the analysis applies straightforwardly to multiple tiers of interferers.

dB footprint, respectively. Assuming the cell size of the -3 dB footprint, $I_{\text{AEA}_1} - I_{\text{AEA}_2}$ and I_{AEA_2} are the intracell and intercell total interference, respectively.

The magnitude of the AEA depends on the presence of transmitting terminals and their signal characteristics, the relative terminal locations with respect to the antenna beam, and signal attenuation, including fading and phase shifts. The AEA is multiplicative, since it represents the varying signal envelope synthesized from the AWN total interference by a moving average. It can be multiplied by an AWN signal in the time domain and convoluted in the frequency domain with the AWN signal PSD to characterize the random signal response in the narrow-beam LEO fading channel. In this section, we utilize a Rice- K fast-fading model.

AEA_1 does not consider any prior interference cancellation. On the contrary, the AEA_2 models the scenarios where intracell interference is mitigated, *e.g.*, using frequency allocation for the transmitters in the served beam [31]. In this section, we will study interference PSD in the two cases, and also present an interference cancellation technique that applies to both scenarios. We propose a scheme in which a partial interference cancellation of the main lobe interference can be feasible at the signal processing stage without any prior mitigation, based on the distinguishable frequency content.

4.1 Correlation functions of the total interference

We follow the standard definitions of the *autocorrelation* and the *autocovariance* functions. For a stationary and ergodic signal $y(t)$, they are defined for the time lag $\tau \in \mathbb{R}$ as

$$C_y(\tau) \triangleq \mathbb{E}(y(t)y(t + \tau)), \quad (4.3)$$

$$K_y(\tau) \triangleq \mathbb{E}(y(t)y(t + \tau)) - \mathbb{E}(y)^2, \quad (4.4)$$

respectively. By definition, $C_y(0) = \mathbb{E}(y^2)$ and $K_y(0) = \text{var}(y)$.

Proposition 4.1.1. (*Autocovariance of the AEA*) Let $h = h(t)$ be a power-normalized amplitude block fading gain; also, assume normalized transmission powers. The autocovariance function of the total interference from the main lobe footprint (technically, infinitely far in the planar model), *i.e.*, the **intercell plus intracell** total interference, is a Gaussian function $K_{\text{AEA}_1\text{-LoS}}(\tau)$ (the antenna attenuation component ²) combined with the

²We use the abbreviation “LoS” here; however, the Gaussian antenna attenuation component is also present in the Rayleigh fading channel. Without fading, this component is the only present.

triangular function $K_{\text{AEA}_1\text{-MP}}(\tau)$ (the multipath fading component):

$$\begin{aligned} K_{\text{AEA}_1}(\tau) &\triangleq K_{\text{AEA}_1\text{-LoS}}(\tau) + K_{\text{AEA}_1\text{-MP}}(\tau) \\ &= \frac{\tilde{\kappa}}{1 + 4\tilde{\kappa}\mathbb{E}(h)^2} ((1 - \text{var}(h)) \exp\{-D_{h,\epsilon,\varphi_{\text{RX}}}(v_{\text{sat}}\tau)^2/4\} + \text{var}(h)\text{triang}(\tau/\tau_c)), \end{aligned} \quad (4.5)$$

where v_{sat} is the orbital speed of the satellite, $D_{h,\epsilon,\varphi_{\text{RX}}} \triangleq \sin^4(\epsilon)/(h^2\varphi_{\text{RX}}^2)$.

The total interference outside the -3 dB footprint, i.e., the **intercell** interference, is given by the exponential antenna attenuation component combined with the triangular multipath component

$$\begin{aligned} K_{\text{AEA}_2}(\tau) &\triangleq K_{\text{AEA}_2\text{-LoS}}(\tau) + K_{\text{AEA}_2\text{-MP}}(\tau) \\ &= \frac{\tilde{\kappa}}{2(1 + 4\tilde{\kappa}\mathbb{E}(h)^2)} ((1 - \text{var}(h)) \exp\{-D_{h,\epsilon,\varphi_{\text{RX}}}v_{\text{sat}}\tau h/50\} + \text{var}(h)\text{triang}(\tau/\tau_c)). \end{aligned} \quad (4.6)$$

Proof. The correlation function consists of the left-hand-side antenna attenuation component and the right-hand-side fading attenuation component. The correlation functions can be estimated with the proposed formulas to a practical accuracy. A theoretical derivation of the intercell plus intracell autocovariance function for the interference power can be found in [Publication V](#), and the theoretical amplitude correlation follows similarly. However, the proposed AEA correlation functions in this section are experimental for both the intercell plus intracell and intercell interference, and are verified in Figure 4.1. In the figure, a Rice-1 block fading channel is modeled with envelope amplitude correlation times $f_c \in \{0.2, 0.1\}$ s (which are the halfwidths of the little triangles around 0). The GP parameter $\tilde{\kappa} = 2$ in both cases. The correlation function of AEA_1 reflects the attenuation rate of the Gaussian antenna, and is experimentally verified by the Monte Carlo simulations. For the AEA_2 , the spectrum is more spread, which leads to the exponential form of the covariance function.

Let us denote $c_{\tilde{\kappa}} \triangleq \tilde{\kappa}/(1 + 4\mathbb{E}(h)^2\tilde{\kappa})$ for the proof. Because the two sum components are well-defined and converge independently, we can use the following decomposition into the two *uncorrelated* (although not independent) components:

$$I_{\text{AEA}}(t) = \sum_{x \in \mathcal{G}_1(t)} h_x(t)x = \underbrace{\sum_{x \in \mathcal{G}_1(t)} x(h_x(t) - \mathbb{E}(h))}_{\triangleq I_{\text{AEA-MP}}(t)} + \underbrace{\mathbb{E}(h) \sum_{x \in \mathcal{G}_1(t)} x}_{\triangleq I_{\text{AEA-LoS}}(t)}. \quad (4.7)$$

According to (3.32) and (3.33), the process $I_{\text{AEA-MP}}$ has a zero mean with the variance $K_{\text{AEA-MP}}(0) = \text{var}(I_{\text{AEA-MP}}) = \tilde{\kappa}\mathbb{E}((h_x - \mathbb{E}(h_x))^2)/(1 + 4\mathbb{E}(g)^2\tilde{\kappa}) = c_{\tilde{\kappa}}\text{var}(h_x)$ (we work with the amplitude, hence, we multiply the expression by the factor of two). Furthermore, in the block fading model, the correlation function of $I_{\text{AEA-MP}}$ is a triangle function determined by coherence length.

We have, $K_{\text{AEA-MP}}(\tau) = c_{\tilde{\kappa}} \text{var}(h_x) \text{triang}(\tau/\tau_c)$. Using the same formulas, (3.32) and (3.33), for the antenna attenuation component, $\text{var}(I_{\text{AEA-LoS}}) = \mathbb{E}(h)^2 c_{\tilde{\kappa}} = (1 - \text{var}(h)) c_{\tilde{\kappa}}$ by assuming the normalized-power $\mathbb{E}(h^2) = 1$. The result follows from the additivity: $K_{\text{AEA}}(\tau) = K_{\text{AEA-MP}}(\tau) + K_{\text{AEA-LoS}}(\tau)$.

Note that, regarding AEA₂, in the light of (3.25), the interference power outside the -3 dB footprint is equivalent to scaling the transmission fading gain h^2 by $1/2$. Namely, such deterministic power fading is a degenerate distribution with an atomic probability measure on $\{1/2\}$, and the corresponding step function CCDF. Should we incorporate the fading gain into the density of the GP, this results exactly in the points lying in $(0, 1/2)$. This results in the variance $\text{var}(I_{\text{AEA}_2}) = c_{\tilde{\kappa}} \mathbb{E}(h^2/2) = c_{\tilde{\kappa}}/2$.

□

We have been exploring autocovariance functions instead of autocorrelation functions. Next, we characterize the autocorrelation functions.

Corollary 4.1.2 (Autocorrelation function of the AEA and the AWN total interference). *Given a signal $y = y(t)$ with the autocorrelation function $C_y(\cdot)$, the autocorrelation function of the signal multiplied by the AEA in the intercell plus intracell interference-limited channel is*

$$\begin{aligned} C_{\text{AEA}_1}(\tau)C_y(\tau) &= (K_{\text{AEA}_1}(\tau) + \mathbb{E}(I_{\text{AEA}_1})^2)C_y(\tau) \\ &= \left(K_{\text{AEA}_1}(\tau) + \frac{(2\tilde{\kappa}\mathbb{E}(h))^2}{1 + 4\mathbb{E}(h)^2\tilde{\kappa}} \right) C_y(\tau). \end{aligned} \quad (4.8)$$

Proof. $\mathbb{E}(I_{\text{AEA}_1})^2$ is given straightforwardly by Theorem 3.3.6. □

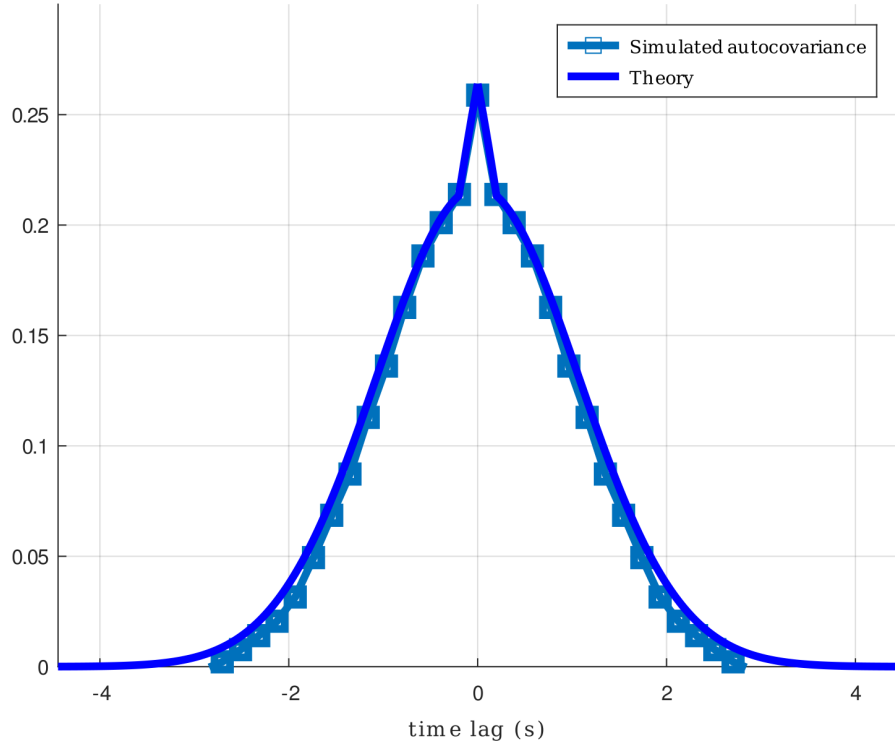
For the intercell interference-limited channel, $\mathbb{E}(I_{\text{AEA}_2})^2 = \mathbb{E}(I_{\text{AEA}_1})^2/2$.

Through the autocorrelation (4.8), we can characterize the total interference, given a waveform y , which essentially corresponds to the interference waveform stripped from the antenna and fading attenuation components (in a sense, it is an interference waveform before passing through the channel). Recall that by Theorem 3.4.4, the AWN total interference is a Gaussian process. It is determined by the second-order statistics and the autocorrelation of the AEA, multiplied by the autocorrelation of a (bandwidth-limited) WN signal (the sinc function).

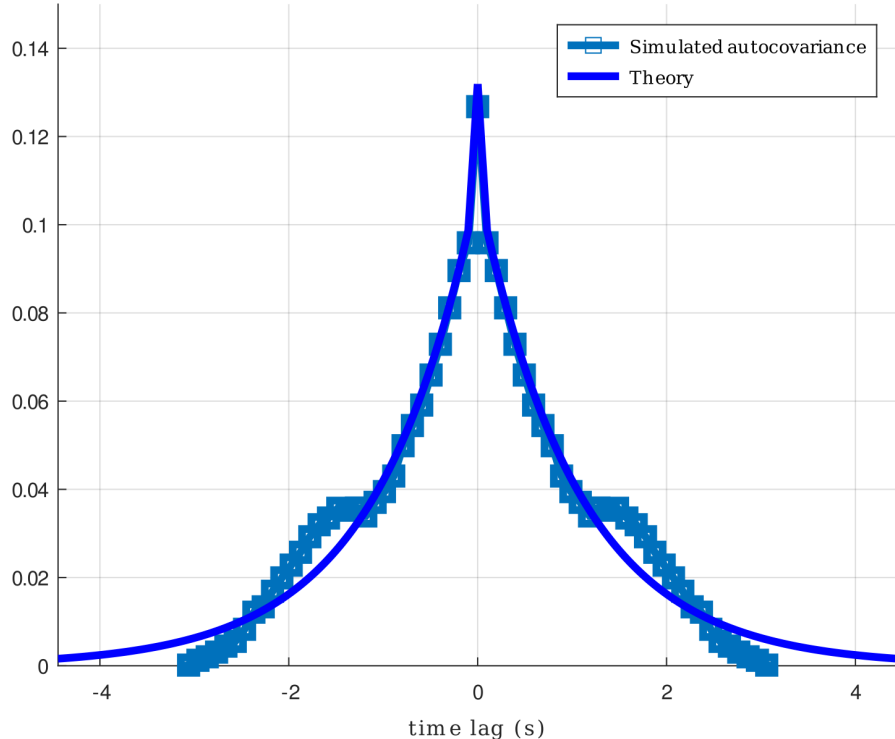
Example 4.1.1 (AWN total interference as a Gaussian process). For the bandwidth B , using Theorem 3.4.4 and the autocovariance (4.5), the main lobe AWN total interference is a stationary Gaussian process with the autocorrelation function

$$\begin{aligned} C_I(\tau) &= \frac{\tilde{\kappa}}{1 + 4\mathbb{E}(h)^2\tilde{\kappa}} \left((1 - \text{var}(h)) \exp\{-D_{h,\epsilon,\varphi_{\text{RX}}}(v_{\text{sat}}\tau)^2/4\} \right. \\ &\quad \left. + \text{var}(h) \text{triang}(\tau/\tau_c) + 4\mathbb{E}(h)^2\tilde{\kappa} \right) \text{sinc}(B\tau). \end{aligned} \quad (4.9)$$

Figures 4.2a and 4.2b show the AEA amplitude and the AWN total interference waveform from interfering signals of bandwidth $B = 30$ Hz (meaning, thirty samples per second). Figure 4.2b is a stationary Gaussian process with the autocorrelation function (4.9). The AWN total interference waveform is modulated from the received samples into the analog baseband waveform. There are, on average, $\log(2)\tilde{\kappa} = \log(2)$ interferers inside the -3 dB footprint (the intracell).

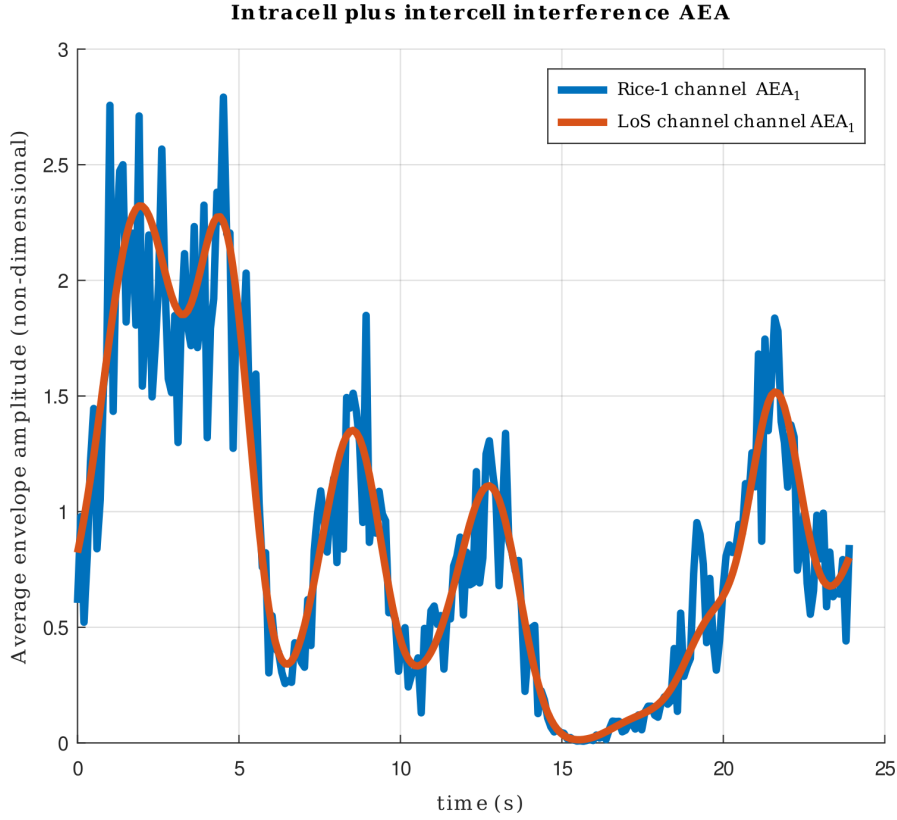
Autocovariance of the intercell plus intracell interference AEA₁

- (a) The Gaussian-form estimate of the autocovariance function. Fading envelope amplitude correlation time $\tau_c = 0.2$ in Rice-1 channel, corresponding to the carrier frequency $f_c \approx 1$ GHz.

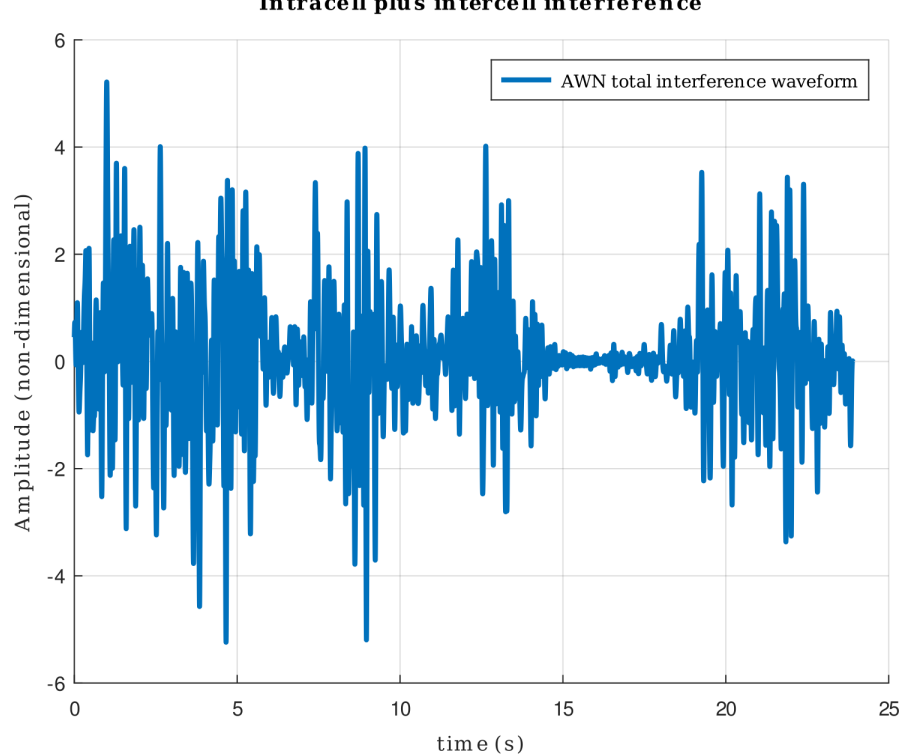
Autocovariance of the intercell interference AEA₂

- (b) The exponential-form estimate of the autocovariance function. Fading envelope amplitude correlation time $\tau_c = 0.1$ in Rice-1 channel, corresponding to the carrier frequency $f_c \approx 2.5$ GHz.

Figure 4.1. The AEA autocovariance functions.



(a) The average envelope amplitude in the Rice-1 channel. The fading coherence time $\tau_c = 0.1$ corresponds to the carrier frequency $f_c \approx 2.5$ GHz.



(b) A baseband AWN total interference waveform in the Rice-1 channel. Interfering signals are Gaussian with a bandwidth $B = 30$ Hz.

Figure 4.2. The intracell plus intercell total interference AEA and a corresponding AWN waveform, which is a Gaussian process. The GP parameter $\tilde{\kappa} = 1$.

4.2 Power spectral density

The frequency response of an interference bandwidth is characterized through the PSD. According to **Wiener-Khinching theorem**, the PSD of a signal is the Fourier transform of its autocorrelation function. It is given as the Fourier transform $\mathcal{F}_{C_{\text{AEA}}}(\cdot)$ of the autocorrelation function of the AEA. The channel response of the typical interfering signal y can be derived accordingly to (4.8) by convolving in the frequency domain with the Fourier transform of $C_y(\cdot)$.

Corollary 4.2.1 (PSD of the AEA). *The PSD of the **intracell plus intercell** AWN total interference is controlled by the Fourier transform of the autocorrelation function derived from the autocovariance (4.5), and it is given for $f \in \mathbb{R}$ by*

$$\begin{aligned} S_{\text{AEA}_1}(f) &\triangleq \mathcal{F}_{C_{\text{AEA}_1}}(f) \triangleq \int_{-\infty}^{\infty} C_{\text{AEA}_1}(t) e^{-i2\pi ft} dt \\ &= \underbrace{\frac{\tilde{\kappa}}{1 + 4\mathbb{E}(h)^2\tilde{\kappa}} \frac{2\sqrt{\pi}(1 - \text{var}(h)) \exp\{-4f^2\pi^2/(\mathsf{D}_{h,\epsilon,\varphi_{\text{RX}}}v_{\text{sat}}^2)\}}{\sqrt{\mathsf{D}_{h,\epsilon,\varphi_{\text{RX}}}v_{\text{sat}}^2}}}_{\mathcal{F}_{K_{\text{AEA}_1\text{-LoS}}}(f)} \\ &\quad + \underbrace{\frac{\tilde{\kappa}}{1 + 4\mathbb{E}(h)^2\tilde{\kappa}} \left(\text{var}(h)\tau_c \text{sinc}^2(f\tau_c) + 4\tilde{\kappa}\mathbb{E}(h)^2\delta(f) \right)}_{\mathcal{F}_{K_{\text{AEA}_1\text{-MP}}}(f)}, \end{aligned} \quad (4.10)$$

where $\delta(\cdot)$ is the Dirac Delta function. Similarly, for the **intercell** total interference, we have

$$\begin{aligned} S_{\text{AEA}_2}(f) &\triangleq \mathcal{F}_{C_{\text{AEA}_2}}(f) \\ &= \underbrace{\frac{\tilde{\kappa}}{2(1 + 4\mathbb{E}(h)^2\tilde{\kappa})} \frac{\mathsf{D}_{h,\epsilon,\varphi_{\text{RX}}}(1 - \text{var}(h))hv_{\text{sat}}}{(100\pi^2f^2 + \mathsf{D}_{h,\epsilon,\varphi_{\text{RX}}}^2h^2v_{\text{sat}}^2/100)}}_{\mathcal{F}_{K_{\text{AEA}_2\text{-LoS}}}(f)} \\ &\quad + \underbrace{\frac{\tilde{\kappa}}{2(1 + 4\mathbb{E}(h)^2\tilde{\kappa})} \left(\text{var}(h)\tau_c \text{sinc}^2(f\tau_c) + 4\tilde{\kappa}\mathbb{E}(h)^2\delta(f) \right)}_{\mathcal{F}_{K_{\text{AEA}_2\text{-MP}}}(f)}. \end{aligned} \quad (4.11)$$

Proposition 4.2.2 (Autocorrelation and PSD of the nearest transmitter). *The variance in the nearest transmitter signal strength x_1 is negligible, as can be deduced from the CCDF of the GP void probability (3.36)); $\text{var}(x_1) = \mathbb{E}(x_1^2) - \mathbb{E}(x_1)^2 = \tilde{\kappa}/(\tilde{\kappa} + 1) - (2\tilde{\kappa}/(2\tilde{\kappa} + 1))^2 < 10^{-1}$ for all $\tilde{\kappa} > 0$. Hence, for simplicity, we neglect the antenna attenuation fluctuation and model the signal strength of the nearest transmitter gain in the LoS channel with a constant autocorrelation function. This approximation is feasible for large $\tilde{\kappa}$; say, $\tilde{\kappa} \geq 2$ (when the nearest transmitter is likely to be reasonably close*

to the boresight). The multipath component of the AEA of the nearest transmitter is a triangular function corresponding to the block fading. The combined autocorrelation is

$$C_{x_1}(\tau) \triangleq \underbrace{\left(\frac{\tilde{\kappa}}{1 + \tilde{\kappa}} - \text{var}(g) \right)}_{\approx \mathbb{E}(x_1 g)^2} + \underbrace{\text{var}(g)}_{\approx \text{var}(x_1 g)} \text{triang}(\tau/\tau_c), \quad (4.12)$$

where the expected power

$$C_{x_1}(0) = \mathbb{E}(x_1^2 g^2) = \mathbb{E}(x_1^2) = \int_0^1 (1 - x^{\tilde{\kappa}}) dx = \tilde{\kappa}/(1 + \tilde{\kappa})$$

is the expected power of the nearest transmitter derived from (3.36). The PSD of the nearest transmitter signals is

$$S_{x_1}(f) \triangleq \mathcal{F}_{C_{x_1}}(f) = \left(\frac{\tilde{\kappa}}{1 + \tilde{\kappa}} - \text{var}(g) \right) \delta(f) + \text{var}(g) \tau_c \text{sinc}^2(f \tau_c). \quad (4.13)$$

The antenna attenuation fluctuation component of the total interference and the spectral spread due to fading can be exploited to mitigate the interference and improve the SIR. We demonstrate this for the nearest transmitter signals. Indeed, in plural, signals: depending on the length of the observation period, the nearest transmitter can change (we do not further address the handover implementation) as the typical LEO BS moves. The typical LEO BS receives the total interference within which the nearest transmitter signals are embedded, whether consisting of single or multiple transmissions. The goal of this section is to recognize and mitigate the frequency components from the total interference that *definitely do not belong to the nearest transmitter signals*. Finally, we study the interference cancellation effect on the average SIR.

4.3 Interference cancellation: Filtering the reducible frequencies

4.3.1 Exploiting the multipath fast-fading: Average SIR in the spread spectrum

In this section, we study how highpass filtering the non-spread frequencies (in the baseband) affects the SIR.

For the sake of analytical rigor, let us consider that the “nearest” transmitter belongs to a distinct (independent) GP \mathcal{G}_{NT} (whose average distance from the origin is controlled by $\tilde{\kappa}$), whereas the interferers belong to \mathcal{G} . Define the *total received signal* as the sum of the nearest transmitter signal and the total interference (“total interference” from the tier \mathcal{G}):

$$Z(t) = I(t) + y_{NT}(t)g_{x_1}(t)x_1(t), \quad (4.14)$$

where $y_{NT}(\cdot)$ is a WN signal. Define the average-signal-to-average-interference ratio as

$$\text{ASIR} \triangleq \frac{\mathbb{E}((y_{NT}g_{x_1}x_1)^2)}{\mathbb{E}(Z^2) - \mathbb{E}((y_{NT}g_{x_1}x_1)^2)} = \frac{\mathbb{E}(x_1^2)}{\mathbb{E}(I^2)}. \quad (4.15)$$

The ASIR without any interference cancellation in the intracell plus intercell and intercell interference-limited channels are

$$\text{ASIR}_1 \triangleq \frac{C_{x_1}(0)}{C_{I_{\text{AEA}_1}}(0)} = \frac{\tilde{\kappa}/(\tilde{\kappa} + 1)}{\tilde{\kappa}} = \frac{1}{1 + \tilde{\kappa}}, \quad (4.16)$$

$$\text{ASIR}_2 \triangleq 2\text{ASIR}_1 = \frac{2}{1 + \tilde{\kappa}}, \quad (4.17)$$

respectively.

Recall Proposition 4.1.1. Since the power in the non-spread frequencies (*i.e.*, non-zero frequencies of the AEA) is given by the autocovariance functions, the ASIRs in the spread spectrum are

$$\begin{aligned} \text{CASIR}_1^{\text{SS}} &\triangleq \frac{K_{x_1}(0)}{K_{\text{AEA}_1}(0)} = \frac{\text{var}(g)}{\tilde{\kappa}/(1 + 4\tilde{\kappa}\mathbb{E}(g)^2)}, \\ \text{CASIR}_2^{\text{SS}} &\triangleq \frac{K_{x_1}(0)}{K_{\text{AEA}_2}(0)} = \frac{\text{var}(g)}{\tilde{\kappa}/(2(1 + 4\tilde{\kappa}\mathbb{E}(g)^2))}, \end{aligned} \quad (4.18)$$

respectively. One can take the limit $\tilde{\kappa} \rightarrow \infty$ and see that

$$\begin{aligned} \text{CASIR}_1^{\text{SS}} &\geq 4\mathbb{E}(g)^2\text{var}(g), \\ \text{CASIR}_2^{\text{SS}} &\geq 8\mathbb{E}(g)^2\text{var}(g). \end{aligned} \quad (4.19)$$

For Rayleigh fading ($\text{var}(g) = 1 - \pi/4$, $\mathbb{E}(g) = \sqrt{\pi}/2$),

$$\begin{aligned} \text{CASIR}_1^{\text{SS}} &\geq (1 - \pi/4)\pi \approx 0.67 \approx -1.7 \text{ dB}, \\ \text{CASIR}_2^{\text{SS}} &\geq 2(1 - \pi/4)\pi \approx 1.35 \approx 1.3 \text{ dB}. \end{aligned} \quad (4.20)$$

for all $\tilde{\kappa}$: In the multipath fast-fading channel, in the spread spectrum, the density of interferers can grow arbitrarily; however, the expected SIR has a strictly positive lower bound (meaning that the spread signal energy has a finite upper bound). Especially in the intercell interference-limited channel, the SIR is considerably good. The theoretical efficiency of this method depends on the severity of the fading: In a severely faded served transmitter channel state, significant improvement in the SIR can be achieved as long as the encoding and decoding are capable of conveying information in the spread frequencies.

4.3.2 Filtering the spread frequencies

In this section, we study how lowpass filtering the spread frequencies affects the SIR. We study the AEA of the total received signal

$$Z_{\text{AEA}_1}(t) \triangleq (I_{\text{AEA}_1} + g_{x_1}x_1)(t)A, \quad (4.21)$$

where the amplitude gain x_1 and I_{AEA} are independent (the nearest transmitter belongs to a separate PPP). The scaling constant

$$A = A(\tilde{\kappa}, g) \triangleq \sqrt{\frac{\mathbb{E}(I_{\text{AEA}}^2) + \mathbb{E}(x_1^2)}{\mathbb{E}(I_{\text{AEA}}^2) + \mathbb{E}(x_1^2) + 2\mathbb{E}(I_{\text{AEA}})\mathbb{E}(gx_1)}} \quad (4.22)$$

is chosen so that the power $\mathbb{E}(Z_{\text{AEA}}^2) = \mathbb{E}(I_{\text{AEA}}^2) + \mathbb{E}(x_1^2)$, as it should be. For the intracell plus intercell interference-limited channel ($I_{\text{AEA}} = I_{\text{AEA}_1}$),

$$A_1 \triangleq \sqrt{\frac{\tilde{\kappa} + \tilde{\kappa}/(\tilde{\kappa} + 1)}{\tilde{\kappa} + \tilde{\kappa}/(\tilde{\kappa} + 1) + 4\tilde{\kappa}\mathbb{E}(g)\sqrt{\tilde{\kappa}/(\tilde{\kappa} + 1) - \text{var}(g)}/\sqrt{1 + 4\tilde{\kappa}\mathbb{E}(g)^2}}}, \quad (4.23)$$

and for the intercell interference-limited channel ($I_{\text{AEA}} = I_{\text{AEA}_2}$),

$$A_2 \triangleq \sqrt{\frac{\tilde{\kappa}/2 + \tilde{\kappa}/(\tilde{\kappa} + 1)}{\tilde{\kappa}/2 + \tilde{\kappa}/(\tilde{\kappa} + 1) + 2\sqrt{2}\tilde{\kappa}\mathbb{E}(g)\sqrt{\tilde{\kappa}/(\tilde{\kappa} + 1) - \text{var}(g)}/\sqrt{1 + 4\tilde{\kappa}\mathbb{E}(g)^2}}}. \quad (4.24)$$

From the standard identities for the correlation function of the sum of two independent random variables, the autocorrelation of Z_{AEA} is

$$\begin{aligned} C_{Z_{\text{AEA}}}(\tau) &= K_{\text{AEA}}(\tau)A^2 + K_{x_1}(\tau)A^2 + \mathbb{E}(Z_{\text{AEA}})^2 \\ &= (K_{\text{AEA-LoS}}(\tau) + K_{\text{AEA-MP}}(\tau) + \text{var}(g)\text{triang}(\tau/\tau_c))A^2 + \mathbb{E}(Z_{\text{AEA}})^2. \end{aligned} \quad (4.25)$$

Accordingly, the PSD of the total received signal AEA in the intercell plus intracell interference-limited channel is

$$\begin{aligned} S_{Z_{\text{AEA}_1}}(f) &= \underbrace{\frac{\tilde{\kappa}}{1 + 4\mathbb{E}(h)^2\tilde{\kappa}} \frac{2\sqrt{\pi}(1 - \text{var}(h))\exp\{-4f^2\pi^2/(\mathbf{D}_{h,\epsilon,\varphi_{\text{RX}}}v_{\text{sat}}^2)\}}{\sqrt{\mathbf{D}_{h,\epsilon,\varphi_{\text{RX}}}v_{\text{sat}}^2}} A_1^2}_{\mathcal{F}_{K_{\text{AEA}_1-\text{MP}}}(f)} \\ &\quad + \underbrace{\left(\frac{\tilde{\kappa}}{1 + 4\mathbb{E}(h)^2\tilde{\kappa}} + 1\right) \text{var}(h)\tau_c \text{sinc}^2(f\tau_c) A_1^2}_{\mathcal{F}_{K_{\text{AEA}_1-\text{LoS}}}(f) + \mathcal{F}_{K_{x_1}}(f)} \\ &\quad + \underbrace{\left(\frac{2\tilde{\kappa}\mathbb{E}(g)}{\sqrt{1 + 4\tilde{\kappa}\mathbb{E}(g)^2}} + \sqrt{\frac{\tilde{\kappa}}{1 + \tilde{\kappa}} - \text{var}(g)}\right)^2 A_1^2 \delta(f)}, \end{aligned} \quad (4.26)$$

and similarly, in the intercell interference-limited channel,

$$\begin{aligned} S_{Z_{\text{AEA}_2}}(f) &= \underbrace{\frac{\tilde{\kappa}}{2(1 + 4\mathbb{E}(h)^2\tilde{\kappa})} \frac{\mathbf{D}_{h,\epsilon,\varphi_{\text{RX}}}(1 - \text{var}(h))hv_{\text{sat}}}{(100\pi^2 f^2 + \mathbf{D}_{h,\epsilon,\varphi_{\text{RX}}}^2 h^2 v_{\text{sat}}^2/100)} A_2^2}_{\mathcal{F}_{K_{\text{AEA}_2-\text{LoS}}}(f)} \\ &\quad + \underbrace{\left(\frac{\tilde{\kappa}}{2(1 + 4\mathbb{E}(h)^2\tilde{\kappa})} + 1\right) \text{var}(h)\tau_c \text{sinc}^2(f\tau_c) A_2^2}_{\mathcal{F}_{K_{\text{AEA}_2-\text{MP}}}(f) + \mathcal{F}_{K_{x_1}}(f)} \end{aligned}$$

$$+ \underbrace{\left(\frac{\sqrt{2}\tilde{\kappa}\mathbb{E}(g)}{\sqrt{1+4\tilde{\kappa}\mathbb{E}(g)^2}} + \sqrt{\frac{\tilde{\kappa}}{1+\tilde{\kappa}} - \text{var}(g)} \right)^2 A_2^2 \delta(f)}_{\mathbb{E}(Z_{\text{AEA}_2})^2}. \quad (4.27)$$

The total interference and the nearest transmitter powers in the spread spectrum are

$$\int_{-\infty}^{\infty} \mathcal{F}_{K_{\text{AEA-LoS}}}(f) df = K_{\text{AEA-LoS}}(0)A^2, \quad \int_{-\infty}^{\infty} \mathcal{F}_{K_{x_1}}(f) df = K_{x_1}(0)A^2,$$

respectively. In the non-spread spectrum, the respective powers are given by subtracting the spread power from the total power in the entire spectrum.

Imagine a scenario with all spread frequencies lowpass filtered from the received signal, and only the non-spread frequencies are preserved (*i.e.*, the signal power is the mass of the Dirac delta function at $f = 0$ in the PSD of the AEA). Analogous to the definition (4.15), the power for the non-spread frequencies for the intercell plus intracell and intercell interference-limited channels are

$$\text{CASIR}_1^{\text{NSS}} \triangleq \frac{\mathbb{E}(x_1^2) - K_{x_1}(0)A_1^2}{\mathbb{E}(Z_{\text{AEA}_1})^2 - (\mathbb{E}(x_1^2) - K_{x_1}(0)A_1^2)} \quad (4.28)$$

$$= \frac{\tilde{\kappa}/(1+\tilde{\kappa}) - \text{var}(g)A_1^2}{\left(\frac{2\tilde{\kappa}\mathbb{E}(g)}{\sqrt{1+4\mathbb{E}(g)^2\tilde{\kappa}}} + \sqrt{\tilde{\kappa}/(1+\tilde{\kappa}) - \text{var}(g)} \right)^2 A_1^2 - (\tilde{\kappa}/(1+\tilde{\kappa}) - \text{var}(g)A_1^2)},$$

$$\text{CASIR}_2^{\text{NSS}} \triangleq \frac{\mathbb{E}(x_1^2) - K_{x_1}(0)A_2^2}{\mathbb{E}(Z_{\text{AEA}_2})^2 - (\mathbb{E}(x_1^2) - K_{x_1}(0)A_2^2)} \quad (4.29)$$

$$= \frac{\tilde{\kappa}/(1+\tilde{\kappa}) - \text{var}(g)A_2^2}{\left(\frac{\sqrt{2}\tilde{\kappa}\mathbb{E}(g)}{\sqrt{1+4\mathbb{E}(g)^2\tilde{\kappa}}} + \sqrt{\tilde{\kappa}/(1+\tilde{\kappa}) - \text{var}(g)} \right)^2 A_2^2 - (\tilde{\kappa}/(1+\tilde{\kappa}) - \text{var}(g)A_2^2)}, \quad (4.30)$$

respectively. Comparing these to (4.16) and (4.17), an pessimistic improvement in the SIR in both cases is

$$\frac{\text{CASIR}^{\text{NSS}}}{\text{ASIR}} \xrightarrow{\tilde{\kappa} \rightarrow \infty} 1 - \text{var}(g). \quad (4.31)$$

This reflects the property that filtering the spread frequencies can be detrimental in the fading channel ($\text{var}(g) > 0$). In the pure LoS channel, $\text{CASIR}^{\text{NSS}}/\text{ASIR} > 0$ dB for all $\tilde{\kappa}$, since a fraction of the interference frequencies are also spread in the LoS channel due to the antenna attenuation.

Furthermore, filtering the spread frequencies can make the link more stable and improve the user fairness (recall the discussion in Section 3.7). However, as observed, in the fading channel, this can deteriorate the average SIR.

4.3.3 Frequency domain interference cancellation of the antenna attenuation components

The total received signal spectrum consists of three distinct parts: the antenna attenuation part $\mathcal{F}_{K_{\text{AEA-LoS}}}(\cdot)$, the triangular multipath scattering part, and the delta function at $f = 0$ (non-spread frequencies). While the latter two are common for the nearest transmitter signal and the total interference, the nearest transmitter signal does not contain the antenna attenuation component, which is clearly separable in the spectrum plot for sufficiently high carrier frequencies. In the time domain, this component can be seen as multiplicative noise to a total interference waveform (which is Gaussian for large densities of interferers or if each interfering signal is Gaussian; *c.f.* Figures 3.6a-3.6d), corresponding to $I_{\text{AEA-LoS}}$, which is uncorrelated with the multipath fading AEA component $I_{\text{AEA-MP}}$. Even though lacking prior information about the channel state or density of interferers, $\mathcal{F}_{K_{\text{AEA-LoS}}}(\cdot)$ can be recognized and mitigated in the frequency domain; consequently, the remaining spectrum resembles the desired nearest transmitter signal, being ideally a scaled version of it. Since the reducible frequency content is eliminated, the ASIR improves. Furthermore, and perhaps more importantly, the variance is reduced, and the instantaneous SIR becomes more stable.

Consider that we are perfectly capable of filtering the antenna attenuation component from the frequency spectrum. Recall that the power and the variance of a total interference waveform AEA are $\mathbb{E}(I_{\text{AEA}_1}^2) = \tilde{\kappa}$ and $\mathbb{E}(I_{\text{AEA}_2}^2) = \tilde{\kappa}/2$. After removing the antenna attenuation components, an upper bound for the power and variance reduction is

$$K_{\text{AEA}_1\text{-LoS}}(0)A_1^2 = \frac{\tilde{\kappa}(1 - \text{var}(g))}{1 + 4\mathbb{E}(g)^2\tilde{\kappa}} A_1(\tilde{\kappa})^2 \stackrel{\tilde{\kappa} \rightarrow \infty}{\leq} \frac{1 - \text{var}(g)}{4\mathbb{E}(g)^2} = \frac{1}{4}, \quad (4.32)$$

$$K_{\text{AEA}_2\text{-LoS}}(0)A_2^2 = \frac{\tilde{\kappa}(1 - \text{var}(g))}{2(1 + 4\mathbb{E}(g)^2\tilde{\kappa})} A_2(\tilde{\kappa})^2 \stackrel{\tilde{\kappa} \rightarrow \infty}{\leq} \frac{1 - \text{var}(g)}{8\mathbb{E}(g)^2} = \frac{1}{8}. \quad (4.33)$$

The relative improvement in the average SIR will deteriorate for large densities of interferers: Even though the aggregate energy would increase unboundedly, only a bounded amount is “transferred into” the antenna attenuation components. However, for small densities of interferers, the reduction of the variance can lead to a considerably more consistent user experience of the link quality (*c.f.*, the discussion in Section 3.7).

Define the ASIR with the $S_{\text{AEA-LoS}}(\cdot)$ canceled as

$$\begin{aligned} \text{CASIR}^{\text{AA}} &\triangleq \frac{\mathbb{E}(x_1^2)}{\int_{-\infty}^{\infty} (S_{Z_{\text{AEA}}}(f) - S_{Z_{\text{AEA-LoS}}}(f)) df - \mathbb{E}(x_1^2)} \\ &= \frac{\mathbb{E}(x_1^2)}{C_{Z_{\text{AEA}}}(0) - K_{\text{AEA-LoS}}(0)A^2 - \mathbb{E}(x_1^2)} \\ &= \frac{\tilde{\kappa}/(\tilde{\kappa} + 1)}{(K_{\text{AEA-MP}}(0) + \text{var}(g))A^2 + \mathbb{E}(Z_{\text{AEA}})^2 - \tilde{\kappa}/(\tilde{\kappa} + 1)}. \end{aligned} \quad (4.34)$$

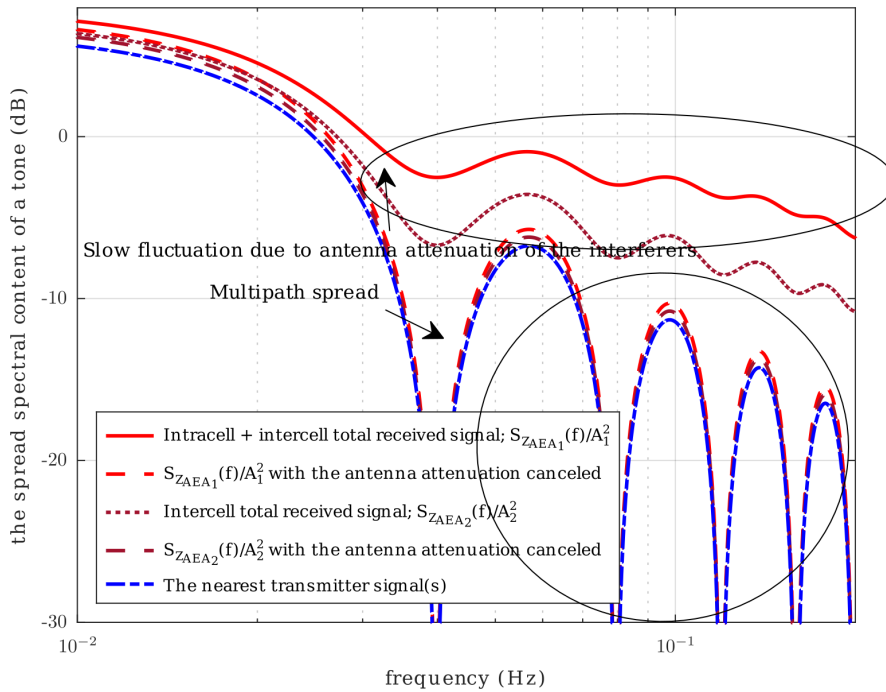
Denote by $\text{CASIR}_1^{\text{AA}}$ and $\text{CASIR}_2^{\text{AA}}$ the canceled SIR in the intracell plus intercell and the intercell interference-limited channels, respectively. The respective A_1 , $\mathbb{E}(Z_{\text{AEA}_1})^2$, A_2 and $\mathbb{E}(Z_{\text{AEA}_2})^2$ are presented in (4.23)-(4.27).

Figure 4.3 demonstrates the PSD of the total received signal AEA and the corresponding PSD with the antenna attenuation components canceled. Figure 4.4 depicts a nearest transmitter signal and total interference waveforms.

Interference cancellation numerical results

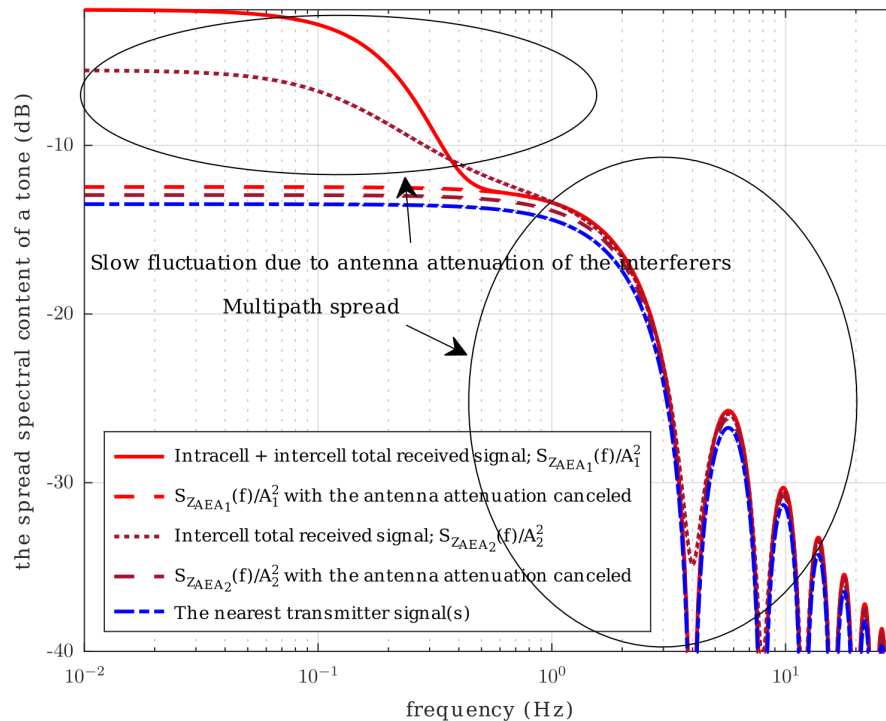
Tables 4.1 and 4.2 compare the ASIRs with and without interference cancellation for various fading channel states $K \in \{1, 10, 100\}$ in the intercell plus intracell and intercell interference-limited channels. In CASIR^{AA} and $\text{CASIR}^{\text{NSS}}$, the improvements are modest. Hence, their application is more substantial in reducing the variance in the SIR, and thus improving the stability of the link and user fairness. However, fading does not affect the efficiency of CASIR^{AA} ; hence, it is robust against the channel state in contrast to merely filtering the high frequencies, which can be detrimental to the SIR, as noted in Section 4.3.2. In the case of a severe fading (of the nearest transmitter), CASIR^{SS} allows for a significant improvement in the average SIR for $K = 1$. Most notably, in the intercell interference-limited channel, the SIR is improved from -7.4 to 0.8 dB for the GP parameter $\tilde{\kappa} = 10$, which corresponds to, on average, $\kappa = \log(2)10 \approx 7$ interferers in a -3 dB footprint-sized area.

PSD of a narrow-beam LEO Rice-1 channel; $f_c = 10 \text{ kHz}$



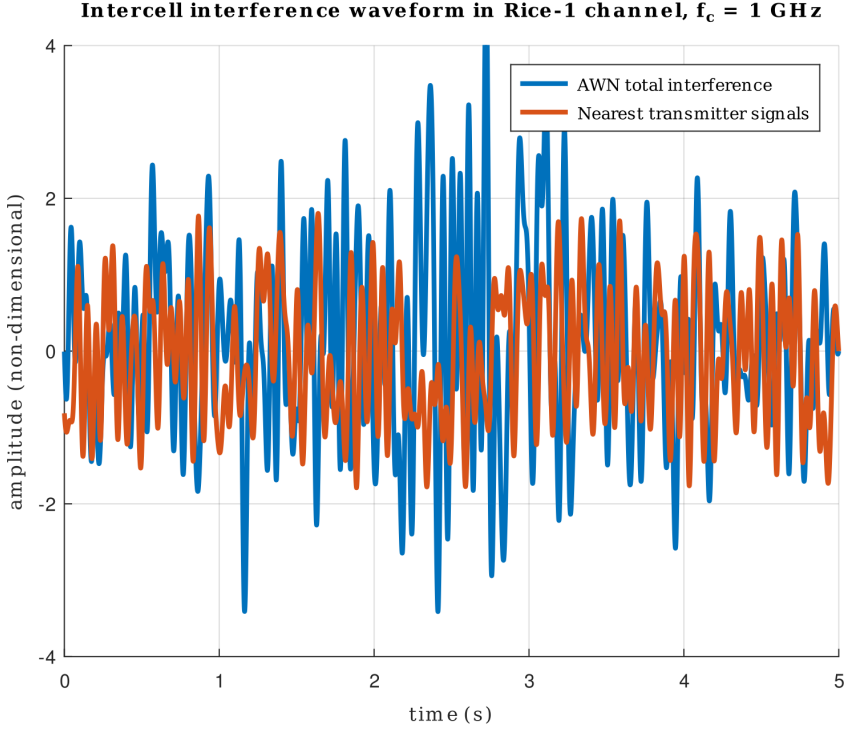
- (a) Small carrier frequency, which results in a long fading coherence time ($\tau_c \approx 25s$): The antenna attenuation mixes into the fading attenuation.

PSD of a narrow-beam LEO Rice-1 channel; $f_c = 1 \text{ GHz}$



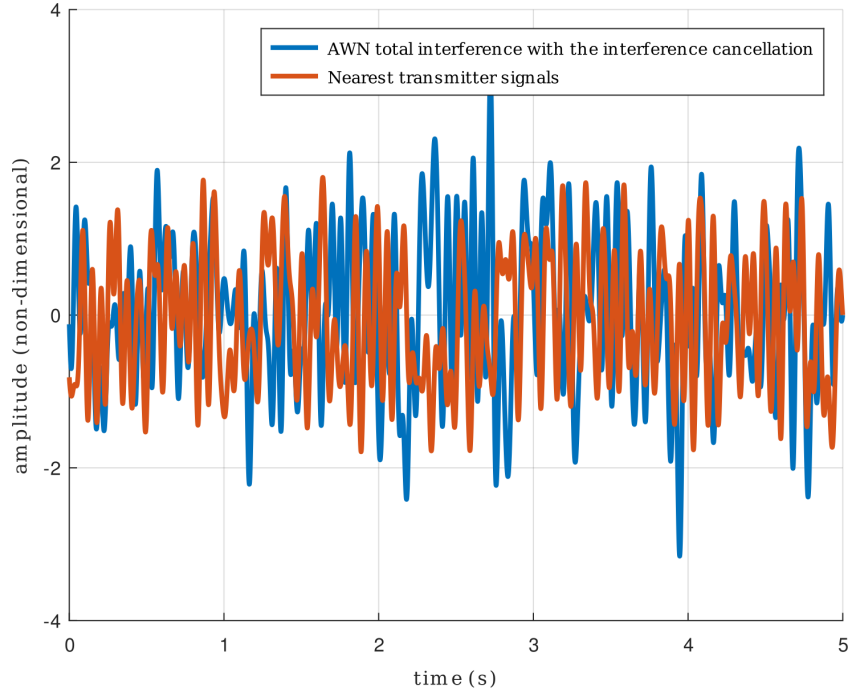
- (b) High carrier frequency and hence short fading coherence time ($\tau_c \approx 0.25s$): The antenna attenuation interference component is visibly separable.

Figure 4.3. Parameters $\tilde{\kappa} = 2$ ($\kappa = 2 \log(2)$ transmitters inside the -3 dB footprint on average), $h = 200 \text{ km}$, and $f_c \in \{10 \text{ kHz}, 1 \text{ GHz}\}$. Higher altitudes would narrow the spectrum of the antenna attenuation component.



(a) The interference varies in power due to antenna attenuation and multi-paths, and the instantaneous SIR is low at $t \approx 2.5s$.

Antenna attenuation fluctuation suppressed



(b) With the reducible frequencies (antenna attenuation components) mitigated, the instantaneous SIR is more stable.

Figure 4.4. A total interference baseband waveform of bandwidth $B = 40$ Hz and its canceled version. The carrier frequency $f_c = 1$ GHz corresponds to the fading coherence time $\tau_c \approx 0.25s$. The total interference and the nearest transmitters (that belong to a separate p.p. and are practically intracell) signals are modulated from Gaussian and BPSK samples, respectively. The GP parameter $\tilde{\kappa} = 2$.

Table 4.1. The ASIRs in the intercell plus intracell interference-limited channel.

Rice-1 fading				
$\tilde{\kappa}$	ASIR ₁	CASIR ₁ ^{SS}	CASIR ₁ ^{NSS}	CASIR ₁ ^{AA}
2	-4.8 dB	-1.7 dB	-5.2 dB	-4.5 dB
5	-7.8 dB	-2.1 dB	-8.2 dB	-7.7 dB
10	-10.4 dB	-2.2 dB	-11.0 dB	-10.3 dB
Rice-10 fading				
$\tilde{\kappa}$	ASIR ₁	CASIR ₁ ^{SS}	CASIR ₁ ^{NSS}	CASIR ₁ ^{AA}
2	-4.8 dB	-7.2 dB	-4.6 dB	-4.5 dB
5	-7.8 dB	-7.5 dB	-7.8 dB	-7.7 dB
10	-10.4 dB	-7.6 dB	-10.5 dB	-10.3 dB
Rice-100 fading				
$\tilde{\kappa}$	ASIR ₁	CASIR ₁ ^{SS}	CASIR ₁ ^{NSS}	CASIR ₁ ^{AA}
2	-4.8 dB	-16.6 dB	-4.5 dB	-4.5 dB
5	-7.8 dB	-16.9 dB	-7.6 dB	-7.7 dB
10	-10.4 dB	-17.0 dB	-10.4 dB	-10.3 dB

Table 4.2. The ASIRs in the intercell interference-limited channel.

Rice-1 fading				
$\tilde{\kappa}$	ASIR ₂	CASIR ₂ ^{SS}	CASIR ₂ ^{NSS}	CASIR ₂ ^{AA}
2	-1.8 dB	1.3 dB	-2.1 dB	-1.5 dB
5	-4.8 dB	0.9 dB	-5.2 dB	-4.7 dB
10	-7.4 dB	0.8 dB	-7.9 dB	-7.3 dB
Rice-10 fading				
$\tilde{\kappa}$	ASIR ₂	CASIR ₂ ^{SS}	CASIR ₂ ^{NSS}	CASIR ₂ ^{AA}
2	-1.8 dB	-4.2 dB	-1.6 dB	-1.5 dB
5	-4.8 dB	-4.5 dB	-4.8 dB	-4.7 dB
10	-7.4 dB	-4.6 dB	-7.5 dB	-7.3 dB
Rice-100 fading				
$\tilde{\kappa}$	ASIR ₂	CASIR ₂ ^{SS}	CASIR ₂ ^{NSS}	CASIR ₂ ^{AA}
2	-1.8 dB	-13.5 dB	-1.5 dB	-1.5 dB
5	-4.8 dB	-13.8 dB	-4.7 dB	-4.7 dB
10	-7.4 dB	-14.0 dB	-7.4 dB	-7.3 dB

```

function [AEAsLOS AEAsRICE AWNtotalsLOS AWNtotalsRICE] ...
    = plotautocovarianceandAWNandAEA()
    ## Simulate and plot the total interference average envelope amplitude
    ## (AEA) and the corresponding interference waveform. Requires the
    ## Octave signal processing and statistics packages:
    ## https://packages.octave.org
    ## Output:
    ## AEAsLOS: A vector of the AEA in the LoS channel
    ## AEAsRICE: A vector of the AEA in the Rician channel
    ## AWNtotalsLOS: A vector of the interference waveform in the LoS channel
    ## AWNtotalsRICE: A vector of the waveform in the Rician channel

    ## tkappa (tildekappa) implicitly encompasses the terrestrial
    ## interferer density, LEO BS altitude, beamwidth, and elevation angle.
    ## kappa = log(2) * tildekappa is the average number of transmitters
    ## inside the -3 dB power footprint---further information in the thesis
    tkappa = 1;
    fc = 1 * 10 ^ 6; # Carrier frequency
    cohtime = 4 * pi * 10 ^ 5 / (5 * fc); # Coherence time (s) (tau_c)
    orbitalspeed = 7.4 * 10 ^ 3; # The LEO BS orbital speed
    h = 200 * 10 ^ 3; # The LEO BS altitude
    ## The constant D_{h, epsilon, varphi} for epsilon = 90 deg and
    ## varphi = 1.6 degrees
    dd = 1 / (h ^ 2 * deg2rad(1.6) ^ 2);
    ## Limit the number of fading blocks, set to frac1 = 1 for more accurate
    ## autocovariance estimate
    frac1 = 1 / 1;
    ## The number of fading blocks is defined such that the LEO BS does not
    ## move outside the rectangular area in planarHPPrefs(.)
    scaling = sqrt(10 ^ 5 / dd); # Scales the PPP region [-0.5 0.5] ^ 2
    fadingblocksN = ceil(frac1 * (scaling / orbitalspeed) / cohtime);

    symbolN = 1; # The symbol sample length
    ## Number of samples per fading block (must have symbolN as a factor).
    ## Each transmitter is in the same block (with independent fading gains)
    signallength = 10 * symbolN;
    K = 1; # The Rice-K fading parameter
    ## Generate a Rice-K distribution of normalized power
    pd = RicianDistribution(sqrt(K / (1 + K)), sqrt(1 / (2 * (1 + K))));
    fadingmean = mean(pd); # The mean of the amplitude fading gain
    fadingvar = var(pd); # The variance of the amplitude fading gain

tic

```

```

## Simulate the signals
[AEAsLOS AEAsRICE AWNtotalsLOS AWNtotalsRICE] = ...
    condAWN(tkappa, fadingblocksN, frac1 / fadingblocksN, ...
        signallength, symbolN, K, fadingmean);
toc

## Scale the envelopes appropriately
AEAsLOS = AEAsLOS / sqrt( 1 + 4 * tkappa * 1 ^ 2 );
AEAsRICE = AEAsRICE / sqrt( 1 + 4 * tkappa * fadingmean ^ 2 );

## Numerically estimate the AEA autocovariance functions
maxlag = 10 * sqrt(log(2) / (2 * dd)); # Maximum lag
[autocovarianceLoS, lag] = ... # The AEA autocovariance in LoS channel
    xcov(AEAsLOS, [ceil((maxlag / orbitalspeed) ...
        * signallength / cohtime)], "unbiased");
[autocovarianceRICE, lag] = ... # The AEA autocovariance in Rice channel
    xcov(AEAsRICE, [ceil((maxlag / orbitalspeed) ...
        * signallength / cohtime)], "unbiased");

## Modulate the samples into an analog signal
frac2 = 1 / 10; # Limit the length of the modulated signal
T = 0 : 0.01 : frac2 * fadingblocksN * signallength;
xbRICE = digitaltoanalog(T, AWNtotalsRICE(1:frac2 * fadingblocksN ...
    * signallength)');
xbLOS = digitaltoanalog(T, AWNtotalsLOS(1:frac2 * fadingblocksN ...
    * signallength)');
T1 = linspace(0, fadingblocksN * cohtime, length(AEAsLOS));
T2 = linspace(0, frac2 * fadingblocksN * cohtime, length(T));
figure;
hold on;

## Plot the Rice channel AEA
plot(T1, AEAsRICE', 'linewidth', 3);
## Plot the LoS channel AEA
plot(T1, AEAsLOS', 'linewidth', 3);
title('Intracell_plus_intercell_interference_AEA',...
    'fontname', 'DejaVu_Serif');
legend("Rice-1_channel_AEA_1", ...
    "LoS_channel_channel_AEA_1",...
    'fontname', 'DejaVu_Serif');
xlabel("time_(s)", 'fontname', 'DejaVu_Serif');
ylabel("Average_envelope_amplitude_(non-dimensional)",...
    'fontname', 'DejaVu_Serif');
set(gca, 'fontsize', 8);
grid on;

```

```

hold off;

figure;
## plot(T2,xbLOS, 'linewidth',2)
hold on;
## Plot the analog Rician response waveform
plot(T2, xbRICE, 'linewidth', 2)
    title('Intracell_plus_intercell_interference',...
        'fontname', 'DejaVu_Serif');
legend('AWN_total_interference_waveform',...
        'fontname','DejaVu_Serif')
xlabel('time_(s)', 'fontname', 'DejaVu_Serif');
ylabel("Amplitude_(non-dimensional)",...
        'fontname', 'DejaVu_Serif');
set(gca, 'fontsize', 8);
grid on;
hold off;

## Plot the theoretical and simulated autocovariance functions
## for the Rice channel
figure;
hold on;
scaledtimelags = lag ./ max(lag) * (maxlag / orbitalspeed);
actualcohtime = cohtime;
plot(scaledtimelags, autocovarianceRICE, '-s', 'linewidth',3);
## plot(scaledtimelags, autocovarianceLoS, '-s','linewidth',3);
axis([-maxlag / orbitalspeed maxlag / orbitalspeed 0 0.3]);
x = linspace(-maxlag / orbitalspeed, maxlag / orbitalspeed, 10000);

## The theoretical autocorrelation function
y1 = (1 - fadingvar) * tkappa ... # The LoS covariance component
    * exp(-dd * (orbitalspeed * x) .^ 2 / 4) ...
    / ( 1 + 4 * tkappa * fadingmean ^ 2 );
## Define the triangular fading autocovariance function
triangr = tkappa * fadingvar * (actualcohtime - x(find(x > 0))) ...
    / actualcohtime .* (abs(x(find(x > 0))) < actualcohtime) ...
    / ( 1 + 4 * tkappa * fadingmean ^ 2 );
## Alternatively, plot the autocovariance of the intercell interference
## The footprint restriction of the interferer domain
## must be set in the function GP(.) for the simulation:
## y1 = (1 - fadingvar) * 1 / 2 * tkappa * ...
##     exp(-dd * (orbitalspeed * abs(x)) * 1 / 50 * h) ...
##     / ( 1 + 4 * tkappa * fadingmean ^ 2 );
## triangr = 1 / 2 * tkappa * fadingvar ...

```

```

##           * (actualcohtime - x(find(x > 0))) / actualcohtime ...
##           .* (abs(x(find(x > 0))) < actualcohtime) ...
##           / ( 1 + 4 * tkappa * fadingmean ^ 2 );

triangl = flip(triangr);
## Plot the autocovariance function
plot(x(find(x <= 0)), (triangl ... # Plot the left side of the triangle
                         + y1(find(x <= 0))), 'linewidth', 3, 'color', 'b');
plot(x(find(x > 0)), (triangr ... # Plot the right side of the triangle
                         + y1(find(x > 0))), 'linewidth', 3, 'color', 'b');
xlabel('time_lag_(s)', 'fontname', 'DejaVu_Serif');
string = 'Autocovariance_of_the_intercell_interference_AEA_2';
title(string, 'fontname', 'DejaVu_Serif');
set(gca, 'fontsize', 8);
legend('Simulated_autocovariance', 'Theory', 'fontname', 'DejaVu_Serif');
grid on;
hold off;

endfunction

function [AEAsLOS AEAsRICE AWNtotalsLOS AWNtotalsRICE] ...
    = condAWN(tkappa, fadingblocksN, cohtime, signallength, ...
               symbolN, K, fadingmean)
a = 10 ^ 5; # Scaling for the PPP sampling region [-0.505, 0.505] ^ 2
## Initialize the memory for the waveform vector
AWNtotalsLOS = zeros(fadingblocksN, signallength / symbolN);
AWNtotalsRICE = zeros(fadingblocksN, signallength / symbolN);
## Initialize the fading gains for the LoS and Rician channels
AEAsLOS = zeros(fadingblocksN, 1);
AEAsRICE = zeros(fadingblocksN, 1);
refs = planarHPPrefs(tkappa * a / pi); # The Earth transmitter locations
refs = [refs(1, :) - 0.5; refs(2, :) + 0.5];
for iii = 1:fadingblocksN
    if(mod(iii, 250) == 0) # Observe the progression
        disp([num2str(iii), "/", num2str(fadingblocksN)]);
    end
    [ithAEAsLOS ithAEAsRICE ithAWNslOS ithAWNslRice] = ...
        nthAEAsandAWNsls(iii, refs, cohtime, signallength / symbolN, K, ...
                           tkappa, fadingmean);
    AEAsRICE(iii) = ithAEAsRICE; # Rice AEA
    AEAsLOS(iii) = ithAEAsLOS; # LoS AEA
    AWNtotalsLOS(iii, 1:signallength / symbolN) = ithAWNslOS;
    AWNtotalsRICE(iii, 1:signallength / symbolN) = ithAWNslRice;
end

```

```

## AEA gains
AEAsLOS = AEAsLOS'(:);
AEAsRICE = AEAsRICE'(:);
AEAsLOS = repmat(AEAsLOS', signallength, 1)();
AEAsRICE = repmat(AEAsRICE', signallength, 1)();
## The aggregate AWN signals in a vector
AWNtotalsLOS = AWNtotalsLOS'();
AWNtotalsRICE = AWNtotalsRICE'();
## The signals are constant within each symbol, so duplicate the vectors
AWNtotalsLOS = repmat(AWNtotalsLOS', symbolN, 1)();
AWNtotalsRICE = repmat(AWNtotalsRICE', symbolN, 1)();
endfunction

## Modulate the given digital samples to an analog signal
function xb = digitaltoanalog(T, digitalsignal)
    xb = zeros(0, length(T));
    iii = 1;
    for t = T
        xb(iii) = ... # Modulated analog signal value at t
        sum(digitalsignal .* sinc(t - (0:length(digitalsignal) - 1)));
        iii = iii + 1;
    end
endfunction

## Locations of the interferers
function refs = planarHPPrefs(density)
    yMin = -0.505; yMax = 0.505; # Scaled dimensions of the rectangle
    xMin = -0.505; xMax = 0.505;
    xDelta = xMax - xMin; yDelta = yMax - yMin; # Rectangle side length
    ## Number of points in the area is a Poisson variable of the given
    ## density
    numbPoints = poissrnd(density + density * (1.01 * 1.01 - 1));
    ## Pick points from uniform distribution
    x = xDelta * (rand(numbPoints, 1)) + xMin;
    ## Map referencepoints to geographical coordinates
    y = yDelta * (rand(numbPoints, 1)) + yMin;
    refs = [x'; y'];
endfunction

## Derive the AEAs and the interference waveforms at nth fading block
function [nthAEAsLOS nthAEAsRICE nthAWNsLOS nthAWNsRICE] ...
    = nthAEAsandAWNs(n, refs, cohtime, signallength, K, tkappa, ...
        fadingmean)
    refs = [refs(1, :) + n * cohtime; refs(2, :)]; # Move refs by n steps

```

```

GPrefs = GP(refs, tkappa, fadingmean); # Interferer locations
## Determine the amplitude fading parameters for normalized power fading
s = sqrt(K / (1 + K)); # Noncentrality parameter
sigma = sqrt(1 / (2 * (1 + K))); # Scale parameter
if s == 0 # Rayleigh fading case
    fadings = raylrnd(sigma, 1, length(GPrefs));
else # Else, Rician samples (for some reason, ricernd can not handle s==0)
    fadings = ricernd(s, sigma, 1, length(GPrefs));
endif
nthAEAsRICE = sum(sqrt(GPrefs) .* fadings); # Interference AEA
nthAEAsLOS = sum(sqrt(GPrefs));

## Alternatively, return the interference powers:
## nthAEAsRICE = sum(GPrefs .* fadings .^ 2);
## nthAEAsLOS = sum(GPrefs);

## Simulate the AWGN waveform samples in each block
signals = normrnd(0, 1, signallength, length(GPrefs));
## Alternatively, simulate binary white noise samples:
## signals = ...
## discrete_rnd([-1, 1], [0.5, 0.5], signallength, length(GPrefs));
nthAWNsRICE = ...
    sum((sqrt(GPrefs) .* signals .* fadings)'), # Rice-K interference
nthAWNsLOS = sum((sqrt(GPrefs) .* signals)'), # The LoS interference
endfunction

## Produces a realization of the GP and sum the signals given refs
function GPrefs = GP(refs, tkappa, fadingmean)
    a = 10 ^ 5; # A scaling factor corresponding to refs in [-0.5 0.5] ^ 2
    GPrefs = exp(-a * norm(refs, 2, "cols") .^ 2);
    ## Here put a footprint restriction (for intercell, GPrefs < 0.5)
    GPrefs = GPrefs(find(GPrefs > 0));
    ## ... or take only the nearest transmitter
    ## (here, the scaling corresponds to the Rice fading):
    ## GPrefs = [0 max(GPrefs) * (1 + 4 * tkappa * fadingmean ^ 2)];
endfunction

```

References

- [1] David Middleton. Statistical-physical models of electromagnetic interference. *IEEE Transactions on Electromagnetic Compatibility*, EMC-19(3):106–127, 1977.
- [2] F. Baccelli and B. Blaszczyszyn. *Stochastic Geometry and Wireless Networks*, volume 2. NoW Publishers, 2009.
- [3] Ruibo Wang, Mustafa A. Kishk, and Mohamed-Slim Alouini. Reliability analysis of multi-hop routing in multi-tier LEO satellite networks. *IEEE Transactions on Wireless Communications*, 23(3):1959–1973, 2024.
- [4] Ilari Angervuori, Risto Wichman, Okati Niloofer, and Taneli Riihonen. On routing protocols in inter-satellite communications. *Proceedings of XXXV Finnish URSI Convention on Radio Science*, 2019.
- [5] Lassi Lapintie. Nyt poltetaan 5G-mastoja, aiemmin murtauduttiin tehtaisiin ja rikottiin koneet – uuden teknologian pelko ei ole uitta. *Suomen Kuvallehti*, 2020.
- [6] Council of European Union. Directive 95/46/EC of the European Parliament and Council Directive. Accessed: 2024-09-18.
- [7] Djalel Oukid. Purism Librem 14 review: The king of privacy-focused laptops! *Linux Tech*, 2025.
- [8] Leivo Leevi and Rami Kurimo. Sananvapaus: Twitter ja some-alustat (Jari Kuikanmäki & Jarkko Tontti) | Puheenaihe 88, 2020.
- [9] Yanis Varoufakis. *Technofeudalism : what killed capitalism*. Vintage Digital, London, 2023.
- [10] Roosa Tuovinen. Moni tekee yksinkertaisen virheen, jonka takia WhatsApp-keskustelut voivat päätyä tuntemattoman käsiin. *Yle*, 2025.
- [11] Marko Höyhtyä, Sandrine Boumard, Anastasia Yastrebova, Pertti Järvensivu, Markku Kiviranta, and Antti Anttonen. Sustainable satellite communications in the 6G era: A european view for multilayer systems and space safety. *IEEE Access*, 10:99973–100005, 2022.
- [12] SMARTer 2020 team. The role of ICT in driving sustainable future. *GeSI SMARTer 2020*, 2012.
- [13] Chih-Lin I, Shuangfeng Han, and Sen Bian. Energy-efficient 5G for a greener future. *Nature Electronics*, 2020.

- [14] Margo Anderson. Ducking, dodging, and disposing in low earth orbit: Can tech scale to meet today's runaway orbital debris problems? *IEEE Spectrum*, 62(10):58–63, 2025.
- [15] Ahmed Elzanaty. 5G and EMF exposure: Misinformation, open questions, and potential solutions. *Frontiers in Communications and Networks*, 2021.
- [16] Henna Korkala. Oulun yliopiston tutkimus: Monet kärsivät ongelmallisesta sosiaalisen median käytöstä, mutta apua on vaikea saada. *Yle*, 2025.
- [17] Saumya Amin Shah and Varsha Dilip Phadke. Mobile phone use by young children and parent's views on children's mobile phone usage. *Journal of family medicine and primary care* vol. 12,12, 2023.
- [18] Min Jia, Xuemai Gu, Qing Guo, Wei Xiang, and Naitong Zhang. Broadband hybrid satellite-terrestrial communication systems based on cognitive radio toward 5G. *IEEE Wireless Communications*, 23(6):96–106, 2016.
- [19] Niloofar Okati, Taneli Riihonen, Dani Korpi, Ilari Angervuori, and Risto Wichman. Downlink coverage and rate analysis of low earth orbit satellite constellations using stochastic geometry. *IEEE Transactions on Communications*, 68(8):5120–5134, 2020.
- [20] C.H. Lee, C.Y. Shih, and Y.S. Chen. Stochastic geometry based models for modeling cellular networks in urban areas. *Wireless Networks*, 19:1063–1072, 2013.
- [21] J. W. Lindeberg. Eine neue herleitung des exponentialgesetzes in der wahrscheinlichkeitsrechnung. *Mathematische Zeitschrift*, 1922.
- [22] J. Ilow and D. Hatzinakos. Analytic alpha-stable noise modeling in a Poisson field of interferers or scatterers. *IEEE Transactions on Signal Processing*, 46(6):1601–1611, 1998.
- [23] Gennady Samorodnitsky and Murad S Taqqu. *Stable Non-Gaussian Random Processes: Stochastic Models with Infinite Variance: Stochastic Modeling*. Routledge, 2017.
- [24] Kapil Gulati, Brian L. Evans, and Keith R. Tinsley. Statistical modeling of co-channel interference in a field of Poisson distributed interferers. In *2010 IEEE International Conference on Acoustics, Speech and Signal Processing*, pages 3490–3493, 2010.
- [25] Ilari Angervuori, Martin Haenggi, and Risto Wichman. Meta distribution of the SIR in a narrow-beam LEO uplink. *IEEE Transactions on Communications*, 73(9):8260–8273, 2025.
- [26] Robert W. Heath, Marios Kountouris, and Tianyang Bai. Modeling heterogeneous network interference using Poisson point processes. *IEEE Transactions on Signal Processing*, 61(16):4114–4126, 2013.
- [27] Martin Haenggi and Radha Krishna Ganti. Interference in large wireless networks. *Foundations and Trends® in Networking*, 3(2):127–248, 2009.
- [28] David Tse and Pramod Viswanath. *Fundamentals of wireless communication*. Cambridge University Press, Cambridge, 1st ed. edition, 2005.
- [29] Ruibo Wang, Mustafa A. Kishk, and Mohamed-Slim Alouini. Ultra-dense LEO satellite-based communication systems: A novel modeling technique. *IEEE Communications Magazine*, 60(4):25–31, 2022.
- [30] Shuai Wang, Jinpeng Song, Xiaqing Miao, and Gaofeng Pan. *Understanding Satellite Communications: The Stochastic Geometry Perspective*. Springer, Singapore, 1 edition, 2024.

- [31] 3GPP. Solutions for NR to support non-terrestrial networks (NTN), TR 38.821. Technical report, 3GPP, 2023.
- [32] International Telecommunication Union. Satellite antenna radiation patterns for non-geostationary orbit satellite antennas operating in the fixed-satellite service below 30 GHz. Recommendation S.1528, ITU-R, 2001.
- [33] Martin Haenggi. Simalysis: Symbiosis of simulation and analysis. <https://stogblog.net/2020/10/15/simalysis-symbiosis-of-simulation-and-analysis/>, October 2020. Accessed: 2024-07-12.
- [34] Mihai Albulet. SpaceX V-band non-geostationary satellite system. Technical Report SAT-LOA-20170301-00027, Space Exploration Technologies Corp., 2017.
- [35] Ruibo Wang, Baha Eddine Youcef Belmekki, Howard H. Yang, and Alouini Mohamed Slim. Non-terrestrial network models using stochastic geometry: Planar or spherical. *arXiv*, 2025.
- [36] Bassel Al Homssi and Akram Al-Hourani. Optimal beamwidth and altitude for maximal uplink coverage in satellite networks. *IEEE Wireless Communications Letters*, 11(4):771-775, 2022.
- [37] Xu Hu, Bin Lin, Ping Wang, Xiao Lu, Haichao Wei, and Shuang Qi. Modeling and analysis of end-to-end LEO satellite-aided shore-to-ship communications. In *2023 IEEE/CIC International Conference on Communications in China (ICCC)*, pages 1-6, 2023.
- [38] Haoge Jia, Chunxiao Jiang, Linling Kuang, and Jianhua Lu. An analytic approach for modeling uplink performance of mega constellations. *IEEE Transactions on Vehicular Technology*, 72(2):2258-2268, 2023.
- [39] D. J. Daley and D. Vere-Jones. *An introduction to the theory of point processes*. 2. Springer, New York, 2nd ed. edition, 2008.
- [40] Talha Ahmed Khan and Mehtnaz Afshang. A stochastic geometry approach to doppler characterization in a LEO satellite network. In *ICC 2020 - 2020 IEEE International Conference on Communications (ICC)*, pages 1-6, 2020.
- [41] Akram Al-Hourani and Bassel Al Homssi. Doppler shift distribution in satellite constellations. *IEEE Communications Letters*, 28(9):2131-2135, 2024.
- [42] Anna Talgat, Mustafa A. Kishk, and Mohamed-Slim Alouini. Stochastic geometry-based uplink performance analysis of IoT over LEO satellite communication. *IEEE Transactions on Aerospace and Electronic Systems*, 60(4):4198-4213, 2024.
- [43] M. Patzold, U. Killat, and F. Laue. An extended suzuki model for land mobile satellite channels and its statistical properties. *IEEE Transactions on Vehicular Technology*, 47(2):617-630, 1998.
- [44] J. D. Parsons. *The mobile radio propagation channel*. Wiley, Chichester, 2nd ed. edition, 2001.
- [45] 3GPP. Study on new radio (NR) to support non-terrestrial networks (release 15), TR 38.811. Technical report, 3GPP, 2020.
- [46] Bartłomiej Blaszczyzyn François Baccelli. *Stochastic Geometry and Wireless Networks*, volume 1. NoW Publishers, 2009.
- [47] Mahmoud I. Kamel, Walaa Hamouda, and Amr M. Youssef. Coverage and capacity analysis with stretched exponential path loss in ultra-dense networks. In *GLOBECOM 2017 - 2017 IEEE Global Communications Conference*, pages 1-6, 2017.

- [48] Kenji Handa. The two-parameter Poisson—Dirichlet point process. *Bernoulli*, 15(4):1082–1116, 2009.
- [49] Bartłomiej Błaszczyzny, Martin Haenggi, Paul Keeler, and Sayandev Mukherjee. *Stochastic Geometry Analysis of Cellular Networks*. Cambridge University Press, 2018.
- [50] Martin. Haenggi. *Stochastic geometry for wireless networks*. Cambridge University Press, Cambridge, 2013.
- [51] Pierre Brémaud. *Mathematical Principles of Signal Processing*. Springer New York, NY, 2002.
- [52] Jim Pitman and Marc Yor. The two-parameter poisson-dirichlet distribution derived from a stable subordinator. *The Annals of Probability*, pages 855–900, 1997.
- [53] Bartłomiej Błaszczyzny and Holger Paul Keeler. Studying the SINR process of the typical user in poisson networks using its factorial moment measures. *IEEE Transactions on Information Theory*, 61(12):6774–6794, 2015.
- [54] Martin Haenggi. The meta distribution of the SIR in Poisson bipolar and cellular networks. *IEEE Transactions on Wireless Communications*, 15(4):2577–2589, 2016.
- [55] Cagatay Candab. A simple proof of ${}_3F_2(1, 1, 1; 2, 2; \rho) = \text{dilog}(1 - \rho)/\rho$, 2012. Accessed: 2024-09-18.
- [56] David Wood. The computation of polylogarithms. Technical Report 15-92*, University of Kent, Computing Laboratory, University of Kent, Canterbury, UK, June 1992.
- [57] Haoge Jia, Zuyao Ni, Chunxiao Jiang, Linling Kuang, and Jianhua Lu. Uplink interference and performance analysis for megasatellite constellation. *IEEE Internet of Things Journal*, 9(6):4318–4329, 2022.
- [58] Horst Alzer. On some inequalities for the incomplete gamma function. *Math. Comput.*, 66:771–778, 1997.
- [59] Congying Li, Zixi Fang, Yikai Wang, and Chenhua Sun. An approach for interference modeling and analysis of low orbit satellite internet. In *2023 IEEE 23rd International Conference on Communication Technology (ICCT)*, pages 1178–1184, 2023.
- [60] Anastasia Yastrebova, Ilari Angervuori, Niloofar Okati, Mikko Vehkaperä, Marko Höyhtyä, Risto Wichman, and Taneli Riihonen. Theoretical and simulation-based analysis of terrestrial interference to LEO satellite uplinks. In *GLOBECOM 2020 - 2020 IEEE Global Communications Conference*, pages 1–6, 2020.
- [61] F. Vatalaro, G.E. Corazza, C. Caini, and C. Ferrarelli. Analysis of LEO, MEO, and GEO global mobile satellite systems in the presence of interference and fading. *IEEE Journal on Selected Areas in Communications*, 13(2):291–300, 1995.
- [62] International Telecommunication Union Recommendation. Analytical method for determining the statistics of interference between non-geostationary-satellite orbit fss systems and other non-geostationary-satellite orbit fss systems or geostationary-satellite orbit fss networks. Technical Report Rec ITU-R S.1529, International Telecommunication Union, 2001.

- [63] Bassel Al Homssi and Akram Al-Hourani. Modeling uplink coverage performance in hybrid satellite-terrestrial networks. *IEEE Communications Letters*, 25(10):3239–3243, 2021.
- [64] Prasanna Madhusudhanan, Juan G. Restrepo, Youjian Liu, and Timothy X. Brown. Carrier to interference ratio analysis for the shotgun cellular system. In *GLOBECOM 2009 - 2009 IEEE Global Telecommunications Conference*, pages 1–6, 2009.
- [65] Ilari Angervuori and R Wichman. A closed-form approximation of the SIR distribution in a LEO uplink channel. In *2022 IEEE Globecom Workshops (GC Wkshps): Workshop on Cellular UAV and Satellite Communications, Rio de Janeiro, Brazil*, 2022.
- [66] Boya Di, Lingyang Song, Yonghui Li, and H. Vincent Poor. Ultra-dense LEO: Integration of satellite access networks into 5G and beyond. *IEEE Wireless Communications*, 26(2):62–69, 2019.
- [67] Niloofar Okati and Taneli Riihonen. Downlink and uplink low earth orbit satellite backhaul for airborne networks. In *2022 IEEE International Conference on Communications Workshops (ICC Workshops)*, pages 550–555, 2022.
- [68] Xinyun Wang and Martin Haenggi. The Chebyshev-Markov inequalities. Technical Report cm22, University of Notre Dame, 2022. Accessed: 2024-09-2.
- [69] Hongxin Lin, Cheng Zhang, Yongming Huang, Rui Zhao, and Luxi Yang. Fine-grained analysis on downlink LEO satellite-terrestrial mmwave relay networks. *IEEE Wireless Communications Letters*, 10(9):1871–1875, 2021.
- [70] Niloofar Okati and Taneli Riihonen. Stochastic analysis of satellite broadband by mega-constellations with inclined LEOs. In *2020 IEEE 31st Annual International Symposium on Personal, Indoor and Mobile Radio Communications*, pages 1–6, 2020.
- [71] Yanshi Sun and Zhiguo Ding. A fine grained stochastic geometry-based analysis on LEO satellite communication systems. *IEEE Networking Letters*, 5(4):237–240, 2023.
- [72] Anna Talgat, Mustafa A. Kishk, and Mohamed-Slim Alouini. Maximizing uplink data transmission of LEO-satellite-based wireless-powered IoT. *IEEE Internet of Things Journal*, 11(17):28975–28987, 2024.
- [73] Chiu Chun Chan, Bassel Al Homssi, and Akram Al-Hourani. A stochastic geometry approach for analyzing uplink performance for IoT-over-satellite. In *ICC 2022 - IEEE International Conference on Communications*, pages 2363–2368, 2022.
- [74] Anastasia Yastrebova, Ilari Angervuori, Niloofar Okati, Mikko Vehkaperä, Marko Höyhtyä, Risto Wichman, and Taneli Riihonen. Theoretical and simulation-based analysis of terrestrial interference to LEO satellite uplinks. In *GLOBECOM 2020 - 2020 IEEE Global Communications Conference*, pages 1–6, 2020.
- [75] Chia-Han Lee, Cheng-Yu Shih, and Yu-Sheng Chen. Stochastic geometry based models for modeling cellular networks in urban areas. *Wirel. Netw.*, 19(6):1063–1072, aug 2013.
- [76] Xueshi Yang and A.P. Petropulu. Co-channel interference modeling and analysis in a Poisson field of interferers in wireless communications. *IEEE Transactions on Signal Processing*, 51(1):64–76, 2003.

- [77] Seungmo Kim, Eugene Visotsky, Prakash Moorut, Kamil Bechta, Amitava Ghosh, and Carl Dietrich. Coexistence of 5G with the incumbents in the 28 and 70 ghz bands. *IEEE Journal on Selected Areas in Communications*, 35(6):1254–1268, 2017.
- [78] Ilari Angervuori, Niloofar Okati, Taneli Riihonen, and Risto Wichman. Uplink interference characterization and coverage analysis of modern LEO and VLEO networks: A stochastic geometry approach. *IEEE Transactions on Communications*, 2022. submitted for publication.
- [79] Thomas D. Novlan, Harpreet S. Dhillon, and Jeffrey G. Andrews. Analytical modeling of uplink cellular networks. *IEEE Transactions on Wireless Communications*, 12(6):2669–2679, 2013.
- [80] E. Lutz, D. Cygan, M. Dippold, F. Dolainsky, and W. Papke. The land mobile satellite communication channel-recording, statistics, and channel model. *IEEE Transactions on Vehicular Technology*, 40(2):375–386, 1991.
- [81] Fulvio Babich, Massimiliano Comisso, Alessandro Cuttin, Mario Marchese, and Fabio Patrone. Nanosatellite-5G integration in the millimeter wave domain: A full top-down approach. *IEEE Transactions on Mobile Computing*, 19(2):390–404, 2020.
- [82] Xavier Artiga, Jose Nunez-Martinez, Ana Perez-Neira, Gorka Juan Lendrino Vela, Juan Mario Fare Garcia, and Georgios Ziaragkas. Terrestrial-satellite integration in dynamic 5g backhaul networks. In *2016 8th Advanced Satellite Multimedia Systems Conference and the 14th Signal Processing for Space Communications Workshop (ASMS/SPSC)*, pages 1–6, 2016.
- [83] Federal Communications Commission. Report and order and further notice of proposed rulemaking. Technical report, Federal Communications Commission, 2016.
- [84] Kapil Gulati, Brian L. Evans, Jeffrey G. Andrews, and Keith R. Tinsley. Statistics of co-channel interference in a field of Poisson and Poisson-Poisson clustered interferers. *IEEE Transactions on Signal Processing*, 58(12):6207–6222, 2010.
- [85] Jiajia Liu, Yongpeng Shi, Zubair Md. Fadlullah, and Nei Kato. Space-air-ground integrated network: A survey. *IEEE Communications Surveys & Tutorials*, 20(4):2714–2741, 2018.
- [86] Peng Wang, Jiaxin Zhang, Xing Zhang, Zhi Yan, Barry G. Evans, and Wenbo Wang. Convergence of satellite and terrestrial networks: A comprehensive survey. *IEEE Access*, 8:5550–5588, 2020.
- [87] Janne Janhunen, Johanna Ketonen, Ari Hulkkonen, Juha Ylitalo, Antti Roivainen, and Markku Juntti. Satellite uplink transmission with terrestrial network interference. In *2015 IEEE Global Communications Conference (GLOBECOM)*, pages 1–6, 2015.
- [88] Eva Lagunas, Sina Maleki, Lei Lei, Christos Tsinos, Symeon Chatzinotas, and Björn Ottersten. Carrier allocation for hybrid satellite-terrestrial backhaul networks. In *2017 IEEE International Conference on Communications Workshops (ICC Workshops)*, pages 718–723, 2017.
- [89] Yueyue Zhang, Yunchi Shi, Fei Shen, Yihuan Pang, Feng Yan, and Lianfeng Shen. Satellite-terrestrial spectrum sensing scheme based on cascaded FNN and FIS. In *2019 IEEE Globecom Workshops (GC Wkshps)*, pages 1–6, 2019.

- [90] Xiangming Zhu, Chunxiao Jiang, Wei Feng, Linling Kuang, Zhu Han, and Jianhua Lu. Resource allocation in spectrum-sharing cloud based integrated terrestrial-satellite network. In *2017 13th International Wireless Communications and Mobile Computing Conference (IWCMC)*, pages 334–339, 2017.
- [91] Hesham ElSawy, Ekram Hossain, and Martin Haenggi. Stochastic geometry for modeling, analysis, and design of multi-tier and cognitive cellular wireless networks: A survey. *IEEE Communications Surveys & Tutorials*, 15(3):996–1019, 2013.
- [92] Oluwatayo Y. Kolawole, Satyanarayana Vuppala, Mathini Sellathurai, and Tharmalingam Ratnarajah. On the performance of cognitive satellite-terrestrial networks. *IEEE Transactions on Cognitive Communications and Networking*, 3(4):668–683, 2017.
- [93] I. Ali, N. Al-Dahir, and J.E. Hershey. Predicting the visibility of LEO satellites. *IEEE Transactions on Aerospace and Electronic Systems*, 35(4):1183–1190, 1999.
- [94] Younes Seyed and Seyed Mostafa Safavi. On the analysis of random coverage time in mobile LEO satellite communications. *IEEE Communications Letters*, 16(5):612–615, 2012.
- [95] Niloofar Okati, Taneli Riihonen, Dani Korpi, Ilari Angervuori, and Risto Wichman. Downlink coverage and rate analysis of low earth orbit satellite constellations using stochastic geometry. *IEEE Transactions on Communications*, 68(8):5120–5134, 2020.
- [96] Niloofar Okati and Taneli Riihonen. Stochastic analysis of satellite broadband by mega-constellations with inclined LEOs. In *2020 IEEE 31st Annual International Symposium on Personal, Indoor and Mobile Radio Communications*, pages 1–6, 2020.
- [97] Anna Talgat, Mustafa A Kishk, and Mohamed-Slim Alouini. Stochastic geometry-based uplink performance analysis of IoT over LEO satellite communication. *IEEE Transactions on Aerospace and Electronic Systems*, 60(4):4198–4213, 2024.
- [98] Felipe Augusto Tondo, Victoria Dala Pegorara Souto, Onel Luis Alcaraz Lopez, Samuel Montejo-Sanchez, Sandra Cespedes, and Richard Demo Souza. Optimal traffic load allocation for aloha-based IoT LEO constellations. *IEEE Sensors Journal*, 23(3):3270–3282, 2022.
- [99] Zakaria Chabou, Adnane Addaim, and Abdessalam Ait Madi. Enhancing performance of slotted ALOHA protocol for IoT covered by constellation low-earth orbit satellites. *Bulletin of Electrical Engineering and Informatics*, 13(6):4030–4040, 2024.
- [100] Xiao Lu, Mohammad Salehi, Martin Haenggi, Ekram Hossain, and Hai Jiang. Stochastic geometry analysis of spatial-temporal performance in wireless networks: A tutorial. *IEEE Communications Surveys & Tutorials*, 23(4):2753–2801, 2021.
- [101] Radha Krishna Ganti and Martin Haenggi. Spatial and temporal correlation of the interference in ALOHA ad hoc networks. *IEEE Communications Letters*, 13(9):631–633, 2009.

Publication I

A. Yastrebova and I. Angervuori and Niloofar Okati and Mikko Vehkaperä and Marko Höyhtyä and Risto Wichman and Taneli Riihonen. Theoretical and Simulation-based Analysis of Terrestrial Interference to LEO Satellite Uplinks. In *IEEE Globecom*, Taipei, Taiwan, 2020, pp. 1-6, doi: 10.1109/GLOBECOM42002.2020.9347980, 2020.

© 2020 IEEE Global Communications Conference

Reprinted with permission.

Theoretical and Simulation-based Analysis of Terrestrial Interference to LEO Satellite Uplinks

Anastasia Yastrebova¹, Ilari Angervuori², Niloofar Okati³, Mikko Vehkaperä¹,
Marko Höyhtyä¹, Risto Wichman², and Taneli Riihonen³

¹VTT Technical Research Centre of Finland, Oulu, Finland

e-mail: {anastasia.yastrebova, mikko.vehkaperä, marko.hoyhtyä}@vtt.fi

²Aalto University School of Electrical Engineering, Helsinki, Finland

e-mail: {ilari.angervuori, risto.wichman}@aalto.fi

³Faculty of Information Technology and Communication Sciences, Tampere University, Finland

e-mail: {niloofar.okati, taneli.riihonen}@tuni.fi

Abstract—The integration of satellite–terrestrial networks is beneficial in terms of the increase of the network capacity and coverage. In such a heterogeneous network, highly efficient spectrum utilization is extremely important. This could be achieved by the single frequency reuse which allows increasing the capacity at the cost of increased interference. Interference is one of the main parameters that limits the link-level performance in such a network. In this paper, we examine the frequency reuse scenario by analyzing the impact of terrestrial interference to the uplink of a low Earth orbiting (LEO) satellite constellation in the high International Mobile Telecommunications (IMT) frequency bands. To this end, we propose a novel stochastic geometry based analytical framework that is able to accommodate various aspects of realistic satellite networks. The accuracy of the analysis is verified by using advanced simulation tools.

I. INTRODUCTION

The rapid proliferation of smart devices has lead to a tremendous increase in data traffic worldwide. To address the challenge of ever-growing network capacity demand, a combination of terrestrial networks and low Earth orbit (LEO) mega-constellations is envisioned to provide a high-throughput low-latency broadband connectivity everywhere [1], [2]. However, one critical question for the satellite–terrestrial network coexistence is how the scarce spectrum resources between the two systems are shared [3]–[5]. Aggressive frequency re-use maximizes the spectral usage but leads to increased interference and degradation in the link quality. Accurate prediction of the interference between the systems is therefore of great practical importance.

In the literature, the coexistence and spectrum sharing between the satellite and terrestrial systems has been studied extensively either through computer simulations or mathematical analysis [4], [6]–[10]. The problem of simulations is that they are time-consuming and require specialized software to be used. A similar problem is also encountered in terrestrial networks, where it has been solved successfully through the use of stochastic geometry; see for example [11]–[13] and references therein for an overview. However, examples of using stochastic geometry in satellite networks are very few. In [14], the interference caused by the terrestrial net-

work to downlink transmission of a multibeam satellite on a geostationary orbit is investigated. The scenario is extended to a cognitive satellite–terrestrial system where the cellular network acts as the secondary user by the same authors in [15]. A general expression for a single LEO satellite’s visibility time is provided in [16], but it is incapable of concluding the general distribution of visibility periods for any arbitrarily positioned user. The deterministic model in [16] was then developed by a statistical analysis of coverage time in mobile LEO during a satellite visit [17]. Very recently, stochastic geometry was used to study various aspects of LEO satellite systems with large constellations in the downlink direction [18], [19].

In this paper, stochastic geometry is applied for the performance analysis of integrated satellite–terrestrial systems in the uplink (UL) direction. In our model, the interfering terrestrial transmitters are randomly distributed according to the Poisson point process. As the distance to the horizon is limited, a satellite can only experience interference from a bounded area, which precludes the use of standard stochastic geometry analysis (as presented, e.g., in [20]), as this often involves an infinite domain. Given satellite constellation is modeled with an appropriate point process which will allow us to perform the theoretical analysis for the LEO constellations.

To the best of our knowledge, this is the first paper that considers the stochastic geometry based analysis of the UL scenario in LEO systems. In contrast to prior works, we also verify the results of stochastic geometry using the industry standard simulator developed by AGI, namely Systems Tool Kit (STK) [21]. This leads to realistic measurements via the accurate physics-based satellite propagation model, path loss models, etc. provided by the STK. In addition, through STK simulations we are able to examine the time evolution of the system as the satellites propagate over the area of interest.

The organization of the remainder of this paper is as follows. Section II describes the uplink scenario for a LEO constellation. As for the main results, in Section III, we derive analytical expressions for coverage probability. Verification of numerical results is provided in Section IV using STK. Finally, we conclude the paper in Section V.

II. SYSTEM MODEL

Let us consider an uplink LEO communication satellite network, as shown in Fig. 1, in which the ground terminals can transmit data to a satellite if they are located within the footprint of satellite's coverage area. The satellite constellation consists of N satellites, which are placed on N_o low circular orbits with the same inclination angle and altitude denoted by ι and h , respectively. On each orbit, N_q satellites are distributed uniformly, i.e., $N = N_o N_q$.

Ground terminals are located on the surface of Earth which is approximated as a perfect sphere with radius $r_E \approx 6371$ km. The serving ground terminal transmits the data to the nearest satellite while other terminals within the coverage footprint of the satellite cause interference. The interfering ground terminals belong to either the satellite network (SN) or the terrestrial network (TN). Different power levels are set for serving and interfering transmitted signals, denoted by p_0 and p_n , respectively.

For our analysis, we consider that the ground terminals, tagged as x_n , $n = 0, 1, \dots, N - 1$, are distributed according to a homogeneous Poisson point process Φ of intensity λ_{gt} , i.e., $x_n \in \Phi$. The distances from the transmitters to the satellite and their corresponding Earth-centered angles are denoted by R_n and γ_n , respectively. Throughout this paper, superscript zero always associates the parameter with the serving transmitter while other subscripts, $n \neq 0$, are reserved for interfering transmitters. As for the propagation model, we consider the mean power attenuation model given in [22] as well as Rician fading.

The ground terminals and satellites are equipped with omnidirectional antennas with antenna gains of G_{gt} and G_{sat} , respectively. The satellite-centered angle between the center of Earth and the ground transmitter, θ , can be obtained from the basic geometry as

$$\theta(\gamma_n) = \frac{\pi}{2} - \gamma_n - \arcsin \left(\frac{\cos(\gamma_n)(r_E + h) - r_E}{R_n(\gamma_n)} \right),$$

where γ_n is the Earth-centered angle between the transmitter and the satellite as depicted in Fig. 1, and

$$R_n(\gamma_n) = \sqrt{(\cos(\gamma_n)(r_E + h) - r_E)^2 + (\sin(\gamma_n)(r_E + h))^2}. \quad (1)$$

Thus, path loss is a function of the radial distance γ_n and given by [22]

$$g(\gamma_n) = \frac{G(\theta(\gamma_n))}{R_n^\alpha(\gamma_n)}, \quad (2)$$

where α is the path loss exponent and $G = G_{\text{sat}} G_{\text{gt}}$.

Based on the above modeling, the signal-to-interference ratio (SIR) at the receiver satellite can be expressed as

$$\text{SIR} = \frac{p_{v_0} g(\gamma_0)}{I} = \frac{p_{v_0} g(\gamma_0)}{\sum_{x_n \in \Phi / x_0} p_{v_n} g(\gamma_n)}, \quad (3)$$

where I is the cumulative interference power from all other transmitters than the serving transmitter, p_{v_0} and p_{v_n} indicate

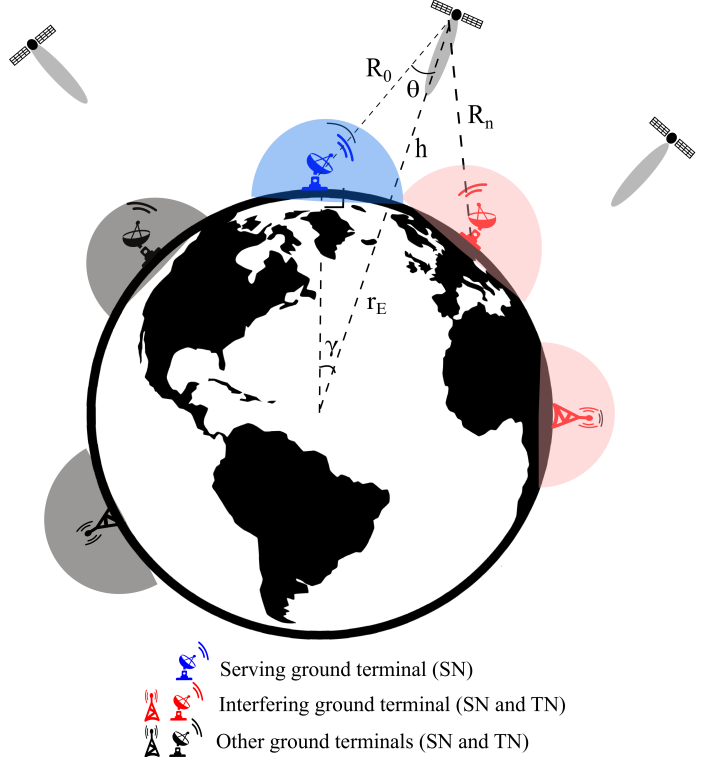


Fig. 1. Illustration of the considered uplink satellite network. The serving ground terminal transmits to its nearest satellite, while other ground terminals consist of satellite ground stations and terrestrial base stations may cause interference.

the virtual transmitted power from the serving and the interfering satellites, respectively. Based on our assumption regarding the Rician fading model, the virtual power is given by

$$p_{v_0} = p_0 q + (1 - q)p'_0, \quad (4)$$

$$p_{v_n} = p_n q + (1 - q)p'_n, \quad (5)$$

where p'_0 and p'_n are exponential with mean p_0 and p_n , respectively, and $q \in [0, 1]$ represents the portion of line-of-sight component in the received signal.

Fading conditions of interfering transmitters are considered to be identically and independently distributed, and spectral efficiency is calculated by averaging over different channel realizations. The interference can be seen as Gaussian noise, and Shannon formula $C = \log_2(1 + \text{SIR})$ can be used to measure the link capacity [23].

III. THEORETICAL ANALYSIS

In this section, we provide the theoretical expression for the probability of coverage to the nearest satellite when the satellites are assumed to be distributed according to a Poisson point process with intensity λ_{sat} . The value for λ_{sat} is chosen so that it corresponds to the average density of satellites in a real constellation. This depends on the user location on Earth.

The theory is facilitated by the shot-noise theory of marked Poisson point processes and we refer to [20] for further information.

Proposition 1. *The uplink probability of coverage when satellites are distributed according to a Poisson point process with intensity λ_{sat} is*

$$p_c(T) = 2\pi\lambda_{\text{sat}} \int_0^\beta \int_{qp_0}^\infty F_I\left(\frac{p_{v_0}g(\gamma_0)}{T}\right) \frac{e^{-\frac{p_{v_0}-p_0q}{p_0(1-q)}}}{p_0(1-q)} \cdot \gamma_0 e^{-\lambda_{\text{sat}}\pi\gamma_0^2} dp_{v_0} d\gamma_0, \quad (6)$$

where T is the SIR threshold for a successful transmission and β refers to radial distance to a satellite at horizon which can be simply obtained from basic geometry as $\beta = \cos^{-1}\left(\frac{r_E}{r_E+h}\right)$.

Proof. To obtain (6), we start with the definition of coverage probability:

$$\begin{aligned} & \mathbb{E}_{\gamma_0} [\mathbb{P}(\text{SIR} > T | \gamma_0)] \\ &= \int_0^\beta \mathbb{P}(\text{SIR} > T | \gamma_0) f_{\gamma_0}(\gamma_0) d\gamma_0 \\ &\stackrel{(a)}{=} 2\pi\lambda_{\text{sat}} \int_0^\beta \mathbb{P}\left(\frac{p_{v_0}g(\gamma_0)}{I} \geq T\right) \gamma_0 e^{-\lambda_{\text{sat}}\pi\gamma_0^2} d\gamma_0 \\ &= 2\pi\lambda_{\text{sat}} \int_0^\beta \mathbb{E}_{p_{v_0}} \left[\mathbb{P}\left(I \leq \frac{p_{v_0}g(\gamma_0)}{T} | p_{v_0} > 0\right) \right] \\ &\quad \cdot \gamma_0 e^{-\lambda_{\text{sat}}\pi\gamma_0^2} d\gamma_0 \\ &\stackrel{(b)}{=} 2\pi\lambda_{\text{sat}} \int_0^\beta \int_{qp_0}^\infty F_I\left(\frac{p_{v_0}g(\gamma_0)}{T}\right) \frac{e^{-\frac{p_{v_0}-p_0q}{p_0(1-q)}}}{p_0(1-q)} \\ &\quad \cdot \gamma_0 e^{-\lambda_{\text{sat}}\pi\gamma_0^2} dp_{v_0} d\gamma_0. \end{aligned} \quad (7)$$

Equation (a) follows from the substitution of the probability density function of γ_0 when satellites are distributed as a Poisson point process, i.e., $f_{\gamma_0}(\gamma_0) = 2\pi\lambda_{\text{sat}}\gamma_0 e^{-\lambda_{\text{sat}}\pi\gamma_0^2}$. Equation (b) is obtained by taking the expectation over the random variable p_{v_0} . Assuming that p'_0 is exponential with mean p_0 , the distribution can be simply obtained as $f_{p_{v_0}}(p_{v_0}) = \frac{e^{-\frac{p_{v_0}-p_0q}{p_0(1-q)}}}{p_0(1-q)}$. \square

In the case of constant transmitting power, i.e., $q = 1$, we have simply

$$p_c(T) = 2\pi\lambda_{\text{sat}} \int_0^\beta F_I\left(\frac{p_0g(\gamma_0)}{T}\right) \gamma_0 e^{-\lambda_{\text{sat}}\pi\gamma_0^2} d\gamma_0. \quad (8)$$

Proposition 2. *The cumulative distribution function $F_I(t)$ in Proposition 1 is given by*

$$F_I(t) = 1 - \frac{2e^{at}}{\pi} \int_0^\infty \Re\left\{\frac{1 - \mathcal{L}_I(a + iu)}{a + iu}\right\} \cos(ut) du. \quad (9)$$

Proof. Proposition (2) is derived using Broomwhich inverse contour integral and the property of the Laplace transform, $\mathcal{L}_X(s) := \mathbb{E}[e^{-sX}]$, which states that the Laplace transform of the CDF can be obtained from Laplace transform of the

PDF by dividing by s in the frequency domain. Thus, we have

$$\begin{aligned} 1 - F_I(t) &= \frac{1}{2\pi i} \int_{a-i\infty}^{a+i\infty} \frac{1 - \mathcal{L}_I(s)}{s} e^{st} ds \\ &= \frac{1}{2\pi} \int_{-\infty}^\infty \frac{1 - \mathcal{L}_I(a + iu)}{a + iu} e^{(a+iu)t} du \\ &= \frac{e^{at}}{2\pi} \int_{-\infty}^\infty \frac{1 - \mathcal{L}_I(a + iu)}{a + iu} (\cos(ut) + i \sin(ut)) du \\ &= \frac{e^{at}}{2\pi} \int_{-\infty}^\infty \Re\left\{\frac{1 - \mathcal{L}_I(a + iu)}{a + iu}\right\} \cos(ut) \\ &\quad - \Im\left\{\frac{1 - \mathcal{L}_I(a + iu)}{a + iu}\right\} \sin(ut) du \\ &\stackrel{(a)}{=} \frac{2e^{at}}{\pi} \int_0^\infty \Re\left\{\frac{1 - \mathcal{L}_I(a + iu)}{a + iu}\right\} \cos(ut) du, \end{aligned} \quad (10)$$

where $\Re\{\cdot\}$ and $\Im\{\cdot\}$ denote the real and imaginary parts of the complex arguments, respectively. Equation (a) follows from properties of real and imaginary parts in Laplace transform. Namely, for non-negatively supported \hat{f} :

$$\begin{aligned} & \Re\{\hat{f}(a + iu)\} \cos(ut) - \Im\{\hat{f}(a + iu)\} \sin(ut) \\ &= 2\Re\{\hat{f}(a + iu)\}. \end{aligned} \quad (11)$$

\square

Proposition 3. *Laplace transform of the interference from Poisson distributed transmitters is given by*

$$\mathcal{L}_I(s) = \exp\left\{-2\pi\lambda_{\text{gt}} \int_0^\beta \gamma_n (1 - \mathcal{L}_{p_{v_n}}(sg(\gamma_n))) d\gamma_n\right\}, \quad (12)$$

where

$$\begin{aligned} \mathcal{L}_{p_{v_n}}(s) &= \mathcal{L}_{p_n q}(s) \mathcal{L}_{(1-q)p'_n}(s) \\ &= \exp(-p_n qs) \cdot \frac{1/p_n}{1/p_n + (1-q)s}. \end{aligned} \quad (13)$$

Proof. Poisson point process in a bounded window $B := B(0, \beta) \subset \mathbb{R}^d$ conditioned on having n points in the window follows a binomial distribution. Furthermore, having n points inside the window B is Poisson distributed in Poisson p.p.

$$\mathbb{P}\{n \text{ points in } B\} = e^{-\lambda_{\text{gt}}\mathcal{V}(B)} \frac{(\lambda_{\text{gt}}\mathcal{V}(B))^n}{n!}, \quad (14)$$

where $\mathcal{V}(B)$ is the Lebesgue volume of B . Let $\gamma_1, \gamma_2, \dots, \gamma_N$ be the distances of the points $x_1, x_2, \dots, x_N \in \Phi$ from the origin and $p_{v_1}, p_{v_2}, \dots, p_{v_N}$ the transmitting powers of the

respective points. From the definition of Laplace transform, we have

$$\begin{aligned}
\mathcal{L}_I(s) &= \mathbb{E}[e^{-sI}] = \mathbb{E}_{p_{v_n}, \gamma_n} \left[e^{-s \sum_{x_n \in \Phi/x_0} p_{v_n} g(\gamma_n)} \right] \\
&= \mathbb{E}_{p_{v_n}, \gamma_n} \left[e^{-\lambda_{gt} \mathcal{V}(B)} \sum_{N=0}^{\infty} \frac{(\lambda_{gt} \mathcal{V}(B))^N}{N!} e^{-s \sum_{n=1}^N p_{v_n} g(\gamma_n)} \right] \\
&= e^{-\lambda_{gt} \mathcal{V}(B)} \sum_{N=0}^{\infty} \frac{(\lambda_{gt} \mathcal{V}(B))^N}{N!} \\
&\quad \cdot \mathbb{E}_{p_{1, \dots, n}, \gamma_{1, \dots, n}} \left[e^{-s \sum_{n=1}^N p_{v_n} g(\gamma_n)} \right] \\
&= e^{-\lambda_{gt} \mathcal{V}(B)} \sum_{N=0}^{\infty} \frac{(\lambda_{gt} \mathcal{V}(B))^N}{N!} \\
&\quad \cdot \mathbb{E}_{p_{v_1}, \gamma_1} \left[e^{-s p_{v_1} g(\gamma_1)} \right] \dots \mathbb{E}_{p_{v_N}, \gamma_N} \left[e^{-s p_{v_N} g(\gamma_N)} \right] \\
&= e^{-\lambda_{gt} \mathcal{V}(B)} \sum_{N=0}^{\infty} \frac{(\lambda_{gt} \mathcal{V}(B))^N}{N!} \\
&\quad \cdot \frac{2\pi}{\mathcal{V}(B)^N} \left(\int_0^\beta \int_0^\infty \gamma e^{-s p_{v_n} g(\gamma_n)} F(dp_{v_n}) d\gamma_n \right)^N \\
&\stackrel{(a)}{=} e^{-\int_0^\beta (1 - \int_0^\infty e^{-s p_{v_n} g(\gamma_n)} F(dp_{v_n})) \lambda_{gt} d\gamma_n},
\end{aligned}$$

where measure F corresponds to the distribution of the power affected by the fading of the transmitters (virtual power). Equation (a) stems from series expansion of the exponential function. Equation (13) follows straightforwardly from the definition of p_{v_n} in (5) and from standard properties of Laplace transform. \square

Point-wise values $F_I(t)$ in (9) can be numerically calculated through the Euler methods described in [24]. The following approximation

$$\begin{aligned}
F_I(t) &= 1 - \sum_{k=0}^m \binom{m}{k} 2^{-m} \frac{e^{A/2}}{2t} \Re \left\{ \frac{1 - \mathcal{L}_I(A/2t)}{A/2t} \right\} \\
&\quad + \frac{e^{A/2}}{t} \sum_{k=1}^n (-1)^k \Re \left\{ \frac{1 - \mathcal{L}_I(\frac{A+2k\pi i}{2t})}{\frac{A+2k\pi i}{2t}} \right\} \quad (15)
\end{aligned}$$

with $A = 18.4$, $m = 11$ and $n = 15$ is suggested here. The approximation is derived from applying trapezoidal method to (9) and improving the accuracy by Euler summation.

IV. NUMERICAL RESULTS

The analyzed scenario was implemented in the simulation environment STK and is depicted in Fig. 2. The system parameters for the simulations are summarized in Table I. The satellite altitude was chosen to be 550 km to partly investigate the performance of emerging very low Earth-orbiting satellite constellations, such as Starlink [25]. The simulated satellite constellation consists of 126 satellites, constructed according to the Walker method [26]. The minimum elevation angle for the ground terminals was chosen to be 10 degrees to

TABLE I
SYSTEM PARAMETERS

Satellite constellation parameters	
Altitude (h) [km]	550
Number of satellite orbits (N_o)	9
Number of satellites per orbit (N_q)	14
Inclination of the orbits (ι)	90°
Ground terminal parameters	
Carrier frequency f [GHz]	26
Power of serving transmitter p_0 [dBW]	-6
Serving transmitter antenna gain [dB]	37
Serving transmitter antenna model	ITU-R S.465
Power of interfering transmitters p_n [dBW]	varying
Number of interfering terminals	1676
Interference antenna model	Isotropic
Satellite antenna model	Isotropic
SIR threshold for successful decoding T [dB]	10

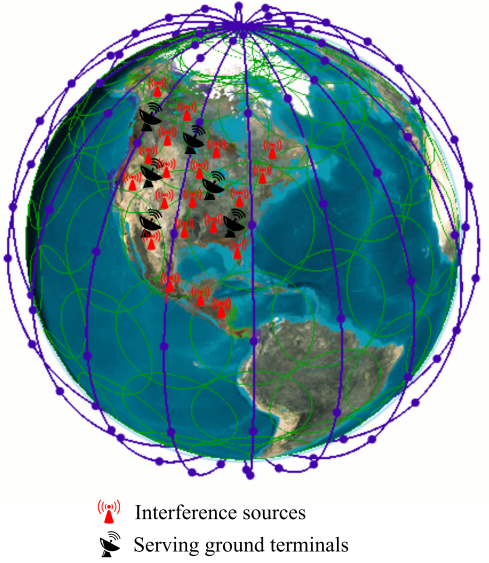


Fig. 2. STK scenario representing used satellite constellation, interference sources, and serving ground terminals. Green circles represent the satellite footprint.

allow satellite connectivity also in the presence of large obstacles such as buildings [27]. In the simulated scenario, 1676 interfering terminals were distributed randomly across the area of interest. The serving ground terminals were placed inside the area of interest in a way that they were surrounded by the interference sources. The analysis was performed over the 12-hour time period from 30 Apr 2020 09:00 to 30 Apr 2020 21:00. As explained in Section II, during this period the serving ground terminal always connects to the closest satellite it can find while other terminals act as interference sources.

Fig. 3 depicts the evolution of the signal-to-interference ratio (SIR) over time in the STK simulations. The spikes represent connections to new satellites and the blue dots represent the ongoing connections with a time step of 10 seconds. The closer the satellite is to the serving ground terminal, the higher the SIR and the better the signal quality is. The aim of the simulations was to investigate the frequency

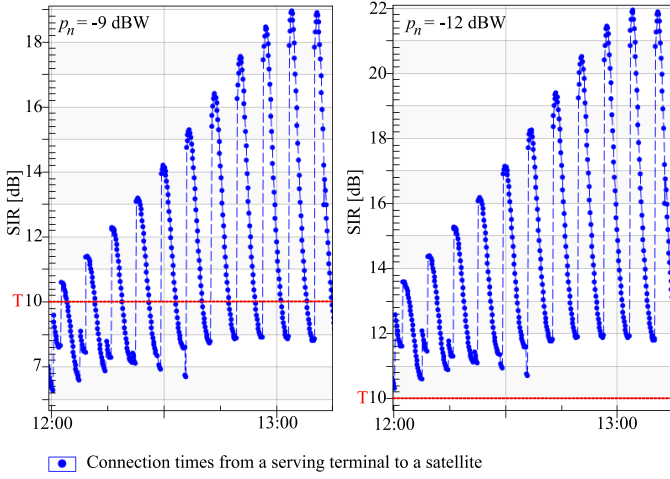


Fig. 3. Time evolution of SIR for serving ground terminal for interference powers $p_n = -9$ dBW and $p_n = -12$ dBW. The blue dots represent the connection times to a satellite with the time step 10 sec. Line-of-sight channel was assumed between the serving ground terminal and the satellite. The threshold (T) for successful decoding is $T = 10$ dB.

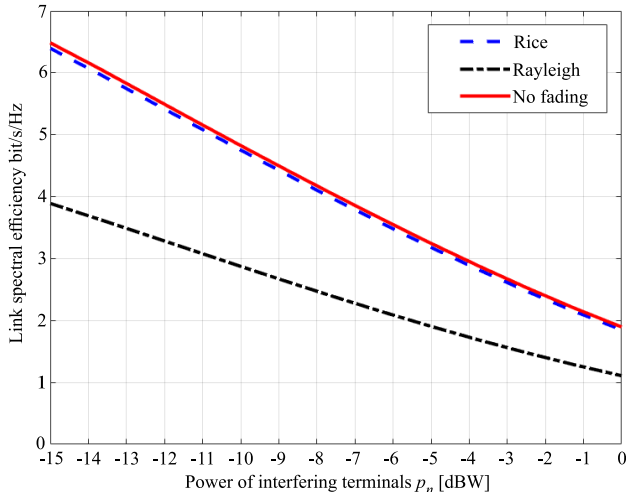


Fig. 4. Spectral efficiency $E[\log_2(1 + \text{SIR})]$ bit/s/Hz of the satellite uplink. Values were acquired by the analysis. Approximately mean 1010 interfering transmitters were assumed to be located inside the satellite footprint. Interfering terminals were assumed to have LoS channel while the serving ground terminal experienced Rayleigh, Rician (with K factor $K = 10$) or LoS fading channels.

reuse performance in the satellite–terrestrial network in a high IMT frequency band, specifically how much the desired link from serving terminals is affected by the interference sources with varying powers. In the considered line-of-sight (LoS) condition, the SIR drops below the chosen decoding threshold $T = 10$ dB multiple times during the considered time period when the power of interfering transmitters is $p_n = -9$ dBW. The probability of successful decoding, or probability of coverage $p_c(T)$, during the entire 12-hour period was around 0.48 in the scenario considered in Fig. 3, implying unacceptable quality of the desired link. When the power of the interfering transmitters was reduced to $p_n = -12$ dBW, the

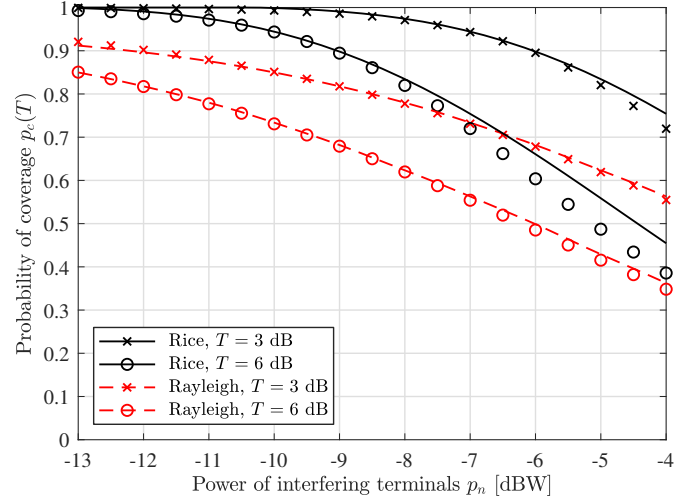


Fig. 5. Coverage probability as a function of the power of interfering sources. Markers depict the STK simulations and the lines correspond to the analytical results. Interfering terminals were assumed to have LoS channels while the serving ground terminal experienced Rayleigh or Rician fading (with K factor $K = 10$) channels.

SIR was above the threshold during the entire depicted period and the probability of coverage for the 12-hour simulation period was $p_c(T) \approx 0.89$. According to the simulation results, the interference power that is lower than -11 dBW provides desired link quality with coverage probability of at least $p_c(T) = 0.80$.

While STK simulations provide accurate results and enable investigation of the time evolution of the system, they require specialized software and are computationally complex for the studied scenario that has multiple simultaneous interfering transmissions. The simulation execution time on the HP EliteBook 840 G5 laptop with the current scenario settings reaches 30 minutes per iteration. The analytical results provided in Section III, on the other hand, provide a very fast method for examining the performance of the system with different parameter values. Fig. 4 represents analytically examined spectral efficiency of the satellite uplink. In the calculations, interfering transmitters were assumed to be located inside the satellite footprint with LoS channel, while the serving ground terminal experienced Rayleigh, Rician (with K factor $K = 10$) or LoS fading channels.

To verify the accuracy of the analysis, Fig. 5 presents the STK simulation results and the corresponding results from the analytical framework described in Section III. In the figure, the STK simulations are depicted with markers and the lines correspond to the analytical results. In this scenario, the interfering terminals have LoS to the satellite, while the serving ground terminal is assumed to experience Rayleigh or Ricean fading with K factor $K = 10$.

Since the STK framework used in this paper did not support direct simulation of fast fading channels, the simulations were carried out in two phases. First, the long term channel effects were simulated with STK and exported as text files. Second,

fast fading was added to the long term channel conditions using Matlab and the final SIR calculations were carried out. It should also be noted that the simplified Rician fading model used in the analysis is only an approximation of the true Rician fading used in the simulations. Herein the parameter q was selected so that the probability density of the channel powers had equal first and second moments. This was achieved by selecting $q = 1 - \sqrt{\frac{1+2K}{(K+1)^2}}$.

The simulations and analysis have a good match in all considered cases when the interference power is low, or the coverage probability satisfies $p_c(T) > 0.85$. With Rayleigh fading in the desired link, the analysis follows the simulations closely also when the coverage probability is much lower. The result implies that the analytical framework proposed in this paper is useful for predicting the performance of real satellite systems in the region of coverage probabilities that is of practical interest. Furthermore, the result shows that if the desired link experiences fading, the interference tolerance is significantly reduced compared to the LoS case considered in Fig. 3.

V. CONCLUSION

In this paper, we presented a mathematical framework for uplink coverage analysis of a terrestrial–satellite network using stochastic geometry. The satellite network is, first, modeled with a Poisson point process which was then utilized to obtain exact expressions for coverage probability in terms of network parameters. Using Systems Tool Kit simulations, we verified the correctness of our derivations. The analytical results provided in this paper can make a huge impact on the development and design of dense satellite networks. Regarding the impact of terrestrial interference to the satellite uplink, current simulations have shown that without a suitable configuration the level of the interference to the uplink can lead to unacceptable performance. Strict power limits for the transmission in the shared bands or mechanisms such as licensed shared access are required to limit the number of simultaneously accessing users in the band.

ACKNOWLEDGMENT

The work of N. Okati and T. Riihonen was supported by a Nokia University Donation. The work of M. Vehkaperä was supported by the PRIORITY project, partly funded by Business Finland.

REFERENCES

- [1] J. Liu, Y. Shi, Z. M. Fadlullah, and N. Kato, “Space-air-ground integrated network: A survey,” *IEEE Communications Surveys & Tutorials*, vol. 20, no. 4, pp. 2714–2741, 2018.
- [2] P. Wang, J. Zhang, X. Zhang, Z. Yan, B. G. Evans, and W. Wang, “Convergence of satellite and terrestrial networks: A comprehensive survey,” *IEEE Access*, vol. 8, pp. 5550–5588, 2020.
- [3] ETSI, “ETSI TR 103 124 V1.1.1, Satellite Earth Stations and Systems (SES); Combined Satellite and Terrestrial Networks scenarios,” European Telecommunications Standards Institute, Tech. Rep., 2013.
- [4] J. Ylitalo, A. Hulkko, M. Höyhtyä, A. Byman, M. Leinonen, J. Janhunen, and A. Roivainen, “Hybrid satellite systems: Extending terrestrial networks using satellites,” in *Cooperative and Cognitive Satellite Systems*. Elsevier, 2015, pp. 337–371.
- [5] M. Höyhtyä, A. Hekkala, M. D. Katz, and A. Mämmelä, “Spectrum awareness: techniques and challenges for active spectrum sensing,” in *Cognitive wireless networks*. Springer, 2007, pp. 353–372.
- [6] Z. Qu, Z. Liu, X. Ding, H. Cao, and G. Zhang, “Co-existence analysis on satellite-terrestrial integrated IMT system,” *Mobile Networks and Applications*, vol. 24, no. 6, pp. 1926–1936, 2019.
- [7] J. Janhunen, J. Ketonen, A. Hulkko, J. Ylitalo, A. Roivainen, and M. Juntti, “Satellite uplink transmission with terrestrial network interference,” in *2015 IEEE global communications conference (GLOBECOM)*. IEEE, 2015, pp. 1–6.
- [8] E. Lagunas, S. Maleki, L. Lei, C. Tsinos, S. Chatzinotas, and B. Ottersten, “Carrier allocation for hybrid satellite-terrestrial backhaul networks,” in *2017 IEEE International Conference on Communications Workshops (ICC Workshops)*. IEEE, 2017, pp. 718–723.
- [9] Y. Zhang, Y. Shi, F. Shen, Y. Pang, F. Yan, and L. Shen, “Satellite-terrestrial spectrum sensing scheme based on cascaded fnn and fis,” in *2019 IEEE Globecom Workshops (GC Wkshps)*, 2019, pp. 1–6.
- [10] X. Zhu, C. Jiang, W. Feng, L. Kuang, Z. Han, and J. Lu, “Resource allocation in spectrum-sharing cloud based integrated terrestrial-satellite network,” in *2017 13th International Wireless Communications and Mobile Computing Conference (IWCMC)*, 2017, pp. 334–339.
- [11] M. Haenggi, *Stochastic geometry for wireless networks*. Cambridge University Press, 2012.
- [12] H. ElSawy, E. Hossain, and M. Haenggi, “Stochastic geometry for modeling, analysis, and design of multi-tier and cognitive cellular wireless networks: A survey,” *IEEE Communications Surveys and Tutorials*, vol. 15, no. 3, pp. 996–1019, Jun. 2013.
- [13] B. Błaszczyzyn, M. Haenggi, P. Keeler, and S. Mukherjee, *Stochastic geometry analysis of cellular networks*. Cambridge University Press, 2018.
- [14] M. Sellathurai, S. Vuppala, and T. Ratnarajah, “User selection for multi-beam satellite channels: A stochastic geometry perspective,” in *Proc. Asilomar Conference on Signals, Systems and Computers*, Nov. 2016.
- [15] O. Y. Kolawole, S. Vuppala, M. Sellathurai, and T. Ratnarajah, “On the performance of cognitive satellite–terrestrial networks,” *IEEE Transactions on Cognitive Communications and Networking*, vol. 3, no. 4, pp. 668–683, Dec. 2017.
- [16] I. Ali, N. Al-Dhahir, and J. E. Hershey, “Predicting the visibility of LEO satellites,” *IEEE Transactions on Aerospace and Electronic Systems*, vol. 35, no. 4, pp. 1183–1190, Oct. 1999.
- [17] Y. Seyedi and S. M. Safavi, “On the analysis of random coverage time in mobile LEO satellite communications,” *IEEE Communications Letters*, vol. 16, no. 5, pp. 612–615, May 2012.
- [18] N. Okati, T. Riihonen, D. Korpi, I. Angervuori, and R. Wichman, “Downlink coverage and rate analysis of low Earth orbit satellite constellations using stochastic geometry,” *IEEE Transactions on Communications*, vol. 68, no. 8, pp. 5120–5134, Aug. 2020.
- [19] N. Okati and T. Riihonen, “Stochastic analysis of satellite broadband by mega-constellations with inclined LEOs,” in *Proc. IEEE 31st Annual International Symposium on Personal, Indoor and Mobile Radio Communications (PIMRC)*, Sep. 2020.
- [20] F. Baccelli and B. Błaszczyzyn, “Stochastic geometry and wireless networks, volume I—Theory, volume 3, no 3–4 of foundations and trends in networking,” 2009.
- [21] Analytical Graphics, Inc., “AGI’s ready-to-use STK and ODTK families of products, enterprise software, and developer tools,” [Online] <https://www.agi.com/products>, 2020.
- [22] F. Baccelli, B. Błaszczyzyn *et al.*, “Stochastic geometry and wireless networks: Volume II applications,” *Foundations and Trends® in Networking*, vol. 4, no. 1–2, pp. 1–312, 2010.
- [23] P. V. Tse. D., *Fundamentals of Wireless Communication*. Cambridge University Press, 2005.
- [24] Abate and W. Whitt, “Numerical inversion of Laplace transforms of probability distributions,” *ORSA Journal on Computing*, vol. 7, no. 1, p. 36–43, 1995.
- [25] Federal Communications Commission, “Application for modification of authorization for the SpaceX NGSO satellite system,” [Online] <https://fcc.report/IBFS/SAT-MOD-20190830-00087/1877764.pdf>, 2019.
- [26] A. Yastrebova, M. Höyhtyä, and M. Majanen, “Mega-constellations as enabler of autonomous shipping,” in *2019 International Communications Satellite Systems Conference (ICSSC)*, Oct. 2019.
- [27] O. L. De Weck, U. Scialom, and A. Siddiqi, “Optimal reconfiguration of satellite constellations with the auction algorithm,” *Acta Astronautica*, vol. 62, no. 2-3, pp. 112–130, 2008.

Publication II

I. Angervuori and R. Wichman. A Closed-Form Approximation of the SIR Distribution in a LEO Uplink Channel. In *IEEE Globecom Workshops (GC Wkshps)*, Rio de Janeiro, Brazil, 2022, pp. 856-861, doi: 10.1109/GCWkshps56602.2022.10008485, 2022.

© 2022

Reprinted with permission.

A Closed-Form Approximation of the SIR Distribution in a LEO Uplink Channel

Ilari Angervuori

*School of Electrical Engineering
Aalto University
02150 Espoo, Finland
ilari.angervuori@aalto.fi*

Risto Wichman

*School of Electrical Engineering
Aalto University
02150 Espoo, Finland
risto.wichman@aalto.fi*

Abstract—The Low Earth Orbit (LEO) satellite networks will improve the quality of future communication networks. The rapid expansion of LEO networks brings up considerations of man-made interference from terrestrial networks or other LEO terminals. Especially the future terrestrial networks will cause interference in satellite receivers as higher frequency bands will be utilized in the emerging 5G and beyond networks. We study the distribution of signal-to-interference ratio (SIR) in a narrow beam LEO satellite receiver affected by a dense heterogeneous set of interfering transmitters. We propose that the distribution of interference power approximates the Gaussian distribution for the positive values. Furthermore, we suggest that the distribution of SIR follows the gamma distribution. We use the tools of stochastic geometry and derive the location, shape, and scale parameters for the distributions of interference and SIR. The parameters depend on the amount of interfering transmitters inside the receiving satellite's 3 dB footprint, the transmitting powers, and the slow and fast fading conditions.

I. INTRODUCTION

The emerging Low Earth Orbit (LEO) satellite communication will play a vital part in the future networks supplementing the traditional terrestrial networks. The advantages of LEO networks include low latency and immunity to natural or man-made calamities. In addition, they can provide reliable and fast connections to remote parts of the world.

LEO networks work in high frequencies up to mm-waves. Today such frequencies have been allocated for satellite communications, but in the future, 5G and beyond technologies utilize these high-frequency bands as well [1], [2], [3]. In addition, the amount of other terrestrial-satellite terminals will increase as the future LEO networks will potentially include thousands or even tens of thousands of satellites. These facts bring up a question about the interference in a satellite uplink in the presence of a heterogeneous set of interfering transmitters.

We will apply the tools from stochastic geometry to study the interference in a terrestrial-satellite uplink, where the satellite will experience additive interference power from multiple overlapping classes of interferers inside its footprint. We assume that each class of interfering transmitters is Poisson distributed on the Earth. The interferers experience slow fading and Rician fast fading conditions. We propose that the

statistical interference power approximates the Gaussian distribution for the positive values. Furthermore, we propose that the signal-to-interference ratio (SIR) follows approximately the gamma distribution. We derive the parameters for the distributions based on the analysis of ratio distributions and second-moment matching. The approximation is especially applicable for high densities of interferers.

A. Related works and motivation

David Middleton's seminal paper [4] derives closed-form approximations for a statistical-physical interference waveform in three qualitatively different situations characterized by the interference's impulsiveness. These distributions are often referred to as Middleton class A, B, and C distributions. As a generic source of interference, Poisson point process (PPP) has been studied, for example, in [5], [6], [7]. In these papers, the distribution of instantaneous in-phase and quadrature components is expressed as the alpha-stable distribution [8]. In [9] Gaussian, Middleton class A and alpha-stable distributions were studied in ad-hoc and cellular networks to model the interference. Using second-order moment matching [10] proposes a gamma distribution approximation for the distribution of interference power in a heterogeneous terrestrial cellular network – this approximation is possible by assuming a non-singular path-loss function. In [11], a semi-analytical expression for the tail probabilities of SIR was obtained.

In these papers, it turns out that modeling interference by Gaussian statistics often works poorly because the tails of Gaussian distribution decay fast. However, in satellite communications, the topology of the Earth facilitates a qualitatively different setting, and the terrestrial models cannot be used as such. Contrary to terrestrial networks, the distribution of interference is not heavy-tailed as the interferers are concentrated in a small area at a high distance inside the receiver's footprint, and the source domain of interference can be considered even point-like in the case of narrow state-of-the-art beamforming. Thus, the path-loss function is constant (contrary to a path-loss function with a singularity), and the expected interference power is well-defined. The aggregate interference power will follow the normal distribution with the parameters derived in this paper.

Stochastic geometry has not been used to model satellite networks until recently. Analysis of interference in a satellite-terrestrial downlink is provided in [12], whereas [13] studies of uplink and downlink coverage probabilities in inclined LEOs. However, contrary to this paper, both [12], and [13] use the binomial process instead of the Poisson point process. The work in [14] used the Poisson process to model interfering transmitters in a terrestrial-satellite uplink evaluating data rates under Rician fading conditions. However, the analysis relies on a rather cumbersome numerical inversion of the Laplace transform. An analysis of data rates in a terrestrial-satellite uplink applying PPP theory is presented in [15]. None of these papers gives closed-form expressions for the distribution of interference or SIR. A survey on possible implementations of future ultra-dense satellite networks can be found in [16].

B. Our contribution

We apply the PPP analysis to satellite communications and exploit the fact that the satellite's main lobe is small with state-of-the-art beamforming technologies, and the distance to the satellite can be approximated to be equal to all transmitters inside a footprint. By this assumption, we are able to characterize the distribution of SIR by the well-known gamma distribution. First, we derive the Laplace transform of the interference from multiple classes of interferers assuming that the interferers are Poisson distributed on Earth's surface. Each class of interferers has distinct fading conditions, mean transmitting powers, density, and antenna pattern. From the Laplace transform, we conclude that the distribution of the additive interference can be approximated by Gaussian distribution for positive values with the parameters we derive. Based on this Gaussian approximation, we derive the distribution of SIR in the terrestrial-satellite transmission, where a terrestrial test transmitter transmits from an Earth station to a satellite at a definite elevation angle and altitude. We validate the approximation by comparing the gamma distribution approximation to Monte Carlo simulated distributions with a Gaussian antenna gain. We will notice that the approximation is very good with higher densities of transmitters and reasonable with lower densities.

Analysis in this paper provides insight and a closed-form distribution that can be used to model the SIR in further studies of LEO networks.

In the case of dense satellite constellations, the locations of the satellites can be modeled as a point process, see [12] - [15]. Hence, the analysis presented in this paper works with minor modifications in a satellite-terrestrial downlink if the density of the interfering satellites is high and the receiver's antenna pattern is narrow enough.

II. SYSTEM MODEL

We consider an interference-limited terrestrial-satellite uplink transmission. A test transmitter (TX) is transmitting to a LEO satellite receiver (RX) with a mean transmitting power p_{TX} . The receiving satellite is at a definite elevation angle w.r.t. the test transmitter, and its boresight faces (approximately) the

Glossary of principal symbols	
Symbol	Explanation
d	Distance between the test transmitter and the satellite
h	Altitude of the satellite
$\Phi^{(i)}$	Poisson point process of class i
$\lambda_{3dB}^{(i)}$	Mean number of class i interferers inside the satellite 3 dB footprint
$\lambda_{km}^{(i)}$	Mean number of class i interferers per square kilometer
$\lambda^{(i)}$	$3/2 \cdot \lambda_{3dB}^{(i)}$
$P_I^{(i)}$	Typical virtual power (power after the fading gain) of an interfering transmitter in class i
$p_I^{(i)}$	Mean power of an interfering transmitter in class i
K	Rician parameter of the test transmitter
$K_i^{(i)}$	Rician parameter of the interferer class i
$L^{(i)}$	Response function of class i transmitters
I	Aggregate interference
μ_I	Mean of the interference
s_I^2	Variance of the interference
p_{TX}	Mean power of the test transmitter
ν_{TX}	LOS component of the test transmitter
σ_{TX}	Scattered path component of the test transmitter

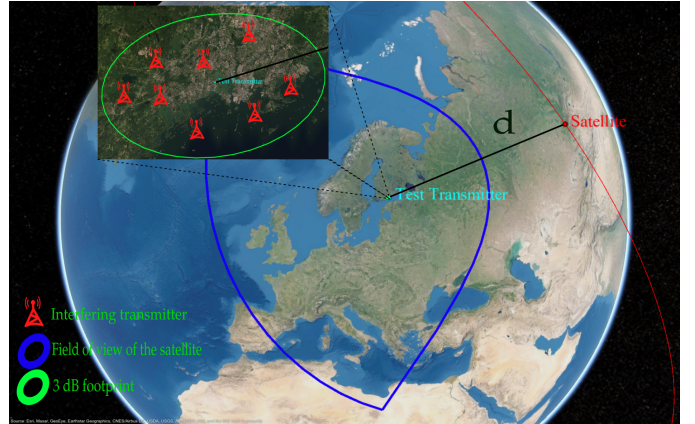


Fig. 1. System model

test transmitter. The test transmitter boresight steers towards the satellite. Inside the field of view of the satellite, there are interfering transmitters. Assuming that the transmitters are independently distributed on Earth, we assume that they follow the Poisson point process. That is, the number of interfering transmitters inside the satellite footprint is Poisson distributed. We treat the interference from the interfering transmitters as additive noise, i.e., the transmitted signals are uncorrelated. We do not consider any interference cancellation techniques. All interferers radiate omnidirectionally.

A. Poisson Point Process

The interfering transmitters $x_i \in \Phi$ are Poisson distributed on Earth's surface \mathcal{E} according to the Poisson point process (PPP) Φ . Vaguely, Φ is a *completely* independent and identically distributed random set of points in the manifold \mathcal{E} . Equivalently, if $\Lambda(A)$ denotes a (deterministic) measure of a

set $A \subset \mathcal{E}$, Φ can be defined as a random measure s.t. $\Phi(A)$ is Poisson distributed and $\mathbb{E}\Phi(A) = \Lambda(A)$ for all measurable A .

Distribution of base stations has been shown to follow PPP in certain cities [17], and PPP can be used in modeling the user locations in a cellular network uplink [18].

B. Response function

Response function $L(\cdot)$ maps a variable $d \in \mathbb{R}^n$ to a positive real number \mathbb{R} . In this work, d represents the distance between the satellite and the test transmitter, and L is a path-loss function

$$L(d) = (Ad)^{-\alpha}, \quad (1)$$

where $A \in \mathbb{R}_+$, and the path-loss power exponent $\alpha \in \mathbb{R}_+$. In other applications, the response function could depend, for example, also on time.

C. Fading

All transmitters experience Rician fading with Rician parameter $K = \nu^2/(2\sigma^2)$, where ν^2 is the power in the line-of-sight (LOS) component and $2\sigma^2$ is the power received from the scattered paths. Consequently, the virtual power seen in the receiver after the fading is generalized noncentral chi-squared distributed.

D. Signal-to-interference ratio

We define the signal-to-interference ratio with interfering transmitters $\{x_j^{(i)}\}_{j=1}^M$ in point processes $\{\Phi^{(i)}\}_{i=1}^N$ as

$$\text{SIR} = \frac{L(d)P_{\text{TX}}}{I} = \frac{L(d)P_{\text{TX}}}{\sum_{x_j^{(i)} \in \cup_i \Phi^{(i)}} P_j^{(i)} L^{(i)}(d_j)}, \quad (2)$$

where $d = d(x_0)$ is the distance from the test transmitter (at x_0) to the satellite, P_{TX} is the virtual power (power after the fading gain) of the test transmitter. Power $P_j^{(i)}$ denotes the virtual power of a transmitter j belonging to the class i , and $L^{(i)}(d_j)$ denotes the path-loss function of the class i at distance d_j .

We assume that all transmitting powers $\{P_j^{(i)}\}_{j=1}^M$ in a class are independent identically distributed (i.i.d.). Often we refer to a typical power of an interferer of class i as $P_I^{(i)}$. The mean power of a typical transmitter is denoted by $p_I^{(i)}$.

E. Shadowing

Transmitters are shadowed with probability S . If the original point process is of density λ , the shadowed transmitters form a Poisson point process of density $S \cdot \lambda$, and the non-shadowed transmitters form a PPP of density $(1 - S)\lambda$. This rather intuitive result is a consequence of the thinning theorem of the PPP [19].

F. Weather model and Doppler shift

We consider that the receiver's antenna beam is narrow, and the interferers are essentially very close to each other. Thus, the weather conditions are approximately equal to all transmitters including the test transmitter, and cancel each other in the definition of SIR (2). Similarly, the Doppler shift is approximately equal to the test transmitter's Doppler shift and hence does not have any effect on the aggregate interference power even after the receivers bandpass filter.

G. Receiver antenna gain

When φ_{RX} is the width of the 3 dB beam, we approximate the receiving antenna gain by a Gaussian beam

$$G_{\text{RX}}(\varphi) = 2^{-\varphi^2/\varphi_{\text{RX}}^2} \text{ for } \varphi \leq \pi/2, \quad (3)$$

where φ denotes the angle w.r.t. the antenna boresight.

III. ANALYSIS

A. Distribution of the interference

The Laplace transform $\mathcal{L} : \mathbb{C} \rightarrow \mathbb{C}$ of the interference I from a point process Φ is given by [19], [14]:

$$\mathcal{L}_I(z) := \mathbb{E}[e^{-Iz}] = e^{-\int_{\mathcal{E}} (1 - \mathcal{L}_{P_I}(L(d(x))G_{\text{RX}}(\varphi(x))z)) \Lambda(dx)}, \quad (4)$$

where P_I denotes the typical virtual power of an interferer.

In the case of a well-steered narrow antenna beam, we can approximate that all transmitters are at an equal distance d from the satellite. Then \mathcal{E} reduces to a single point x_0 of mass $\Lambda(\{x_0\}) := \lambda$ and (4) gets the form;

$$\mathcal{L}_I(z) = e^{-\lambda(1 - \mathcal{L}_{P_I}(L(d)z))}. \quad (5)$$

In this paper, we define $\lambda := 3/2 \cdot \lambda_{3dB}$, where λ_{3dB} is the mean number of transmitters inside the satellite's 3 dB footprint, and $3/2$ is an empirical parameter that compensates the energy from the side lobes – it was obtained by matching the Monte Carlo simulations to the theory, and it works for general altitudes and elevation angles. Should the satellite be in the zenith, the mean number of interferers can be calculated by the area formula of a spherical cap: $\lambda_{3dB} = \lambda_{km} 2\pi R_{\oplus}^2 (1 - \cos(\theta))$, where θ denotes the central angle of the 3dB footprint, λ_{km} is the mean number of transmitters per square kilometer and R_{\oplus} is the radius of Earth. For lower elevation angles of the satellite, the footprint is elliptical and the expressions are more complicated. We leave the geometrical considerations out of the scope of this paper, and λ_{3dB} will be always given.

We know that the Laplace transform of the non-central chi-squared distributed faded power variable is given by

$$\mathcal{L}_{P_I}(z) = \frac{e^{-\frac{\nu_I^2 z}{1+2z\sigma_I^2}}}{1+2z\sigma_I^2}. \quad (6)$$

Substituting (6) to (5) and applying a second-degree Taylor expansion to the exponent yields

$$\begin{aligned} \mathcal{L}_I(z) & \\ & \approx \exp \left\{ -\lambda p_I L(d) z + 1/2 \lambda L(d)^2 \frac{2+4K_I+K_I^2}{(1+K_I)^2} p_I^2 z^2 \right\}. \end{aligned} \quad (7)$$

where $K_I = \nu_I^2/(2\sigma_I^2)$ is the Rician parameter of an interferer.

One can observe that for $z = -it \in \mathbb{C}$,

$$\begin{aligned} \mathcal{L}_I(-it) & \approx \\ & \exp \left\{ \lambda p_I it L(d) - 1/2 \lambda L(d)^2 \frac{2+4K_I+K_I^2}{(1+K_I)^2} p_I^2 t^2 \right\}, \end{aligned} \quad (8)$$

which is the characteristic function $t \mapsto \varphi(t) = \mathcal{L}(-it)$ of the normal distribution with mean $\mu_I = \lambda p_I$ and variance $s_I^2 = \lambda(2+4K_I+K_I^2)/(1+K_I)^2 p_I^2$.

For the Laplace transform it holds that $\mathcal{L}_{I^{(1)}+I^{(2)}}(s) = \mathcal{L}_{I^{(1)}}(s)\mathcal{L}_{I^{(2)}}(s)$ for all s . Thus, it is easy to see from (8) that in case of multiple classes of point processes $\{\Phi^{(i)}\}$:

Proposition 1 (Distribution of I). *The interference I is distributed as the **normal distribution** $\mathcal{N}(\mu_I, s_I^2)$ with mean*

$$\mu_I = \sum_i \lambda^{(i)} L^{(i)}(d) p_I^{(i)} \quad (9)$$

and variance

$$s_I^2 = \sum_i \lambda^{(i)} L^{(i)}(d)^2 \frac{2+4K_I^{(i)}+(K_I^{(i)})^2}{(1+K_I^{(i)})^2} (p_I^{(i)})^2, \quad (10)$$

where $\lambda^{(i)}, L^{(i)}, K_I^{(i)}, p_I^{(i)}$ are the density, response function, Rician parameter and mean transmitting power of the interferer class i , respectively.

Finally, let us make the following observation that comes later III-D1 into use in a special case of a Rayleigh faded test transmitter signal: for $z = t \in \mathbb{R}_+$, the first term in (7) is dominating in the exponent and

$$\mathcal{L}_I(t) \approx \exp \left\{ -\sum_i \lambda^{(i)} L^{(i)}(d) p_I^{(i)} t \right\}. \quad (11)$$

B. Inverse distribution of the interference

It can be shown that the inverse of a Gaussian distributed random variable is approximately Gaussian under certain conditions [20]. We propose a similar approximation by a log-normal distribution. The following proposition applies under the conditions presented in this paper, and it can be verified, e.g., by Monte Carlo simulations.

Proposition 2 (Inverse of I). *Let $I \sim \mathcal{N}(\mu_I, s_I^2)$, then*

$$1/I \sim \text{Lognormal}(-\mu_{LN}, s_{LN}^2),$$

where μ_{LN} and s_{LN} are given by $\mu_{LN} = \log \sqrt{\frac{\mu_I^4}{\mu_I^2+s_I^2}}$ and $s_{LN} = \sqrt{2} \sqrt{\log \frac{\sqrt{\mu_I^2+s_I^2}}{\mu_I}}$.

Proof. First, approximate the normal distribution $\mathcal{N}(\mu_I, s_I^2)$ by a log-normal distribution $\text{Lognormal}(\mu_{LN}, s_{LN}^2)$ with mean μ_I and variance s_I^2 . The inverse distribution is simply $\text{Lognormal}(-\mu_{LN}, s_{LN}^2)$. \square

Consequently, the mean of $1/I$ is

$$\mathbb{E}[1/I] = \exp\{-\mu_{LN} + s_{LN}^2/2\} = \frac{\mu_I^2 + s_I^2}{\mu_I^3} \quad (12)$$

and the variance is

$$\begin{aligned} \mathbb{V}[1/I] &= \exp\{-2\mu_{LN} + s_{LN}^2\}(-1 + \exp\{s_{LN}^2\}) \\ &= \frac{s_I^2(\mu_I^2 + s_I^2)^2}{\mu_I^8}, \end{aligned} \quad (13)$$

where the mean μ_I and variance s_I^2 of the interference is given in (9) and (10).

C. Moments of ratio distribution

Should we know the distributions of P_{TX} and $1/I$, we can calculate the moments of the distribution of P_{TX}/I by the algebra of random variables.

The mean of the ratio distribution P_{TX}/I is

$$\mathbb{E}[P_{TX}/I] = \mathbb{E}[P_{TX}]\mathbb{E}[1/I], \quad (14)$$

and the variance is

$$\begin{aligned} \mathbb{V}[P_{TX}/I] &= \mathbb{V}[P_{TX}] \cdot \mathbb{V}[1/I] + \\ & \mathbb{V}[P_{TX}] \cdot (\mathbb{E}[1/I])^2 + \\ & \mathbb{V}[1/I] \cdot (\mathbb{E}[P_{TX}])^2, \end{aligned} \quad (15)$$

where for the generalized noncentral chi-squared distribution

$$\mathbb{E}[P_{TX}] = \nu_{TX}^2 + 2\sigma_{TX}^2, \quad (16)$$

and

$$\mathbb{V}[P_{TX}] = 4(\nu_{TX}^2 \sigma_{TX}^2 + \sigma_{TX}^4), \quad (17)$$

and $\mathbb{E}[1/I]$ and $\mathbb{V}[1/I]$ are given in (12) and (13).

D. Distribution of SIR

Finally, we will derive the closed-form distribution for the SIR. The analysis is divided into two sections: for the non-LOS case ($K = 0$) in III-D1, and for the partial LOS ($K > 0$) in III-D2.

1) *Rayleigh fading case:* Assuming that the test transmitter signal is Rayleigh faded (i.e. Rician faded with parameter $K = 0$), i.e. the power is exponentially faded, we have according to the approximation (11):

$$\begin{aligned} \mathbf{P}[\text{SIR} \geq t] &= \mathbf{P} \left[\frac{P_{TX}}{I} \geq t \right] = \mathbf{P} [P_{TX} \geq tI] \\ &= \mathbb{E}_I \left[e^{-t/P_{TX}I} \right] = \mathcal{L}_I(t/P_{TX}) \\ &\approx e^{-\sum_i \lambda^{(i)} L^{(i)} \frac{p_I^{(i)}}{P_{TX}} t}. \end{aligned} \quad (18)$$

In other words, the SIR is exponentially distributed with rate $1/\mu_{\text{SIR}} = \sum_i \lambda^{(i)} L^{(i)} p_I^{(i)} / P_{TX}$ should there be no LOS between the test transmitter and the satellite.

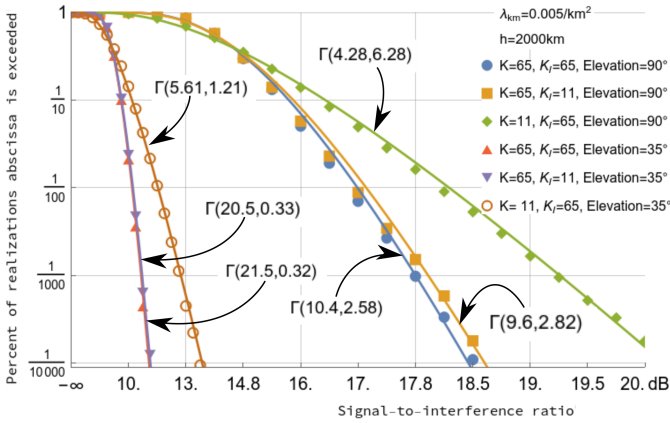


Fig. 2. Comparison of the simulated SIR distributions with gamma distribution models. Here, K_I is the Rician parameter of the non-shadowed interferers.

2) *General fading case:* The gamma distribution is the conjugate prior of the exponential distribution. Thus, we propose that the distribution of SIR follows a gamma distribution in the general Rician fading case.

Gamma distribution depends on the shape parameter $k > 0$ and scale parameter $\theta > 0$. The mean is given by $k\theta$, and the variance is given by $k\theta^2$. To approximate the distribution of SIR by the gamma distribution, we match the mean (14) and variance (15) to the corresponding moments of the Gamma distribution;

$$\begin{cases} k\theta = \mathbb{E}[\text{SIR}] = L(d)\mathbb{E}[P_{\text{TX}}/I] \\ k\theta^2 = \mathbb{V}[\text{SIR}] = L(d)\mathbb{V}[P_{\text{TX}}/I]. \end{cases} \quad (19)$$

Solving the parameters k and θ and substituting (14) and (15), yields

Proposition 3 (Distribution of SIR). *The distribution of SIR approximates the **gamma distribution** $\Gamma(k, \theta)$ with parameters*

$$\begin{aligned} k &= L(d)\mathbb{E}[P_{\text{TX}}/I]^2/\mathbb{V}[P_{\text{TX}}/I] \\ &= L(d)(\mathbb{E}[P_{\text{TX}}]\mathbb{E}[1/I])^2/(\mathbb{V}[P_{\text{TX}}]\cdot\mathbb{V}[1/I]+ \\ &\quad \mathbb{V}[P_{\text{TX}}]\cdot(\mathbb{E}[1/I])^2+ \\ &\quad \mathbb{V}[1/I]\cdot(\mathbb{E}[P_{\text{TX}}])^2), \end{aligned} \quad (20)$$

$$\begin{aligned} \theta &= \mathbb{V}[P_{\text{TX}}/I]/\mathbb{E}[P_{\text{TX}}/I] \\ &= (\mathbb{V}[P_{\text{TX}}]\cdot\mathbb{V}[1/I]+ \\ &\quad \mathbb{V}[P_{\text{TX}}]\cdot(\mathbb{E}[1/I])^2+ \\ &\quad \mathbb{V}[1/I]\cdot(\mathbb{E}[P_{\text{TX}}])^2)/\mathbb{E}[P_{\text{TX}}]\mathbb{E}[1/I], \end{aligned} \quad (21)$$

where the means $\mathbb{E}[\cdot]$ and variances $\mathbb{V}[\cdot]$ are given for P_{TX} in (16) and (17), and for $1/I$ in (12) and (13).

IV. RESULTS

We compare the derived gamma distribution approximation to Monte Carlo simulated values in the figures 2 and 3 with varying altitudes and elevation angles. The parameters for the gamma distribution are given in Proposition 3

We consider that the path-loss function is equal to all transmitters. This implies that the path-loss function cancels

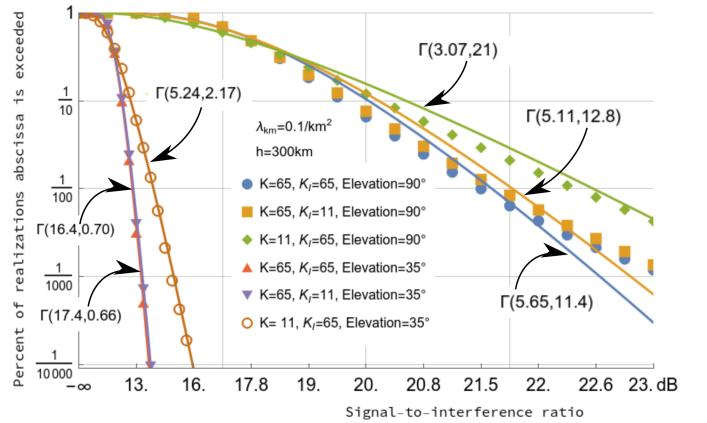


Fig. 3. Comparison of the simulated SIR distributions with gamma distribution models. Here, K_I is the Rician parameter of the non-shadowed interferers. For the elevation angles 90° of the receiving satellite, the gamma distribution approximation diverges from the actual values because the density of interferers is small ($\lambda_{3dB} \approx 5$), and the theory presented in this paper does not apply.

itself out in the expression of SIR (2). In other words, the altitude or the elevation angle of the satellite does not affect the distribution of SIR should λ_{3dB} remain constant. The only parameters affecting the distribution of SIR are the mean transmitting powers and fading conditions.

The simulated values are acquired by Monte Carlo simulations by calculating an average over different realizations of the PPP and fading. In simulations, we use a Gaussian antenna as given in (3). Furthermore, an additive -84 dBm noise component is present.

A. Transmitter and receiver characteristics

We consider one type of omnidirectional interfering transmitters transmitting with power 43 dBm. Shadowing is present at a probability 0.44 in the elevation angles of 35° , and the powers of the shadowed transmitters are reduced by 11 dBm. This leads us to two classes of interferers: shadowed $\Phi^{(1)}$ and non-shadowed transmitters $\Phi^{(2)}$. Shadowed interferers experience Rayleigh fading $K_I^{(1)} = 0$, and non-shadowed interferers experience Rician fading with Rician parameter $K_I^{(2)} = 65$ or $K_I^{(2)} = 11$. No shadowing is present with elevation angles 90° . Test transmitter power is 69.1 dBm, and it experiences Rician fading with $K = 65$ or $K = 11$. The interfering transmitters' properties are set to mimic a realistic LEO network. The interfering transmitting powers follow FCC regulations for mobile interfaces operating in 28, 39, and 37 GHz bands in [21]. The fast and slow fading conditions follow the values given in the survey on terrestrial-satellite transmitters [22]. Path-loss function $L(d) = (3.55d)^{-2}$ and receiving satellites gain width $\varphi_{RX} = 1.5/2^\circ$ follows the characteristics of a SpaceX constellation [23].

B. Remarks on the results

With small densities of interferers (figure 3elevation angle 90°), the approximation is reasonable, but the tail distribution diverges as seen in the figure. With high densities (figure

effig:dens2 elevation angle 35° and figure 2), the gamma distribution approximation matches very well. Depending also on the relative transmitting powers, densities, and shadowing and fading conditions in the different classes of interferers, we suggest that at least $\lambda_{3dB} \approx 5$ so that the gamma function approximation is valid. The variance and skewness of the distribution increase with lower densities of interferers. However, the tails are not heavy-tailed (neither in simulations nor in gamma function approximation) in the sense that they decay faster than the exponential distribution.

The SIR is smaller with low satellite elevation angles if the density of interferers is kept constant; approximately 5 dB variation is present in the figures 2 and 3. This is due to the widening of the footprint of the satellite that causes more interferers to be present inside the main lobe. It is evident that a satellite receiver in the lower altitudes tolerates more interferers per km^2 than a receiver in the high altitudes. In these contexts, the gamma distribution approximation of SIR can be used to study power control in a terrestrial-satellite link. The test transmitter fading conditions have a bigger effect on the SIR distribution than fading conditions of the interferers.

V. CONCLUSION

We derived a gamma distribution approximation for the distribution of SIR in a terrestrial-satellite link. The approximation is applicable when the receiver antenna beam pattern is narrow and the density of interferers is large. With smaller densities, the interference will become impulsive as there is a high chance of having no interferers inside the receiving satellite's main lobe. We suggest that the gamma distribution is a good approximation when there are 5 interferers on average – or more – inside the satellite's 3 dB footprint. The 1.5° 3 dB beamwidth of the receivers used in this paper is sufficiently narrow for the approximation to work. We conclude that the gamma distribution can be used as a prior distribution for the SIR in a terrestrial-satellite uplink in highly populated areas, such as cities, where dense (possibly heterogeneous) networks are causing additive co-channel interference.

The closed-form SIR distribution presented in this paper is straightforward to derive and applies to various fading conditions and transmitter characteristics as well as different altitudes and elevation angles of a LEO satellite. Furthermore, overlapping heterogeneous interfering networks can be considered. A downside is that the transmitters have to be considered to be Poisson distributed, that is, completely independently located. Furthermore, only omnidirectional antenna patterns for the interferers were considered. However, these are realistic assumptions, particularly in the case of mobile user devices.

This paper provides essential insight into the SIR distribution in an LEO network.

REFERENCES

- [1] F. Babich, M. Comisso, A. Cuttin, M. Marchese, and F. Patrone, "Nanosatellite-5g integration in the millimeter wave domain: A full top-down approach," *IEEE Transactions on Mobile Computing*, vol. 19, no. 2, pp. 390–404, 2020.
- [2] S. Kim, E. Visotsky, P. Moorut, K. Bechta, A. Ghosh, and C. Dietrich, "Coexistence of 5g with the incumbents in the 28 and 70 ghz bands," *IEEE Journal on Selected Areas in Communications*, vol. 35, no. 6, pp. 1254–1268, 2017.
- [3] X. Artiga, J. Nunez-Martinez, A. Perez-Neira, G. J. L. Vela, J. M. F. Garcia, and G. Ziargkas, "Terrestrial-satellite integration in dynamic 5g backhaul networks," in *2016 8th Advanced Satellite Multimedia Systems Conference and the 14th Signal Processing for Space Communications Workshop (ASMS/SPSC)*, pp. 1–6, 2016.
- [4] D. Middleton, "Statistical-physical models of electromagnetic interference," *IEEE Transactions on Electromagnetic Compatibility*, vol. EMC-19, no. 3, pp. 106–127, 1977.
- [5] K. Gulati, B. L. Evans, J. G. Andrews, and K. R. Tinsley, "Statistics of co-channel interference in a field of poisson and poisson-poisson clustered interferers," *IEEE Transactions on Signal Processing*, vol. 58, no. 12, pp. 6207–6222, 2010.
- [6] X. Yang and A. Petropulu, "Co-channel interference modeling and analysis in a poisson field of interferers in wireless communications," *IEEE Transactions on Signal Processing*, vol. 51, no. 1, pp. 64–76, 2003.
- [7] J. Ilow and D. Hatzinakos, "Analytic alpha-stable noise modeling in a poisson field of interferers or scatterers," *IEEE Transactions on Signal Processing*, vol. 46, no. 6, pp. 1601–1611, 1998.
- [8] G. Samorodnitsky and M. S. Taqqu, *Stable Non-Gaussian Random Processes: Stochastic Models with Infinite Variance: Stochastic Modeling*. Routledge, 2017.
- [9] K. Gulati, B. L. Evans, and K. R. Tinsley, "Statistical modeling of co-channel interference in a field of poisson distributed interferers," in *2010 IEEE International Conference on Acoustics, Speech and Signal Processing*, pp. 3490–3493, 2010.
- [10] R. W. Heath, M. Kountouris, and T. Bai, "Modeling heterogeneous network interference using poisson point processes," *IEEE Transactions on Signal Processing*, vol. 61, no. 16, pp. 4114–4126, 2013.
- [11] P. Madhusudhanan, J. G. Restrepo, Y. Liu, and T. X. Brown, "Carrier to interference ratio analysis for the shotgun cellular system," in *GLOBECOM 2009 - 2009 IEEE Global Telecommunications Conference*, pp. 1–6, 2009.
- [12] N. Okati, T. Riihonen, D. Korpi, I. Angervuori, and R. Wichman, "Downlink coverage and rate analysis of low earth orbit satellite constellations using stochastic geometry," *IEEE Transactions on Communications*, vol. 68, no. 8, pp. 5120–5134, 2020.
- [13] N. Okati and T. Riihonen, "Stochastic analysis of satellite broadband by mega-constellations with inclined LEOs," in *2020 IEEE 31st Annual International Symposium on Personal, Indoor and Mobile Radio Communications*, pp. 1–6, 2020.
- [14] A. Yastrebova, I. Angervuori, N. Okati, M. Vehkaperä, M. Höyhtyä, R. Wichman, and T. Riihonen, "Theoretical and simulation-based analysis of terrestrial interference to LEO satellite uplinks," in *GLOBECOM 2020 - 2020 IEEE Global Communications Conference*, pp. 1–6, 2020.
- [15] B. A. Homssi and A. Al-Hourani, "Modeling uplink coverage performance in hybrid satellite-terrestrial networks," *IEEE Communications Letters*, vol. 25, no. 10, pp. 3239–3243, 2021.
- [16] B. Di, L. Song, Y. Li, and H. V. Poor, "Ultra-dense LEO: Integration of satellite access networks into 5g and beyond," *IEEE Wireless Communications*, vol. 26, no. 2, pp. 62–69, 2019.
- [17] C. Y.-S. Lee C.-H, Shih C.-Y., "Stochastic geometry based models for modeling cellular networks in urban areas," *Wireless Netw*, no. 19, p. 1063–1072, 2012.
- [18] T. D. Novlan, H. S. Dhillon, and J. G. Andrews, "Analytical modeling of uplink cellular networks," *IEEE Transactions on Wireless Communications*, vol. 12, no. 6, pp. 2669–2679, 2013.
- [19] B. B. François Baccelli, *Stochastic Geometry and Wireless Networks*, vol. 1. NoW Publishers, 2009.
- [20] E. Díaz-Francés and F. J. Rubio, "On the existence of a normal approximation to the distribution of the ratio of two independent normal random variables," *Statistical Papers*, 2013.
- [21] F. C. Commission, "Report and order and further notice of proposed rulemaking," tech. rep., Federal Communications Commission, 2016.
- [22] E. Lutz, D. Cygan, M. Dippold, F. Dolainsky, and W. Papke, "The land mobile satellite communication channel-recording, statistics, and channel model," *IEEE Transactions on Vehicular Technology*, vol. 40, no. 2, pp. 375–386, 1991.
- [23] M. Albulet, "SpaceX v-band non-geostationary satellite system," tech. rep., Space Exploration Technologies Corp., 2017.

Publication III

I. Angervuori, M. Haenggi and R. Wichman. Meta Distribution of the SIR in a Narrow-Beam LEO Uplink. *IEEE Transactions on Communications*, vol. 73, no. 9, pp. 8260-8273, Sept. 2025, doi: 10.1109/TCOMM.2025.354773, 2025.

© 2025

Reprinted with permission.

Meta Distribution of the SIR in a Narrow-Beam LEO Uplink

Ilari Angervuori[✉], Student Member, IEEE, Martin Haenggi[✉], Fellow, IEEE,
and Risto Wichman[✉], Senior Member, IEEE

Abstract—We focus on stochastic geometry analysis of a low Earth orbit (LEO) narrowband terrestrial-satellite uplink with satellite base stations (SBSs) in a uniform constellation equipped with narrow Gaussian beams. The served and interfering omnidirectional user equipments (UEs) are distributed on the Earth’s surface according to a homogeneous Poisson point process (HPPP) with Nakagami faded signals. This study presents a detailed but comprehensive mathematical analysis of several key metrics: the signal-to-interference ratio (SIR), the SIR meta distribution (MD), the signal-to-interference-plus-noise ratio (SINR), and the average throughput. Many results are presented in simple analytical and closed forms containing more insight than the expressions proposed in prior works. The results indicate an optimal UE density depending on the altitude, elevation angle, and the width of the antenna gain, maximizing the average throughput. However, this optimal density leads to a significant variance in the user experience regarding link quality (*i.e.*, the users are not treated fairly).

Index Terms—Low Earth orbit, stochastic geometry, coverage probability, meta distribution, average throughput, Lomax distribution.

I. INTRODUCTION

A. Motivation

FIFTH-GENERATION (5G) and beyond wireless communication systems are setting new standards of reliability and connectivity [1]. The emerging Low Earth Orbit (LEO) satellite networks have the potential to significantly increase coverage, especially in far-flung areas: incorporating such networks with terrestrial networks can facilitate a seamless coverage continuum [2]. Several large LEO constellation projects are already being developed and planned, including Starlink, Kuiper, LeoSat, OneWeb, and Telesat. Kuiper, LeoSat, OneWeb, and Telesat. 3GPP aims to adapt existing satellite and terrestrial networks to provide direct connectivity from hand-held equipment to LEO satellites using frequencies assigned to mobile satellite services or those assigned to legacy terrestrial networks. An extensive study of potential

Received 10 December 2024; accepted 17 February 2025. The work was supported by the Research Council of Finland Grant 339446 and the Vilho, Yrjö and Kalle Väisälä Foundation. The associate editor coordinating the review of this article and approving it for publication was N. Mokari. (*Corresponding author: Ilari Angervuori.*)

Ilari Angervuori and Risto Wichman are with the Department of Electrical Engineering, Aalto University, 02150 Espoo, Finland (e-mail: ilari.angervuori@aalto.fi; risto.wichman@aalto.fi).

Martin Haenggi is with the Department of Electrical Engineering, University of Notre Dame, Notre Dame, IN 46556 USA (e-mail: mhaenggi@nd.edu).

Digital Object Identifier 10.1109/TCOMM.2025.3547734

LEO network configurations is presented in [3], indicating that numerous implementations are possible. Due to the large footprint, a single satellite can serve several user equipments (UEs). At the same time, the large cell size causes interference between terrestrial and non-terrestrial users and systems.

The stochastic geometry system-level analysis offers valuable insights that complement other link and system-level models and simulations of terrestrial and non-terrestrial communications. This analytical method helps us understand how different deployment parameters affect performance metrics. In particular, it provides comprehensive information on the satellite base station (SBS) reliability, coverage probability, and throughput. Ultimately, this knowledge aids in determining optimal network configurations and allows for more efficient allocation of simulation resources.

B. Related Work

As a relatively new concept introduced in [4], the analysis of the signal-to-interference ratio (SIR) meta distributions (MD) for terrestrial networks has become well-established in the literature. Additionally, SIR MD has been applied to the LEO networks. An analysis of the SIR MD under the Nakagami fading model was proposed in [5] and [6], where the SIR MD was studied in a LEO downlink. Both papers model the satellites by either the homogeneous Poisson point process (HPPP) or the homogeneous binomial point process (HBPP) on a sphere and the transmitters as a HPPP, allowing the ergodic interpretation of the SIR MD as “what fraction of users can achieve a given transmission reliability for a given SIR threshold”.¹ In [5], the satellites were assumed to have an omnidirectional antenna beam. In contrast, in [6], a perfect beam alignment with the terrestrial base station was assumed, causing no interference to the other devices. To the best of our knowledge, the SIR MDs for the LEO uplink are yet to be explored.

The following literature review focuses on papers on the proposed state-of-the-art stochastic geometry frameworks in the LEO uplink. A comprehensive literature review addressing other LEO scenarios can be found in [8]. Furthermore, the book [9] has been published on the subject. The work in [10] is one of the first papers addressing the stochastic geometry

¹Although strictly speaking, the HPPP is not ergodic on the sphere, the condition for the ergodicity [7, Def. 2.30] holds approximately for large densities.

TABLE I
STOCHASTIC GEOMETRY LEO UPLINK AND LEO SIR MD MODELS IN THE LITERATURE

Proposed by	Scenario	Earth transmitter model	Satellite constellation model	Earth-to-satellite fading and shadowing model	System metrics and results in C=closed-form expression A=analytic expression M=mathematical expression	System type	Satellite antenna model
This paper	Uplink direct communication	HPPP	Uniform constellation	Nakagami fading	SIR MD (M for the moments), Coverage probability (A), Average throughput (C)	Interference-limited, Interference-plus-noise-limited	Narrow Gaussian beam
[5]	Downlink direct communication	HPPP	HPPP	Nakagami fading	SIR MD (A for the moments)	Interference-limited	Omnidirectional
[6]	Downlink hybrid network	HPPP	HBPP	Nakagami fading	SIR MD (A for the moments)	Interference-limited	Perfect beam alignment
[10]	Uplink direct communication	HPPP	HPPP	Shifted exponential power fading	Coverage probability (M), Average throughput (M)	Interference-limited	Omnidirectional
[11]	Uplink direct communication	HPPP	Uniform constellation	Rician fading with a two-tier shadowing model	Coverage probability (A)	Interference-limited	Narrow Gaussian beam
[12]	Uplink direct communication	HPPP	Walker-Star,	Shadowed Rician fading	Coverage probability (M), Average throughput (M)	Interference-plus-noise-limited	ITU-R beam
[13]	Uplink direct communication	HPPP	Deterministic polar constellation	Shadowed Rician fading	Coverage probability (M), Average throughput (M)	Interference-plus-noise-limited	ITU-R beam
[14]	Uplink direct communication	HBPP	HBPP, Walker-Star, Walker-Delta	Gaussian mixture shadowing model	Coverage probability (M)	Interference-plus-noise-limited	Boxcar function
[15]	Uplink hybrid communication	HPPP	HPBP, Walker-Star, Walker-Delta	Gaussian mixture shadowing model	Coverage probability (M)	Interference-plus-noise-limited	Boxcar function
[16]	Uplink direct and hybrid communication	Poisson cluster process	HBPP	Shadowed Rician fading	Coverage probability (M)	Interference-plus-noise-limited	Boxcar function
[17]	Uplink direct communication	HPPP, Poisson hard-core p.p.	Deterministic two altitude circular orbits	Rician fading	Coverage probability (A)	Interference-plus-noise-limited	Perfect beam alignment and constant sidelobes

modeling of the LEO uplink, where the coverage probability and average throughput were studied assuming omnidirectional antennas for both the satellite and the transmitters. As in many similar works, the PPP model for the satellites has proven effective in approximating deterministic constellations. In [11], the SIR distribution was studied for large network densities in an interference-only channel with a Gaussian antenna beam under Rician fading with a two-tier shadowing model. A shadowed Rician model and a realistic ITU-R antenna beam were used in [12] and [13]. Similar to this paper, in [12], it was noted that a particular constellation density maximizes the throughput. The system model is realistic; however, the derived formulas are complicated to evaluate and may lack clear insight. A Gaussian mixture model for the fading with a boxcar-type antenna beam model was used in [14] and [15]. Modeling was based on working with the mean interference from the transmitters, which may be accurate with wide antenna beams; however, the mean fails to grasp the highly varying nature of the interference in narrow antennas. Uplink hybrid and direct communication with IoT devices, including battery lifetime, were studied in [16]. Similar to this paper and [12], in [16], an optimal density for the satellites (proportional to the number of Earth transmitters) was found to maximize the performance. Similar to this paper, a planar HPPP model was used in [17]. Additionally, in [17], the Poisson hard-core model was introduced. All of the mentioned papers and the system model details are summarized in Table I.

We present a tractable analytical framework for the narrow-beam LEO that yields insightful results distinct from

previous works. Additionally, our paper offers a fine-grained analysis of the variation in the uplink quality of the SBSs, which has yet to be addressed in the existing literature.

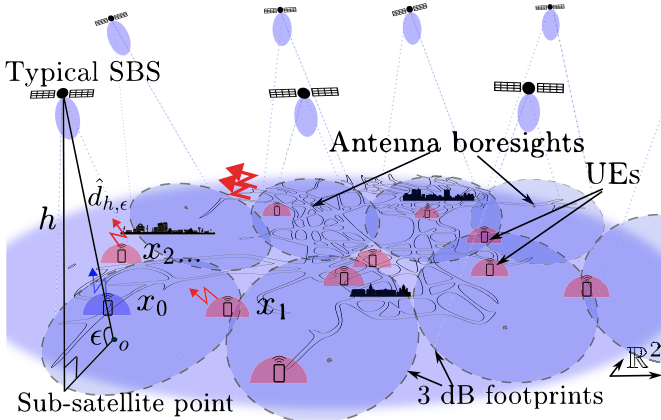
C. Our Contributions

The contributions of the work are listed as follows.

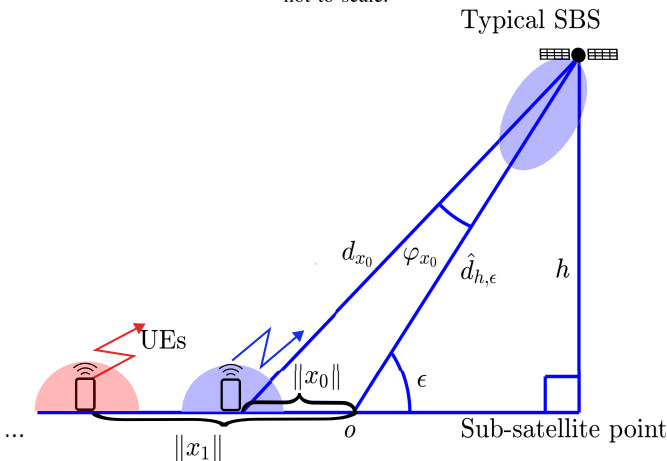
- We present a novel, simplified, narrow-beam LEO system model that provides a tractable analytical framework for stochastic geometry analysis.
- We derive the moments of the SIR MD and study user experiences in different network settings through the distribution.
- We derive the SIR distribution in a closed form and the signal-to-interference-plus-noise ratio (SINR) distribution in analytic form.
- We derive the average throughput in a simple closed form and an optimal density for the Poisson layout of UEs that maximizes the average rate.
- We observe a significant trade-off between the optimal average throughput and user experience consistency regarding the link quality.

D. Organization of the Paper

In Section II, we formulate and compare the planar and spherical system models and introduce the fading and antenna pattern models. Section III derives the moments of the SIR MD and provides two different approximations based on the



(a) Interpretation of the *planar* system model with the SBSs in adjacent orbits serving an urban area and a realization of the UEs. The altitudes are not to scale.



(b) The typical SBS as seen from the side. The transmitters are projected into line $(0, \infty)$ according to their norm.

Fig. 1. The simplified narrow-beam LEO uplink system model. The SBS antenna boresight is oriented towards o , the focus point of the elliptical footprint. The omnidirectionally transmitting UEs $\{x_i\}$ are located according to the HPPP on the plane. The nearest transmitter, x_0 , is the served UE.

moments: beta distribution and Chebyshev-Markov inequalities. In Section IV, we study the SIR, SINR, and throughput distributions. The key insights of the results are summarized in Section V.

II. SYSTEM MODEL

We present two system models: the simplified planar system model used in the analysis and the spherical system model used in the simulations. A sketch of the simplified planar system model is depicted in Figures 1a and 1b.

A. Approximate Planar Model of the Narrow-Beam LEO Uplink

We study a short period of use over multiple coherence times in a high-frequency narrow-band terrestrial-satellite uplink Nakagami fast-fading channel in a single-tier network. The link quality from the perspective of a SBS is investigated. We assume that UEs with omnidirectional antennas, like mobile phones, are randomly located on the Earth surface,

TABLE II
GLOSSARY OF PRINCIPAL SYMBOLS

Symbol	Explanation
h	Altitude of the SBSs.
ϵ	Elevation angle of the SBSs.
$G[\cdot]$	The SBS antenna gain.
φ_{RX}	Halfwidth of the SBSs -3 dB gain.
$\Theta \subset E$	HPPP on the Earth surface $E \subset \mathbb{R}^3$ of density λ .
$\Phi \subset \mathbb{R}^2$	HPPP on the plane of density λ .
$\ x\ $	Distance of $x \in \Phi$ from the origin $o = (0, 0) \in \mathbb{R}^2$.
x_0	Nearest point to the origin in Φ .
$D_{h,\epsilon}$	A scaling constant of $\ x\ $; $D_{h,\epsilon} = \sin^2(\epsilon)/h$.
κ	Parameter that reflects the approximate mean number of UEs inside a SBS -3 dB footprint; $\kappa = \lambda\pi(h\varphi_{RX}/\sin^2(\epsilon))^2/\kappa/\log(2)$.
m	Nakagami- m fading parameter.
g_x	The power fading gain of mean 1 of a transmitter $x \in \Phi$ or $x \in \Theta$. Corresponds to a Nakagami- m distributed amplitude fading; $m = 1$ corresponds to the exponential distribution, and $m = \infty$ is deterministic.
θ	SIR or SINR threshold for a successful transmission.
I	Interference at the typical SBS in the planar model.
S	The signal power of the served UE at the typical SBS in the planar model.
\hat{I}	Interference at the typical SBS in the spherical model.
\hat{S}	The signal power of the served UE at the typical SBS in the spherical model.
$\hat{d}_{h,\epsilon}/d_0$	The distance between the SBS and the focus point in the planar model divided by a normalizing distance.
W	Constant noise power.
γ	Power path loss exponent.

represented as a plane. The SBSs can work as an independent network or complement a terrestrial network, and the interfering transmitters can be considered to be within the same cell, adjacent cells, overlapping cells, or part of a terrestrial network served by a terrestrial BS.

The UEs form a HPPP $\Phi \subset \mathbb{R}^2$ of density λ . The Poisson assumption can be justified by the independent mobility patterns of UEs. Furthermore, the multipath fading of the signals can make an arbitrary network seem Poisson at the receiver [18, Sec. 4.3]. The SBSs form a homogeneous point pattern (deterministic or random), allowing the ergodic interpretation of the performance metrics over the SBSs. Because the HPPP is translation invariant, all points are statistically equivalent. Therefore, we can refer to the concept of a *typical* SBS. The SBS antennas are narrow-beam considered to serve a local homogeneous environment, such as a rural or urban area. Consequently, the scattering and attenuation caused by the weather conditions and Doppler shifts are the same for all relevant UEs, thus not affecting their relative signal strengths at the SBS.

We study the SIR and SINR distributions at the typical SBS serving the terrestrial UE from which it receives the maximum mean signal power. The UEs are transmitting at the normalized power $P = 1$. The typical SBS is at altitude h , and its Gaussian antenna's $G[\cdot]$ gain boresight is directed toward a point on the Earth surface for which the SBS is at the elevation angle ϵ —this is a focus point of the elliptical footprint, considered the origin $o \triangleq (0, 0) \in \mathbb{R}^2$. The values of h and ϵ determine the distance to the satellite from o , given by the geometric relation $\hat{d}_{h,\epsilon} \triangleq h/\sin(\epsilon)$. In this work, we focus

on LEO altitudes of $h \in [200, 2000]$ km. We will consider that $\epsilon \geq 45^\circ$. (We restrict the elevation angle to ensure the simplified narrow-beam LEO model is accurate. However, we make an exception in Figures 3a, 3b and 4, where we compare the spherical and the planar models with the elevation angle $\epsilon = 35^\circ$, which is the minimum elevation angle in a LEO system proposed in [19].)

This work focuses on the SIR and SINR of the nearest transmitter. The served UE is formally defined as

$$x_0 \triangleq \arg \min \{x \in \Phi : \|x\|\}, \quad (1)$$

where $\|\cdot\|$ is the Euclidean distance.

In the following, we write $f(x) \sim g(x)$, as $x \rightarrow a$, if the limit $\lim_{x \rightarrow a} f(x)/g(x) = 1$. Considering Figure 1b, for each angle φ_x between the transmitter $x \in \Phi$ and the typical SBS antenna boresight, we have

$$\varphi_x \sim D_{h,\epsilon} \|x\|, \quad \|x\| \rightarrow 0, \quad (2)$$

where $D_{h,\epsilon} \triangleq \sin^2(\epsilon)/h$ is the derivative of the function $\|x\| \mapsto \varphi_x$ at $\|x\| = 0$ (the details given in Appendix A). Note that (2) is only the first-order Taylor expansion of φ_x at $\|x\| = 0$; the approximation is sufficient if the antenna pattern decays fast for large φ_x .

Let us define the path loss law by

$$\ell(x) \triangleq \frac{G[\varphi_x]}{(d_x/d_0)^\gamma}, \quad \gamma \geq 0, \quad (3)$$

where d_x is the distance between the UE and the SBS, and d_0 is a normalizing distance. Combining (2) with (3) yields $\ell(x) \sim G[D_{h,\epsilon} \|x\|]/(d_x/d_0)^\gamma, \|x\| \rightarrow 0$.

Furthermore, we assume a narrow antenna beam and the relevant transmitters are located in a small region close to each other around o and $d_x \approx \hat{d}_{h,\epsilon}$ for the relevant $x \in \Phi$. Along these lines, the random process of path losses $\{\ell(x) : x \in \Phi\}$ is approximated with the gain process (GP)

$$\mathcal{G} = \{x \in \Phi : G[D_{h,\epsilon} \|x\|]\} \quad (4)$$

multiplied by the constant $(\hat{d}_{h,\epsilon}/d_0)^{-\gamma}$.

\mathcal{G} is a particular case of the projection process that has been extensively studied in the literature [18, Ch. 4]. By the mapping theorem [7, Thm. 2.34], it is a PPP on $(0, 1)$.²

Because of its analytical tractability, we model the small-scale fading with the Nakagami- m fading model, where $m \in \mathbb{N}$ is the Nakagami fading parameter. For each UE $x \in \Phi$, the amplitude fading gain follows an independent Nakagami distribution with shape parameter m and spread parameter 1. Hence, each transmission power is multiplied by an independent gamma-distributed fading gain g_x of mean 1 with shape and scale parameters m and $1/m$, respectively. The Nakagami distribution closely approximates the Rician distribution, widely utilized as a fading model in satellite communications [20, Sec. 6.7.1]. Furthermore, the gamma distributed power fading can be used to approximate the shadowed Rician power fading distribution [16].

²Interestingly, incorporating independent fading r.v.'s $\{H_x\}$ the projection process with the fading $\{x \in \Psi : H_x G[D_{h,\epsilon} \|x\|]\}$ can appear Poisson, even if the underlying Ψ is not a PPP [18, Sec. 4.3].

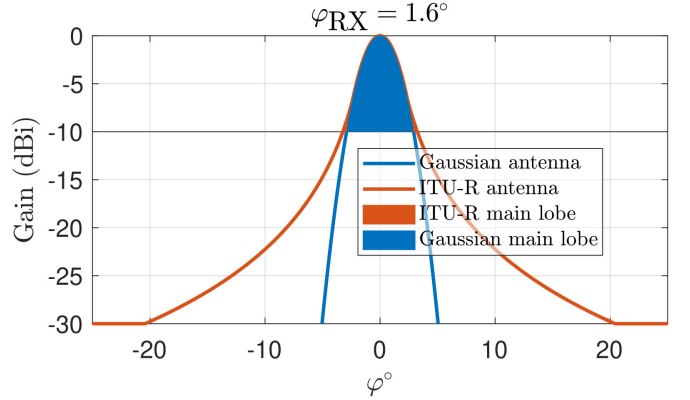


Fig. 2. Comparison between the Gaussian and [21, ITU-R LEO reference radiation patterns]. The gain of the Gaussian antenna in the main lobe (-10 dB lobe) is almost identical to the ITU-R main lobe. However, there is a slight difference towards the edges of the main lobe. The fast-decaying Gaussian beam essentially corresponds to the main lobe component.

The antenna gain $G[\cdot] : [0, \infty) \rightarrow (0, 1]$ is assumed to be Gaussian, i.e.,

$$G[\varphi] = 2^{-\varphi^2/\varphi_{RX}^2}, \quad (5)$$

where φ_{RX} is the halfwidth of the -3 dB antenna gain. Except Section II-C, we use the value $\varphi_{RX} = 1.6^\circ$, corresponding to the LEO antenna pattern proposed in the International Telecommunication Union Recommendations (ITU-R) [21]. Despite being an idealized antenna pattern, the Gaussian response accurately models the main lobe (-10 dB lobe) of many antenna patterns, particularly the ITU-R pattern, cf. Figure 2. This work considers the interference energy from the sidelobes a nonnegative constant noise but is not explicitly characterized. This approach works as long as the UE density is high enough and the served UE is likely to be in the main lobe.³

B. Spherical System Model and Monte Carlo Simulation

A sketch of the geometry of the spherical model is presented in Appendix B.

We compare the analytical results from the planar model to Monte Carlo simulations of the spherical model. The Monte Carlo simulations assume a spherical Earth with a radius of $R_\oplus = 6378$ km. We denote the HPPP of the UEs visible to the satellite of density λ on the Earth surface by $\Theta \subset E$. The number of samples depends on the density: we simulate, on average, 10^6 UEs inside the -100 dB footprint (of the Gaussian beam). The elliptical footprint's antenna boresight location is the ellipse's nearest focus point, o_E —the ellipse represented in terms of latitude and longitude. The PPP on the sphere can be constructed from the PPP on the plane by the *area-preserving* mapping $(x_1, x_2) \mapsto (1, x_1, \sin^{-1}(x_2))$ from the rectangle $[-\pi, \pi] \times [-1, 1]$ to the spherical coordinates. We use a homography from the ellipse to a circle to find the

³Analogously to the semi-analytical simulation methods [22], the possible interference component from the sidelobes can be modeled with a constant corresponding to the mean aggregate power from the interferers outside the main lobe because of the relatively small variance of the total interference. Hence, the sidelobe component can be incorporated in a constant noise term.

SBS antenna gain of each UE. In the Monte Carlo simulations, the angles $\{\varphi_u\}$, the distances $\{d_u\}$, $u \in \Theta$, and consequently the path loss law (3) are based on the spherical Earth model and calculated by basic geometry. For example, we have

$$d_{h,\epsilon} \triangleq d_{o_E} = \sqrt{R_\oplus^2 + (R_\oplus + h)^2 - 2R_\oplus(R_\oplus + h)\cos(\xi)} \quad (6)$$

for the distance between the SBS and the focus point o_E , where $\xi = \xi(\epsilon)$ is the central angle between o_E and the sub-satellite point on the spherical Earth's surface (the details given in Appendix B). The fading model is the Nakagami- m , and the antenna gain is Gaussian (5).

C. Total Received Power and Its Convergence Properties in the Planar Model w.r.t. the Spherical Model

In this section, we compare the *total received power* from all transmitters in the system model presented in Section II with that of the spherical model in Section II-B.

We define $u_0 \triangleq \arg \min\{u \in \Theta : d_u\}$. The total received power at the typical SBS from the UEs in the PPP Θ on the Earth's surface above the horizon is defined as

$$\mathring{P}_{\text{tot}} \triangleq \mathring{I} + \mathring{S} = \sum_{u \in \Theta} g_u \ell(u) = \sum_{u \in \Theta} \frac{g_u G[\varphi_u]}{(d_u/d_0)^\gamma}, \quad (7)$$

where \mathring{S} is the signal strength at the receiver of the nearest transmitter u_0 , and \mathring{I} is the interference component consisting of the received signal powers from $\Theta \setminus \{u_0\}$.

We validate the approximate system model by studying the convergence properties of the mean and the second moment of the simulated $\mathring{P}_{\text{tot}}$ to the mean and the second moment of

$$P_{\text{tot}} \triangleq I + S = \frac{\sum_{x \in \Phi} g_x G[D_{h,\epsilon} \|x\|]}{(\hat{d}_{h,\epsilon}/d_0)^\gamma} = \frac{\sum_{x' \in \mathcal{G}} g_x x'}{(\hat{d}_{h,\epsilon}/d_0)^\gamma}. \quad (8)$$

The fading models are equal in the planar and spherical models, and the difference is in the geometry. Hence, we focus on the geometric accuracy of the approximate model and set $g_x \equiv 1$, i.e., $m = \infty$, in this subsection. The fading does not affect the first moment of the total received power. In the following, we refer to Lemma 1 regarding the density $\lambda_G(r) = \tilde{\kappa}/r$, $\tilde{\kappa} = \lambda\pi(h\varphi_{\text{RX}}/\sin^2(\epsilon))^2/\log(2)$, and the Poisson property of the GP (which is needed for the variance). For $g_x \equiv 1$, [7, Cor. 4.8] gives the expected value and the variance, $\text{var}(P_{\text{tot}}) = \mathbb{E}(P_{\text{tot}}^2) - \mathbb{E}(P_{\text{tot}})^2$, of P_{tot} :

$$\begin{aligned} \mathbb{E}(P_{\text{tot}}) &= \left(\frac{d_0}{\hat{d}_{h,\epsilon}} \right)^\gamma \int_{\mathbb{R}^2} G[D_{h,\epsilon} \|x\|] \lambda dx \\ &= \left(\frac{d_0}{\hat{d}_{h,\epsilon}} \right)^\gamma \int_0^1 r \lambda_G(r) dr = \frac{d_0^\gamma h^{2-\gamma} \pi \lambda \varphi_{\text{RX}}^2}{\sin^{4-\gamma}(\epsilon) \log(2)}, \quad (9) \\ \text{var}(P_{\text{tot}}) &= \left(\frac{d_0}{\hat{d}_{h,\epsilon}} \right)^{2\gamma} \int_{\mathbb{R}^2} G[D_{h,\epsilon} \|x\|]^2 \lambda dx \\ &= \left(\frac{d_0}{\hat{d}_{h,\epsilon}} \right)^{2\gamma} \int_0^1 r^2 \lambda_G(r) dr = \frac{d_0^\gamma \sin^\gamma(\epsilon)}{2h^\gamma} \mathbb{E}(P_{\text{tot}}). \end{aligned} \quad (10)$$

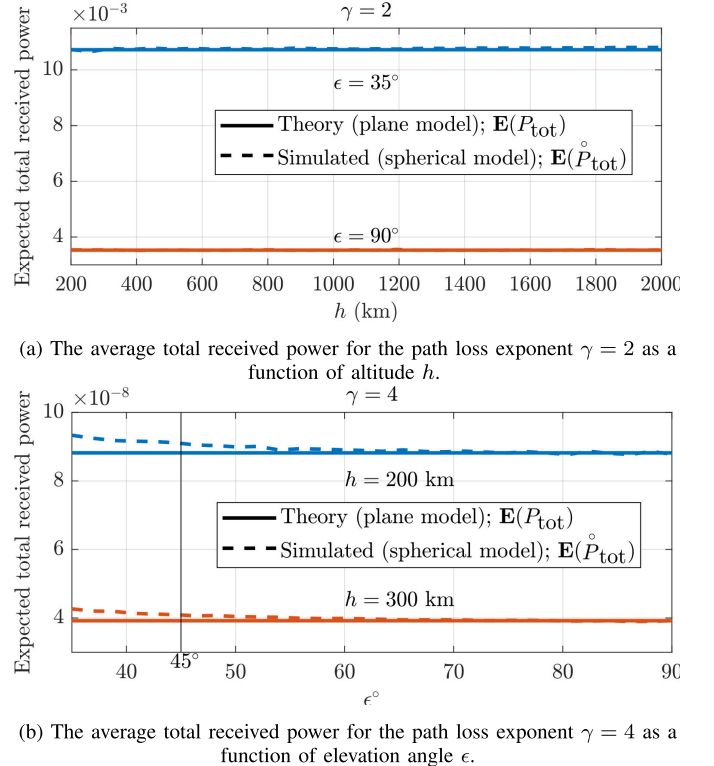


Fig. 3. Comparison of the expected total received power based on the simulated spherical model and the theoretical planar model. The parameters $\varphi_{\text{RX}} = 1.6^\circ$, $P = 1$, $\lambda = 1/\text{km}^2$, $\gamma \in \{2, 4\}$, $h \in [200, 2000]$ km, $\epsilon \in [35^\circ, 90^\circ]$ are used.

An interesting observation from (9) and (10) is that for the free-space path loss exponent $\gamma = 2$, for given λ , ϵ , and φ_{RX} , the mean of the total received power does not depend on the altitude of the typical SBS; the path loss becomes increasingly prominent, but there are more UEs present in the main lobe as we increase h . However, $\text{var}(P_{\text{tot}})$ rapidly increases when we decrease the altitude. On the other hand, P_{tot} approaches a constant for large h . For $\gamma > 2$, the expected total received power decreases as the altitude increases. For $\gamma = 4$, $\mathbb{E}(P_{\text{tot}})$ does not depend on the elevation angle of the SBS.

Figures 3a and 3b show the total received powers $\mathring{P}_{\text{tot}}$ and P_{tot} for $\gamma \in \{2, 4\}$ for different ϵ and h . The insights derived from the theoretical model of mean and variance apply to the spherical model, especially for $\gamma = 2$. For $\gamma = 2$, the average total received power is approximately independent of the altitude, and for $\gamma = 4$, the received power is almost independent of the elevation angle.

Figure 4 shows the ratio of the second moments $\mathbb{E}(\mathring{P}_{\text{tot}}^2)/\mathbb{E}(P_{\text{tot}}^2)$ w.r.t. the antenna width $\varphi_{\text{RX}} \in [0.6^\circ, 6.7^\circ]$ for different values of h and γ . The density $\lambda = 1/\text{km}^2$, and the elevation angle $\epsilon = 35^\circ$, which is the minimum elevation angle in a LEO system proposed in [19]. Due to the geometry, it is the worst-case scenario for the error between the models. The ratios for $\epsilon > 35^\circ$ are closer to 1 for each h . The ratios tend to 1 for $\gamma = 2$ as $\varphi_{\text{RX}} \rightarrow 0$. There is a threshold after which $\mathbb{E}(\mathring{P}_{\text{tot}}^2)$ becomes exponentially larger than $\mathbb{E}(P_{\text{tot}}^2)$. This is caused by the differences in the geometry. However, the horizon restricting the energy from the UEs in the spherical model limits this exponential increase for

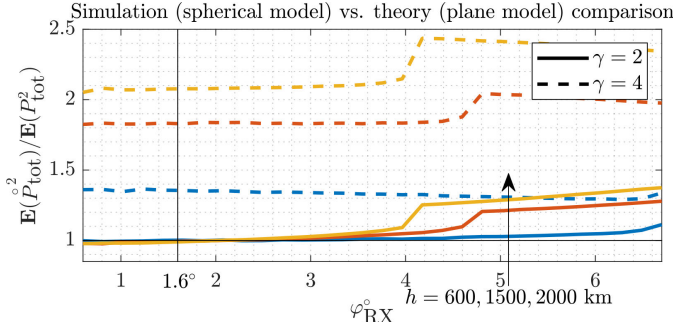


Fig. 4. The ratio of the second moments of the simulated and theoretical total received powers. The parameters $h \in \{600, 1500, 2000\}$ km, $\lambda = 1/\text{km}^2$, $\epsilon = 35^\circ$, $\varphi_{\text{RX}} \in [0.6^\circ, 6.7^\circ]$ and $\gamma \in \{2, 4\}$ are used.

larger φ_{RX} . For $\gamma = 4$, convergence to 1 does not happen. This is due to the difference in the averages of $\{d_u\}_{u \in \Theta}$ and $\{d_x\}_{x \in \Phi}$, which cancels out for $\gamma = 2$. The theoretical model could be improved using the more complicated $d_{h,\epsilon}$ instead of $\hat{d}_{h,\epsilon}$ in (8). However, the theoretical SIR is independent of the path loss exponent, which also holds (up to the accuracy we are interested in) in the spherical model. We will validate this using the path loss exponents $\gamma \in \{2, 4\}$ in the simulations in Sections III and IV.

Similar but faster convergence to 1 was observed for the first moments $\mathbb{E}(\dot{P}_{\text{tot}})/\mathbb{E}(P_{\text{tot}})$ than for $\mathbb{E}(\dot{P}_{\text{tot}}^2)/\mathbb{E}(P_{\text{tot}}^2)$.

Based on these observations, we put forth that, for $\gamma = 2$ or $\epsilon = \pi/2$, $\mathbb{E}(P_{\text{tot}}) \sim \mathbb{E}(\dot{P}_{\text{tot}})$ and $\mathbb{E}(P_{\text{tot}}^2) \sim \mathbb{E}(\dot{P}_{\text{tot}}^2)$ as $\varphi_{\text{RX}} \rightarrow 0$. Furthermore, it is natural to conjecture that the convergence holds for any moment and thus for the distribution. Hence, in distribution, $\dot{P}_{\text{tot}} \approx P_{\text{tot}}$ for the narrow beams. We will demonstrate that similar convergence also applies to the SIR and SINR.

D. Relative Gain Process

The analysis of Sections III and IV is based on the following formulation of the relative gain process.

Definition 1 (Relative Gain Process (RGP)): Let $\Phi \subset \mathbb{R}^2$ be a HPPP. The relative gain process is defined as

$$\mathcal{G} \triangleq \left\{ x \in \Phi \setminus \{x_0\} : \frac{G[D_{h,\epsilon}\|x\|]}{G[D_{h,\epsilon}\|x_0\|]} \right\}. \quad (11)$$

The following lemma gives the density function of the RGP. The equivalence GP = RGP is a useful implication of the lemma, with the GP defined in (4).

Lemma 1: The GP and the RGP are inhomogeneous PPPs on $(0, 1) \ni r$ with the density function

$$\lambda_{\mathcal{G}}(r) = \tilde{\kappa}/r, \quad (12)$$

where $\tilde{\kappa} = \kappa/\log(2)$ and

$$\kappa \triangleq \lambda\pi \left(\frac{h\varphi_{\text{RX}}}{\sin^2(\epsilon)} \right)^2 \quad (13)$$

is approximately the mean number of UEs inside a SBS -3 dB footprint.

Proof: The process $\{x \in \Phi : \|x\|^2\}$ is Poisson distributed on $(0, \infty)$ with the density $2\pi\lambda$ [7, Example 2.9]. Consequently, the distances $\|x_k\|^2 - \|x_0\|^2$ in $G[D_{h,\epsilon}\|x_k\|]$ /

$G[D_{h,\epsilon}\|x_0\|] = 2^{-(\|x_k\|^2 - \|x_0\|^2)/\varphi_{\text{RX}}^2}$ between the k th nearest point and the nearest point are Erlang distributed with parameters $k \geq 1$ and $2\pi\lambda$ regardless of x_0 . Hence, without loss of generality, we can condition $x_0 = o$. Furthermore, by Slivnyak's theorem, $\{x \in \Phi \setminus \{x_0\} : \|x\|^2 - \|x_0\|^2\}$ reduces to the process $\{x \in \Phi : \|x\|^2\}$ for $x_0 = o$, and the result follows by applying the mapping theorem [7, Thm. 2.34] to the GP;

$$\int_r^1 \lambda_{\mathcal{G}}(y) dy = \lambda\pi \left(\frac{G^{-1}[r]}{D_{h,\epsilon}} \right)^2 = \lambda\pi \left(\frac{h\varphi_{\text{RX}} \sqrt{-\log(r)}}{\sin^2(\epsilon)\sqrt{\log(2)}} \right)^2$$

for $0 < r < 1$. $G^{-1}[\cdot]$ is the inverse function of $G[\cdot]$. $\lambda_{\mathcal{G}}(r)$ follows by derivation w.r.t. r and taking the minus sign.

The interpretation of κ as the mean number of UEs inside the -3 dB footprint follows by solving $D_{h,\epsilon}\|x_{\text{RX}}\| = \varphi_{\text{RX}}$ for the distance $\|x_{\text{RX}}\|$ to the edge of the -3 dB footprint and from the area formula of a circle and Campbell's theorem. In line with (2), this interpretation of κ is exact in the limit $\varphi_{\text{RX}} \rightarrow 0$. \square

For any measurable function $v(\cdot) : \mathbb{R}^d \rightarrow [0, 1]$ such that $\int_{\mathbb{R}^d} |\log v(x)|\lambda_{\Psi}(x)dx < \infty$, the probability-generating functional (PGFL) $\mathfrak{G}_{\Psi}(\cdot)$ of a point process (p.p.) Ψ is defined by

$$\mathfrak{G}_{\Psi}[v] \triangleq \mathbb{E} \prod_{x \in \Psi} v(x). \quad (14)$$

We use Lemma 1 to derive the PGFL of the RGP [18, Eq. (3.30)];

$$\begin{aligned} \mathfrak{G}_{\mathcal{G}}[v] &= \exp \left\{ - \int_{\mathbb{R}} (1 - v(r))\lambda_{\mathcal{G}}(r)dr \right\} \\ &= \exp \left\{ -\tilde{\kappa} \int_0^1 (1 - v(r))/rdr \right\}. \end{aligned} \quad (15)$$

E. The Signal-to-Interference Ratio

The SIR at the typical SBS can be represented in terms of the GP. It is defined as

$$\begin{aligned} \text{SIR}_{\kappa,m} &\triangleq \frac{S}{I} = \left(\frac{I}{S} \right)^{-1} \\ &= \left(\frac{\sum_{x \in \Phi \setminus \{x_0\}} Pg_x G[D_{h,\epsilon}\|x\|]/(\hat{d}_{h,\epsilon}/d_0)^{\gamma}}{Pg_{x_0} G[D_{h,\epsilon}\|x_0\|]/(\hat{d}_{h,\epsilon}/d_0)^{\gamma}} \right)^{-1} \\ &= g_{x_0} / \sum_{x' \in \mathcal{G}} g_x x', \end{aligned} \quad (16)$$

where $x' = G[D_{h,\epsilon}\|x\|]/G[D_{h,\epsilon}\|x_0\|]$ and $\{g_x\}_{x \in \Phi}$ are i.i.d. Gamma distributed r.v.'s. We represent the SIR in terms of the interference-to-signal ratio (ISR) in order to represent the SIR in terms of the relative gain process \mathcal{G} . The terms $(\hat{d}_{h,\epsilon}/d_0)^{\gamma}$ are canceled; therefore, the spatial path loss does not affect the SIR. This property follows from the planar system model of the narrow-beam LEO with equal spatial path losses for all UEs. However, this also holds for the performance metrics using the spherical model, namely for $\text{SIR} \triangleq \dot{S}/\dot{I}$, where \dot{S} and \dot{I} are defined in (7); this is a substantial difference from

the usual terrestrial models, where the SIR depends strongly on the path loss exponent [18, Eq. (6.64)].

Note that, from Lemma 1, the GP = RGP: the nearest transmitter distance $\|x_0\|$ in \mathcal{G} can be conditioned arbitrarily or have an arbitrary distribution as long as the p.p. of the other transmitters is a HPPP of density λ . It follows that, after decoding and canceling the signal of the nearest UEs, the SIR distribution remains the same for the second nearest transmitters (considered now the nearest). Therefore, for such *successive interference cancellation*, the model describes the SIR at the nearest UEs to their serving SBS and the second nearest, third nearest, and so on. This property is due to the second power exponential path loss function, *i.e.*, the Gaussian antenna gain, that preserves the Poisson property of the RGP (11).

III. META DISTRIBUTION OF THE SIR

The SIR MD at the typical SBS is the distribution of the r.v. $\mathcal{P}_{\kappa,m}(\theta) \triangleq \mathbb{P}(\text{SIR}_{\kappa,m} > \theta|\Phi)$, and it is defined for $0 \leq y \leq 1$ as

$$\begin{aligned} \mathbb{P}(\mathcal{P}_{\kappa,m}(\theta) > y) &= \mathbb{P}(\mathbb{P}(\text{SIR}_{\kappa,m} > \theta|\Phi) > y) \\ &= \mathbb{E}_\Phi \mathbb{1}(\mathbb{P}(\text{SIR}_{\kappa,m} > \theta|\Phi) > y), \end{aligned} \quad (17)$$

where $\mathbb{1}(\cdot)$ is the indicator function.

The averaging in (17) is taken over the *ensemble* of Φ at the typical location. However, because Φ is ergodic, the ensemble average is equal to the spatial average, given a realization of Φ . In this sense, the SIR MD describes the SBS reliability in a uniform (or homogeneous) constellation. The SIR MD gives the fraction of SBSs that reach reliability y , which is the fraction of time during a short use period that the SIR threshold θ is reached.

A. Moments of the SIR MD

We use multi-indices to simplify the notation. For the nonnegative integer tuples $\Gamma = (\Gamma_1, \Gamma_2, \dots, \Gamma_m)$ and $B = (B_1, B_2, \dots, B_m)$, we define the product $B^\Gamma = B_1^{\Gamma_1} B_2^{\Gamma_2} \cdots B_m^{\Gamma_m}$, the multinomial coefficient $\binom{b}{\Gamma} = b! / (\Gamma_1! \Gamma_2! \cdots \Gamma_m!)$, and the absolute value $|\Gamma| = \Gamma_1 + \Gamma_2 + \cdots + \Gamma_m$. We are ready to derive the moments of the SIR MD $M_{\kappa,m}^b(\theta) \triangleq \mathbb{E}[\mathcal{P}_{\kappa,m}(\theta)^b]$.

Proposition 1 (Moments of the SIR MD): The b th moment in a narrow-beam LEO uplink when all transmitters experience Nakagami- m fading is approximately given as a sum over all Γ such that $|\Gamma| = b$:

$$\begin{aligned} M_{\kappa,m}^b(\theta) &\approx \hat{M}_{\kappa,m}^b(\theta) \\ &\triangleq \sum_{|\Gamma|=b} \binom{b}{\Gamma} \exp \left\{ -\tilde{\kappa} \int_0^1 \frac{1 - A(\theta, r)^\Gamma}{r} dr \right\} B^\Gamma, \end{aligned} \quad (18)$$

where $A_n(\theta, r) = (1 + m!^{-1/m} \theta n r)^{-m}$ and $B_n = \binom{m}{n} (-1)^{n+1}$, $n = 1, \dots, m$. For $m = 1$, $\hat{M}_{\kappa,m}^b(\theta) = M_{\kappa,m}^b(\theta)$.

Proof: We utilize the PGFL of the RGP (15). The proof is given in Appendix C. \square

For Rayleigh fading, we provide multiple representations (19)-(23) for the moments.

Corollary 1 (Moments of the SIR MD for Rayleigh Fading): With $m = 1$, the expression (18) can be further evaluated as follows. The first and the second moments of the SIR MD in a narrow-beam LEO uplink, when all transmitters experience Rayleigh fading, are given by (recall that $\hat{M}_{\kappa,1}^b(\theta) = M_{\kappa,1}^b(\theta)$)

$$M_{\kappa,1}^1(\theta) = (1 + \theta)^{-\tilde{\kappa}}, \quad (19)$$

$$M_{\kappa,1}^2(\theta) = e^{-\tilde{\kappa}\theta/(1+\theta)} (1 + \theta)^{-\tilde{\kappa}}, \quad (20)$$

respectively. The general moments $b \in \mathbb{C}$ are given by

$$M_{\kappa,1}^b(\theta) = \exp \left\{ -\tilde{\kappa} \int_0^1 \left(1 - \frac{1}{(1 + \theta r)^b} \right) / rdr \right\} \quad (21)$$

$$= \exp \left\{ -\theta b \tilde{\kappa} {}_3F_2(1, 1, 1+b; 2, 2; -\theta) \right\}, \quad (22)$$

where ${}_3F_2(\cdot)$ is the hypergeometric function. Furthermore, for $b \in \mathbb{N}$,

$$M_{\kappa,1}^b(\theta) = \exp \left\{ \frac{\tilde{\kappa}}{(b-1)!} \sum_{k=1}^b \binom{b}{k} \text{Li}_{2-k}(-\theta) \right\}, \quad (23)$$

where $\binom{n}{k}$ is the unsigned Stirling number of the first kind, and $\text{Li}_{2-k}(\cdot)$ is the polylogarithm.

Proof: Equation (21) follows from (18) for $m = 1$. The first two moments can be evaluated through elementary integration methods from (21). The derivation of (23) is given in Appendix D. \square

As a mathematical curiosity, $\text{Li}_{2-k}(-\theta)$ also has closed-form expressions for $k \geq 3$ [23, Eq. (6.3)], although relatively complicated.

B. Approximation of the SIR MD

Using the moments, we present two ways to approximate the SIR MD: the beta distribution and Chebyshev-Markov Inequalities.

1) The Beta Distribution: The beta distribution effectively approximates the SIR MD, especially if no *inflection points* exist. If α and β are the shape parameters of the beta distribution, the first and the second moments are given by $\alpha/(\alpha + \beta)$ and $\alpha(\alpha + 1)/((\alpha + \beta)(\alpha + \beta + 1))$, respectively. Using the expression (18), or in the Rayleigh fading case, (19) and (20) for the first two moments and matching them to the corresponding moments of the beta distribution, we can solve for α and β :

Proposition 2 (Approximation of the SIR MD With the Beta Distribution): The parameters α and β for the beta distribution are given as

$$\begin{aligned} \alpha &= \left(\frac{\hat{M}_{\kappa,m}^1(\theta)(1 - \hat{M}_{\kappa,m}^1(\theta))}{\hat{M}_{\kappa,m}^2(\theta) - \hat{M}_{\kappa,m}^1(\theta)^2} - 1 \right) \hat{M}_{\kappa,m}^1(\theta) \\ \beta &= \left(\frac{\hat{M}_{\kappa,m}^1(\theta)(1 - \hat{M}_{\kappa,m}^1(\theta))}{\hat{M}_{\kappa,m}^2(\theta) - \hat{M}_{\kappa,m}^1(\theta)^2} - 1 \right) (1 - \hat{M}_{\kappa,m}^1(\theta)) \end{aligned} \quad (24)$$

The SIR MD can be approximated by the beta distribution:

$$\mathbb{P}(\mathcal{P}_{\kappa,m}(\theta) > y) \approx \begin{cases} 1 - I_y(\alpha, \beta), & y \in [0, 1], \\ 1, & y < 0, \\ 0, & y > 1, \end{cases} \quad (25)$$

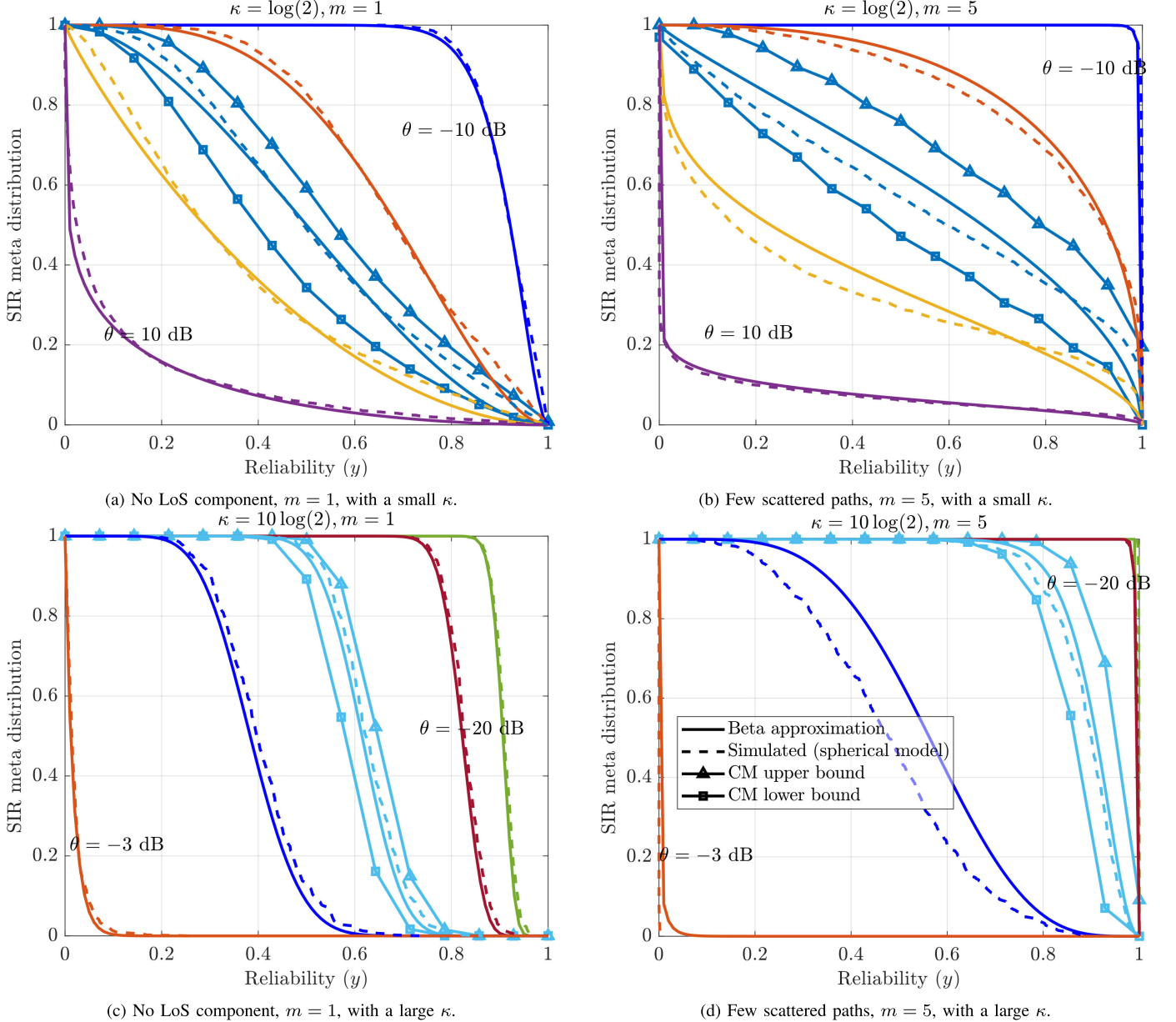


Fig. 5. Simulated SIR MD and the beta distribution approximations with different SIR thresholds θ and fading variables $m \in \{1, 5\}$. We plot the thresholds $\theta \in \{-10, -3, 0, 3, 10\}$ dB and $\theta \in \{-20, -17, -13, -10, -3\}$ dB (from top to bottom) for $\kappa \in \{\log(2), 10 \log(2)\}$, respectively. The path loss exponent $\gamma = 2$ (recall that, like in the analysis, this does not notably affect the distribution) and the parameters $\lambda \in 1.9 \cdot \{10^{-3}, 10^{-4}\} / \text{km}^2$, $h = 1200 \text{ km}$, $\epsilon = 80^\circ$ and $\varphi_{\text{RX}} = 1.6^\circ$ corresponding to $\kappa \in \{\log(2), 10 \log(2)\}$, respectively. (Recall that the only essential spatial system parameter is κ . The other parameters have only a minor impact on the simulated values.) Order 15 CM inequalities are depicted for $\theta \in \{0, -13\}$ dB for $\kappa \in \{\log(2), 10 \log(2)\}$, respectively.

where $I_{(\cdot)}(\alpha, \beta)$ is the regularized incomplete beta function.

2) Chebyshev-Markov Inequalities: Given a moment sequence $(\hat{M}_{\kappa,m}^b(\theta))_{b=0}^n$, the order n CM inequalities give the pointwise infimum and supremum

$$\inf_{F \in \mathcal{F}_n} F(y), \sup_{F \in \mathcal{F}_n} F(y) \quad (26)$$

for any $y \in [0, 1]$, where \mathcal{F}_n is the set of the distributions that agree with the moment sequence. The inequalities established by the infima and suprema are called the CM inequalities [24, Th. 1]. We use the CM inequalities to validate the theory by comparing the CM inequalities derived from the moments (18) to the simulated SIR MD in the spherical model.

C. SIR MD Numerical Results

Figure 5 depicts the SIR MDs for varying densities and fading parameters. The beta distribution approximations are shown with the simulated SIR MD $\mathbb{P}(\mathbb{P}(\text{SIR} > \theta | \Theta) > y)$ using the spherical model, $\text{SIR} = \dot{S}/\dot{I}$. We also plot order 15 CM inequalities for different θ (we omit the other inequalities to avoid cluttering the figures). The beta distribution approximation is particularly feasible for the Rayleigh fading. One can see that for $\kappa = \log(2)$, the variance in reliability is significant: some SBSs have relatively good reliability, whereas others have a bad connection. In particular, for $m = 5$, 1/5 of the SBSs reach $\theta = 10$ dB during the use period, and the rest are experiencing an outage at this threshold. On the

contrary, for $\kappa = 10 \log(2)$, especially in the Rayleigh fading case, the variance in the reliability is small. With $m = 5$, the variance is more considerable for $\theta = -10$ dB. Otherwise, the reliability is near 0 or 1; depending on the SIR threshold needed for the transmission, all SBSs perform very well, or the connection is permanently down.

IV. SIR, SINR AND THROUGHPUT DISTRIBUTIONS

A. SIR Distribution

The SIR distribution is straightforward to obtain from the SIR MD since the first moment is just the complementary cumulative distribution function (CCDF) $F_{\kappa,m}^{\text{SIR}}(\theta) \triangleq \mathbb{P}(\text{SIR}_{\kappa,m} > \theta) = M_{\kappa,m}^1(\theta)$ of the SIR. We denote $\hat{F}_{\kappa,m}^{\text{SIR}}(\theta) \triangleq \hat{M}_{\kappa,m}^1(\theta)$ the approximation of the SIR distribution. If θ is the SIR threshold needed for successful transmission, $\hat{F}_{\kappa,m}^{\text{SIR}}(\theta)$ is the *transmission success probability*. We provide multiple representations (27) – (30) for the transmission success probability.

Corollary 2 (SIR Distribution): The transmission success probability in a narrow-beam LEO Nakagami- m fading interference-only uplink channel is given for $m \in \{1, 2\}$ by

$$F_{\kappa,1}^{\text{SIR}}(\theta) = \hat{F}_{\kappa,1}^{\text{SIR}}(\theta) = \hat{M}_{\kappa,1}^1(\theta) = (1 + \theta)^{-\tilde{\kappa}}, \quad (27)$$

$$\begin{aligned} F_{\kappa,2}^{\text{SIR}}(\theta) &\approx \hat{F}_{\kappa,2}^{\text{SIR}}(\theta) = \hat{M}_{\kappa,2}^1(\theta) \\ &= 2e^{-\frac{\sqrt{2}\theta\tilde{\kappa}}{\sqrt{2}\theta+2}} \left(\frac{\theta}{\sqrt{2}} + 1 \right)^{-\tilde{\kappa}} \\ &- e^{-\frac{\sqrt{2}\theta\tilde{\kappa}}{\sqrt{2}\theta+1}} \left(\sqrt{2}\theta + 1 \right)^{-\tilde{\kappa}}, \end{aligned} \quad (28)$$

respectively. The expression for general $m \in \mathbb{N}$ is

$$\begin{aligned} F_{\kappa,m}^{\text{SIR}}(\theta) &\approx \hat{F}_{\kappa,m}^{\text{SIR}}(\theta) = \hat{M}_{\kappa,m}^1(\theta) \\ &= \sum_{n=1}^m \exp \left\{ -\tilde{\kappa} \int_0^1 \frac{1 - (1 + C_n\theta r)^{-m}}{r} dr \right\} B_n \\ &= \sum_{n=1}^m \exp \left\{ \frac{\tilde{\kappa}}{(m-1)!} \sum_{k=1}^m \begin{bmatrix} m \\ k \end{bmatrix} \text{Li}_{2-k}(-C_n\theta) \right\} B_n, \end{aligned} \quad (29)$$

$$(30)$$

where $\begin{bmatrix} m \\ k \end{bmatrix}$ is the unsigned Stirling number of the first kind, $B_n = \binom{m}{n}(-1)^{n+1}$ and $C_n = (m!)^{-1/m} n$, $n = 1, \dots, m$. In the Rayleigh fading case, $F_{1,\kappa}^{\text{SIR}}(\theta) = \hat{F}_{1,\kappa}^{\text{SIR}}(\theta)$. Recall that the exponent also has the hypergeometric representation as in (22).

Proof: The first moment follows directly by substituting $b = 1$ to (18). The polylogarithmic expression of the integral in (29) is derived in Appendix D. The Rayleigh case follows directly from (19), and the $m = 2$ case follows from substituting $\text{Li}_1(-C_n\theta) = -\log(1 + C_n\theta)$ and $\text{Li}_0(-C_n\theta) = -C_n\theta/(1 + C_n\theta)$ to (30). \square

With Rayleigh fading, the SIR distribution (27) is a Lomax (Pareto Type II) distribution with the shape parameter $\tilde{\kappa}$.

1) *Average SIR and Variance:* Fading has little effect on the first moment of the SIR (cf. Section IV-C). Hence, an expression for the average SIR over the uniformly distributed SBSs

is simply given by integrating the SIR CCDF in the Rayleigh fading case over the positive half-line:

$$\mathbb{E}(\text{SIR}_{\kappa,m}) \approx \mathbb{E}(\text{SIR}_{\kappa,1}) = \int_0^\infty F_{\kappa,1}^{\text{SIR}}(y) dy = \frac{1}{\tilde{\kappa} - 1}, \quad (31)$$

for $\tilde{\kappa} > 1$. The mean is divergent for $\tilde{\kappa} \leq 1$, that is, $\kappa \leq \log(2)$: On average, having less than $\log(2)$ UEs inside the -3 dB footprint, a significant fraction of SBSs have a very high SIR, and a significant fraction has a low SIR. Consequently, the expected SIR and the variance are undefined. Under this threshold, the interference-only channel is inadequate in modeling the mean SINR even for minimal noise values—physically bounded by the noise. Furthermore, the n th moment of the Lomax distribution exists if and only if $\tilde{\kappa} > n$, implying that the variance of the SIR is infinite for $1 < \tilde{\kappa} \leq 2$ and undefined for $0 < \tilde{\kappa} \leq 1$.

2) *Decay Rate of the Tail:* The asymptotic decay rate helps to gain insight into the SIR distribution. Heuristically, we know that $\lim_{y \rightarrow \infty} \text{Li}_{2-k}(-C_n y) = 0$ for $k > 2$; otherwise, the term $\exp\{\text{Li}_{2-2}(-C_n y)\} = \exp\{-C_n y/(1 + C_n y)\}$ decays the slowest in (30). Estimating the polylogarithm, the asymptotic decay rate

$$\rho_{\text{SIR}} \triangleq -\lim_{y \rightarrow \infty} \frac{\log(\hat{F}_{\kappa,m}^{\text{SIR}}(y))}{y} \leq 0. \quad (32)$$

The condition $\rho_{\text{SIR}} = 0$ is equivalent to the heavy-tailed distribution in that the exponential moment $\mathbb{E}(e^{t\text{SIR}_{\kappa,m}})$ is divergent for any $t > 0$ [25, Th. 2.6]. The SIR distribution has a slowly decaying tail for all κ and m . In practice, one may expect frequent outliers in the SIR.

3) *SIR Numerical Results:* In Figure 6, we plot the theoretical and simulated transmission success probability for various κ : $\hat{F}_{\kappa,m}^{\text{SIR}}(\theta)$ and $\mathbb{P}(\text{SIR} > \theta)$, respectively. The Lomax distribution (27) approximates all SIR distributions in the tail. It can generally be used to model the SIR distribution in the simple coverage region $\theta \geq 1$. Other than the tail distribution, the Lomax distribution gives pessimistic values for the probability of coverage.

B. SINR Distribution

The tail behavior observed in the model is due to the lack of sidelobes or noise. In this section, we add a constant dimensionless noise power term $W > 0$ to I and analyze the $\text{SINR}_{\kappa,W,m} \triangleq S/(I + W)$. Define the transmission success probability $F_{\kappa,W,m}^{\text{SINR}}(\theta) \triangleq \mathbb{P}(\text{SINR}_{\kappa,W,m} > \theta)$.

Proposition 3 (SINR Distribution): In the interference-plus-noise-limited channel, for $m = 1$,

$$F_{\kappa,W,1}^{\text{SINR}}(\theta) = (1 + \theta)^{-\tilde{\kappa}} E_{\tilde{\kappa}+1} \left(W(\hat{d}_{h,\epsilon}/d_0)^\gamma \theta \right) \tilde{\kappa}, \quad (33)$$

and for general $m \in \mathbb{N}$:

$$\begin{aligned} F_{\kappa,W,m}^{\text{SINR}}(\theta) &\approx \hat{F}_{\kappa,W,m}^{\text{SINR}}(\theta) \\ &\triangleq \sum_{n=1}^m \exp \left\{ \frac{\tilde{\kappa}}{(m-1)!} \sum_{k=1}^m \begin{bmatrix} m \\ k \end{bmatrix} \text{Li}_{2-k}(-C_n\theta) \right\} B_n \\ &\cdot E_{\kappa+1} \left(mC_n W(\hat{d}_{h,\epsilon}/d_0)^\gamma \theta \right) \tilde{\kappa}, \end{aligned} \quad (34)$$

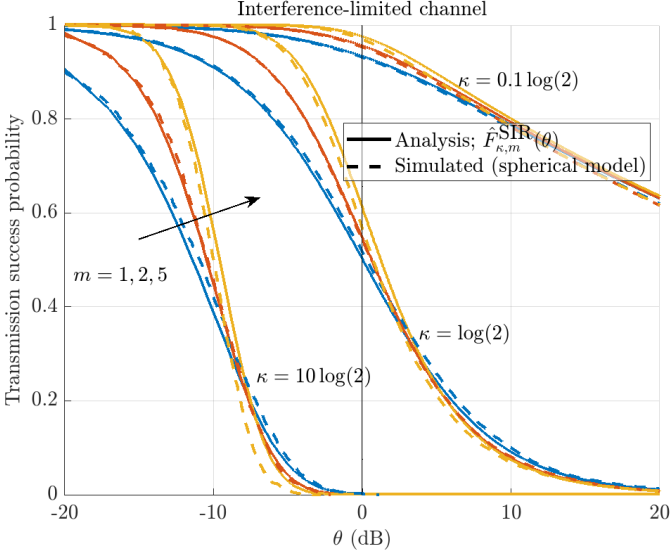


Fig. 6. Simulated SIR distributions using the spherical model and the corresponding theoretical distribution for $\kappa \in \log(2) \cdot \{0.1, 1, 10\}$ and $m \in \{1, 2, 5\}$. The parameters $\gamma = 4$, $h = 600$ km, $\epsilon = 80^\circ$, $\varphi_{RX} = 1.6^\circ$ and $\lambda \in 7.4 \cdot \{10^{-5}, 10^{-4}, 10^{-3}\}/\text{km}^2$ were used, which match the respective κ . (Recall that the only essential spatial system parameter is κ . The other parameters have only a minor impact on the simulated values.)

where $E_{\tilde{\kappa}+1}(\cdot)$ is the generalized exponential integral, $[m]_k$ is the unsigned Stirling number of the first kind, $B_n = \binom{m}{n}(-1)^{n+1}$ and $C_n = (m!)^{-1/m}n$, $n = 1, \dots, m$. Recall that the exponent has the integral and hypergeometric representations (21) and (22), respectively.

Proof: We give the proof with Rayleigh fading. The proof for the general m is analogous by using the exponential form to approximate the CCDF of the gamma distributed g_{x_0} , similar to the derivation given in Appendix C.

$$\begin{aligned} & F_{\kappa,W,1}^{\text{SINR}}(\theta) \\ &= \mathbb{P}\left(g_{x_0} > \sum_{x \in \mathcal{G}} g_x x + \frac{W(\hat{d}_{h,\epsilon}/d_0)^\gamma \theta}{G[D_{h,\epsilon} \| x_0 \|]}\right) \\ &\stackrel{(a)}{=} \mathbb{E}_\Phi \mathbb{E}_g \left(e^{-\theta \sum_{x \in \mathcal{G}} g_x x}\right) \mathbb{E}_\Phi \left(e^{-W(\hat{d}_{h,\epsilon}/d_0)^\gamma \theta / G[D_{h,\epsilon} \| x_0 \|]}\right) \\ &\stackrel{(b)}{=} \mathbb{E} \prod_{x \in \mathcal{G}} \frac{1}{1 + \theta x} E_{\tilde{\kappa}+1} \left(W(\hat{d}_{h,\epsilon}/d_0)^\gamma \theta\right) \tilde{\kappa} \\ &\stackrel{(c)}{=} (1 + \theta)^{-\tilde{\kappa}} E_{\tilde{\kappa}+1} \left(W(\hat{d}_{h,\epsilon}/d_0)^\gamma \theta\right) \tilde{\kappa}. \end{aligned} \quad (35)$$

(a) follows from the equivalence of the GP and RGP, and thus, \mathcal{G} is independent of the served UE x_0 , and the expectation of the exponential term (that follows from the CCDF of the exponential r.v. g_{x_0}) can be separated into the product. In (b), we used the Laplace transform $\mathcal{L}_{1/G[D_{h,\epsilon} \| x_0 \|]}(s) \triangleq \mathbb{E} \exp\{-s/G[D_{h,\epsilon} \| x_0 \|]\} = E_{\tilde{\kappa}+1}(s)\tilde{\kappa}$ of the inverse largest gain, which can be derived directly from the definition of the Laplace transform using the (derivative of the) CDF $\mathbb{P}(1/G[D_{h,\epsilon} \| x_0 \|] < r) = 1 - (1/r)^{\tilde{\kappa}}$, which is not difficult to establish by using the nearest-neighbor distribution of the PPP on \mathbb{R}^2 [7, Example 2.11]. (c) follows by evaluating the PGFL (15) of \mathcal{G} . \square

For $W = 0$, we directly retrieve the SIR distribution; $F_{\kappa,0,m}^{\text{SINR}}(\theta) = F_{\kappa,m}^{\text{SIR}}(\theta)$.

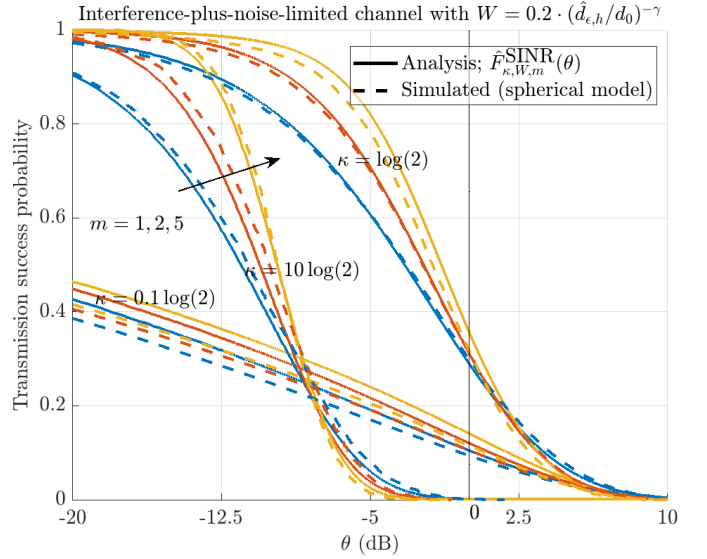


Fig. 7. Simulated SINR distributions using the spherical model and the corresponding theoretical distribution for $\kappa \in \log(2) \cdot \{0.1, 1, 10\}$ and $m \in \{1, 2, 5\}$. The parameters $\gamma = 2$, $h = 200$ km, $\epsilon = 45^\circ$, $\varphi_{RX} = 1.6^\circ$, $W = (\hat{d}_{h,\epsilon}/d_0)^{-\gamma}$ and $\lambda \in 1.8 \cdot \{10^{-4}, 10^{-3}, 10^{-2}\}/\text{km}^2$ were used, which match the respective κ . (Recall that the only essential spatial system parameter is κ . The other parameters have only a minor impact on the simulated values.)

1) *SINR Numerical Results:* In Figure 7, we plot the theoretical SINR distribution and the simulated $\mathbb{P}(\text{SINR} > \theta) \triangleq \mathbb{P}(\dot{S}/(\dot{I} + W) > \theta)$ distribution for various κ . The noise is set to $W = 0.2 \cdot (\hat{d}_{h,\epsilon}/d_0)^{-\gamma}$, or equivalently, measured in decibels w.r.t. the average signal strength of a UE at o is $10 \log_{10}(W/(\hat{d}_{h,\epsilon}/d_0)^{-\gamma}) = -7$ dB. Contrary to the SIR distribution, smaller κ does not necessarily produce better coverage probabilities: With a small κ , the served UE is likely to be far away from the SBS, and because of the path loss, the noise will restrict the SINR. Approximately at $\kappa = \log(2)$, the coverage probabilities are at maximum.

The error, particularly visible for $\kappa = 0.1 \log(2)$, is due to the low elevation angle $\epsilon = 45^\circ$, which causes a significant difference between $\hat{d}_{h,\epsilon}$ and $d_{h,\epsilon}$ and a significantly elliptical main lobe footprint in the simulations.

The simple analytic expression $F_{\kappa,W,1}^{\text{SINR}}(\theta)$ (33) derived for the exponential power fading can be used to model the SINR tail distribution, generally in the simple coverage region $\theta \geq 1$. Other than the tail distribution, $F_{\kappa,W,1}^{\text{SINR}}(\theta)$ gives pessimistic values for the probability of coverage.

C. Throughput Distribution

The instantaneous channel capacity is defined by $\mathcal{T}_{\kappa,W,m} \triangleq \log(1 + \text{SINR}_{\kappa,W,m}) / \log(2)$ [18, Eq. (7.19)]. As observed from Figure 8, the type of fading has a negligible effect on the average normalized throughput, or spectral efficiency. Being simplest, we derive the throughput for the Rayleigh fading and denote $\hat{\tau}_{\kappa,W} \triangleq \mathbb{E}(\mathcal{T}_{\kappa,W,1})$. For other fading cases, the exact values can be derived similarly to $\hat{\tau}_{\kappa,W}$.

1) *Average Throughput in the Interference-Limited Channel:* Recall the SIR distribution $F_{\kappa,1}^{\text{SIR}}(\cdot)$ (27). Without noise,

one can evaluate the average throughput:

$$\begin{aligned}\hat{\tau}_{\kappa,0} &= \frac{1}{\log(2)} \int_0^\infty \mathbb{P}(\text{SIR}_{\kappa,1} > e^t - 1) dt \\ &= \int_0^\infty \frac{F_{\kappa,1}^{\text{SIR}}(e^t - 1)}{\log(2)} dt \stackrel{(a)}{=} \int_0^\infty \frac{(1+v)^{-\tilde{\kappa}-1}}{\log(2)} dv = 1/\kappa,\end{aligned}\quad (36)$$

where we use the integration by substitution $v = e^t - 1$ in (a). Recall that $\kappa = \tilde{\kappa} \log(2)$ (13) is the mean number of UEs inside the -3 dB footprints of the SBSs.

2) Average Throughput in the Interference-Plus-Noise-Limited Channel: Recall the SINR distribution $F_{\kappa,W,1}^{\text{SINR}}(\cdot)$ (33). With noise, similar to (36), the average throughput is given by

$$\begin{aligned}\hat{\tau}_{\kappa,W} &= \frac{1}{\log(2)} \int_0^\infty \frac{F_{\kappa,W,1}^{\text{SINR}}(v)}{1+v} dv \\ &= \frac{1}{\log(2)} \int_0^\infty (1+v)^{-\tilde{\kappa}-1} E_{\tilde{\kappa}+1}(W(\hat{d}_{h,\epsilon}/d_0)^\gamma v) \tilde{\kappa} dv.\end{aligned}\quad (37)$$

Throughout the rest of the work, let us (vaguely) mean by *moderate noise* that the expected SNR is around 1 for the served UE at o , i.e., $W \approx (\hat{d}_{h,\epsilon}/d_0)^{-\gamma}$, or equivalently, the decibels w.r.t. the average signal strength of a UE at o is $10 \log_{10}(W/(\hat{d}_{h,\epsilon}/d_0)^{-\gamma}) \approx 0$ dB.

$\hat{\tau}_{\kappa,W}$ is complex to evaluate other than numerically for $W > 0$. For this reason, we will utilize two approximations of the exponential integral $E_{\tilde{\kappa}+1}(y)$ to help evaluate the integral (37). The following closed-form approximation of the average throughput is simple yet suitable for moderate or large noise. It is pessimistic except, not visibly, optimistic for small κ . Furthermore, $\mathfrak{T}_{\kappa,W} \sim \hat{\tau}_{\kappa,W} \sim \hat{\tau}_{\kappa,0} = 1/\kappa, \kappa \rightarrow \infty$.

Approximation 1 (A Simple Approximation of the Average Throughput): For moderate to large noise, the average normalized throughput can be approximated by

$$\hat{\tau}_{\kappa,W} \approx \mathfrak{T}_{\kappa,W} \triangleq \frac{\tilde{\kappa}}{(\tilde{\kappa} + 1)(\tilde{\kappa} + W(\hat{d}_{h,\epsilon}/d_0)^\gamma) \log(2)}. \quad (38)$$

Proof: First, we use the first order asymptotic approximation $E_{\tilde{\kappa}+1}(y) \approx e^{-y}/(\tilde{\kappa} + 1)$ [26, Th. 51] for $E_{\tilde{\kappa}+1}(W(\hat{d}_{h,\epsilon}/d_0)^\gamma v)$ to help to evaluate (37):

$$\hat{\tau}_{\kappa,W} \approx \frac{\tilde{\kappa} e^{W(\hat{d}_{h,\epsilon}/d_0)^\gamma} E_{\tilde{\kappa}+1}(W(\hat{d}_{h,\epsilon}/d_0)^\gamma)}{(\tilde{\kappa} + 1) \log(2)}.$$

The final result is achieved by using approximation $E_{\tilde{\kappa}+1}(y) \approx e^{-y}/(\tilde{\kappa} + y)$ instead of the exponential integral. \square

3) Optimal Average Throughput: We can solve $d\mathfrak{T}_{\kappa,W}/d\kappa = 0$ for κ , and get the maximizing

$$\kappa_{\tau}^{\max} \triangleq \arg \max\{\kappa : \mathfrak{T}_{\kappa,W}\} = \sqrt{W(\hat{d}_{h,\epsilon}/d_0)^\gamma \log(2)}. \quad (39)$$

For $W = (\hat{d}_{h,\epsilon}/d_0)^{-\gamma}$, $\kappa_{\tau}^{\max} = \log(2)$: This follows the intuition that, with moderate noise, the performance metric is maximized at UE density where the expected SIR approaches infinity (recall (31)). By the void probability of the PPP, at $\kappa = \log(2)$, the served UE is inside the -3 dB

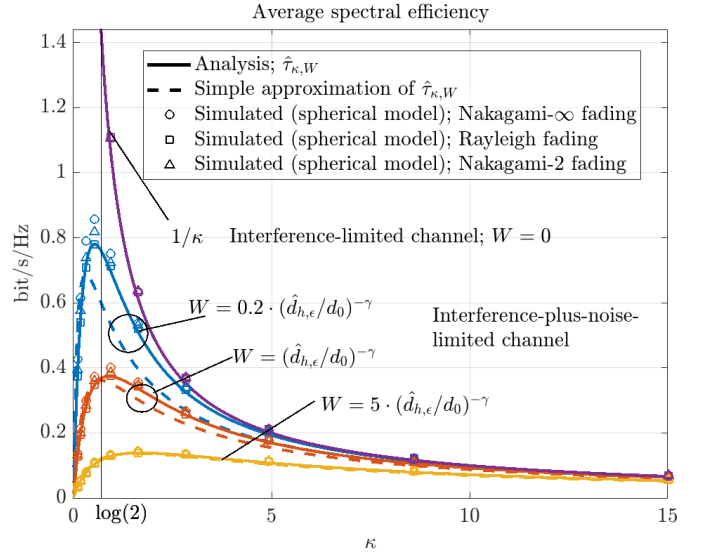


Fig. 8. Simulated actual and the theoretical expected normalized throughput for $\kappa \in [0, 15]$ and $W \in \{0, 0.2, 1, 5\} \cdot (\hat{d}_{h,\epsilon}/d_0)^{-\gamma}$ (from top to bottom) and $m \in \{1, 2, \infty\}$. The parameters $\gamma = 4$, $h = 1200$ km, $\epsilon = 85^\circ$, $\varphi_{RX} = 1.6$ and $\lambda \in [0, 4.2 \cdot 10^{-3}]/\text{km}^2$ were used, which match the respective κ . (Recall that the only essential spatial system parameter is κ . The other parameters have only a minor impact on the simulated values.)

footprint at the probability $1 - \exp\{-\log(2)\} = 1/2$ and inside the -10 dB footprint at the probability $1 - \exp\{-\log(10)\} = 9/10$ —this reflects a physically sensible cell size. For $W \rightarrow 0$, we approach the interference-only channel, and $\kappa_{\tau}^{\max} = 0$ reflects the no-noise-nor-interferers case, trivially maximizing the throughput (recall (16) and the independence of the SIR from the distance to the served UE).

4) Average Throughput Numerical Results: In Figure 8, we plot the average throughput for various κ and W and compare the theoretical $\mathbb{E}(\mathcal{T}_{\kappa,0,m}) \approx 1/\kappa$ and $\mathbb{E}(\mathcal{T}_{\kappa,W,m}) \approx \hat{\tau}_{\kappa,W}$ to the simulated $\mathbb{E} \log(1 + \text{SIR})$ and $\mathbb{E} \log(1 + \text{SINR})$, respectively. We show the simulated values in Rayleigh, Nakagami-2, and Nakagami- ∞ scenarios. The simulated results are similar in all fading scenarios. The simple approximation $\mathfrak{T}_{\kappa,W}$ is very good for moderate and large noise. For $W = 0.2 \cdot (\hat{d}_{h,\epsilon}/d_0)^{-\gamma}$, the interference-only expression (36) closely approximates the throughput for $\kappa > 1$. The optimal κ is close to $\log(2)$ with all depicted noise values, as implied by (39). Further, the average spectral efficiency is relatively flat w.r.t. κ for large noise.

Recall the SIR MD analysis in Section III and Figure 5: Even though $\kappa \approx \log(2)$ maximizes the *average* throughput for moderate noise, the SBS reliability significantly vary at this κ . The same insight is reflected in the undefined or infinite variance of the Lomax SIR distribution (27) for $\kappa \leq 2 \log(2)$.

V. CONCLUSION

We derived the SIR and its meta distribution (MD), as well as the SINR distribution and the expected throughput in a narrow-beam LEO uplink Nakagami channel in the presence of Poisson distributed interferers. Some expressions of the distributions are very simple; the SIR follows a Lomax distribution in the simple coverage region (and in the general coverage region for the Rayleigh fading), and the average

throughput is proportional to the inverse of the density of the user equipments (UEs) in the interference-only channel. In the interference-plus-noise-limited channel, we obtained a UE density maximizing the average throughput. Regardless of the antenna gain width, altitude, or elevation angle, with moderate noise levels, the maximizing density approximately corresponds to, on average, $\kappa \approx \log(2)$ UEs inside the satellite base stations (SBS) -3 dB footprints. On the contrary, it was observed that to maintain a consistent user experience, we must make the distribution of UEs dense because of the highly varying received signal strengths from the UEs if they are sparsely located (the Lomax distribution representing the SIR distribution has a divergent variance for $\kappa \leq 2\log(2)$).

In other words, maximizing average performance by optimizing the UE density comes with the cost of reduced user fairness. In light of the presented model, a possible solution for maintaining a consistent user experience is to increase the density of the constellation: should we consider that each UE has a serving satellite, the density of UEs determines the satellite constellation density directly. Furthermore, interference cancellation and combination can be implemented so that a single SBS can serve single or even multiple densely located UEs with satisfactory SIR and SINR. Alternatively, it is possible to complement the satellite network with a terrestrial network that serves the UEs during an outage in the LEO network. This work helps to characterize the achievable average performance and the SBS reliability with different co-channel UE densities, altitudes, elevation angles, and SBS antenna gain widths.

The paper introduces a novel and analytically tractable framework for modeling narrow-beam LEO communications using stochastic geometry. The approach yields simpler results than existing models in the literature while maintaining high accuracy. Future research could improve the model's applicability by investigating explicit shadowing effects and the more realistic distribution of UEs, particularly regarding the impact of interference on the narrow-beam and narrowband LEO performance. Furthermore, studying interference cancellation and signal combination within the framework would be interesting. The proposed model and the insights of this paper also apply to the downlink, considering that the SBS footprint locations on the Earth are distributed according to the HPPP.

APPENDIX A SCALING CONSTANT

See Figure 9. We have that $\zeta_z = \tan^{-1}(z/h)$. The derivative of φ_x around o is given approximately by

$$\begin{aligned} \frac{d}{d\|x\|}\varphi_x &= \frac{d}{dz}\zeta_z = \frac{d\tan^{-1}(z/h)}{dz} = \frac{h}{h^2+z^2} \\ &\stackrel{(a)}{\approx} \frac{h}{h^2-h^2+\hat{d}_{h,\epsilon}^2} \stackrel{(b)}{=} \frac{h}{h^2/\sin^2(\epsilon)} = \frac{\sin^2(\epsilon)}{h} = D_{h,\epsilon}, \end{aligned} \quad (40)$$

where (a) follows from Pythagoras's theorem, and (b) is standard trigonometry.

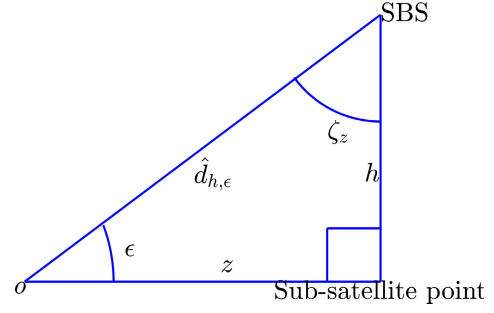


Fig. 9. Geometric interpretation of the variables in Appendix A.

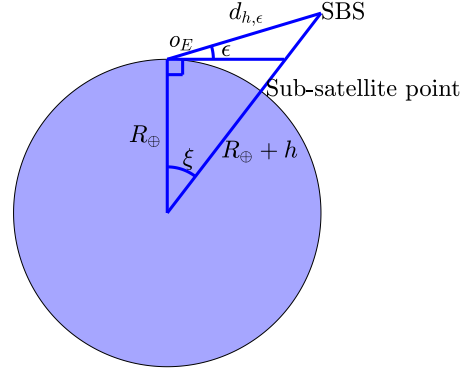


Fig. 10. Sketch of the geometry of the spherical model.

APPENDIX B GEOMETRY OF THE SPHERICAL SYSTEM MODEL

See Figure 10. Directly from the law of cosines, we have

$$d_{h,\epsilon}(\xi) = \sqrt{R_\oplus^2 + (R_\oplus + h)^2 - 2R_\oplus(R_\oplus + h)\cos(\xi)}. \quad (41)$$

Furthermore, we may derive the relation between ϵ and ξ : The law of cosines states that

$$(R_\oplus + h)^2 = d_{h,\epsilon}(\xi)^2 + R_\oplus^2 - 2d_{h,\epsilon}(\xi)R_\oplus\cos(\pi/2 + \epsilon), \quad (42)$$

which is analytically solvable for ξ .

APPENDIX C MOMENTS OF THE SIR MD WITH NAKAGAMI FADING

The moments of the SIR MD are derived as follows.

$$\begin{aligned} M_{\kappa,m}^{(b)}(\theta) &= \mathbb{E} \left[\mathbb{P} \left(g_{x_0} > \theta \sum_{x \in \mathcal{G}} g_x x \middle| \Phi \right)^b \right] \\ &\stackrel{(a)}{\approx} \mathbb{E} \left[\left(1 - \mathbb{E}_g \left[\left(1 - \exp \left\{ -m(m!)^{-1/m} \theta \sum_{x \in \mathcal{G}} g_x x \right\} \right)^m \right] \right)^b \right] \\ &\stackrel{(b)}{=} \mathbb{E} \left[\left(\sum_{n=1}^m \binom{m}{n} (-1)^{n+1} \right)^b \right] \end{aligned}$$

$$\begin{aligned}
& \cdot \mathbb{E}_g \exp \left\{ -nm(m!)^{-1/m} \theta \sum_{x \in \mathcal{G}} g_x x \right\} \right) \Big] \\
& \stackrel{(c)}{=} \sum_{\substack{k_1 + \dots + k_m = b; \\ k_1, \dots, k_m \geq 0}} \binom{b}{k_1, \dots, k_m} \\
& \cdot \exp \left\{ -\tilde{\kappa} \int_0^1 \frac{\left[1 - \prod_{n=1}^m (1 + (m!)^{-1/m} \theta nr)^{-k_n m} \right]}{r} dr \right\} \\
& \cdot \prod_{n=1}^m \binom{m}{n}^{k_n} (-1)^{k_n(n+1)}. \tag{43}
\end{aligned}$$

In (a), we use the upper bound for the incomplete gamma function presented in the proof of Theorem 2 in [27]. In (b), we use the binomial theorem. In (c), we use the multinomial theorem and the Laplace transform of the gamma distribution and PGFL (15) of the GP. We denote (43) as $\hat{M}_{\kappa, m}^{(b)}(\theta)$. With $m = 1$, the approximation is exact: $M_{\kappa, m}^{(b)}(\theta) = \hat{M}_{\kappa, m}^{(b)}(\theta)$.

APPENDIX D POLYLOGARITHMIC REPRESENTATION

It is straightforward to see that for $m = 1$, the moment (43) can be expressed with an exponential with the following integral, which is further represented as the generalized hypergeometric function.

$$\int_0^1 \left(1 - \frac{1}{(1 + \theta r)^b} \right) / r dr = \theta {}_3F_2(1, 1, 1 + b; 2, 2; -\theta) \tag{44}$$

for $b \in \mathbb{C}, \theta \in \mathbb{C} \setminus \{-1\}$. Furthermore, the hypergeometric series have a polylogarithmic representation. Using the definition of the hypergeometric series, for $|\theta| < 1$ and $b \in \mathbb{N}$:

$$\begin{aligned}
& {}_3F_2(1, 1, 1 + b; 2, 2; -\theta) \\
&= \sum_{n=0}^{\infty} \frac{(1)_n (1)_n (1+b)_n}{(2)_n (2)_n} \frac{(-\theta)^n}{n!} \\
&= \sum_{n=0}^{\infty} \frac{(1+b)_n}{(n+1)^2 n!} (-\theta)^n = \frac{1}{b!} \sum_{n=0}^{\infty} \frac{(n+1)_b}{(n+1)^2} (-\theta)^n \\
&\stackrel{(a)}{=} \frac{1}{b!} \sum_{n=0}^{\infty} \frac{\sum_{k=0}^b \binom{b}{k} (n+1)^k}{(n+1)^2} (-\theta)^n \\
&= \frac{1}{b!} \sum_{k=0}^b \binom{b}{k} \sum_{n=0}^{\infty} \frac{(-\theta)^n}{(n+1)^{2-k}} \stackrel{(b)}{=} -\frac{1}{b!} \sum_{k=0}^b \binom{b}{k} \frac{\text{Li}_{2-k}(-\theta)}{\theta}. \tag{45}
\end{aligned}$$

In (a), we used the expansion of the rising Pochhammer factorial; in (b), we used the definition of the polylogarithm. The expression can be generalized for $\theta \in \mathbb{C} \setminus \{-1\}$ through the analytic continuation of the polylogarithm.⁴

⁴To the best of our knowledge, the interesting connection between the polylogarithm and the generalized hypergeometric function (45) is not presented in other sources except for the special case of $b = 0$ [28].

REFERENCES

- [1] M. Höyhtyä, S. Boumard, A. Yastrebova, P. Järvensivu, M. Kiviranta, and A. Anttonen, "Sustainable satellite communications in the 6G era: A European view for multilayer systems and space safety," *IEEE Access*, vol. 10, pp. 99973–100005, 2022.
- [2] M. Jia, X. Gu, Q. Guo, W. Xiang, and N. Zhang, "Broadband hybrid satellite-terrestrial communication systems based on cognitive radio toward 5G," *IEEE Wireless Commun.*, vol. 23, no. 6, pp. 96–106, Dec. 2016.
- [3] *Solutions for NR to Support Non-Terrestrial Networks (NTN)*, document TR 38.821, 3GPP, 2023.
- [4] M. Haenggi, "The meta distribution of the SIR in Poisson bipolar and cellular networks," *IEEE Trans. Wireless Commun.*, vol. 15, no. 4, pp. 2577–2589, Apr. 2016.
- [5] Y. Sun and Z. Ding, "A fine grained stochastic geometry based analysis on LEO satellite communication systems," *IEEE Netw. Lett.*, vol. 5, no. 4, pp. 237–240, Dec. 2023.
- [6] H. Lin, C. Zhang, Y. Huang, R. Zhao, and L. Yang, "Fine-grained analysis on downlink LEO satellite-terrestrial mmWave relay networks," *IEEE Wireless Commun. Lett.*, vol. 10, no. 9, pp. 1871–1875, Sep. 2021.
- [7] M. Haenggi, *Stochastic Geometry for Wireless Networks*. Cambridge, U.K.: Cambridge Univ. Press, 2013.
- [8] R. Wang, M. A. Kishk, and M.-S. Alouini, "Ultra-dense LEO satellite-based communication systems: A novel modeling technique," *IEEE Commun. Mag.*, vol. 60, no. 4, pp. 25–31, Apr. 2022.
- [9] S. Wang, J. Song, X. Miao, and G. Pan, *Understanding Satellite Communications: The Stochastic Geometry Perspective*, 1st ed., Singapore: Springer, 2024.
- [10] A. Yastrebova et al., "Theoretical and simulation-based analysis of terrestrial interference to LEO satellite uplinks," in *Proc. GLOBECOM-IEEE Global Commun. Conf.*, Dec. 2020, pp. 1–6.
- [11] I. Angervuori and R. Wichman, "A closed-form approximation of the SIR distribution in a LEO uplink channel," in *Proc. IEEE Globecom Workshops (GC Wkshps)*, Rio de Janeiro, Brazil, Dec. 2022, pp. 856–861.
- [12] H. Jia, C. Jiang, L. Kuang, and J. Lu, "An analytic approach for modeling uplink performance of mega constellations," *IEEE Trans. Veh. Technol.*, vol. 72, no. 2, pp. 2258–2268, Feb. 2023.
- [13] H. Jia, Z. Ni, C. Jiang, L. Kuang, and J. Lu, "Uplink interference and performance analysis for megasatellite constellation," *IEEE Internet Things J.*, vol. 9, no. 6, pp. 4318–4329, Mar. 2022.
- [14] B. Al Homssi and A. Al-Hourani, "Optimal beamwidth and altitude for maximal uplink coverage in satellite networks," *IEEE Wireless Commun. Lett.*, vol. 11, no. 4, pp. 771–775, Apr. 2022.
- [15] B. A. Homssi and A. Al-Hourani, "Modeling uplink coverage performance in hybrid satellite-terrestrial networks," *IEEE Commun. Lett.*, vol. 25, no. 10, pp. 3239–3243, Oct. 2021.
- [16] A. Talgat, M. A. Kishk, and M.-S. Alouini, "Stochastic geometry-based uplink performance analysis of IoT over LEO satellite communication," *IEEE Trans. Aerosp. Electron. Syst.*, vol. 60, no. 4, pp. 4198–4213, Aug. 2024.
- [17] C. Li, Z. Fang, Y. Wang, and C. Sun, "An approach for interference modeling and analysis of low orbit satellite Internet," in *Proc. IEEE 23rd Int. Conf. Commun. Technol. (ICCT)*, Oct. 2023, pp. 1178–1184.
- [18] B. Blaszczyzyn, M. Haenggi, P. Keeler, and S. Mukherjee, *Stochastic Geometry Analysis of Cellular Networks*. Cambridge, U.K.: Cambridge Univ. Press, 2018.
- [19] M. Albulet, "SpaceX V-band non-geostationary satellite system," Space Exploration Technol. Corp., Hawthorne, CA, USA, Tech. Rep., 2017.
- [20] *Study on New Radio (NR) to Support Non-Terrestrial Networks (Release 15)*, document TR 38.811, 3GPP, 2020.
- [21] "Satellite antenna radiation patterns for non-geostationary orbit satellite antennas operating in the fixed-satellite service below 30 GHz," Int. Telecommun. Union, Geneva, Switzerland, Tech. Rep. ITU-R S.1528, 2001. [Online]. Available: https://www.itu.int/dms_pubrec/itu-r/rec/s/R-REC-S.1528-0-200106-I!PDF-E.pdf
- [22] M. Haenggi. (2020). *Simalysis: Symbiosis of Simulation and Analysis*. Accessed: Jul. 12, 2024. [Online]. Available: <https://stogblog.net/2020/10/15/simalysis-symbiosis-of-simulation-and-analysis/>
- [23] D. Wood, "The computation of polylogarithms," Dept. Computing Laboratory, Univ. Kent, Canterbury, U.K., Tech. Rep. 15-92, 1992. [Online]. Available: <http://www.cs.kent.ac.uk/pubs/1992/110>

- [24] X. Wang and M. Haenggi, “The Chebyshev-Markov inequalities,” Univ. Notre Dame, Notre Dame, IN, USA, Tech. Rep., 2022. Accessed: Sep. 2, 2024. [Online]. Available: https://www3.nd.edu/~mhaenggi/pubs/techreport_cm22.pdf
- [25] S. Foss, D. Korshunov, and S. Zachary, *An Introduction to Heavy-Tailed and Subexponential Distributions* (Springer Series in Operations Research and Financial Engineering), 2nd ed., New York, NY, USA: Springer, 2013.
- [26] G. Navas-Palencia, “Fast and accurate algorithm for the generalized exponential integral $E_v(x)$ for positive real order,” *Numer. Algorithms*, vol. 77, no. 2, pp. 603–630, Feb. 2018.
- [27] H. Alzer, “On some inequalities for the incomplete gamma function,” *Math. Comput.*, vol. 66, no. 218, pp. 771–778, 1997. [Online]. Available: <https://api.semanticscholar.org/CorpusID>
- [28] C. Candan. (2012). *A Simple Proof of ${}_3F_2(1,1,1;2,2;\rho) = \text{dilog}(1-\rho)/\rho$* . Accessed: Sep. 18, 2024. [Online]. Available: https://users.metu.edu.tr/ccandan/pub_dir/hyper_rel.pdf



Ilari Angervuori (Student Member, IEEE) received the B.Sc. and M.Sc. degrees (Hons.) in applied mathematics from the University of Helsinki, Finland, in 2016 and 2018, respectively. He is currently pursuing the Ph.D. degree with the School of Electrical Engineering, Aalto University, under the supervision of Prof. Risto Wichman. Since 2018, he has been with the School of Electrical Engineering, Aalto University, as a Research Assistant. From Summer 2023 to Winter 2024, he was a Visiting Researcher with the University of Notre Dame, under the supervision of Prof. Martin Haenggi. His Ph.D. research subject is stochastic geometry in LEO networks. He thrives on tractable system models and clear analytical insights regarding the nature and performance of terrestrial-LEO communication. He is one of the pioneering authors in stochastic geometry modeling of LEO, mostly specialized in the uplink, and has been well-recognized and cited. Other aerial base stations, heterogeneous networks, including small cells and mmWaves, MIMO, intelligent reflecting surfaces, and their adaptations in aerial communications are in his interest—only some to mention—and he is currently looking for new challenges and opportunities in the industry or academia, particularly regarding the system-level (and why not link-level) design and modeling. He believes in global connectivity among the people to better the world, and the environmental and ethical factors further challenge the development of communication systems.



Martin Haenggi (Fellow, IEEE) received the Dipl.-Ing. (M.Sc.) and Dr.sc.techn. (Ph.D.) degrees in electrical engineering from the Swiss Federal Institute of Technology, Zürich (ETHZ), in 1995 and 1999, respectively. From 2007 to 2008, he was a Visiting Professor with the University of California at San Diego. From 2014 to 2015, he was an Invited Professor with EPFL, Switzerland, and from 2021 to 2022, he was a Guest Professor with ETHZ. Currently, he is the Freimann Professor of electrical engineering and a Concurrent Professor of applied and computational mathematics and statistics with the University of Notre Dame, Notre Dame, IN, USA. He is the co-author of the monographs *Interference in Large Wireless Networks* (NOW Publishers, 2009) and *Stochastic Geometry Analysis of Cellular Networks* (Cambridge University Press, 2018) and the author of the textbook *Stochastic Geometry for Wireless Networks* (Cambridge, 2012) and the blog stogblog.net. His scientific research interests include networking and wireless communications, with an emphasis on cellular, amorphous, ad hoc (including D2D and M2M), cognitive, vehicular, and wirelessly powered networks. He was a Steering Committee Member of TMC. For both his M.Sc. and Ph.D. theses, he was awarded the ETH Medal. He also received the CAREER Award from the U.S. National Science Foundation in 2005 and three paper awards from the IEEE Communications Society, the 2010 Best Tutorial Paper Award, the 2017 Stephen O. Rice Prize Paper Award, and the 2017 Best Survey Paper Award, and he is a Clarivate Analytics Highly Cited Researcher. He was the Chair of the Executive Editorial Committee of IEEE TRANSACTIONS ON WIRELESS COMMUNICATIONS (TWC). He served as an Associate Editor for *Journal of Ad Hoc Networks* (Elsevier), IEEE TRANSACTIONS ON MOBILE COMPUTING (TMC), and *ACM Transactions on Sensor Networks*, and a Guest Editor for IEEE JOURNAL ON SELECTED AREAS IN COMMUNICATIONS, IEEE TRANSACTIONS ON VEHICULAR TECHNOLOGY, and EURASIP Journal on Wireless Communications and Networking. From 2017 to 2018, he was the Editor-in-Chief of IEEE TRANSACTIONS ON WIRELESS COMMUNICATIONS.



Risto Wichman (Senior Member, IEEE) received the M.Sc. and D.Sc. (Tech.) degrees in electrical engineering from Tampere University of Technology, Finland, in 1990 and 1995, respectively. From 1995 to 2001, he was with the Nokia Research Center as a Senior Research Engineer. In 2002, he joined the Department of Information and Communications Engineering, School of Electrical Engineering, Aalto University, Finland, where he has been a Full Professor since 2008. His research interests include the physical layer of wireless communication systems, specifically in signal processing and communication theory.

Publication IV

I. Angervuori and R. Wichman. Order statistics of the SIR and Interference Cancellation in a Narrow-Beam LEO Uplink. Submitted to *IEEE Letters on communications*, 2025.

© 2025

Reprinted with permission.

Order Statistics of the SIR and Interference Cancellation in a Narrow-Beam LEO Uplink

Ilari Angervuori, *Student Member, IEEE* and Risto Wichman, *Senior Member, IEEE*

Abstract—We investigate the factorial moment measure of the signal-to-interference ratios (SIR) at the typical low Earth orbit satellite base station (SBS) with a narrow Gaussian antenna serving an urban area, with a Gaussian mixture shadowing model. This SIR process is characterized by a Poisson-Dirichlet distribution $\text{PD}(0, \cdot)$, which allows us to derive the density of the factorial moment measure. We analyze the coverage probability at the typical SBS receiving the three strongest signals and implement successive interference cancellation (SIC). Our results demonstrate that SIC can notably reduce the variance of the SIR while maintaining robust performance.

I. INTRODUCTION AND MOTIVATION

Successive interference cancellation (SIC) techniques are used in non-orthogonal multiple access (NOMA) methods. In this regard, while the order statistics of the signal-to-interference (SIR) under interference cancellation (and signal combination) have been studied for terrestrial networks [1] by using stochastic geometry, they are yet to be explored in low Earth orbit (LEO) networks. We study the SIR of user equipments (UEs) at the typical LEO base station (BS) by utilizing the narrow-beam LEO uplink system model from [2] in an urban environment. We utilize the Gaussian Mixture shadowing model, similar to [3] and [4], using the parameters presented in [5]. The density of the factorial moment measure of the signal-to-total-interference (STIR) process follows a Poisson-Dirichlet distribution $\text{PD}(0, \cdot)$ (contrary to $\text{PD}(\cdot, 0)$ in [1]), of which the factorial moment measure is well-known. We derive the joint PDF of the STIR and SIR and study the performance metrics of the three strongest UE signals with and without SIC. In [2], it was observed that the system parameters optimizing the average throughput, corresponding to mean $\log(2)$ user equipments (UEs) inside a satellite base station SBS -3 dB footprint, lead to a high variation in the SIR over the SBSs. We demonstrate that the link is more stable with interference cancellation. We show that with the SIC, the number of UEs inside a SBS -3 dB footprint can be doubled while maintaining the average performance of the strongest UE, but profoundly reducing the variance in the SIR. Furthermore, the coverage probability of UEs with weaker signals drastically improves.

The proposed methods straightforwardly generalize to signal combination: An emerging topic in the LEO networks utilizing over-the-air computation (AirComp).

The work was supported by the Research Council of Finland Grant 339446.

Ilari Angervuori and Risto Wichman are with the Department of Electrical Engineering, Aalto University, Espoo, 02150, Finland. (email: ilari.angervuori@aalto.fi; risto.wichman@aalto.fi).

TABLE I: Principal symbols the values and units in the numerical results. We denote (approximate) proportionality “ \propto ” or equality “ $=$ ” to a variable. For a dimensional number, we denote the units “SI” and “[non-SI].”

Symbol	Explanation	Values and units
h	Receiving SBS altitudes.	1000 km
α	Power path loss exponent.	4
λ	The density of Φ and Θ , <i>i.e.</i> , the mean number of UEs inside an unit area.	{0.83, 13.3}
ϵ	The typical SBS elevation angle w.r.t o .	$10^{-4}/\text{km}^2$
p_{LoS}	LoS probability; $p_{\text{LoS}} \propto \sin(\epsilon)$.	$(\pi/2, \pi/6)$ rad
μ_{LoS}	Mean of the LoS component of the Gaussian mixture shadow fading model.	$= (90, 30)^{\circ}$ (0.992, 0.493)
μ_{NLoS}	Mean of the NLoS component.	0 [dB]
σ_{LoS}^2	Variance of the LoS component.	-26 [dB]
σ_{NLoS}^2	Variance of the NLoS component.	4^2 [dB]
φ_{RX}	Half-width of the -3 dB antenna gain.	6^2 [dB]
κ	Average number of UEs inside a -3 dB footprint; $\kappa = \pi\lambda (\varphi_{\text{RX}} h / \sin^2(\epsilon))^2$.	$0.028 = 1.6^{\circ}$ (1.63, 6.51)
v	Fraction of effective UEs; $v \propto \sin(\epsilon)$.	(0.85, 0.426)
κv	Average number of effective UEs inside a -3 dB footprint.	$\{2, 4\} \times \log(2)$
$\tilde{\kappa}$	$\kappa / \log(2)$.	
θ	SIR threshold of a successful transmission.	$(0.2, 10) = (-7, 10)$ [dB]
τ	SIR threshold of a successful interference cancellation.	0.2 = -7 [dB]

II. SYSTEM MODEL

A narrow-band LEO uplink is considered. The UEs follow a homogeneous PPP $\Phi \subset \mathbb{R}^2$ of density λ . The SBSs form a homogeneous point process (p.p.) possibly with a different density than the UEs. Because of the translation invariancy of the PPP, all locations are statistically equivalent, and we define the origin o to represent *the typical SBS footprint focus point*.

The path loss, representing the antenna gain at the typical SBS, is given over the planar distance $r \in [0, \infty)$ as a Gaussian function

$$G(r) = 2^{-(D_{h,\epsilon} r)^2 / \varphi_{\text{RX}}^2}. \quad (1)$$

The angle φ_{RX} denotes the -3 dB antenna gain width. Furthermore, the scaling constant $D_{h,\epsilon} \triangleq \sin^2(\epsilon)/h$ is a first-order coefficient of the Taylor expansion of the angle φ_r w.r.t. the boresight of the typical antenna pattern. (Thorough details in [2].)

A. Shadowing

1) Gaussian mixture shadowing model

Consider a two-tier $\{\text{LoS}, \text{NLoS}\}$ (line-of-sight and non-line-of-sight) Gaussian mixture shadow fading model with the parameters $\mu_{\text{LoS}} = 0$ dB, $\sigma_{\text{LoS}} = 4$ dB, $\mu_{\text{NLoS}} = -26$ dB, and

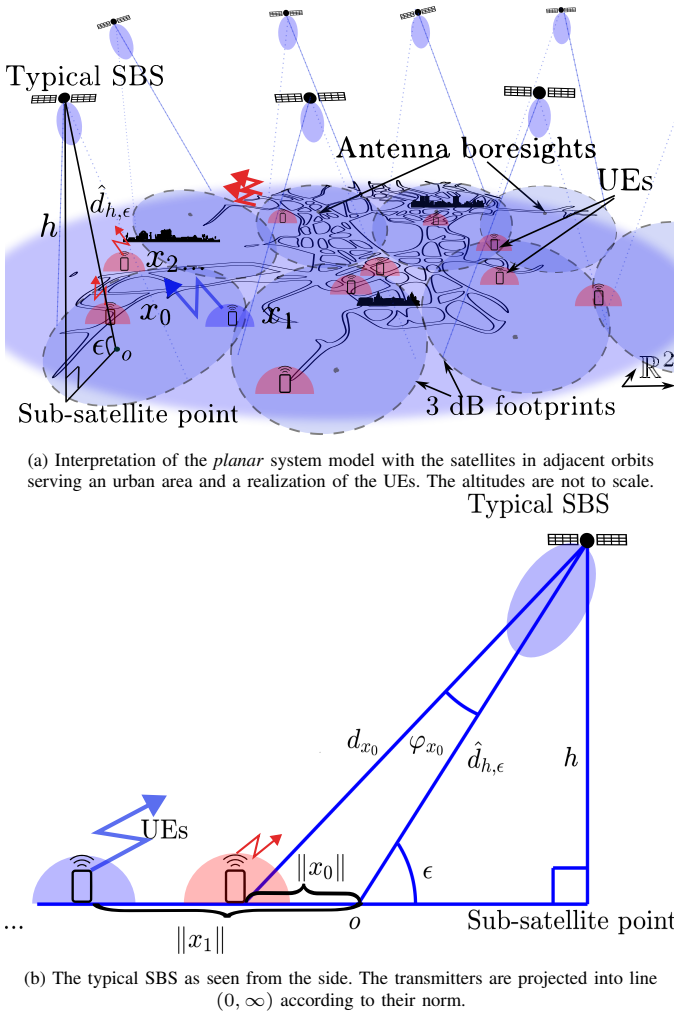


Fig. 1: The simplified narrow-beam LEO uplink system model. The satellite antenna boresight is oriented towards ϵ , the focus point of the elliptical footprint. The omnidirectionally transmitting UEs $\{x_i\}$ are located according to the homogeneous PPP on the plane. The transmitter with the strongest signal is the first-served UE.

$\sigma_{\text{NLoS}} = 6 \text{ dB}$, which correspond to an urban environment [5]. Assuming i.i.d. power shadow fading for all UEs, the typical shadowed transmit power $H_{\mathcal{MLN}}$ follows a log-normal mixture distribution;

$$H_{\mathcal{MLN}} \sim p_{\text{LoS}} \mathcal{LN}(\rho \mu_{\text{LoS}}, (\rho \sigma_{\text{LoS}})^2) + p_{\text{NLoS}} \mathcal{LN}(\rho \mu_{\text{NLoS}}, (\rho \sigma_{\text{NLoS}})^2), \quad (2)$$

where $p_{\text{LoS}} = 1 - p_{\text{NLoS}}$ is the LoS probability as in Figure 2b. Considering a natural base for the log-normal distribution, the constant $\rho \triangleq \log(10)/10$ normalizes the parameters μ_{LoS} , σ_{LoS} , μ_{NLoS} , and σ_{NLoS} , ensuring that the conditioned r.v.'s $10 \log_{10}(H_{\mathcal{MLN}}|\text{LoS})$ and $10 \log_{10}(H_{\mathcal{MLN}}|\text{NLoS})$ evaluate to r.v.'s following the normal distributions $\mathcal{N}(\mu_{\text{LoS}}, \sigma_{\text{LoS}}^2)$ and $\mathcal{N}(\mu_{\text{NLoS}}, \sigma_{\text{NLoS}}^2)$, respectively.

2) Defective exponential shadowing distribution

As a compromise between analytical tractability and realism, we introduce a *defective* exponential power fading distribution for the UEs, described by the distribution function

$$F_{H_{\text{Exp}}}(t) = ve^{-t}, t > 0. \quad (3)$$

Essentially, this is a mixture distribution. Namely, $0 \leq 1 - v < 1$ denotes the probability that the shadowed signal is entirely attenuated and takes the value of zero, otherwise, the power follows the exponential distribution.

We introduce a scaling term, Υ , to ensure that the means of the log-normal mixture distribution and the defective exponential distribution match: $\mathbb{E}(\Upsilon H_{\mathcal{MLN}}) = \mathbb{E}(H_{\text{Exp}}) = v$. By equating the first two moments of H_{Exp} (l.h.s.) and $\Upsilon H_{\mathcal{MLN}}$ (r.h.s.)

$$\begin{cases} v = \Upsilon \left(p_{\text{LoS}} e^{\mu_{\text{LoS}} + \sigma_{\text{LoS}}^2/2} + p_{\text{NLoS}} e^{\mu_{\text{NLoS}} + \sigma_{\text{NLoS}}^2/2} \right) \\ 2v = \Upsilon^2 \left(p_{\text{LoS}} e^{2(\mu_{\text{LoS}} + \sigma_{\text{LoS}}^2)} + p_{\text{NLoS}} e^{2(\mu_{\text{NLoS}} + \sigma_{\text{NLoS}}^2)} \right), \end{cases} \quad (4)$$

we can solve for the parameter v :

$$v = \frac{2 \left(p_{\text{LoS}} e^{\mu_{\text{LoS}} + \sigma_{\text{LoS}}^2/2} + p_{\text{NLoS}} e^{\mu_{\text{NLoS}} + \sigma_{\text{NLoS}}^2/2} \right)^2}{p_{\text{LoS}} e^{2(\mu_{\text{LoS}} + \sigma_{\text{LoS}}^2)} + p_{\text{NLoS}} e^{2(\mu_{\text{NLoS}} + \sigma_{\text{NLoS}}^2)}}. \quad (5)$$

The parameter $v = v(\epsilon)$ varies with the elevation angle, influencing the shadow fading characteristics. The parameter Υ holds no significance in an interference-limited scenario, as the equal scaling of all UE powers neutralizes its effect.

Remark. The variable $0 < v \leq 1$ is not generally solvable for all log-normal distribution parameters (by matching the first two moments). Broadly speaking, the variance of the shadowing has to be large enough. However, the variable $0 < v \leq 1$ is solvable for almost every shadowing scenario in [5], particularly for the urban scenario.

B. The spherical Earth model in the Monte Carlo simulations

The planar model approximates the spherical system model, where the UEs are located on the spherical Earth surface of radius $R_{\oplus} = 6378 \text{ km}$ according to a homogeneous PPP Θ of density λ represented in spherical coordinates. This p.p. can be constructed from $\Phi \subset \mathbb{R}^2$ by an area preserving mapping. Namely, for $x = (x_1, x_2) \in [-\pi, \pi] \times [-1, 1] \cap \Phi / R_{\oplus}$,

$$(x_1, x_2) \mapsto (R_{\oplus}, x_1, \sin^{-1}(x_2)) = (R_{\oplus}, \theta_{x_1}, \vartheta_{x_2}) \in \Theta. \quad (6)$$

The total interference at the typical SBS from the UEs in the PPP $\Theta \cap E$, with E denoting the area above the horizon of the typical SBS, is defined as

$$\bar{I} \triangleq \sum_{x \in \Theta \cap E} \frac{H_{\mathcal{MLN}} G(\varphi_x)}{(d_x/d_0)^{\alpha}}, \quad (7)$$

where d_0 is a normalizing constant. The simulated values are based on the spherical model, the angle φ_x and distance d_x calculated precisely for each $x \in \Theta \cap E$, and accurate i.i.d. Gaussian mixture shadowing $H_{\mathcal{MLN}} x$.

For a more detailed analysis and planar model comparison to the spherical model, please refer to [2].

III. ANALYSIS

Given i.i.d. shadowing variables $\{H_x\}_{x \in \Phi}$, we define the process of the received signal powers at the typical location, referred to as the gain process (GP), by

$$\mathcal{G} \triangleq \{H_x G(\|x\|) : x \in \Phi\}, \quad (8)$$

where $\|x\|$ is the Euclidean distance from o .

The GP is a *projection process* mapping the points from \mathbb{R}^2 into $(0, \infty)$ and, as such, forms a nonhomogeneous PPP [6, Section 4.2.5].

Since the variables $\{H_x\}_{x \in \Phi}$ are i.i.d., we can denote the typical shadowing variable simply as H without the subscript.

Proposition 1 (Density of the GP). *Let $F_H(\cdot)$ be the (possibly degenerate) complementary cumulative distribution function (CCDF) of a fading variable H . The density function of \mathcal{G} is given by*

$$\lambda_{\mathcal{G}}(t) = \tilde{\kappa} F_H(t)/t, \quad t \in (0, \infty), \quad (9)$$

where $\tilde{\kappa} = \kappa/\log(2)$ and

$$\kappa \triangleq \pi \lambda \left(\frac{\varphi_{RX} h}{\sin^2(\epsilon)} \right)^2 \quad (10)$$

is approximately the average number of UEs inside a -3 dB footprint.

Proof. Let $f_H(\cdot)$ be the PDF of H . Denote $G^{-1}(\cdot)$ as the generalized inverse of G , defined as $G^{-1}(y) = \inf\{x : G(x) < y\}$. According to [6, Eq. 4.55],

$$\begin{aligned} \int_t^\infty \lambda_{\mathcal{G}}(y) dy &= \pi \lambda \mathbb{E} \left[(G^{-1}(t/H))^2 \right] \\ &= \pi \lambda \int_t^\infty \left(-\frac{\varphi_{RX} \sqrt{-\log(t/h)}}{D_{h,\epsilon} \sqrt{\log(2)}} \right)^2 f_H(h) dh \\ &= -\tilde{\kappa} \int_t^\infty \log(t/h) f_H(h) dh \\ &\stackrel{(a)}{=} -\tilde{\kappa} \left[\log(t/h) F_H(h)|_t^\infty + \int_t^\infty \frac{F_H(h)}{h} dh \right]. \end{aligned}$$

In (a), we use integration by parts. The result follows by differentiating with respect to t and applying the negative sign. Note that a necessary condition for this procedure is that $\int_t^\infty \log(t/h) f_H(h) dh$ converges for all $t > 0$.

Please refer to [2, Lemma 1] for throughout explanation of the interpretation of κ . \square

The total interference, or total received power, is defined as the sum of the GP at the footprint location o of the typical SBS:

$$I \triangleq \sum_{x \in \Phi} H_x G(\|x\|) = \sum_{x \in \mathcal{G}} x. \quad (11)$$

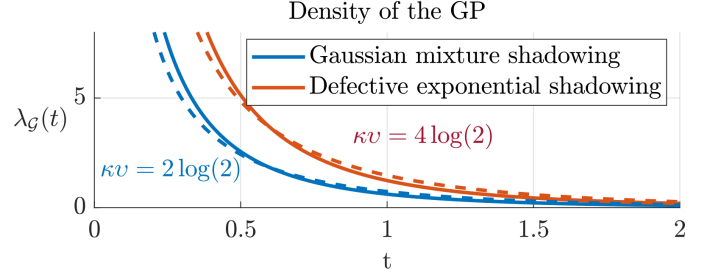
The mean and the variance of I are respectively given by

$$\mathbb{E}(I) = \int_0^\infty t \lambda_{\mathcal{G}}(t) dt = \tilde{\kappa} \int_0^\infty F_H(t) dt = \tilde{\kappa} \mathbb{E}(H), \quad (12)$$

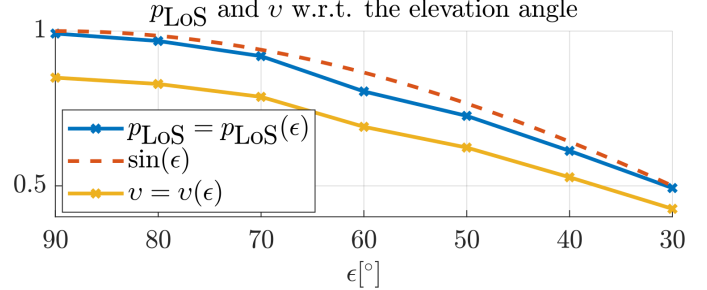
and

$$\begin{aligned} \text{Var}(I) &= \int_0^\infty t^2 \lambda_{\mathcal{G}}(t) dt = \tilde{\kappa} \int_0^\infty t F_H(t) dt \\ &= \tilde{\kappa} \frac{\text{Var}(H) + \mathbb{E}(H)^2}{2} = \tilde{\kappa} \mathbb{E}[H^2]/2. \end{aligned} \quad (13)$$

Note that matching the first two moments of the fading distributions (2) and (3) is equivalent to matching the mean and the variance of the total interference.



(a) The density of the GP for $\kappa v \in \{2 \log(2), 4 \log(2)\}$ using $\epsilon = \pi/2$. Interestingly, the elevation angle did not have visible effect on the density in the Gaussian mixture model.



(b) The dependence of the shadowing parameters p_{LoS} and v on the elevation angle. The parameters are approximately proportional to the sine function.

Fig. 2: The density of the GP and shadowing parameters in the Gaussian mixture and defective exponential shadowing models.

A. Laplace transform of the total received power

With defective exponential shadowing H_{exp} , for $\text{Re}(s) > 1$,

$$\begin{aligned} \mathcal{L}_I(s) &\triangleq \mathbb{E}(e^{-sI}) = \exp \left\{ - \int_0^\infty (1 - e^{-sr}) \lambda_{\mathcal{G}}(r) dr \right\} \\ &= \exp \left\{ -\tilde{\kappa} \int_0^\infty (1 - e^{-sr}) F_{H_{\text{exp}}}(r) / r dr \right\} \\ &= \exp \left\{ -\tilde{\kappa} v \int_0^\infty (1 - e^{-sr}) e^{-r} / r dr \right\} = (1 + s)^{-\tilde{\kappa} v}, \end{aligned} \quad (14)$$

which is the Laplace transform of the gamma distribution with the shape parameter $\tilde{\kappa} v$.

B. Order statistics of the STIR and SIR processes

At the typical SBS, we denote the signal-to-interference ratio (SIR) process of the UEs as follows:

$$\begin{aligned} \Psi &= \{Z : Z \in \Psi\} \triangleq \left\{ \frac{u}{I - u} : u \in \mathcal{G} \right\} \\ &= \left\{ \frac{H_x G(D_{h,\epsilon} \|x\|)}{I - H_x G(D_{h,\epsilon} \|x\|)} : x \in \Phi \right\}, \end{aligned} \quad (15)$$

where I is defined in (11). Similarly, the signal-to-total-interference ratio (STIR) process is defined as

$$\Psi' = \{Z' : Z' \in \Psi'\} \triangleq \left\{ \frac{u}{I} : u \in \mathcal{G} \right\}. \quad (16)$$

We can always recover the process from another:

$$\Psi = \left\{ \frac{Z'}{1 - Z'} : Z' \in \Psi' \right\}, \quad \Psi' = \left\{ \frac{Z}{1 + Z} : Z \in \Psi \right\}. \quad (17)$$

Let θ denote the SIR threshold for successful transmission. The event $\Psi \ni Z > \theta$ is equivalent to $\Psi' \ni Z' > \theta'$ with $\theta' \triangleq \theta/(1+\theta)$ and $\theta \triangleq \theta'/(1-\theta')$.

We denote $Z'_{(1)} > Z'_{(2)} > Z'_{(3)} \dots$ as the order statistics of the STINR process Ψ' , such that $Z'_{(1)}$ is the largest value in Ψ' . Through the monotonicity of the relations (17), the order statistics of the STIR process are equivalent to the order statistics of the SIR process.

Proposition 2. *The density of the nth factorial moment measure of the STIR process at the typical SBS with a narrow Gaussian antenna beam and Gaussian mixture shadow fading is (approximately) given by*

$$\mu'^{(n)}(t'_1, \dots, t'_n) = (\tilde{\kappa}v)^n \prod_{j=1}^n t'_j{}^{-1} \left(1 - \sum_{j=1}^n t'_j \right)^{\tilde{\kappa}v-1}, \quad (18)$$

whenever $t'_1 > \dots > t'_n$ and $\sum_{i=1}^n t'_i \leq 1$, and 0 otherwise.

Proof. The total interference can be characterized by the gamma process at time $\tilde{\kappa}v$ [7, Eq. 8] (recall (14)). Hence, the STIR process Ψ' can be characterized by a Poisson-Dirichlet distribution $\text{PD}(0, \tilde{\kappa}v)$ that has the given density [8, Eq. 2.3]. \square

The partial densities can be derived from the density of the nth factorial moment measure as [1, Eq. 62]

$$\begin{aligned} & \mu_n^{(n+i)}(z'_1, \dots, z'_n) \\ &= \int_{z'_n}^1 \dots \int_{z'_n}^1 \mu'^{(n+i)}(z'_1, \dots, z'_n, \zeta'_1, \dots, \zeta'_i) d\zeta'_1 \dots d\zeta'_i, \end{aligned} \quad (19)$$

the support of the density being in the region $\sum_{j=1}^n z'_j + iz'_n \leq 1$.

The joint PDF of the n strongest values of the STIR process $(Z'_{(1)}, \dots, Z'_{(n)})$ is given as a series expansion involving the partial densities [1, Eq. 64]

$$f'_{(n)}(z'_1, \dots, z'_n) = \sum_{i=0}^{i_{\max}} \frac{(-1)^i}{i!} \mu_n^{(n+i)}(z'_1, \dots, z'_n), \quad (20)$$

for $z'_1 > z'_2 > \dots > z'_n$ and $f'_{(n)}(z'_1, \dots, z'_n) = 0$ otherwise. The upper bound for the index $i_{\max} < 1/z'_n - n$ corresponds to the non-zero terms of the series expansion.

The n -coverage probability that the first n strongest signals reach the threshold θ is given by

$$\mathcal{P}^{(n)}(\theta) \triangleq \int_{\theta'}^1 \dots \int_{\theta'}^1 f'_{(n)}(z'_1, \dots, z'_n) dz'_1 \dots dz'_n, \quad (21)$$

with $\theta' = \theta/(1+\theta)$ and $i_{\max} < 1/\theta' - n$.

The density of the nth factorial moment measure of the SIR process can be extracted from $\mu'^{(n)}$ [6, Corollary 6.1.3]:

$$\begin{aligned} & \mu^{(n)}(z_1, \dots, z_n) \\ &= \prod_{j=1}^n \frac{1}{(1+z_j)^2} \mu'^{(n)}\left(\frac{z_1}{1+z_1}, \dots, \frac{z_n}{1+z_n}\right) \end{aligned} \quad (22)$$

C. SIR under interference cancellation

Let $(u_{(1)}, \dots, u_{(k)}) \subset \mathcal{G}$ represent an ordered set of points in the GP, where $u_{(1)}$ denotes the strongest signal at the typical SBS. The signals with indices in the set $[k] \triangleq (1, \dots, k)$, $k \geq n$, are canceled from the total interference. We denote the SIR with interference cancellation as

$$\text{SIR}_{n,[k]} \triangleq \frac{u_{(n)}}{I - \sum_{j \in [k]} u_{(j)}}. \quad (23)$$

Let us first study $\text{SIR}_{1,[1]}$. Combining (18), (20), and (22), we can derive a closed-form for the SIR PDF of the strongest signal in the simple coverage region $z \geq 1$: $f_{(1)}(z) = \tilde{\kappa}v(z+1)^{-\tilde{\kappa}v}/z^1$. The second moment of the SIR is bounded by

$$\mathbb{E}(\text{SIR}_{1,[1]}^2) \geq \int_1^\infty f_{(1)}(z) z^2 dz = \frac{2^{1-\tilde{\kappa}v} (\tilde{\kappa}v)^2}{(\tilde{\kappa}v-1)(\tilde{\kappa}v-2)}, \quad (24)$$

which is divergent for $\tilde{\kappa}v \leq 2$, i.e., for less than $2 \log(2)$ effective UEs inside a -3 dB footprint on average, the first and second moments—hence, also the variance—are infinite (or undefined). Despite the strong average SIR, the infinite variance for $\tilde{\kappa}v \leq 2$ is not desirable if we want a consistent user experience in the link quality. We demonstrate that successive interference cancellation (SIC) can improve user fairness.

Under interference cancellation, we have the following identity in terms of the STIR process [1, Eq. 69]:

$$\mathbb{P}(\text{SIR}_{n,[k]} > \theta) = \mathbb{P}\left(Z'_{(n)} + \theta' \sum_{j \in [k] \setminus \{n\}} Z'_{(j)} > \theta'\right). \quad (25)$$

Following the Poisson-Dirichlet order statistics of $Z'_{(1)} > Z'_{(2)} > \dots$, if $Z'_{(1)}$ has a finite variance, each $\{Z'_{(j)}\}_{j \in [k]}$ also has a finite variance, hence $\text{SIR}_{n,[k]}$ has a finite variance.

Finally, we consider the SIR under the (perfect) successive signal cancellation (SIC-SIR). A necessary condition for the successful reception of the n th strongest UE at the typical SBS is that the preceding n signals are successively decoded and removed from the interference. Formally, $\{Z'_m + \tau' \sum_{j=1}^{m-1} Z'_j > \tau'\}$ for all $m \in \{1 \dots n\}$, where the signal detection threshold is denoted as $\tau = \tau'/(1-\tau') \leq \theta$. When the first n signals are successfully removed from the interference, the n th UE is considered covered if $\text{SIR}_{n,[n]} > \theta$. If not, the SIC continues until the $\text{SIR}_{n,[k]} > \theta$ or the maximum number of interference cancellation stages K is reached.

Proposition 3. *Consider the SIC with at most $K \geq n$ interference cancellation stages. The coverage probability of the UE with nth strongest signal is given by*

$$\mathcal{P}_{\text{SIC}}^{(n,K)}(\theta, \tau) \triangleq \sum_{k=n}^K \Delta_{\text{SIC}}^{(n,k)}(\theta, \tau), \quad (26)$$

¹The SIR has a heavy-tailed distribution, cf. [2, Eq. (32)].

where

$$\begin{aligned} \Delta_{\text{SIC}}^{(n,k)}(\theta, \tau) &\triangleq \\ &\times \int_0^1 \cdots \int_0^1 f_{(k)}(z'_1, \dots, z'_k) \prod_{m=1}^k \mathbb{1} \left(z'_m + \tau' \sum_{j=1}^{m-1} z'_j > \tau' \right) \\ &\times \left(\mathbb{1}(k > n) \mathbb{1} \left(z'_n + \theta' \sum_{j \in [k-1] \setminus \{n\}} z'_j < \theta' \right) + \mathbb{1}(k = n) \right) \\ &\times \mathbb{1} \left(z'_n + \theta' \sum_{j \in [k] \setminus \{n\}} z'_j > \theta' \right) dz'_1 \dots dz'_k \end{aligned} \quad (27)$$

with the upper summation limit bounded by $i_{\max} < 1/\tau' - 1 = 1/\tau$.

Proof. The expression follows using the joint PDF of the order statistics (20). Furthermore, the first condition (with the form $\prod \mathbb{1}(\cdot)$) allows the relaxation of i_{\max} . Namely, a necessary condition is $z'_k + \tau' \sum_{j=1}^{k-1} z'_j > \tau'$. By simple algebra, $\sum_{j=1}^{k-1} z_j > 1 - z_k/\tau'$. Recall the condition on the non-zero terms of $\mu'^{(k+i)}$: $\sum_{j=1}^k z'_j + iz'_k = \sum_{j=1}^{k-1} z'_j + z'_k + iz'_k \leq 1$. The condition certainly does not hold if $1 - z_k/\tau' + z'_k + iz'_k > 1$. We arrive at the inequality $z'_k (-1/\tau' + 1 + i) > 0$. Divide both sides by $z'_k > 0$, and the general upper bound of i follows. \square

IV. NUMERICAL RESULTS AND CONCLUSIONS

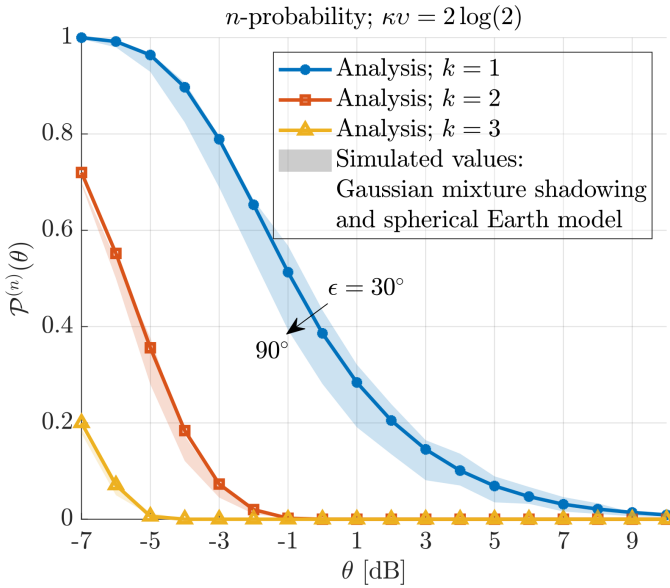


Fig. 3: The n -probabilities for $\kappa v = 2 \log(2)$ (the average number of effective UEs inside a -3 dB footprint).

Figures 3 and 4 depict the n -probabilities (21) and SIC-SIR for $\tilde{\kappa}v = 2$, and $\tilde{\kappa}v = 4$ (27) with $K = 3$, respectively. The signal detection threshold $\tau = -7$ dB. We use the values presented in Table I in the simulations.

The figures illustrate that SIC-SIR can achieve comparable coverage probabilities for the strongest UE within the region $\theta \in (-7, 10)$ dB while doubling the average number of effective UEs inside a -3 dB footprint, denoted as κv . Additionally, the performance of the 2nd and 3rd UEs is significantly

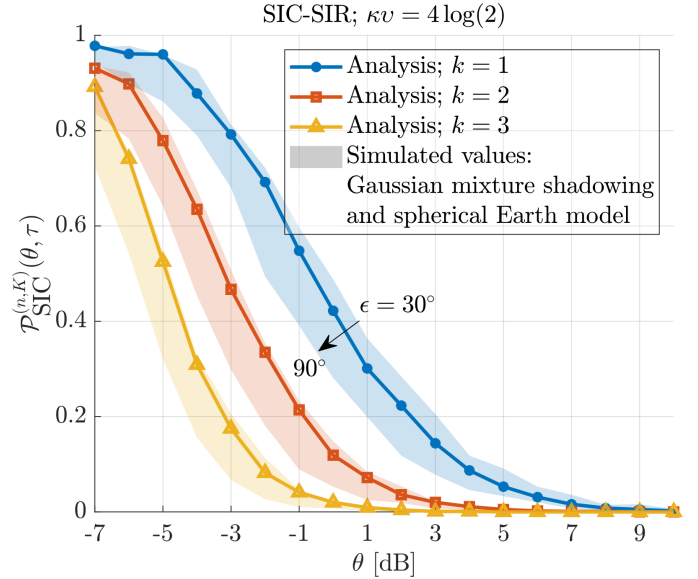


Fig. 4: The SIC-SIR for the transmitters $n \in \{1, 2, 3\}$ by doubling the average number of effective UEs inside the -3 dB footprints compared to Figure 3; $\kappa v = 4 \log(2)$. The SIC parameter $K = 3$.

enhanced. Consequently, a single SBS could potentially serve multiple UEs effectively.

Further, similar to (24), we can calculate an upper bound for the variance of the SIR of the strongest signal before interference cancellation for $\tilde{\kappa}v = 4$: $\text{var}(\text{SIR}_{1,[1]}) = \mathbb{E}(\text{SIR}_{1,[1]}^2) - \mathbb{E}(\text{SIR}_{1,[1]})^2 \leq 1.2$. This represents a significant improvement compared to the infinite variance for $\tilde{\kappa}v = 2$.

We conclude that interference cancellation, particularly successive interference cancellation (SIC), is a viable solution for mitigating the considerable variability in link quality experienced by users in a narrow-beam low Earth orbit (LEO) uplink.

REFERENCES

- [1] B. Blaszczyzyn and H. P. Keeler, "Studying the SINR process of the typical user in poisson networks using its factorial moment measures," *IEEE Transactions on Information Theory*, vol. 61, no. 12, pp. 6774–6794, 2015.
- [2] I. Angervuori, M. Haenggi, and R. Wichman, "Meta distribution of the SIR in a narrow-beam LEO uplink," *IEEE Transactions on Communications*, vol. 73, no. 9, pp. 8260–8273, 2025.
- [3] B. A. Homssi and A. Al-Hourani, "Modeling uplink coverage performance in hybrid satellite-terrestrial networks," *IEEE Communications Letters*, vol. 25, no. 10, pp. 3239–3243, 2021.
- [4] B. Al Homssi and A. Al-Hourani, "Optimal beamwidth and altitude for maximal uplink coverage in satellite networks," *IEEE Wireless Communications Letters*, vol. 11, no. 4, pp. 771–775, 2022.
- [5] 3GPP, "Study on new radio (NR) to support non-terrestrial networks (release 15), TR 38.811," 3GPP, Tech. Rep., 2020.
- [6] B. Blaszczyzyn, M. Haenggi, P. Keeler, and S. Mukherjee, *Stochastic Geometry Analysis of Cellular Networks*. Cambridge University Press, 2018.
- [7] J. Pitman and M. Yor, "The two-parameter poisson-dirichlet distribution derived from a stable subordinator," *The Annals of Probability*, pp. 855–900, 1997.
- [8] K. Handa, "The two-parameter Poisson–Dirichlet point process," *Bernoulli*, vol. 15, no. 4, pp. 1082–1116, 2009. [Online]. Available: <http://www.jstor.org/stable/20680193>

Publication V

I. Angervuori, A. Afidi and R. Wichman. Spatial and Temporal Correlation of the Interference in a Narrow-Beam LEO network with ALOHA Medium Access Control. Submitted to *IEEE Letters on communications*, 2025.

© 2025

Reprinted with permission.

Spatial and Temporal Correlation of the Interference in a Narrow-Beam LEO Network With ALOHA Medium Access Control

Ilari Angervuori, *Student Member, IEEE*, Abid Afidi and Risto Wichman, *Senior Member, IEEE*

Abstract—Interference is a significant limiting factor, particularly in emerging dense Low Earth Orbit (LEO) networks. In the LEO network, the interference is spatially and temporally correlated. Especially at narrow-beam LEO base stations, the spatial variation in the interference can be significant, and multipath fading introduces short-term temporal variation. While developing novel stochastic geometry analysis, we explore the spatio-temporal interference correlation properties in the LEO uplink. Furthermore, we propose an ALOHA medium access control scheme to equalize the performance at each link while preserving the optimal average throughput.

Index Terms—LEO, interference, Poisson point process, correlation coefficient, ALOHA

I. INTRODUCTION

The rapid proliferation of low Earth orbit (LEO) satellite constellations has revolutionized global connectivity, enabling low-latency communications for diverse applications, particularly in narrowband communication. However, the dense LEO networks introduce significant interference challenges, particularly in the uplink, where user terminals compete for limited spectrum resources amid dynamic orbital geometries [1]. This interference experiences significant variation due to the mobility of LEO satellites, leading to time-varying channel conditions. To address these challenges, medium access control (MAC) schemes like ALOHA have been adapted for LEO uplinks, offering simplicity and scalability while aiming to optimize link performance [2]. In particular, slotted ALOHA variants optimize throughput by allocating traffic loads dynamically, mitigating packet collisions in multi-satellite scenarios [3].

Stochastic geometry has emerged as a powerful tool for analyzing these spatio-temporal correlations, providing tractable models for coverage probability, rate, and interference distribution. By treating the transmitters as random point processes, such as the homogeneous Poisson point process (PPP), one can derive closed-form expressions for performance metrics in the terrestrial networks, capturing both long-term spatial dependencies and short-term temporal fluctuations induced by fading [4], [5]. Building on these works, this letter develops a stochastic geometry-based framework to explore spatio-temporal interference properties in the LEO networks, specifically in a LEO uplink. We propose an ALOHA protocol

The work was supported by the Research Council of Finland Grant 339446. Ilari Angervuori, Abid Afidi and Risto Wichman are with the Department of Electrical Engineering, Aalto University, Espoo, 02150, Finland. Emails: {ilari.angervuori;abid.afidi;risto.wichman}@aalto.fi.

that preserves optimal average throughput while ensuring consistent link performance, leading to more resilient LEO networks.

To the best of our knowledge, the correlation functions in the LEO networks are yet to be theoretically explored, at least in the stochastic geometry context.

II. SYSTEM MODEL

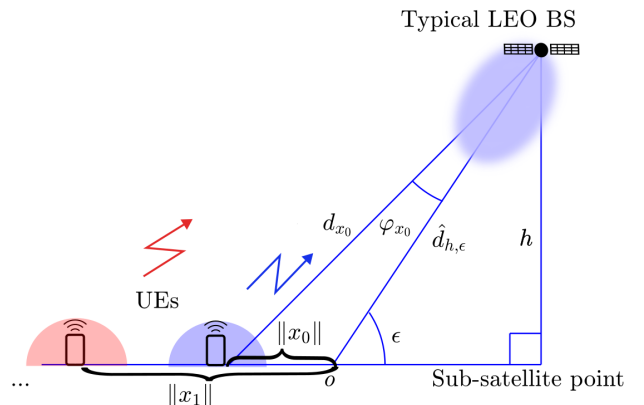


Fig. 1. The typical LEO BS seen from the side. The transmitters are projected into line $(0, \infty)$ according to their norm.

A LEO narrowband uplink is considered with narrow-beamed LEO base stations (BSs). The LEO BSs form a uniform constellation, whereas the Earth transmitters, called user equipments (UEs), form a homogeneous PPP Φ of density λ on the plane \mathbb{R}^2 , and they have omnidirectional antennas. Each LEO BS serves the nearest UE at each time instant. The time instants are coherent regarding fading. We consider an ALOHA medium access control (MAC), and each UE is scheduled to transmit at an independent probability p . Because we assume a narrow Gaussian beam, which decays fast, the UEs are spread in a relatively small area. Hence, the distances between the LEO BS and each (relevant) transmitter are approximated as equal $d_x \approx \hat{d}_{h,\epsilon}$ for all $x \in \Phi$, where h is the altitude of the LEO BS and ϵ is the elevation angle. Since the spatial path losses cancel in the SIR, without loss of generality, we may assume a normalized $\hat{d}_{h,\epsilon}$. Similarly, the transmitting powers are normalized. We study a typical

LEO BS, of which the antenna boresight is directed at origin $o \triangleq (0, 0) \in \mathbb{R}^2$. A sketch of the system model is depicted in Figure 1 (however, h is not to scale).

TABLE I
GLOSSARY OF PRINCIPAL SYMBOLS

Symbol	Explanation
$G(\cdot)$	The LEO BS antenna gain.
φ_{RX}	Halfwidth of the LEO BS -3 dB gain.
$\Phi \subset \mathbb{R}^2$	Homogeneous PPP on the plane.
λ	Density of Φ .
$p \in (0, 1]$	The ALOHA parameter.
$\Phi(k) \subset \Phi$	The homogeneous PPP of the user equipments (UEs) scheduled by the ALOHA at time k .
$H_x = H_x(k)$	The fading gain of mean 1 of a transmitter $x \in \Phi$.
$\mathcal{G}, \mathcal{G}_1$	The gain process (GP)—latter denotation if $H_x \equiv 1$.
$\mathcal{G}(k) \subset \mathcal{G}$	The gain process of the ALOHA scheduled $\Phi(k)$.
$\ x\ $	Distance of $x \in \Phi$ from the origin $o = (0, 0) \in \mathbb{R}^2$.
$x_0 = x_0(k)$	The nearest UE to the typical LEO BS in $\Phi(k)$.
x	A point location $x \in \mathbb{R}^2$.
h	Altitude of the LEO BSs.
ϵ	Elevation angle of the LEO BSs.
$D_{h,\epsilon}$	A scaling constant of $\ x\ $; $D_{h,\epsilon} = \sin^2(\epsilon)/h$.
κ	Parameter that reflects the approximate mean number of UEs inside a LEO BS -3 dB footprint.
$\tilde{\kappa}$	The GP parameter; $\kappa/\log(2)$.
θ	SIR threshold for a successful transmission.
$I_o = I_o(k)$	Total interference at the typical LEO BS at time k .

The Gaussian antenna pattern is defined at the location $x \in \mathbb{R}^2$

$$G(\|x\|) \triangleq 2^{-(D_{h,\epsilon}\|x\|)^2/\varphi_{\text{RX}}^2}, \quad (1)$$

where $\varphi_{\text{RX}} = 0.028$ ($= 1.6^\circ$) corresponds to the -3 dB gain half-width proposed in [6, ITU-R LEO reference radiation patterns]. The scaling constant $D_{h,\epsilon} \triangleq \sin^2(\epsilon)/h \approx \varphi_x/\|x\|$ is the first-order coefficient of the Taylor expansion of the angle φ_x between the antenna boresight and the location $x \in \mathbb{R}^2$. See details in [7][Appendix A].

Let Φ be a homogeneous PPP representing the UEs on the Earth surface. Let $\{H_x\}_{x \in \Phi}$ be i.i.d. RVs with finite variance (representing power fading in this work). The **Gain process** (GP) is defined as the Gaussian projection process

$$\mathcal{G} \triangleq \{H_x G(\|x\|) : x \in \Phi\}. \quad (2)$$

Furthermore, denote $\mathcal{G}_1 \triangleq \{G(\|x\|) : x \in \Phi\}$.

Let $\Phi(k) \subset \Phi$ be the set of transmitting UEs scheduled by the ALOHA at time k . The corresponding GP at the typical LEO BS is denoted as $\mathcal{G}(k) \subset \mathcal{G}$.

The total interference at time instant k at the location $z \in \mathbb{R}^2$ is

$$\begin{aligned} I_z &= I_z(k) \triangleq \sum_{x \in \Phi(k)} H_x(k) G(\|x - z\|) \\ &= \sum_{x \in \Phi} \mathbf{1}(x \in \Phi(k)) H_x(k) G(\|x - z\|), \end{aligned} \quad (3)$$

where $\mathbf{1}(\cdot)$ is the indicator function modeling the ALOHA with the transmission probability p . Each $H_x(k)$ is assumed to be ergodic, and because of the i.i.d. property, we can refer to a typical fading gain (or more generally, a signal) H . Since the homogeneous PPP is translation invariant, the interference at

each point is identically distributed. We denote the interference at the typical LEO BS with

$$I_o(k) = \sum_{x \in \Phi(k)} H_x(k) G(\|x\|) = \sum_{x \in \mathcal{G}_1(k)} H_x(k) x = \sum_{x \in \mathcal{G}(k)} x. \quad (4)$$

The nearest (and served) UE is formally defined as

$$x_0 = x_0(k) \triangleq \arg \min \{x \in \Phi(k) : \|x\|\}. \quad (5)$$

1) The planar system model versus the spherical model:

The proposed planar system model, with simplified spatial path loss, is highly accurate in modeling the aggregate interference power, SIR, and SINR at the narrow-beam LEO BS. The reader can find Monte Carlo simulated comparisons to the respective metrics in a more realistic spherical system model in [7]. The motivation behind the PPP modeling of the UE locations and uniform constellation model is also addressed in the referred paper. Since the total interference and SIR distributions match the realistic system model and no additive approximation layer is introduced, we omit the Monte Carlo simulated comparison metrics in the scope of this letter.

III. ANALYSIS

Corollary 1 (Density of the GP). *The GP with a deterministic $H \equiv 1$ is an inhomogeneous PPP on $(0, 1) \ni t$ with the density*

$$\lambda_{\mathcal{G}_1}(t) \triangleq \tilde{\kappa}/t, \quad (6)$$

where the GP parameter $\tilde{\kappa} = \kappa/\log(2)$ and

$$\kappa \triangleq \pi \lambda \left(\frac{\varphi_{\text{RX}}}{D_{h,\epsilon}} \right)^2 \quad (7)$$

is the average number of UEs inside the -3 dB footprint. Furthermore, for general H , with the support in $(-\infty, \infty) \ni t$

$$\lambda_{\mathcal{G}}(t) \triangleq \frac{\tilde{\kappa} F_H(t)}{t} \Big|_{t \in \mathbb{R}_+} - \frac{\tilde{\kappa}(1 - F_H(t))}{t} \Big|_{t \in \mathbb{R}_-}, \quad (8)$$

where $F_H(t)$ is the CCDF of the RV H .

Proof. See [7][Lemma 1] for the proof of $\lambda_{\mathcal{G}_1}(\cdot)$ and for the interpretation of κ , which is based on simple geometry. The density of general \mathcal{G} is encompassed in the proof of Lemma 2. \square

Lemma 2 (PGFL of the GP). *Let $f(\cdot) : \mathbb{R}_+ \rightarrow [0, 1]$, s.t. $f(x) \rightarrow 1$ as $x \rightarrow \infty$. The probability generating functional (PGFL) of \mathcal{G} is*

$$\mathfrak{G}_{\mathcal{G}}(f) = \mathbb{E} \left(\prod_{x \in \mathcal{G}} f(x) \right) = \exp \left\{ - \int_{-\infty}^{\infty} (1 - f(t)) \lambda_{\mathcal{G}}(t) dt \right\}. \quad (9)$$

Proof. Multiplying each $x \in \mathcal{G}_1 \subset (0, 1)$ by the i.i.d. H_x , the probability kernel [8][Thm. 1.3.9 (Dispacement Theorem)] is $\rho(x, y) = f_H(y/x)/x$, where $f_h(\cdot)$ is the PDF of H . We have

$$\begin{aligned}
& \mathbb{E} \left(\prod_{y \in \mathcal{G}} g(y) \right) = \mathbb{E}_{\mathcal{G}_1} \left(\int_{-\infty}^{\infty} g(y) \prod_{x \in \mathcal{G}_1} \rho(x, y) dy \right) \\
&= \mathbb{E} \left(\prod_{x \in \mathcal{G}_1} \left(\int_{-\infty}^{\infty} g(y) \rho(x, y) dy \right) \right) \\
&\stackrel{(a)}{=} \exp \left\{ -\tilde{\kappa} \int_0^1 \left(1 - \int_{-\infty}^{\infty} g(y) \rho(t, y) dy \right) / t dt \right\} \\
&= \exp \left\{ -\tilde{\kappa} \int_{-\infty}^{\infty} (1 - g(y)) \int_0^1 \rho(t, y) / t dt dy \right\} \\
&= \exp \left\{ -\tilde{\kappa} \int_{-\infty}^{\infty} (1 - g(y)) \int_0^1 f_H(y/t) / t^2 dt dy \right\} \\
&\stackrel{(b)}{=} \exp \left\{ - \int_{-\infty}^{\infty} (1 - g(y)) \lambda_{\mathcal{G}}(y) dy \right\}, \tag{10}
\end{aligned}$$

where in (a) we use the PGFL of \mathcal{G}_1 (see [7][Eq. (15)]). (b) follows by partial integration of the inner integral separately for $y < 0$ and $y > 0$. \square

Corollary 3. *The SIR of the nearest UE signal at the typical LEO BS is given by*

$$\begin{aligned}
\text{SIR} &\triangleq \frac{G(\|x_0\|)}{I_o} = \left(\frac{I_o}{G(\|x_0\|)} \right)^{-1} \\
&= \left(\frac{\sum_{x \in \Phi \setminus \{x_0\}} H_x G(\|x\|)}{H_{x_0} G(\|x_0\|)} \right)^{-1} \\
&= H_{x_0} / \sum_{x \in \mathcal{G}_1} H_x x = H_{x_0} / I_o. \tag{11}
\end{aligned}$$

Proof. The result follows by conditioning $x_0 = o$ and applying Slivnyak's theorem on the ratio $G(\|x\|)/G(\|x_0\|)$. See details in [7][Lemma 1]. \square

Remark 1. Indeed, the SIR representation (11) is equivalent to conditioning the nearest UE at o (when $G(\|x_0\|) = 1$): it follows that the SIR distribution does not depend on the location distribution of the nearest UE, which can also be conditioned arbitrarily at any location as long as the other transmitters form a homogeneous PPP outside that distance. This peculiar property is due to the Gaussian form of the path loss (gain) $G(\cdot)$.

IV. SPATIAL CORRELATION

The first and second-order statistics of the total interference are up to constants determined by the corresponding statistics of the typical signal H :

Theorem 4 (Mean and the variance of the total interference). *Assume that the mean and the average second power*

$|\mathbb{E}(H)|, \mathbb{E}(H^2) < \infty$, respectively. The mean and the variance of the total interference are

$$\mathbb{E}(I_o) = \mathbb{E} \left(\sum_{x \in \mathcal{G}} x \right) \stackrel{(a)}{=} \int_0^1 \lambda_{\mathcal{G}}(x) dx = \tilde{\kappa} \mathbb{E}(H), \tag{12}$$

$$\begin{aligned}
\text{var}(I_o) &= \text{var} \left(\sum_{x \in \mathcal{G}} x \right) \stackrel{(b)}{=} \int_{-\infty}^{\infty} x^2 \lambda_{\mathcal{G}}(x) dx \\
&= \tilde{\kappa} \left(\int_0^{\infty} x F_H(x) dx - \int_{-\infty}^0 x(1 - F_H(x)) dx \right) \\
&= \tilde{\kappa} \mathbb{E}(H^2)/2. \tag{13}
\end{aligned}$$

Proof. The integral identities (a) and (b) for the mean and the variance of the sum of the PPP can be found in [9, Cor. 4.8]. \square

Denote $c \triangleq \|u - v\|$, where $u, v \in \mathbb{R}^2$. The spatio-temporal correlation coefficient of the interferences $I_u(k)$ and $I_v(l)$ is

$$\begin{aligned}
\zeta(u, v) &= \zeta(\|u - v\|) = \zeta(c) \\
&\triangleq \mathbb{E}((I_u(k) - \mathbb{E}(I_o))(I_v(l) - \mathbb{E}(I_o))) / \text{var}(I_o) \\
&= \mathbb{E} \left(\sum_{x \in \Phi(k)} H_x(k) 2^{-(D_{h,\epsilon}\|x-u\|)^2/\varphi_{\text{RX}}^2} \times \right. \\
&\quad \left. \sum_{y \in \Phi(l)} H_y(l) 2^{-(D_{h,\epsilon}\|y-v\|)^2/\varphi_{\text{RX}}^2} \right) / \text{var}(I_o) \\
&= \frac{p^2 \mathbb{E}(H)^2 \lambda}{p \tilde{\kappa} \mathbb{E}(H^2)/2} \int_{\mathbb{R}^2} 2^{-(D_{h,\epsilon}\|x\|)^2/\varphi_{\text{RX}}^2 - (D_{h,\epsilon}\|x-c\|)^2/\varphi_{\text{RX}}^2} dx \\
&= \frac{p \lambda}{\tilde{\kappa} \mathbb{E}(H^2)/2} \frac{\tilde{\kappa}}{2 \lambda} \exp \left\{ -(D_{h,\epsilon} c)^2 / \varphi_{\text{RX}}^2 \log(2) \right\} \\
&= \frac{p}{\mathbb{E}(H^2)} \exp \left\{ -(D_{h,\epsilon} c)^2 / \varphi_{\text{RX}}^2 \log(2) \right\}. \tag{14}
\end{aligned}$$

In Figure 2, the spatial correlation coefficient is plotted for various altitudes (c.f., [5]). The Gaussian correlation reflects the antenna gain at each location.

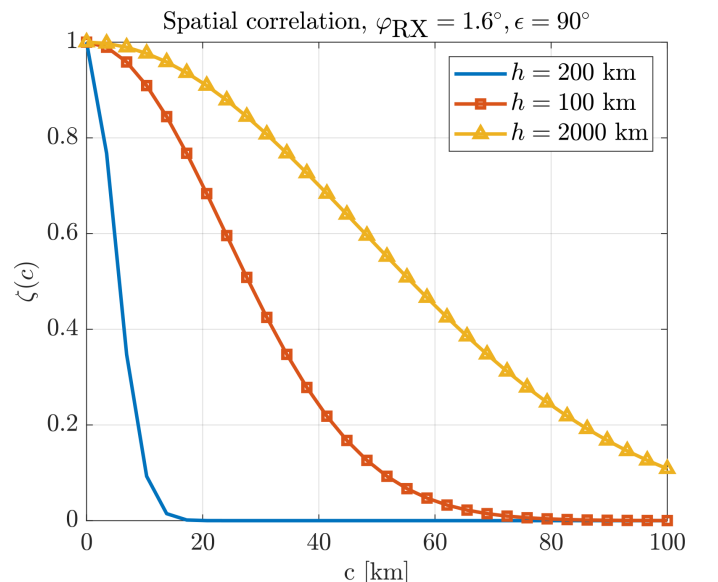


Fig. 2. The spatial correlation at altitudes $h \in \{200, 1000, 2000\}$ km, $H_x \equiv 1, p = 1$.

V. TEMPORAL CORRELATION OF LINK OUTAGES

Let A_k denote the event that the nearest UE SIR exceeds the threshold θ at time instant k at the typical LEO BS, *i.e.*,

$$\text{SIR} = H_{x_0}(k) / \sum_{x \in \mathcal{G}_1(k)} H_x(k)x > \theta. \quad (15)$$

The SIR distribution with Rayleigh fading approximates the SIR distribution with general Nakagami- m fading closely in the simple coverage region $\theta > 1$ (see [7][Fig. 6]); hence, we use $H_x \sim \exp(1)$. Similar methods can be used for Nakagami- m fading, should one be interested in general θ .

The joint probability of the sequential events $A_k, A_l, l \neq k$, occurring is as follows (see [5] for an analogous derivation for a terrestrial network).

$$\begin{aligned} & \mathbb{P}(A_k, A_l) \\ &= \mathbb{P}\left(H_{x_0}(k) > \theta \sum_{x \in \mathcal{G}_1(k)} H_x(k)x, H_{x_0}(l) > \theta \sum_{x \in \mathcal{G}_1(l)} H_x(l)x\right) \\ &= \mathbb{E}_{H, \mathcal{G}}\left(\prod_{x \in \mathcal{G}_1(k)} \exp\{-\theta H_x(k)x\}\right) \times \\ & \quad \mathbb{E}_{H, \mathcal{G}}\left(\prod_{x \in \mathcal{G}_1(l)} \exp\{-\theta H_x(l)x\}\right) \\ &\stackrel{(a)}{=} \mathbb{E}_{\mathcal{G}}\left(\prod_{x \in \mathcal{G}_1} \left(\frac{p}{1 + \theta x} + 1 - p\right)^2\right) \\ &\stackrel{(b)}{=} \exp\left\{-\tilde{\kappa} \int_0^1 \left(1 - \left(\frac{p}{1 + \theta r} + 1 - p\right)^2\right) / rdr\right\} \\ &= e^{-p^2 \theta \tilde{\kappa} / (1 + \theta)} (1 + \theta)^{p \tilde{\kappa} (p-2)}. \end{aligned} \quad (16)$$

In (a), we average over the fading RVs (Laplace transform of the exponential RV) and the ALOHA, and (b) is the PGFL of the GP.

Similarly, one can derive¹

$$\mathbb{P}(A_l) = (1 + \theta)^{-p \tilde{\kappa}}, \quad (17)$$

and the conditional probability is

$$\mathbb{P}(A_k | A_l) = \frac{\mathbb{P}(A_k, A_l)}{\mathbb{P}(A_l)} = e^{-p^2 \theta \tilde{\kappa} / (1 + \theta)} (1 + \theta)^{p^2 \tilde{\kappa}} (1 + \theta)^{-p \tilde{\kappa}}. \quad (18)$$

We have $\mathbb{P}(A_k | A_l) > \mathbb{P}(A_l)$; hence, the probability of connecting in the next time instance is more likely if the link is connected at the current time instance: this reflects the property that while some LEO BSs may be constantly in an outage, others serve with a consistently good connection. The link formation of the satellites is correlated across time to various degrees depending on the GP parameter $\tilde{\kappa}$ and the ALOHA parameter p . These notions on the temporal correlation apply as long as the typical LEO BS operates within the spatially correlated region.

Example 1 demonstrates the conditional outage probability for an indefinitely large successful transmission SIR threshold in a non-ALOHA network. The probabilities are independent

of $\tilde{\kappa}$. The limiting probabilities reflect how the outages are significantly temporally correlated and depend on the current states of the links.

Example 1 (The conditional outage probabilities in the non-ALOHA network). *Let $p = 1$. The probability that the link at the typical LEO BS will be in outage if it is connected is*

$$\begin{aligned} \mathbb{P}(A_k^c | A_l) &= \frac{\mathbb{P}(A_k^c, A_l)}{\mathbb{P}(A_l)} = \frac{\mathbb{P}(A_l) - \mathbb{P}(A_k, A_l)}{\mathbb{P}(A_l)} \\ &= \frac{(1 + \theta)^{-\tilde{\kappa}} - e^{-\theta \tilde{\kappa} / (1 + \theta)} (1 + \theta)^{-\tilde{\kappa}}}{(1 + \theta)^{-\tilde{\kappa}}} \\ &= 1 - e^{-\theta \tilde{\kappa} / (1 + \theta)} = 1 - 1/e \approx 0.63 \text{ as } \theta \rightarrow \infty. \end{aligned} \quad (19)$$

On the other hand, the probability that the link will be in outage if it is in outage is, by De Morgan's law,

$$\begin{aligned} \mathbb{P}(A_k^c | A_l^c) &= \frac{\mathbb{P}(A_k^c, A_l^c)}{\mathbb{P}(A_l^c)} = \frac{1 - (\mathbb{P}(A_k) + \mathbb{P}(A_l) - \mathbb{P}(A_k, A_l))}{1 - \mathbb{P}(A_l)} \\ &= \frac{1 - ((1 + \theta)^{-\tilde{\kappa}} + (1 + \theta)^{-\tilde{\kappa}} - e^{-\theta \tilde{\kappa} / (1 + \theta)} (1 + \theta)^{-\tilde{\kappa}})}{1 - (1 + \theta)^{-\tilde{\kappa}}} \\ &= 1 \text{ as } \theta \rightarrow \infty. \end{aligned} \quad (20)$$

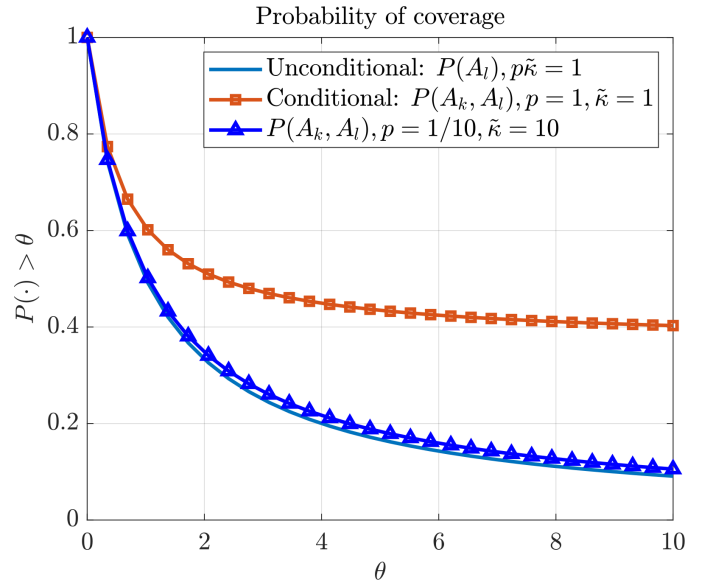


Fig. 3. The conditional and unconditional coverage probabilities for $p\tilde{\kappa} = 1$ with $\tilde{\kappa} \in \{1, 10\}$, and the ALOHA parameter $p \in \{1/10, 1\}$.

A. Maximal average throughput without spatial correlation

The average bandwidth-normalized Shannon throughput of the LEO network is given by

$$\mathbb{E}(\log(1 + \text{SIR})) = 1/(p\tilde{\kappa}). \quad (21)$$

Furthermore, in an interference-plus-noise-limited channel (or a channel with sidelobe interference), the optimal throughput is given for $p\tilde{\kappa} \approx 1$ (which means, on average, $\kappa \approx \log(2) \approx 0.7$ UEs in a -3 dB footprint area). Accordingly, the optimal throughput over the LEO BSs for small noise values is $\mathbb{E}(\log(1 + \text{SIR})) \approx 1$. However, due to the significant spatial

¹The SIR distribution is the Lomax distribution with shape parameter $p\tilde{\kappa}$.

variation in the interference, some of the LEO BSs serve transmitters with a high (average) throughput, and others serve with a low (average) throughput, as long as they remain in the spatially correlated region. This notion is made precise in the meta distribution analysis in [7].

Utilizing ALOHA with a suitable transmission probability p , we can remove the spatio-temporal correlation between the SIRs and improve consistency in the throughput across the network, while preserving the average throughput. Namely, set $p = 1/\tilde{\kappa}$. Then the throughput $\mathbb{E}(\log(1 + \text{SIR})) = 1$, but it is easy to see that

$$\mathbb{P}(A_k, A_l) = \mathbb{P}(A_k)\mathbb{P}(A_l) \quad (22)$$

in the limit $\tilde{\kappa} \rightarrow \infty$. That is, the distributions of the SIR and the throughput of sequential transmissions are independent: Conditioning on any constellation configuration, the temporal average throughput, averaged over sufficiently many transmissions, at each LEO BS is equivalent.

Example 2 (An equivalent ALOHA network). Let $\varphi_{\text{RX}} = 0.0278$, $\epsilon = \pi/2$, $h = 200$ km, and $\lambda = 10^{-2}/\text{km}^2$. The GP parameter is

$$\tilde{\kappa} = \pi\lambda \left(\frac{\varphi_{\text{RX}}}{\sin^2(\epsilon)/h} \right)^2 \approx 1,$$

which is also the average network throughput. To stabilize the performance of each LEO BS while preserving the average throughput, we can make the number of co-channel transmissions ten times denser, $\lambda = 10^{-1}$, and set the ALOHA scheduling at $p = 1/10$.

In Figure 3, we plot the unconditional and conditional coverage probabilities for various $\tilde{\kappa}$ and p . In each plot, $p\tilde{\kappa} = 1$, which corresponds to optimal network throughput. One can see that increasing $\tilde{\kappa}$ (while decreasing p) causes the conditional distribution $\mathbb{P}(A_k, A_l) > \theta$ to approach the unconditional distribution $\mathbb{P}(A_k) > \theta$.

VI. CONCLUSIONS

To wrap up the observations:

- 1) The spatial correlation coefficient of the interference at the typical LEO BS has a simple Gaussian form, (14).
- 2) Should the link be in outage, the probability that it continues to be in outage is increased compared to a connected link (Example 1).
- 3) The ALOHA scheduling can mitigate the temporal (and spatial) correlation in the SIR while preserving the average network performance (22).
- 4) On the downside, this entails increasingly frequent handovers at the typical LEO BS from a served user equipment (UE) to another (the less correlation in the SIR, the more frequent handovers are required).

In this paper, we have derived the spatial and temporal interference correlations in an ALOHA LEO network. We have proved that the outages are temporally correlated, and the average performance of the LEO BSs serving the nearest UE at each time instant can vary significantly over the network. However, the temporal correlation can be mitigated by an

appropriate ALOHA scheduling while preserving the average network throughput, leading—instead of wasting potential throughput resources—to a more consistent LEO BS performance. The system-level insight acquired by the stochastic geometry analysis has a firm role in a better general view and the design of the modern LEO networks, in optimizing the performance.

1) Model variations and extensions: The proposed interference model is general and can be straightforwardly applied to arbitrary fading distributions, shadowing, weather attenuation, the Doppler effect, intercell or intracell, etc., as long as the signal variance remains finite. Furthermore, the interference model applies to amplitude modeling and to arbitrary typical interfering UE signal waveforms or the envelope amplitude. In this regard, the proposed model and the derived first and second-order statistics of the interference—that have the strikingly simple closed forms—can be utilized for theoretical, even closed-form estimates of the interference waveform distribution, the temporal and spatial correlation functions, and, further, to derive and study the interference power spectral density and other channel characteristics at the typical narrow-beam LEO BS (moving at its orbital speed).² Regarding statistical signal processing, including implementations that utilize machine learning, such comprehensive and tractable a priori interference estimations are highly valuable, for which we put forth a tractable framework.

The model also translates to a downlink, considering that the LEO BS footprint locations follow a homogeneous PPP on the Earth's surface.

REFERENCES

- [1] A. Talgat, M. A. Kishk, and M.-S. Alouini, “Stochastic geometry-based uplink performance analysis of IoT over LEO satellite communication,” *IEEE Transactions on Aerospace and Electronic Systems*, vol. 60, no. 4, pp. 4198–4213, 2024.
- [2] F. A. Tondo, V. D. P. Souto, O. L. A. Lopez, S. Montejo-Sanchez, S. Cespedes, and R. D. Souza, “Optimal traffic load allocation for aloha-based IoT LEO constellations,” *IEEE Sensors Journal*, vol. 23, no. 3, pp. 3270–3282, 2022.
- [3] Z. Chabou, A. Addaim, and A. Ait Madi, “Enhancing performance of slotted ALOHA protocol for IoT covered by constellation low-earth orbit satellites,” *Bulletin of Electrical Engineering and Informatics*, vol. 13, no. 6, pp. 4030–4040, 2024.
- [4] X. Lu, M. Salehi, M. Haenggi, E. Hossain, and H. Jiang, “Stochastic geometry analysis of spatial-temporal performance in wireless networks: A tutorial,” *IEEE Communications Surveys & Tutorials*, vol. 23, no. 4, pp. 2753–2801, 2021.
- [5] R. K. Ganti and M. Haenggi, “Spatial and temporal correlation of the interference in ALOHA ad hoc networks,” *IEEE Communications Letters*, vol. 13, no. 9, pp. 631–633, 2009.
- [6] International Telecommunication Union, “Satellite antenna radiation patterns for non-geostationary orbit satellite antennas operating in the fixed-satellite service below 30 GHz,” ITU-R, Recommendation S.1528, 2001. [Online]. Available: https://www.itu.int/dms_pubrec/itu-r/rec/s/R-REC-S.1528-0-200106-I/PDF-E.pdf
- [7] I. Angervuori, M. Haenggi, and R. Wichman, “Meta distribution of the SIR in a narrow-beam LEO uplink,” *IEEE Transactions on Communications*, vol. 73, no. 9, pp. 8260–8273, 2025.
- [8] B. B. François Baccelli, *Stochastic Geometry and Wireless Networks*. Now Publishers, 2009, vol. 1. [Online]. Available: <https://hal.inria.fr/inria-00403039v4>
- [9] M. Haenggi, *Stochastic geometry for wireless networks*. Cambridge: Cambridge University Press, 2013.

²The temporal interference correlation function due to the satellite movement is directly determined by the spatial correlation, since the well-defined orbital speed.